NIST Technical Note 1438

Optical Radiation Measurement with Selected Detectors and Matched Electronic Circuits Between 200 nm and 20 μm

George P. Eppeldauer, Editor

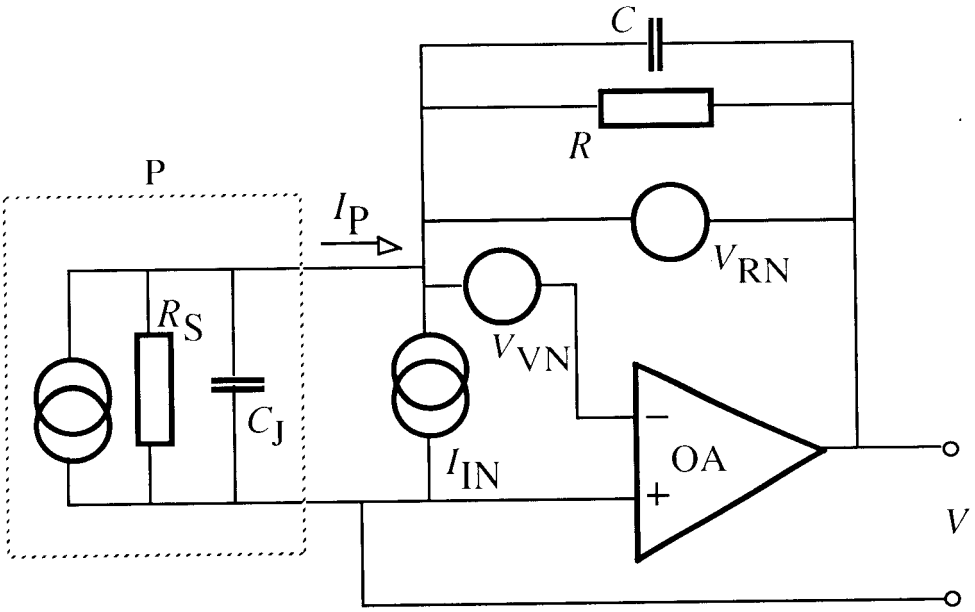

National Institute of Standards and Technology
Technology Administration, U.S. Department of Commerce

The National Institute of Standards and Technology was established in 1988 by Congress to "assist industry in the development of technology . . . needed to improve product quality, to modernize manufacturing processes, to ensure product reliability . . . and to facilitate rapid commercialization . . . of products based on new scientific discoveries."

NIST, originally founded as the National Bureau of Standards in 1901, works to strengthen U.S. industry's competitiveness; advance science and engineering; and improve public health, safety, and the environment. One of the agency's basic functions is to develop, maintain, and retain custody of the national standards of measurement, and provide the means and methods for comparing standards used in science, engineering, manufacturing, commerce, industry, and education with the standards adopted or recognized by the Federal Government.

As an agency of the U.S. Commerce Department's Technology Administration, NIST conducts basic and applied research in the physical sciences and engineering, and develops measurement techniques, test methods, standards, and related services. The Institute does generic and precompetitive work on new and advanced technologies. NIST's research facilities are located at Gaithersburg, MD 20899, and at Boulder, CO 80303. Major technical operating units and their principal activities are listed below. For more information contact the Publications and Program Inquiries Desk, 301-975-3058.

Office of the Director
- National Quality Program
- International and Academic Affairs

Technology Services
- Standards Services
- Technology Partnerships
- Measurement Services
- Information Services

Advanced Technology Program
- Economic Assessment
- Information Technology and Applications
- Chemistry and Life Sciences
- Materials and Manufacturing Technology
- Electronics and Photonics Technology

Manufacturing Extension Partnership Program
- Regional Programs
- National Programs
- Program Development

Electronics and Electrical Engineering Laboratory
- Microelectronics
- Law Enforcement Standards
- Electricity
- Semiconductor Electronics
- Radio-Frequency Technology[1]
- Electromagnetic Technology[1]
- Optoelectronics[1]

Materials Science and Engineering Laboratory
- Intelligent Processing of Materials
- Ceramics
- Materials Reliability[1]
- Polymers
- Metallurgy
- NIST Center for Neutron Research

Chemical Science and Technology Laboratory
- Biotechnology
- Physical and Chemical Properties[2]
- Analytical Chemistry
- Process Measurements
- Surface and Microanalysis Science

Physics Laboratory
- Electron and Optical Physics
- Atomic Physics
- Optical Technology
- Ionizing Radiation
- Time and Frequency[1]
- Quantum Physics[1]

Manufacturing Engineering Laboratory
- Precision Engineering
- Manufacturing Metrology
- Intelligent Systems
- Fabrication Technology
- Manufacturing Systems Integration

Building and Fire Research Laboratory
- Applied Economics
- Structures
- Building Materials
- Building Environment
- Fire Safety Engineering
- Fire Science

Information Technology Laboratory
- Mathematical and Computational Sciences[2]
- Advanced Network Technologies
- Computer Security
- Information Access
- Convergent Information Systems
- Information Services and Computing
- Software Diagnostics and Conformance Testing
- Statistical Engineering

[1] At Boulder, CO 80303.
[2] Some elements at Boulder, CO.

NIST Technical Note 1438

Optical Radiation Measurement with Selected Detectors and Matched Electronic Circuits Between 200 nm and 20 μm

George P. Eppeldauer, Editor
Optical Technology Division
Physics Laboratory
National Institute of Standards and Technology
Gaithersburg, MD 20899-8440

April 2001

U.S. Department of Commerce
Donald L. Evans, Secretary

Technology Administration
Dr. Karen H. Brown, Acting Under Secretary of Commerce for Technology

National Institute of Standards and Technology
Dr. Karen H. Brown, Acting Under Secretary of Commerce for Technology

Front Cover:
Equivalent circuit of a photodiode current-meter. The feedback impedance, R and C, of an operational amplifier, OA, converts the photocurrent I_P of photodiode P into a voltage V. R and C together with the impedance of the photodiode, R_S and C_J, attenuate V to the OA input. The inverse of this feedback attenuation is the (closed-loop) voltage gain for the OA input drift and noise. Single circles illustrate voltage sources and double circles illustrate current sources. One signal (the photocurrent) source and three noise sources are shown in the circuit. The product of the feedback attenuation and the OA open-loop gain gives the loop gain that determines the uncertainty of the photocurrent-to-voltage conversion at a given signal frequency. Design considerations and performance evaluation of photodiode current-meters are discussed in Papers 1, 3 and 4 for Si photodiodes, in Paper 5 for Si trap detectors, in Paper 6 for Ge and InGaAs photodiodes, and in Paper 7 for InSb photodiodes.

National Institute of Standards
and Technology
Technical Note 1438
Natl. Inst. Stand. Technol.
Tech. Note 1438
117 pages (April 2001)
CODEN: NTNOEF

U.S. Government Printing Office
Washington: 2001

For Sale by the
Superintendent of Documents
U.S. Government Printing Office
Internet: bookstore.gpo.gov
Phone: (202) 512-1800
Fax: (202) 512-2250
Mail: Stop SSOP, Washington, DC
20402-0001

Preface

Improved detector technology in the past decade opened a new era in the field of radiometric and photometric calibrations. Now, cryogenic electrical substitution radiometers with 0.01 % optical power measurement uncertainty are the primary standards of the field. New generation radiometers, built with high electronic and radiometric performance detectors, became the transfer and working standards to propagate the high accuracy from the primary standard to field level measurements. The importance of high quality detector standards has greatly increased as a result of demands in a wide range of technical areas. Nowadays, lamp standards, traditionally calibrated against source standards, are calibrated against detector standards to obtain improved calibration accuracy.

The purpose of this Technical Note is to summarize the results of the research and development work carried out at the Optical Sensor Group of the Optical Technology Division for constructing accurate and wide dynamic range radiometers with high performance detectors for the 200 nm to 20 μm wavelength range. Linear and stable operation was required from these radiometers to achieve detector spectral responsivity transfer with low uncertainty. Large area thermal, pyroelectric, photoconductive (PC), and photovoltaic (PV) detectors were selected, applied, and characterized at different controlled temperatures between 4.2 K and 300 K. The resistance of these detectors ranged from 15 Ω to 50 GΩ, their capacitance ranged from 0.18 nF to 36 nF. The detector output-signal measuring electronic circuits had to be designed and individually matched to the complex impedance of the selected detector to optimize radiometer performance. The frequency dependent fundamental gain-equations of operational-amplifier photocurrent-meters have been worked out and applied for a large number of different types of photodiodes operating in both dc and ac signal measurement modes. The gain equations were utilized to achieve signal measurement uncertainties between 0.1 % and 0.01 % . Drift and noise were minimized for the radiometer outputs to obtain high signal-to-noise ratios even at high signal gains.

The NIST developed radiometer standards are the key components of several recently realized high accuracy scales. These are the spectral power and irradiance responsivity scales on the Spectral Comparator Facilities (for the ultraviolet, visible, and infrared ranges), the spectral power, irradiance, and radiance responsivity scales of the Spectral Irradiance and Radiance Responsivity Calibrations with Uniform Sources Facility (SIRCUS), the detector-based illuminance (photometric) scale, and the spectral irradiance scale (disseminated by lamps).

Related additional papers, describing the input geometry, electronic and radiometric characterizations, and spectral responsivity calibrations of the transfer and working standard radiometers are not included here. These subjects are beyond the scope of this Technical Note.

George P Eppeldauer
Ph.D. Electronics Engineer
Radiometer and Calibration Development
Optical Sensors Group, Optical Technology Division
National Institute of Standards and Technology
100 Bureau Drive, Gaithersburg, MD 20899-8441

Table of Contents

Introduction to the Papers

George P. Eppeldauer

Paper 1

"Fourteen-decade photocurrent measurements with large-area silicon photodiodes at room temperature," Applied Optics, Vol. 30, No.22. 3091-3099, 1991. G. Eppeldauer and J. E. Hardis

The noise and drift characteristics of large area silicon photodiode current meters are analyzed at low (dc) frequencies in this paper. High shunt-resistance silicon photodiodes and operational amplifiers with large feedback resistors were used to achieve high photocurrent sensitivity at room temperature. Operational amplifiers with very low input-bias-current were selected to minimize $1/f$ noise from the amplifier. The dominant resistor noise was equalized to the $1/f$ amplifier noise by decreasing the electrical bandwidth to 1.25 mHz. The drift was also equalized to the noise floor by regulating the temperature of the Si radiometer within +/- 0.02 °C of the operating 25 °C value. The equivalent photocurrent of the measured noise floor was 10^{-16} A at a measurement time of 400 s. This implies a signal measurement range of 14 decades. When the bandwidth was increased to 0.3 Hz, the noise increased and ranged between 0.6 fA and 1 fA.

Paper 2

"Temperature Monitored/Controlled Silicon Photodiodes for Standardization," SPIE Proceedings, Vol. 1479, 71-77, 1991. G. Eppeldauer

The paper describes how to monitor or control the temperature of photodiodes to obtain improved accuracy in photocurrent measurements. Temperature monitored detectors are easier to construct, but they require more calibration data and analysis as well as additional steps to interpret the results of measurements. Temperature regulated detectors make measurement taking simpler, with the expenses of additional and more complex hardware. Design considerations and examples for both methods are described.

Paper 3

"Chopped Radiation Measurement With Large Area Si Photodiodes," Journal of Research of the National Institute of Standards and Technology, Vol. 103, No. 2, 153-162, 1998. G. P. Eppeldauer

The different frequency-dependent gains of photodiode current meters were analyzed in this paper. The gain equations are needed to perform constant (flat) signal-gains up to a high enough roll-off frequency, to understand and minimize the noise-boosting effect with increasing frequencies (this caused the factor of 10 noise increase in Paper 1), and to achieve small uncertainties in the current-to-voltage conversions. The different gain characteristics were illustrated with Bode plots. The Bode plots were made from the gain equations using spread-sheets. Computer simulators were not used. Signal-gain dependent frequency compensations were applied to optimize dc and ac photocurrent measurements with large area Si photodiodes.

Paper 4

"Noise-optimized silicon radiometers," J. Res. Natl. Inst. Stand. Technol. Vol. 105, No. 209, 209-219, 2000. G. Eppeldauer

This paper is an extension of Paper 3. In addition to the design considerations of the dynamic (frequency dependent) characteristics of photodiode current meters, an experimentally verified noise

analysis is described. After optimizing the dynamic characteristics, the noise floor was minimized in an ac measurement mode using Si photodiodes of different shunt resistance and operational amplifiers with low $1/f$ voltage and current noise. An equivalent root-mean-square (rms) photocurrent noise of 8×10^{-17} A was performed at a 9 Hz chopping frequency and 30 s integration time constant. The radiometers, optimized for ac measurements, were tested in a dc measurement mode as well. Performances in ac and dc measurement modes were compared. In the ac mode, a ten times shorter (40 s) overall measurement time was needed than in the dc mode (described in Paper 1) to obtain the same 10^{-16} A noise floor.

Paper 5

"Opto-mechanical and electronic design of a tunnel-trap Si-radiometer," to be published in the J. Res. Natl. Inst. Stand. Technol. G. P. Eppeldauer and D. C. Lynch

The design methods described in Papers 3 and 4 were applied to a transmission-type light-trap silicon detector. Six Si photodiodes of two different sizes, selected for equal shunt resistance, were connected in parallel in this power/irradiance mode transfer standard. The capacitance and the resultant shunt resistance of the device were measured and frequency compensations were applied in the feedback network of the photocurrent-to-voltage converter to optimize signal-, voltage-, and loop-gain characteristics. The trap-radiometer can measure either dc or ac optical radiation with high sensitivity. The noise-equivalent power of the optimized device was 47 fW in dc mode and 5.2 fW at 10 Hz chopping. The deviation from the cosine responsivity in irradiance mode was measured to be equal to or less than 0.02 % within 5° FOV and 0.05 % at 8° FOV. Both the electronic and the optical-mechanical design considerations are discussed in detail.

Paper 6

"Electronic characteristics of Ge and InGaAs radiometers," SPIE, Proceedings, Vol. 3061-97, 833-838, 1997. G. Eppeldauer

Equal size (5 mm diameter) Ge and InGaAs photodiodes were tested in NIST-developed radiometers and compared for sensitivity and stability. The electronic characteristics of the radiometers were measured versus photodiode temperature with a bandwidth of 0.3 Hz. At –30°C, a limit-sensitivity of 22 fA and a dark-current stability of 0.2 pA/16 hours were achieved with the InGaAs radiometer, which was three times better than the results obtained with the Ge radiometer. The frequency dependent gain characteristics were calculated and compared for the two types of radiometer as well. The 36 nF capacitance of the Ge photodiode caused a noise boosting effect (voltage-gain increase) for frequencies higher than 0.3 Hz. Accordingly, the Ge radiometer was restricted for dc signal measurements only. The 0.5 nF capacitance of the InGaAs photodiode did not produce any noise boosting up to about 8 Hz. The 10^4 loop gain at 8 Hz resulted in a 0.01% (coverage factor k=1) current-to-voltage conversion uncertainty. The InGaAs radiometer could measure an 80 Hz signal with a relative uncertainty of 0.1 % (k=1).

Paper 7

"InSb Working Standard Radiometers," Metrologia, Vol. 35, 485-490, 1998. G. P. Eppeldauer, A. L. Migdall, and L. M. Hanssen

Characterization of custom-made transfer standard InSb radiometers is described in this paper. The InSb radiometers maintain the spectral radiant power and irradiance responsivity scales of NIST between 2 μm and 5.4 μm. The field-of-view of the 77 K detectors is limited to 17°. The InSb detectors were selected for high shunt impedance to achieve high sensitivity. The transimpedance-,

voltage-, and loop-gains of the current-to-voltage converters were optimized for optical radiation chopped at 40 Hz. At the peak responsivity, the noise-equivalent-power (NEP) is 0.6 pW in an electrical bandwidth of 0.3 Hz. The ratio of the dc ambient-background-current to the ac noise-equivalent-current is 10^7. Spatial and angular responsivities, linearity, stability, and flashing were also characterized.

Paper 8

"Domain-engineered pyroelectric radiometer," Applied Optics, Vol. 38, No. 34, 7047-7055, 1999. J. Lehman, G. Eppeldauer, J. A. Aust, and M. Racz

A domain-engineered pyroelectric transfer standard radiometer has been developed at NIST to extend the spectral responsivity scale from the visible to the ultraviolet and near-infrared ranges. The domain engineering consisted of inverting the spontaneous polarization over a 10 mm diameter area in the center of a uniformly poled, 15.5 mm x 15.5 mm square, 0.25 mm thick $LiNbO_3$ plate. Gold black was used as the optical absorber on the detector surface, and an aperture was added to define the optically sensitive detector area. The radiometer included a temperature monitor for the detector and a current-to-voltage converter optimized for signal- and loop-gain. The results indicate that the acoustic sensitivity was significantly reduced without loss of optical sensitivity. The detector noise-equivalent-power was not exceptionally low but was nearly constant for different acoustic backgrounds. In addition, the detector's spatial response uniformity variation was less than 0.1 % across the 7.5 mm diameter aperture, and reflectance measurements indicated that the gold black coating was spectrally uniform, within 0.2 %, from 800 nm to 1800 nm. Other detailed evaluations of the radiometer include detector responsivity as a function of temperature, electrical frequency response, angular response, and field of view.

Paper 9

"A cryogenic silicon resistance bolometer for use as an infrared transfer standard detector," in *Thermal Phenomena at Molecular and in Cryogenic Infrared Detectors,* M. Kaviany, D. A. Kaminski, A. Majumdar, P. E. Phelan, M. M. Yovanovich, and Z. M. Zhang, eds., book H00908-1994 (American Society of Mechanical Engineers, New York), pp. 63-67. G. Eppeldauer, A. L. Migdall, and C. L. Cromer

A transfer standard cryogenic bolometer has been developed to maintain the NIST spectral power responsivity scale between 2 μm and 20 μm. The resistance of the heavily doped Si sensor increased six orders of magnitude when it was cooled down from room temperature to the 4.2 K operating temperature. The computer controlled bolometer has high sensitivity, accuracy, stability and dynamic range as well as a large detector area, fast time response and flat spectral response. The design and testing of the silicon composite bolometer is described in this paper. This device has a dynamic range of 5 decades, a noise floor of 36 $pW/Hz^{1/2}$, a nonlinearity of less than 1%, a spatial response nonuniformity of about 0.3% and a constant frequency-dependent response out to about 100 Hz.

Paper 10

"Linear HgCdTe radiometer," SPIE Proceedings, Vol. 1110, 267-273, 1989. G. Eppeldauer and L. Novak

The basic modes of electrical operation of photoconductive optical radiation detectors are analyzed in this paper. The nonlinearity in voltage-mode measurements can be eliminated by using current-mode measurements. A HgCdTe photoconductive radiometer has been designed, based on this analysis,

which measures the current through a biased detector. A built-in calibrating capability in the circuits of the radiometer makes it possible to eliminate the effects of a long-term drift in the bias voltage, thereby achieving a lower uncertainty.

Paper 11

"Photocurrent measurement of PC and PV HgCdTe detectors," to be published in the J. Res. NIST. G. P. Eppeldauer and R. J. Martin

Novel photocurrent meters for working standard photoconductive (PC) and photovoltaic (PV) HgCdTe detectors have been developed to maintain the spectral responsivity scale of NIST in the wavelength range of 5 μm to 20 μm. The linear PC mode preamplifier does not need any compensating source to zero the effect of the detector bias current for the preamplifier output. The impedance multiplication concept with a positive feedback buffer amplifier was analyzed and utilized in a bootstrap transimpedance amplifer to measure photocurrent of a 200 Ω shunt resistance photodiode with a maximum signal gain of 10^8 V/A. In spite of the high performance lock-in used as a second-stage signal-amplifier, the signal-to-noise ratio had to be optimized for the output of the photocurrent preamplifiers. Noise and drift were equalized for the output of the PV mode preamplifier. The signal gain errors were calculated to determine the signal frequency range where photocurrent-to-voltage conversion can be performed with very low uncertainties. For the design of both PC and PV detector preamplifiers, the most important gain equations are described. Measurement results on signal ranges and noise performance are discussed.

a reprint from Applied Optics

Fourteen-decade photocurrent measurements with large-area silicon photodiodes at room temperature

G. Eppeldauer and J. E. Hardis

Recent improvements in commercial silicon photodiodes and operational amplifiers permit electrical noise to be reduced to an equivalent of 0.1 fA of photocurrent when a measurement time of 400 s is used. This is equivalent to a photocurrent resulting from fewer than 800 photons/s, and it implies a dynamic range of 14 orders of magnitude for a detector circuit. We explain the circuit theory, paying particular attention to the measurement bandwidth, the causes of noise and drift, and the proper selection of circuit components. These optical radiation detectors complement the primary radiometric standards. These detectors may replace photomultiplier tubes that have been used traditionally and or that were too costly to be used.

Key words: Bandwidth, dynamic range, noise, optical detection, photodiode, photonics, radiometry, sensitivity.

I. Introduction

The improvements in commercial silicon photodiodes and operational amplifiers over the past several years permit a corresponding increase in the performance of optical radiation measurements. Important electrical properties of photodiodes and operational amplifiers that affect high-sensitivity applications have been reported in the literature.[1] A limiting factor is the $1/f$ noise of the operational amplifier, which is chosen to be an electrometer-grade device characterized by a high input impedance and a low input bias current. Another limiting factor is the shunt resistance of the photodiode. This is the effective resistance that connects in parallel to the photocurrent source and is the slope of the diode's I–V curve at the operating point. For the study in Ref. 1 photodiodes were not available with shunt resistances >1.4 GΩ. More recently, the shunt resistances of the best silicon photodiodes have increased by an order of magnitude. Further, operational amplifiers have become available with an order of magnitude less input noise. These developments have made it necessary to reanalyze the behavior of these devices in a complete measurement circuit. Our goals in this study were to get optimum performance and to extend the application of these detectors to situations in which greater sensitivity would be required.

There is a growing market for such solid-state detectors. One photodiode manufacturer offers an integrated silicon-photodiode and monolithic-operational-amplifier package with a specification of 5-fW noise equivalent power (NEP) in the band of dc to 1 Hz at 750-nm peak response.[2] The manufacturer uses a small-surface-area (6.7 mm^2) photodiode and a fixed-gain amplifier of 10^{10} V/A. The product literature compares this device with a photomultiplier tube (R374 with an S-20 photocathode), as its NEP is less than the photomultiplier for wavelengths longer than 760 nm.

An intended application of this product is in optical communication, where greater detector sensitivity permits longer ranges. However, there are a large number of other applications in which silicon detectors could replace large and expensive photomultiplier tubes or inspire new, better, or less-expensive products. There is an increasing demand for high-sensitivity radiant-power measurements in such diverse fields as chemiluminescence and bioluminescence, radiometry, photometry, pyrometry, materials science (optical density and surface-scatter measurements), astronomy (Earth- and space-based stellar radiometry), and night vision. Silicon photodiodes offer the additional advantages of higher stability, greater reliability, linearity over a greater dynamic range,[3] and simpler operation.

The authors are with the Radiometric Physics Division, National Institute of Standards and Technology, Gaithersburg, Maryland 20899.

Received 12 October 1990.
0003-6935/91/223091-09$05.00/0.

The field of stellar radiometry illustrates an application for which high stability is as important as high sensitivity. Searching for planets around stars depends on the observance of small decreases in starlight (0.01% for terrestrial-sized planets) produced by the transit of a planet across a stellar disk.[4,5] To measure a 10^{-4} change requires a signal-to-noise ratio of 10^5 or better and a correspondingly high stability.

The goals of high sensitivity, wide dynamic range, stability, and linearity complement the silicon photodiode detectors that are used as self-calibrated, primary standards.[6] These photodiodes are inversion-layer silicon devices, which have a limited range of linear operation.[7,8] When they are combined in a light-trap arrangement to eliminate reflectance losses,[9] the range of operation for highest accuracy is further limited to less than a decade. The appropriate radiant power level used in realizing primary standards is a few tenths of a milliwatt, which typically requires a laser light source. However most applications that use traditional light sources and monochromators involve much lower radiant power levels. The silicon photodiode detectors discussed in this paper could act as transfer standards and improve the overall dynamic range of silicon-based radiometric standardization.

II. Circuit Theory

Consider the basic circuit of Fig. 1(a). The photodiode operates without a bias voltage, in the so-called short-circuit arrangement.[10] The output voltage (V_{Out}) of the amplifier is proportional to the photocurrent from the diode, as determined by the feedback transimpedance R_f. From the viewpoint of the photodiode, the amplifier and the feedback resistor appear as an impedance of R_f/A across its terminals, where A is the open-loop gain of the amplifier. As A is of the order of 10^6, the short-circuit impedance across the photodiode is very small compared with typical values of the photodiode's shunt resistance, R_{sh}, even when R_f is of the order of 10^{11} Ω.

Figure 1(b) emphasizes the aspects of this circuit that contribute to the measurement noise. The amplifier contains two noise sources. The first is V_{VN}, input voltage noise, which manifests itself as an effective voltage fluctuation at the input terminal of the amplifier. V_{VN} is the principal source of $1/f$ noise. That is, it has equal power in each decade of the measurement passband. The other is I_{IN}, input current noise, which is caused by the fluctuation of the input bias current of the amplifier. I_{IN} is a white noise, with a power proportional to the bandwidth.

Although ideal operational amplifiers are usually modeled as having a high, if not infinite, input impedance (and nothing more), real ones are the source of a small amount of current at the input pins. This input bias current is of the order of 10^{-12}–10^{-13} A in good devices and may occur with either polarity on a piece-by-piece basis. I_{IN} is caused by the shot noise of the charge carriers of the input bias current. Current shot noise has the well-known rms value of $\sqrt{2eI\Delta f}$, where e is the charge of the electron and Δf is the frequency

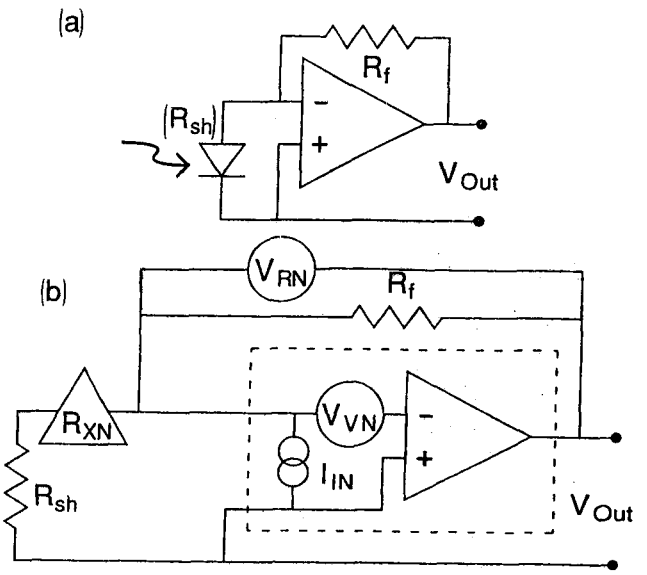

Fig. 1. Model circuit (a) components and (b) noise sources.

bandwidth of the measurement. In a typical operational amplifier with differential inputs, the current fluctuations would be larger. We approximate I_{IN} as $(4eI_{Bias}\Delta f)^{1/2}$.[11]

The effect of I_{IN} depends on the amplifier's source impedance. In our case, the source resistance, R_{so}, is the parallel combination of R_{sh} and R_f [$R_{so} = R_{sh} \times R_f/(R_{sh} + R_f)$]. The input current noise is reflected as an input voltage on the amplifier of $I_{IN}R_{so}$.

In manufacturers' specifications the claim "low noise" usually refers to V_{VN}. "Low input bias current" implies low I_{IN}. Choosing which attribute is the most important for a particular application depends on R_{so}, the bandwidth of the measurement, and the temperature stability of the measuring circuit. This theme is a major purpose of this paper.

Figure 1(b) also illustrates two other noise sources of concern. One is the voltage that is due to resistor noise, V_{RN}, which is also known as Johnson noise or thermal noise. This noise is an inevitable consequence of charge carriers in resistors. Its rms value is $(4kTR_{so}\Delta f)^{1/2}$, where k is Boltzmann's constant and T is the absolute temperature.[12] Like I_{IN}, V_{RN} is a white noise.

The last noise that we consider, R_{XN}, is often called excess noise, and it is due to resistance fluctuations. It is excess in the sense that resistors can be noisier than the Johnson noise formula predicts. This noise used to be called current noise because it requires a current through the resistors to detect it. However, the current does not produce the noise, and the association was misleading.[13] Good, low-noise component resistors may be obtained for R_f. For us the excess noise is due to the fluctuation of R_{sh} of the photodiode.

Excess noise includes the generation–recombination noise of semiconductors, which corresponds to fluctuations in the number of charge carriers.[14] This can be a white noise also. However the various factors that determine the I–V relationship of a diode[15] include the

mobility of the carriers as well as their number. Fluctuations of these other factors may cause $1/f$ noise.[16]

When we fail to include excess noise in our circuit model it does not mean that this noise is insignificant or unimportant but only that it is unpredictable without a deeper knowledge of the inner workings of the photodiode. It may also vary because of environmental conditions, such as exposure of the photodiode to humid air.[17] Nevertheless, the circuit's response to photocurrent does not depend on R_{sh}, nor then to fluctuations in R_{sh}. These fluctuations matter in that they impose a noise voltage on the amplifier because of the amplifier's I_{Bias}.

Each of the four noise sources produces an independent, randomly varying voltage. The resistor noise V_{RN} can be directly measured at the amplifier output. The rms value of the total input noise voltage as seen by the amplifier is:

$$V_{IN} = [V_{VN}^2 + 4eI_{Bias}R_{so}^2\Delta f + (I_{Bias}R_{XN})^2] \quad (1a)$$

The sensitivity of the photocurrent measurement is limited by the total output noise voltage of the amplifier:

$$V_{ON} = [(A_V V_{IN})^2 + 4kTR_{so}\Delta f]^{1/2} \quad (1b)$$

where the closed loop voltage gain A_V is equal to $(R_f+R_{sh})/R_{sh}$.

This explains the critical importance of the photodiode shunt resistance in determining the ultimate sensitivity of the measuring circuit. To enable us to measure weak photocurrents, R_f must be made large. However, when $R_f > R_{sh}$, increasing R_f increases A_V significantly as well, implying an amplification of the noise along with the amplification of the signal. Larger values of R_{sh} permit larger values of R_f to increase amplification of the signal without undue noise.

III. Measuring Voltage Noise

Before selecting a type of operational amplifier to be used for high-sensitivity applications, we independently measured the voltage noise of various candidates. Although bias current is often specified by the manufacturer, voltage noise, particularly at low frequencies, is a more subtle attribute. In this context, the noise is manifested as the scatter of repeated measurements of the amplifier's output offset voltage.

Output offset voltage is the nominal output value of the amplifier when no signal is applied and when the source resistance is low (so that input bias current effects are negligible). Like output voltage noise, it is usually proportional to A_V. The input offset voltage is the measured output offset voltage as reduced by this factor, and we take it to be an intrinsic amplifier characteristic. For this purpose, adjustment need not be made to reduce it.

Figure 2 shows the circuit used for these measurements as well as others that are discussed below. The circuit was enclosed in a lighttight and electrically shielded package. The amplifiers were installed in a socket for ease of substitution. Component resistors were sometimes substituted for the photodiode to replicate different source resistances. Both R_f and M were selected with switches. Here, M is a multiplier, an extra gain that could be introduced by reducing the feedback voltage through a resistive divider. This feature is appropriate only when R_f is well above the 1-kΩ output impedance of the divider.

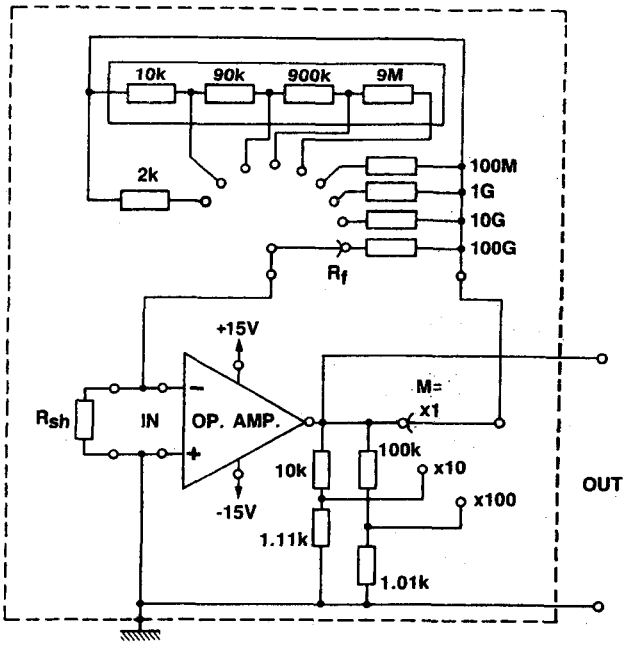

Fig. 2. Circuit details.

[Whereas M may be used for amplifying the output from the detector, measurements showed that it does not improve the signal-to-noise ratio. Note that, while the signal gain is $M \times R_f$, the noise gain A_V is $M \times (R_f + R_{sh})/R_{sh}$. On the other hand, because the output of the amplifier remains bounded by the supply voltage, the dynamic range of the circuit is reduced when $M > 1$. Therefore the multiplication switch should be eliminated in most circumstances.]

The output of the circuit was connected directly to a microcomputer-controlled digital voltmeter (DVM). This multislope-type DVM integrated the output voltage for a selectable time period, a count of the power line cycles. To produce longer integration times than the DVM normally allowed, an external microcomputer averaged a sequence of repeated measurements.

Table I compares multiple samples of three types of operational amplifier from the Burr Brown product line. All are designed to be electrometer-type amplifiers, with a low input bias current. The OPA128LM and OPA104CM amplifiers are categorized as ultralow bias current devices. They are specified as having a bias current below 75 fA, the lowest of the product line. The OPA111BM amplifier has a higher bias current (specified as 1 pA, maximum) but is described as having lower noise. Nevertheless the manufacturer provides no specifications about noise below 0.1 Hz. Both the OPA128LM and the OPA111BM are newer generation products.

To measure the offset voltage and voltage noise of

Table I. Statistics of Amplifier Output Measurements Showing the Mean (the Offset Voltage) and the Standard Deviation (the Voltage Noise)[a]

	OPA104CM		OPA128LM		OPA111BM	
Sample	Mean	Std Dev	Mean	Std Dev	Mean	Std Dev
1	−23.84	7.94	−146.68	0.24	144.83	0.21
2	−36.81	9.10	67.24	0.53	−30.57	0.09
3	39.07	3.05	−111.02	0.55	−21.65	0.05
4	−79.14	8.27	158.66	1.30	−5.52	0.11
5	−107.05	6.71	30.19	0.42	—	—

[a] Values are quoted in millivolts, and the system gain A_V was 1000.

these candidate operational amplifiers, a 1-kΩ resistor was substituted for the photodiode to make the current and resistor noises negligibly small. R_f was set to 1 MΩ, and $M = 1$ was used for an overall gain A_V of 10^3.

The DVM was set to integrate for 100 power line cycles (10 cycles repeated 10 times and digitally averaged within the DVM). This integration time of 1.67 s would correspond to a measurement bandwidth for white noise of 0.3 Hz. One hundred of these readings were externally averaged, resulting in a single measurement of the output offset voltage. The measurement bandwidth for white noise in the latter case would be 1.25 mHz. The reason is explained in Appendix A.

The offset voltage was measured a nominal 10 times for each amplifier in this fashion, and the statistics of these 10 measurements are reported in Table I. The columns labeled Mean contain the results of final averaging of the 10 values. The columns labeled Std Dev contain the standard deviations of the 10 intermediate averages. The standard deviations of all 1000 individual readings were similar, showing that this noise was not much affected by the longer integration.

This behavior is indicative of $1/f$ noise. A measurement passband depends on two characteristic times. The integration time of the individual data points determines the high-frequency rolloff, since the higher-frequency components are averaged out. Similarly the time spent making the repeated measurements determines the low-frequency rolloff, because lower-frequency components will not be noticed. That is, noise frequencies that act too slowly will not cause a scatter in the data during the time that one watches for it. Both rolloff frequencies are inversely proportional to their characteristic times in roughly the same way. For P quickly repeated measurements, the lower rolloff frequency is $\sim 1/P$ of the higher.

For white noise with a large P, the measurement bandwidth is essentially determined by the upper rolloff frequency, as the difference between the lower rolloff and 0 Hz (i.e., dc) is small. Usually the lower rolloff frequency is ignored, and the noise is predicted by the integration time only. In contrast, $1/f$ noise is more sensitive to the lower rolloff frequency. The rms voltage fluctuation owing to $1/f$ noise goes as $[\log(f_{high}/f_{low})]^{1/2}$, the radicand being the number of decades in the noise passband. This equals $[\log(P)]^{1/2}$, a slowly varying function of P. Whereas data scatter caused by white noise depends mostly on the integration time, data scatter caused by $1/f$ noise depends mostly on the number of (equally timed) data points, independent of their integration time.

Here, if the noise were truly a $1/f$ noise we would expect the standard deviation of the 1000 individual readings to be roughly $\sqrt{3}$ times larger than that of the 10 intermediate averages. If it were a white noise instead, the standard deviation of the 10 intermediate averages would have been roughly $\sqrt{240}$ times smaller, following the ratio of the bandwidths. Our data for the various amplifiers showed that the noise decreased by less than a factor of 2. Therefore, for simplicity in the remainder of this paper, input voltage noise will be treated as a constant, a characteristic of an amplifier, and independent of integration time. This relies on the slowly varying nature of $[\log(P)]^{1/2}$ and says that the data in Table I ($P = 10$) should be similar to the results obtained when $10 < P < 30$.

The data in Table I show that the OPA128LM amplifier has an order of magnitude less voltage noise than does the OPA104CM, the earlier generation amplifier having a consistently low noise level, used in our previous research.[1] However, on average the OPA128LMs' have approximately five times the voltage noise of the OPA111BM's.

Table I also shows noise variation among individual samples of OPA128LM amplifiers within a factor of 2 of the mean. This compares favorably with variations in other makes and models of operational amplifiers which, in our experience, can have noise levels that vary among samples by an order of magnitude. For most purposes this variation would not be significant, and individual selection of these amplifiers for low V_{VN} would not be necessary.

Also, please note that in product literature noise voltage is often reported peak to peak, not rms. As a rule of thumb, for 1000 measurements the peak-to-peak value will be ~6.6 times larger than the rms one.[18]

IV. Temperature Dependence and Drift

It is not enough to develop new photodiodes with greater R_{sh} to achieve greater measurement sensitivity. R_{sh} and R_f affect the noise level in Eq. (1) through their combination, R_{so}. The current noise term is quadratic in R_{so}, and the resistor noise term depends on it linearly. As current noise becomes the dominant noise when R_{so} is large, care must be taken to use an amplifier with a sufficiently low I_{Bias}. Fortunately this is an easy criterion to meet. However, the bias current poses a greater problem because it changes with temperature. This is an aspect of the problem called drift.

In addition to random fluctuations (noise), there are also changes in the amplifier output that appear on inspection to be distinctively slower and often of larger magnitude. We interpret these changes as being caused by such things as the aging of the electronic components and their temperature dependence. We will elaborate on the latter effect for purposes of illustration and because it is the easiest source of drift to control. Drift is particularly bothersome in this re-

search because it may be confused with the low-frequency noise that we seek to compare.

As an example the manufacturer specifies that the OPA128LM amplifier has a typical input offset voltage V_O of ±140 μV (±500 μV, maximum) and an input offset voltage drift V_D of ±5 μV/°C. Its typical input bias current I_{Bias} is ±40 fA (at 25°C), and it grows geometrically at a rate I_D of 6.7%/°C. (In light of the above discussion about input bias current noise, since the noise goes as the square root of the bias current the noise grows geometrically 3.3%/°C.) In addition, we previously determined[1] the decrease of the photodiode shunt resistance with increasing temperature to be ~11%/°C, which we call R_{SD}. A nominal R_{sh} is 5 GΩ. In the worst case, R_f is 100 GΩ, with a negligible temperature dependence of <500 parts in 10^6/°C. These values lead to an A_V of 21, which increases 11%/°C, and an R_{so} of 4.8 GΩ, which decreases 11%/°C.

Referring again to Fig. 1, we see the effect of V_O and I_{Bias} on the output voltage,

$$V_{Offset} = -A_V(V_O + I_{Bias}R_{so}). \quad (2)$$

For small temperature changes ΔT with these typical component values, $\Delta V_{Offset}/\Delta T$ = 0.7 mV/°C for the worst case alignment of the signs of V_D, V_O, and I_{Bias}. In our experience, the value is closer to 1.2 mV/°C, still well within specification limits.

It will simplify matters to cast the temperature effects in terms of a photocurrent change, ΔI_{Offset}, that would yield an equivalent change in the magnitude of the output voltage. Because the photocurrent gain is R_f, $I_{Offset} = V_{Offset}/R_f$, and

$$I_{Offset} = V_O/R_{so} + I_{Bias} \quad (3)$$

$$\Delta I_{Offset} = (V_D/R_{so} + V_O R_{SD}/R_{so} + I_D I_{Bias})\Delta T. \quad (4)$$

ΔT refers to the small temperature changes that occur during the course of a sequence of measurements.

Similarly noise may be expressed as the photocurrent that would give an equivalent deviation to the output voltage, on average:

$$I_{Noise} = V_{ON}/R_f = V_{IN}/R_{so}. \quad (5)$$

Of course, the detector–amplifier combination cannot effectively distinguish actual photocurrents smaller than these values. An appropriate design goal of the circuit is to equalize the effects of noise and drift, choosing an amplifier type that balances both problems for reasonable integration times and temperature control.

V. Amplifier-Type Selection

Figure 3 predicts the performance of OPA111BM and OPA128LM amplifiers in this circuit. Drift and noise are computed by using Eqs. (4) and (5), respectively, and are shown as a function of source resistance R_{so}. The data for the typical amplifier characteristics are taken from the manufacturer's catalog, with the exception of V_{VN}, for which we use the average of the values in Table I. In the upper part of Fig. 3, ΔT is 0.1°C, and Δf is 300 mHz. Both are easy to realize in an actual

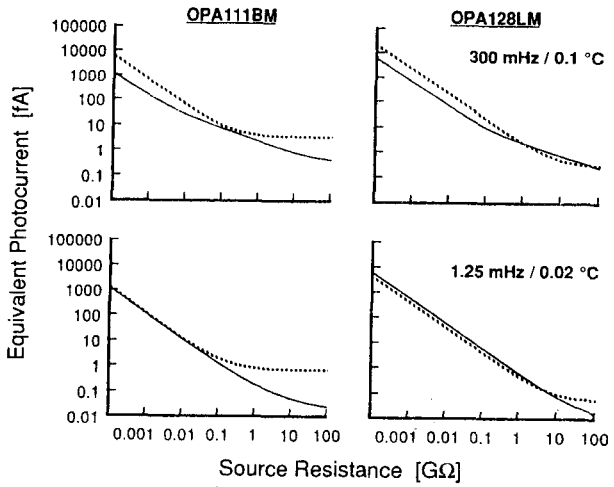

Fig. 3. Balancing noise and drift. The noise (solid curves) and thermal drift (dotted curves) are expressed in terms of the photocurrent that would cause an equal change in amplifier output. The two figures at the left show the expected performance of the OPA111BM amplifier; those on the right show the performance of the OPA128LM amplifier. The two top figures show easy specifications for integration time and temperature stability; the bottom two show tight specifications.

measurement. In the lower part of Fig. 3, ΔT is 0.02°C, and Δf is 1.25 mHz.

Figure 3 shows that when $R_{so} > 1$ GΩ the most severe limit on sensitivity would be the drift caused by the temperature fluctuations of an OPA111BM amplifier. That is, the drift of the OPA111BM is much larger than both the noise and the drift of the OPA128LM. The last term of Eq. (4) is the culprit. For high-sensitivity investigations (when R_{so} must be large), it is generally better to choose an amplifier with low-input bias current (hence low bias current drift) than one with low voltage noise. However when $R_{so} < 300$ MΩ, the lower input offset voltage of the OPA111BM would provide the advantage. (Indeed in this situation it might be worthwhile to trim the amplifier to reduce V_O.)

There is an additional aspect to the combinations of Δf and ΔT shown in Fig. 3. Photodiodes specially selected for high shunt resistance are available in the range of 1–50 GΩ. In this range of source resistance, the noise and the drift that would result from the use of an OPA128LM amplifier are roughly equal. At the upper right of the figure, both Δf and ΔT constrain the sensitivity of the detector electronics to ~1 fA. A sensitivity of 0.1 fA requires reducing both Δf and ΔT in tandem, as shown at the lower right, as well as a larger R_{sh}.

For the remainder of this paper we discuss results obtained while using OPA128LM amplifiers. The use of these amplifiers is consistent with the possibility of having excess detector noise, which would also be proportional to the input bias current.

VI. Noise Characteristics of the Operational Amplifiers

Figure 4 shows noise measurements similar to those described in Section III made on OPA128LM amplifi-

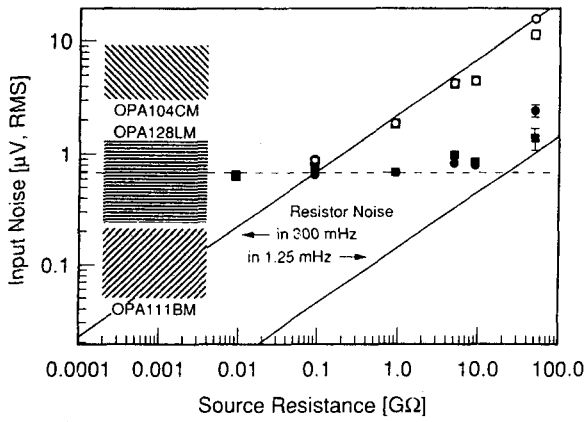

Fig. 4. Noise measurements of OPA128LM amplifiers with different source resistances. The hatched areas at the left show the range of the characteristic input voltage noises of the amplifier types reported in Table I. The dashed line guides the eye toward the voltage noise level of these particular amplifiers. This level of minimum noise cannot be much reduced by longer integration. The solid lines are the Johnson noise of the source resistances for our two integration times (300 mHz in open symbols and 1.25 mHz in filled symbols).

ers with various combinations of R_{sh} and R_f (both component resistors) at room temperature in a thermally insulated (but not regulated) box. This test determines whether the electrical noise from the electronics assembly is consistent with the predictions of the previous sections. The square data points were taken with one copy of the circuit, and the circular data points with another. The format parallels Eq. (1).

The DVM took 100 readings with integration times of 1.67 s. For each collection of 100 readings, the voltmeter reported their mean (measured in a bandwidth of 1.25 mHz) and their standard deviation (representing the noise in a bandwidth of 300 mHz). This cycle was repeated at least 40 times; sometimes the apparatus was run overnight and repeated the cycle ~140 times.

The open points in Fig. 4 represent the total input noise [Eq. (1)] in a 300-mHz bandwidth. As before, the input noise is the measured (output) noise divided by A_V. The output noise is taken to be the average of the standard deviation reports from the voltmeter (each covering 100 individual readings). The single standard deviation of all the individual readings is not used in order to reduce the effect of long-term drift.

The filled points in Fig. 4 indicate the scatter of the means computed by the voltmeter. These points represent the total input noise in a bandwidth of 1.25 mHz. Nominally 30 consecutive readings were considered a group. However temperature-induced drift over the span of 30 measurements was a significant problem at large values of R_{so}. To reduce the effect of drift on the reported values, a least-squares fit was made to a line through the 30 consecutive values, and the implied time-dependent background was subtracted from the raw data. In effect, the noise below 1.25 mHz is taken to be the rms value of the residuals after the fit. The results of multiple sets of equal size were averaged when enough data were available.

The fitting procedure had the side effect of raising the low-frequency rolloff that affects the magnitude of $1/f$ noise. It also narrowed the meaning of ΔT in Eq. (4) to those temperature fluctuations that occurred on the time scale of a few measurements but not so slowly that they could be accounted for by background subtraction.

The resistor noise, as calculated at 300 K, is shown in Fig. 4 for the two bandwidths of interest. The ranges of voltage noises, as reported in Table I, are shown as shaded blocks at the left of the figure. This should be taken as a rough guide to the reproducibility of this experiment when other amplifiers of the same types are used. In our case, the two amplifiers used have very similar V_{VN} values. The dashed line represents an input voltage noise of 0.68 μV. As expected for a bias current of only 75 fA, there is no evidence of current noise (noise proportional to R_{so}) in this range of R_{so}. The voltage noise ($1/f$ noise independent of R_{so}) was remarkably consistent between the two bandwidths despite the different number of samples used and the differences in the way the data were treated.

The results show that the construction and the packaging of the complete amplifier circuits have not created an electrical noise much beyond that expected. At the longer integration time, the slight additional noise may be due either to temperature fluctuations >0.02°C or to excess noise in the component resistors.

Finally note that in the viewpoint of Fig. 4 at a source resistance of 12 GΩ, the effects of voltage noise and resistor noise are equal in a measurement bandwidth of 1.25 mHz. The sensitivity of the circuit could not be readily improved there by simply integrating longer (which reduces resistor noise). Indeed, the shunt resistance of each photodiode implies an integration time that need not be exceeded.

VII. Photodiode Noise

In this section we discuss noise measurements made when Hamamatsu photodiodes were used in the circuit. These diodes were specially manufactured and then selected for the highest shunt resistances that Hamamatsu could offer. The maximum R_{sh} requires the highest fabrication skill of the photodiode vendor and is limited by the number of crystal defects in the starting material. The type S1226-8BQ photodiode is a PNN$^+$ device; types S2386-8K and S2956-8BQ are made by P on N planar diffusion.

High-sensitivity applications suggest the use of large-area photodiodes to intercept more optical radiation. However with increasing area the shunt resistance is reduced, and the junction capacitance increases. To the extent that R_{sh} is due to leakage around the junction, R_{sh} will scale inversely by the square root of the diode's active area. To the extent that R_{sh} is an effect of the P–N junction itself, R_{sh} will scale inversely with the active area. The diodes used in this work all had active areas of 1/3 cm^2.

Table II. Noise and Drift of Complete Detector–Amplifier Packages Cast in Terms of the Photocurrent that Would Cause the Same Change in Output

Photodiode Type	R_{sh} (GΩ)	C_j (nF)	Circuit Copy	Limit Sensitivity (fA) Δf = 300 mHz	Limit Sensitivity (fA) Δf = 1.25 mHz
S1226-8BQ	6.5	1.3	A	0.66 ± 0.05	0.20 ± 0.07
S2956-8BQ	50	4	A	1.0 ± 1.2	0.16 ± 0.05
S1226-8BQ	8	1.3	B	0.61 ± 0.05	0.101 ± 0.021
S1226-8BQ	6.5	1.3	B	0.61 ± 0.05	0.102 ± 0.015
S2386-8K	20	3.2	B	0.83 ± 0.35	0.095 ± 0.020

We independently estimated the R_{sh} values of the photodiodes using a Hewlett-Packard 4145A semiconductor parameter analyzer to measure and display their I–V curves. Depending on the photodiode type, the highest shunt resistances available were in the range of 5–50 GΩ. These measurements have a tolerance of ~20% because the 4145A is not designed for such small currents. Additionally, these measurements are somewhat subjective, resulting from eyeball fits of the data with a visual guide provided on the screen of the analyzer.

When an actual photodiode is used in the circuit, the shunt impedance consists of the shunt resistance and a parallel junction capacitance. Because the shunt impedance is reduced at high frequencies, increased amplification of high-frequency noise will result. This can be compensated by adding parallel capacitance to the feedback resistor. We note the typical junction capacitance C_j of the various diodes. These data come from the manufacturer's catalog.

To determine the noise inherent in five different photodiodes, we used the procedure discussed in Section VI. The data are shown in Table II. Two different copies of the circuit were used. The B copy had a temperature monitor, which showed that the temperature was stable within 0.01°C during a 400-s measurement cycle. The reported uncertainties are due to the reproducibility of the measurements. They are the statistical standard deviation (1 σ) of >100 repeated measurements (consisting of 100 samples each) with 300-mHz bandwidth and 3 repeated measurements (consisting of 30 samples each) with 1.25-mHz bandwidth.

Note that the noise in Δf = 300 mHz increases with increasing R_{sh} contrary to the expected trend. The scatter of the measurements increases as well. This is explained in part by noting that the RC time constants, which are of the order of 10–200 s, are much larger than the integration time of 1.6 s. The shunt impedance is reduced for noise frequencies within the detection bandpass, giving them extra amplification. With longer integration, the effect of junction capacitance is reduced.

The data show that noise-equivalent photocurrents of 0.1 fA have been achieved. This implies a dynamic range of 14 orders of magnitude for these devices since Hamamatsu specifies a saturation current of ~10 mA. (In practice, the OPA128LM amplifier can drive only 5 mA; a second-stage amplifier would be required for the full dynamic range.)

VIII. Practical Considerations

In practice, the effect of long-term drift is mitigated by background subtraction. Each measurement should consist of a cycle containing intervals when the detector is exposed and when it is blocked. These periods of integration are separated by settling times, during which the output from the amplifier is ignored. When using the highest feedback resistor, 100 GΩ, we found that 2 min of settling was required for equilibrium to be reached. (This was considerably slower than the settling time for the 10-GΩ resistor, which was <1 s.)

In our experience, the maximum R_f that was suitable for the OPA128LM was 100 GΩ. For larger R_f the amplifier became noticeably nonlinear.

A fixed R_f of 100 GΩ gives the circuit a dynamic range of ~6 orders of magnitude. Note that 0.1 fA of photocurrent corresponds to an output voltage of 10 μV, whereas the maximum output voltage is ~10 V, determined by the power supply. For field work, voltmeters with resolutions of 0.1 mV are readily available. With these, the minimum detectable photocurrent would be 1.0 fA, and the dynamic range would be one decade less. R_f values <100 GΩ might be appropriate depending on the brightness of the source.

It is customary to discuss noise in terms of the NEP incident upon a detector. Typical silicon photodiodes have a peak response of 0.4–0.6 A/incident W at approximately λ = 720 nm. Here the NEP corresponding to 0.1 fA would be ~6 fW $Hz^{-1/2}$ (reflecting the 1-mHz bandwidth). 0.1 fA also corresponds to 780 photons/s for a diode with a typical external quantum efficiency of 80%.

IX. Conclusion

For high-sensitivity applications, large-area (1/3 to 1 cm^2) silicon photodiodes with high shunt resistance (>2 GΩ) and little excess noise are the detectors of choice. They are best used in combination with an amplifier having the smallest possible input bias current because the high shunt resistance mitigates the input voltage noise. With the high-quality components now available, electrical noise can be reduced to an equivalent of 0.1 fA of photocurrent by using an integrated measurement time of 400 s. This is equivalent to a photocurrent caused by <800 photons/s, and it implies a dynamic range of 14 orders of magnitude for a detector circuit.

We have successfully built such a detector–amplifier package. While its NEP is comparable with that of

commercial offerings, the photodiode in our design has five times the active area.

Research continues at the National Institute of Standards and Technology to establish better the optical properties, such as their linearity over the whole dynamic range, of these detector circuits. Our goal is to package the circuits in a simple and practical manner and to calibrate them optically for distribution. We believe that these detector-based transfer standards will serve the needs of the radiometric community for traceability to the National Institute of Standards and Technology's primary standards, which serve a more limited dynamic range. In addition, the spectral response of the detector may be customized by the addition of a colored filter for special applications, such as in photometry.

Beyond their application in standards research, the improved performance of the detectors now possible should find them application in many areas of commercial interest. Of particular note is the band of near-infrared wavelengths between 700 and 1000 nm, where photomultiplier tubes are generally less efficient and require noisy photocathodes. However the relative simplicity and lower cost of high-sensitivity, silicon photodiode detectors might make them more appropriate than photomultiplier tubes, even for visible light, in many circumstances. We hope that as photodiode manufacturers become more aware of the significance of a high shunt resistance, devices featuring this characteristic will become more widely available.

Appendix A: Determining the Measurement Bandwidth

The magnitude of the white noise discussed in Section II was dependent on the bandwidth of the measurement. Although it is commonly known that the bandwidth Δf is inversely proportional to the integration time τ of a system, the value of the proportionality constant is the source of perpetual confusion.

Consider a signal, which need not be noisy, which we shall call $f(t)$. In our case, this signal is the output voltage of our amplifier circuit. By integration of this signal we mean a transformation to another signal, $f'(t)$, which could be, for example, either of the following:

$$f'(t) = \frac{1}{\tau}\int_{t-\tau}^{t} f(t')\mathrm{d}t' \quad \text{(Case I)}, \tag{A1}$$

$$f'(t) = \frac{1}{\tau}\int_{-\infty}^{t} \exp\left[\frac{-(t-t')}{\tau}\right] f(t')\mathrm{d}t' \quad \text{(Case II)}. \tag{A2}$$

In each of these cases the integration, expressed as a convolution integral, is an averaging with a particular weighting function. The first case is pure integration over a finite time interval. It is the continuous analog to the practice of digitally averaging a certain number of the most recent points. The second case is that of a simple, single-pole filter.

Consider now the effect of these time-domain filters upon a signal $f(t) = e^{-i\omega t}$. After integration

$$f'(t) = \left(\frac{e^{i\omega\tau} - 1}{i\omega\tau}\right) e^{-i\omega t} \quad \text{(Case I)}, \tag{A3}$$

$$f'(t) = \left(\frac{1}{1 - i\omega\tau}\right) e^{-i\omega t}. \quad \text{(Case II)}. \tag{A4}$$

The expressions in parentheses correspond to attenuations in the frequency domain due to the filters [Eqs. (A1) and (A2)] in the time domain. Note that they approach 1 for small ω and that their magnitudes approach 0 for large ω. They are perhaps best recognized as the Fourier transformations of the weighting functions.

For a signal $f(t)$ that contains white noise, there is equal noise power in all intervals of ω and in both quadrature phases. Therefore the attenuation in Eq. (A3) or (A4) would have the same effect on white-noise power as an equivalent frequency-domain attenuator that is 1 over an interval $\Delta\omega$ and 0 elsewhere, where $\Delta\omega$ is the integral of the squared magnitude of the (voltage) attenuation over all frequencies:

$$\Delta\omega = \int_0^\infty \frac{2[1 - \cos(\omega\tau)]}{(\omega\tau)^2}\,\mathrm{d}\omega = \frac{\pi}{\tau} \quad \text{(Case I)}, \tag{A5}$$

$$\Delta\omega = \int_0^\infty \frac{1}{1 + (\omega\tau)^2}\,\mathrm{d}\omega = \frac{\pi}{2\tau} \quad \text{(Case II)}, \tag{A6}$$

As $\omega = 2\pi f$, $\Delta f = 1/(2\tau)$ in Case I, and $\Delta f = 1/(4\tau)$ in Case II. That is, the value of the proportionality constant depends on the details of what makes up the integration time, τ. Here the two different results reflect the fact that it takes more high frequencies to represent an abrupt function of time than a gradual one.

There are, of course, many other low-pass filters that commercial dc voltmeters might use. One does not know *a priori* what the proportionality should be between Δf and $1/\tau$.

In this research we used Hewlett-Packard Models 3456A and 3457A voltmeters. Their analog-to-digital converters use variations of the well-known dual-slope technique. However for long integration times, successive samples made with shorter integration times are digitally averaged. The upramp portion of a single analog-to-digital cycle consists of the integration described in Eq. (A1), with $\tau = 0.167$ s (10 power line cycles). These are repeated N times, $T = 0.4$ s apart (for the 3457A; 0.34 s for the 3456A).

The bandwidth of this class of instrument is

$$\Delta\omega = \int_0^\infty \left\{\frac{2[1 - \cos(\omega\tau)]}{(\omega\tau)^2}\right\}\left\{\frac{[1 - \cos(N\omega T)]}{N^2[1 - \cos(\omega T)]}\right\}\mathrm{d}\omega. \tag{A7}$$

This follows directly from the choice of a weighting function [as in Eqs. (A1) and (A2)] that is a sequence of N square pulses each with amplitude $1/N$. Equation (A1) is the special case with $N = 1$, and the first factor in the integrand of Eq. (A7) parallels the integrand in Eq. (A5). Using the well-known property of Fourier transforms that the transform of a convolution is the product of the transforms of its constituents, we recognize the second factor in Eq. (A7) as the squared magnitude of the transform of a sequence of N delta functions (impulses).

We have confirmed the behavior of this expression by numerical integration. In the low-N limit ($N < 30$

for these τ and T), $\Delta f \approx 1/(2N\tau)$. In the high-$N$ limit ($N > 1000$ for these τ and T), $\Delta f \approx 1/(2NT)$.

In this paper a bandwidth of 0.3 Hz refers to a panel setting on an HP 3457A of 100 power line cycles (1.67 s) of integration time. Internally the HP 3457A implements this as $\tau = 0.167$ and $N = 10$. A bandwidth of 1.25 mHz refers to panel settings of 100 power line cycles repeated 100 times. While the integration time is 166.7 s, as $N = 1000$ in this case, the elapsed time of 400 s determines the bandwidth.

Incidentally, nothing in the preceding analysis is connected with the problem of detecting low noise frequencies. When trying to measure the noise by determining the scatter (standard deviation) of many samples, noise at low frequencies is not resolvable from the signal (the mean). Just as τ provided a characteristic time that determined the upper bound of the passband, the total time T spent making measurements provides the characteristic time for the lower bound. The actual bandwidth when we are trying to measure white noise is $(1 - C\tau/T)\Delta f$, where C is a constant of order unity (and which depends on the details of the measurements). Nevertheless Δf is still the bandwidth that reflects the statistical uncertainty in a real signal that is due to the noise.

The authors thank Joel Fowler, Jon Geist, and Ed Zalewski for the encouragement that started this project, Steve Southworth for sharing his valuable experiences in the use of these detector circuits, Tom Larason for the long hours spent measuring the noise, Alan Migdall for many helpful discussions on the nature of the noise, Raju Datla for a careful reading of the manuscript, and Al Parr, Klaus Mielenz, and Chris Kuyatt for their assistance and support.

References and Notes

1. G. Eppeldauer, "Measurement of very low light intensities by photovoltaic cells," in *Eleventh International Symposium on Photon Detectors, Weimar (GDR), 1984*, Proc. 182 (IMEKO, Budapest, 1984).
2. Data sheet of the HC210-3314 and HC212-3314, "Integrated silicon photodiode and amplifier for low light level detection," (Hamamatsu Corp., 1988).
3. W. Budde, "Multidecade linearity measurements on Si photodiodes," Appl. Opt. **18,** 1555–1558 (1979).
4. W. J. Borucki, "Photometric precision needed for planetary detection," in *Proceedings of the Workshop on Improvements to Photometry, San Diego, 1984*, NASA Conf. Publ. **CP-2350,** 15–27 (1984); W. J. Borucki and A. L. Summers, "The photometric method of detecting other planetary systems," Icarus **58,** 121–134 (1984).
5. G. Eppeldauer and A. R. Schaefer, "Application of PN and avalanche silicon photodiodes to low-level optical radiation measurements," in *Second Workshop on Improvements to Photometry, Gaithersburg, 1987*, NASA Conf. Publ. **CP-10015,** 111–151 (1988).
6. E. F. Zalewski and J. Geist, "Silicon photodiode absolute spectral response self-calibration," Appl. Opt. **19,** 1214–1216 (1980).
7. A. R. Schaefer, E. F. Zalewski, and J. Geist, "Silicon detector nonlinearity and related effects," Appl. Opt. **22,** 1232–1236 (1983).
8. J. L. Gardner and F. J. Wilkinson, "Response time and linearity of inversion layer silicon photodiodes," Appl. Opt. **24,** 1531–1534 (1985).
9. E. F. Zalewski and C. R. Duda, "Silicon photodiode device with 100% external quantum efficiency," Appl. Opt. **22,** 2867–2873 (1983).
10. C. L. Wyatt, *Radiometric System Design* (Macmillan, New York, 1987), Chap. 18.
11. A. Ambrózy, *Electronic Noise* (McGraw Hill, New York, 1982), p. 190.
12. It is incorrect to say that the shunt resistance, defined as dV/dI at the operating point, is the effective resistance for thermal noise in the Johnson–Nyquist equation. However for the well-known exponential I–V relation of a junction diode, it is an appropriate approximation when the diode current is much less than its reverse saturation current. That is the case in this research, where $I_s \approx 5$ pA and $I \approx 0.05$ pA owing to the op–amp input bias current. In general, the effective resistance (and hence the noise generated) will be less, approaching $1/2\ dV/dI$ when $I \gg I_s$; see Eq. (19) in M. S. Gupta, "Thermal noise in nonlinear resistive devices and its circuit representation," Proc. Inst. Electr. Eng. **70,** 788–804 (1982).
13. K. M. van Vliet, "Classification of noise phenomena," in *Sixth International Conference on Noise in Physical Systems, Gaithersburg, 1981*, Natl. Bur. Stand. (U.S.) Tech. Note **614,** 3–11 (1981).
14. R. Müller, "Generation–recombination noise," in *Noise in Physical Systems, Proceedings of the Fifth International Conference on Noise, Bad Nauheim (FRG), 1978* (Springer-Verlag, New York, 1978).
15. S. M. Sze, *The Physics of Semiconductor Devices*, 2nd ed. (Wiley, New York, 1981), Chap. 2.
16. See, e.g., D. A. Bell, "The role of mobility in $1/f$ noise" in *Sixth International Conference on Noise in Physical Systems, Gaithersburg, 1981*, Natl. Bur. Stand. (U.S.) Tech. Note **614,** 169–172 (1981); R. P. Jindal and A. Van der Ziel, "A model for $1/f$ mobility fluctuations in elemental semiconductors," *ibid.*, 173–177; B. K. Jones, "Excess conduction noise in silicon resistors," *ibid.*, 206–209.
17. G. L. Pearson, H. C. Montgomery, and W. L. Feldmann, "Noise in silicon p-n junction photocells," J. Appl. Phys. **27,** 91–92 (1956).
18. *Linear Products Databook* (Analog Devices, Inc., 1988), pp. 2–9.

Temperature Monitored/Controlled Silicon Photodiodes for Standardization

George Eppeldauer
Radiometric Physics Division
National Institute of Standards and Technology
Gaithersburg, MD 20899

ABSTRACT

Two alternative approaches to reducing errors in radiometers and photometers caused by temperature variations involve temperature monitoring and temperature control. In the first method, the measurement results are interpreted using the temperature of the detector at the time of measurement. The other method is to control the temperature of the detector to a constant value. Design considerations and examples of both approaches are discussed.

1. INTRODUCTION

Radiometric standardization today depends in large part on silicon photodiodes. However, the responsivity of these detectors-particularly towards the red end of the spectrum-depends on their temperature. While the temperature dependence varies among device types, its existence is unavoidable, even among "good" photodiodes.

In detector based photometry and colorimetry (including color temperature measurement), photodiodes are combined with filters to alter their spectral response. Such filters, as well, are affected by temperature changes.

Experience shows that the filters are often more temperature sensitive than the detectors. At NIST, we often use detectors that are chosen for their high shunt resistance (which leads to lower noise and a wider dynamic range). We find that the response varies less than 0.02%/°C, for small variations in temperature (not larger than 2 °C), between 400 and 650 nm. This figure increases to about 0.1%/°C at 750 nm and to about 1.2%/°C at 1100 nm, which is consistent with the manufacturer's product data. On the other hand, when the detector is fitted with a $V(\lambda)$ filter for photometry, its broadband response varies by about 0.1%/°C when viewing a CIE Standard Illuminant A source [1].

Therefore, measurement accuracy depends in large part on taking temperatures into account. It is essential to either maintain the detector at the temperature at which it was calibrated, or else to measure the temperature of the detector as it is calibrated and used, applying a correction factor to measured values. Both approaches have their advantages.

Temperature regulated detectors, while simplest to interpret, are the more complicated to construct. They naturally require more components and circuitry to form the temperature control loop, and there are additional considerations having to do with the optics. We will describe our recent design, later.

SPIE Vol. 1479 Surveillance Technologies (1991) /

Temperature monitored detectors can have a simpler design, at the expense of more work required to calibrate them as a function of temperature, and additional steps are required to interpret the data.

2. TEMPERATURE-MONITORED RADIOMETERS AND PHOTOMETER

A typical temperature monitored detector in use at NIST has an AD590* temperature sensor mounted in the front piece of its aluminum housing as shown in Fig. 1. The photodiode, the filter package (if any), and a precision aperture (if required) are in metal holders, allowing good thermal contact between them. The remainder of the detector, in the housing, includes electronics associated with the sensor and the photodiode. The signal from the sensor is provided along with the signal from the photodiode, both of which require measurement with external voltmeters.

In this type of design, where a temperature probe is dedicated to a particular detector, the calibration of the temperature sensor is unimportant. Provided that the sensor is stable over time, the optical response of the detector may be consistently described with reference to it alone.

Calibration of temperature monitored detectors is necessarily more involved, since the calibration needs to be made as a function of temperature, rather than at a single temperature. Some simplification can be made if the detector can be calibrated on a relative basis with good precision as a function of temperature. Then, only one absolute calibration needs be made to fix the scale. As a practical matter, such detectors are often used under circumstances where the temperatures are bound within a narrow range, such as by the building utilities in a laboratory. We find it is often sufficient to use a linear approximation to the temperature dependence, and to express the temperature dependence factor as a percent change per degree change.

3. TEMPERATURE CONTROL OF RADIOMETERS AND PHOTOMETERS

The simplest temperature regulators use resistive heating to set a temperature above the ambient value. (Ref. [2] provides an example.) However, optical detectors are sometimes used in sealed, light-tight boxes that may contain other heat-dissipating equipment, such as lamps and positioning motors. Because the ambient temperature may sometimes be too high, we recently designed and built temperature stabilized detectors that use thermoelectric coolers. They can either heat or cool depending on the sign of the drive current. An ILX-Lightwave LDT-5910* controller provides the temperature regulation.

With visible light, the temperature of silicon photodiodes need not be lowered to reduce noise, however, providing a stable temperature avoids problems of drift [3]. It is our practice to regulate the temperature to approximately 20 °C, where room temperature varies between 20 and 24 °C. We find that we can control the temperature to within 0.1 °C without much difficulty. But, just as in the temperature monitored case, the method depends on the long term stability of the temperature sensor.

When the detector is cooled below the ambient temperature, condensation of water from the air becomes a problem. This requires that the cooled components be sealed from outside air. Additionally, there is a close connection between this problem and a problem associated with measuring laser light. Parallel optical surfaces form resonant cavities, which can have a noticeable effect on the transmittance of narrow bandwidth light. Among the parallel surfaces that should be eliminated are those of the protective window of the photodiode. However, removing the window subjects the photodiode to humidity variations, which can change its quantum efficiency. Both problems are resolved by hermetically sealing the windowless photodiode and other cooled components in a region with a wedged entrance window, slightly tilted with respect to the plane of the photodiode.
Fig. 2 shows the design of a temperature-controlled silicon radiometer based on these principles. A large area (1 cm^2) silicon photodiode is inserted into two pin-sockets pressed into a black plastic disc. When the photodiode is installed, its underside rests on a temperature-controlled copper plate. The thermoelectric cooler is placed between the copper plate and a mesa on the aluminum cover plate. The cover plate closes the cylindrical housing for the electronics and also serves to dissipate the heat of the thermoelectric cooler. The black plastic disc has a rectangular center cut-out which fits over the mesa. The disk and the copper plate are held by three nylon screws, which provide support to, and thermal insulation from, the cover plate. This arrangement provides some flexibility in accommodating different photodiode pin lengths. The pins, insulated by teflon tubing, straddle the copper plate and the thermoelectric cooler.

The temperature sensor is a thermistor, positioned in a side hole in the copper plate. There is also a threaded hole in the copper plate which allows an electrical connection to be made to the shielding junction. The wires of the thermoelectric cooler, the thermistor, and the shielding lead go through holes in the black plastic disk and the aluminum cover plate.

This hole in the cover plate and two other holes for the photodiode leads are sealed with silicone caulk of low outgas rate and high insulation resistance. An O-ring provides the seal between the cover plate and a cap. A window is formed in the top of the cap by using a wedged, fused silica beamsplitter. It is mounted and sealed using an epoxy of low outgas rate.

This design can be adapted for use as a photometer. Instead of the copper plate, a copper mount could be used as shown in Fig. 2(b). The spectrally correcting filters with a precision aperture are also placed inside the copper mount, above the silicon photodiode.

The circuit diagram of the temperature controlled detector is shown in Fig. 3. The most important requirement for the temperature controlling circuit and its associated components is its separation from the high sensitivity optical radiation measuring circuit. This requires careful shielding and grounding. The electrical common for the light measuring circuit and that for the temperature controlling circuit must be separated. Additionally, components composing a shield are tied together, separately. The copper plate, S, between the photodiode, P, and the thermoelectric cooler, TE, was connected to the shield junction, as was the aluminum housing. This improved the output AC ripple

voltage by a factor of two. One lead of the thermoelectric cooler was covered by a braid, which was also attached to the shield junction. The other lead was connected to the shield junction directly. As a result, we observed little or no excess noise in the photocurrent circuit as a result of operating the thermoelectric cooler.

It should be noted that in the discussion of temperature effects in Ref. [3], pertaining to the drift of the output signal, the temperature fluctuations of the amplifier caused a greater effect than the temperature fluctuations of the photodiode. Since this design does not temperature-regulate the amplifier, the discussion of drift in Ref. [3] applies almost unchanged.

4. SUMMARY

Both temperature-monitored and temperature-regulated detectors are tractable approaches to improve the accuracy of radiometric measurements. Temperature-monitored detectors are easier to construct, but they require more calibration data and analysis as well as additional steps to interpret the results of measurements. Temperature-regulated detectors make measurement taking simpler, with the expenses of additional and more complex hardware.

ACKNOWLEDGEMENTS

The author would like to extend thanks to Chris Cromer and Tom Larason for their participation in the temperature dependent spectral response measurement of photodiodes, to Hong Sun for temperature dependent broadband response measurements of photometers, and to Jonathan Hardis for help in preparing this manuscript.

*Certain commercial products are identified in order to more completely describe this work. Such identification does not imply endorsement or recommendation by the National Institute of Standards and Technology, nor does it imply that these items are the best available for the purpose.

REFERENCES

1. G. Andor: Temperature dependence of high accuracy photometer heads, Appl. Opt. 28, 4733-4, 1989.

2. E. F. Zalewski: NBS Measurement Services: The NBS Photodetector Spectral Response Calibration Transfer Program, NBS Special Publication 250-17, March, 1988, p. 7.

3. G. Eppeldauer and J. E. Hardis: Fourteen decade photocurrent measurements with large area silicon photodiodes at room temperature, Submitted to Applied Optics, September, 1990.

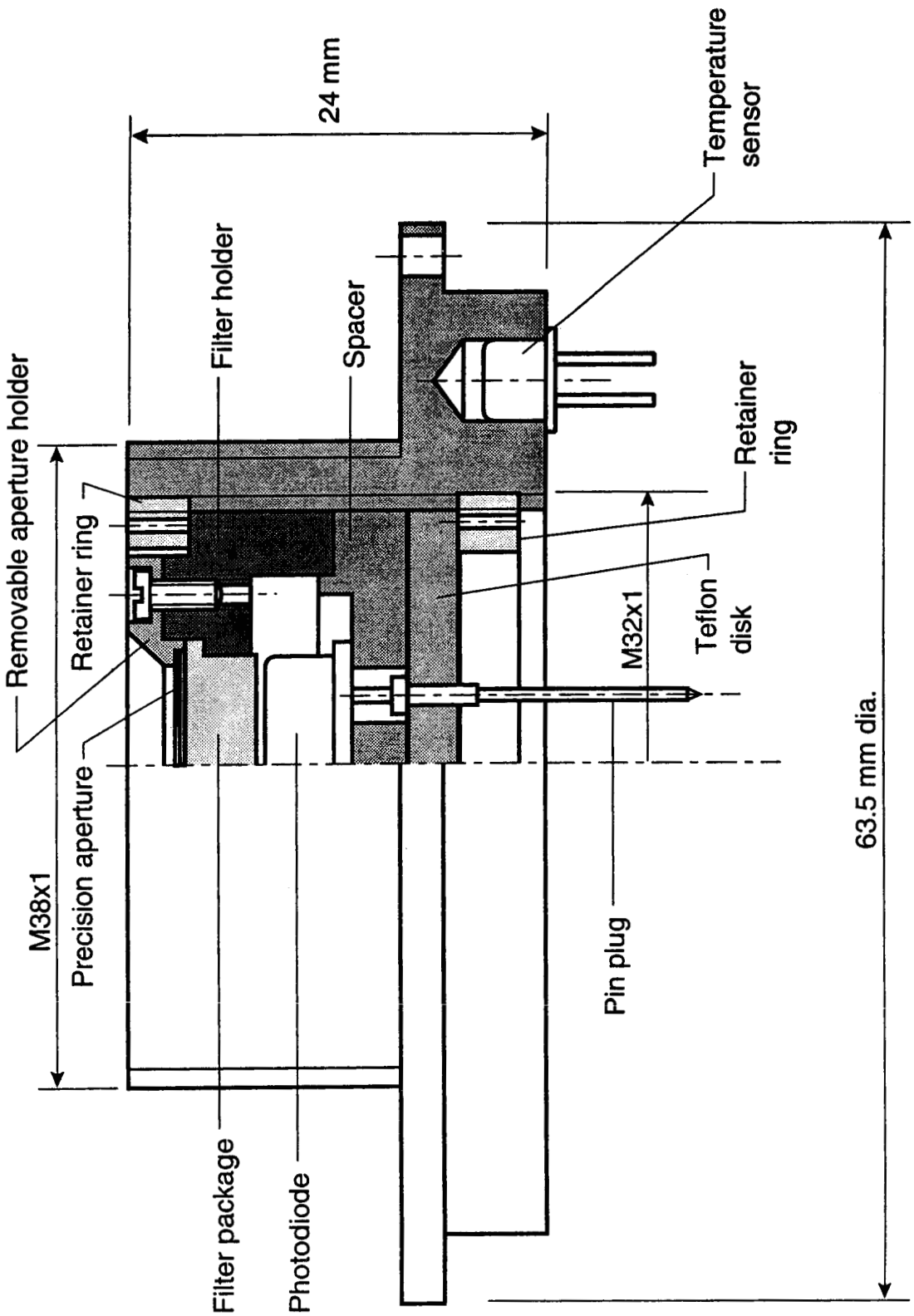

Figure 1. Construction of a temperature-monitored photometer. The construction of a temperature-monitored radiometer is similar with the exception of the filter package.

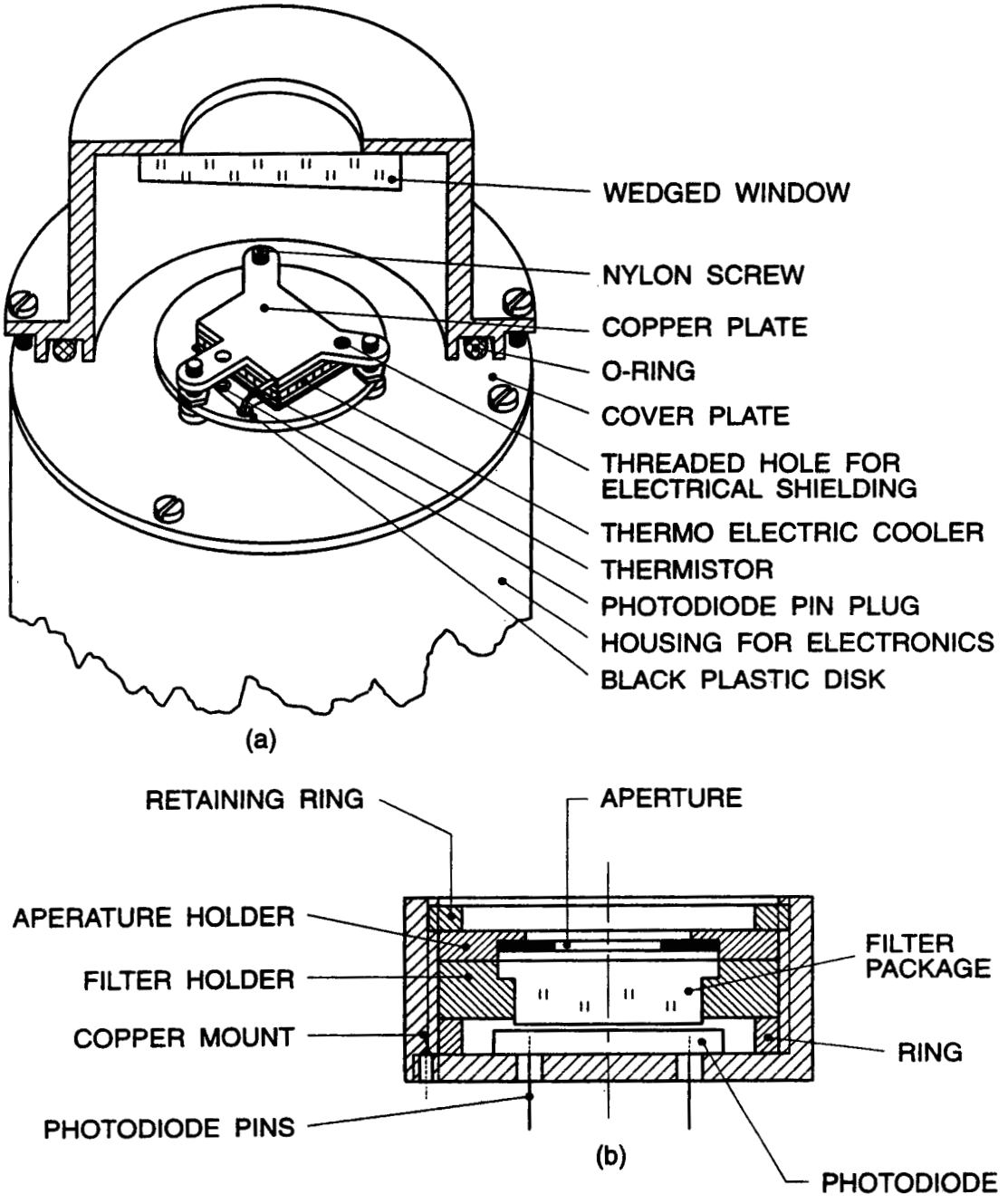

Figure 2. (a) Temperature controlled silicon radiometer. The silicon photodiode is not shown for clarity but would be placed on top of copper plate. (b) Cross-section of a copper mount containing silicon photodiode, filters and aperature that would be placed directly on thermo-electric cooler in the temperature controlled photometer.

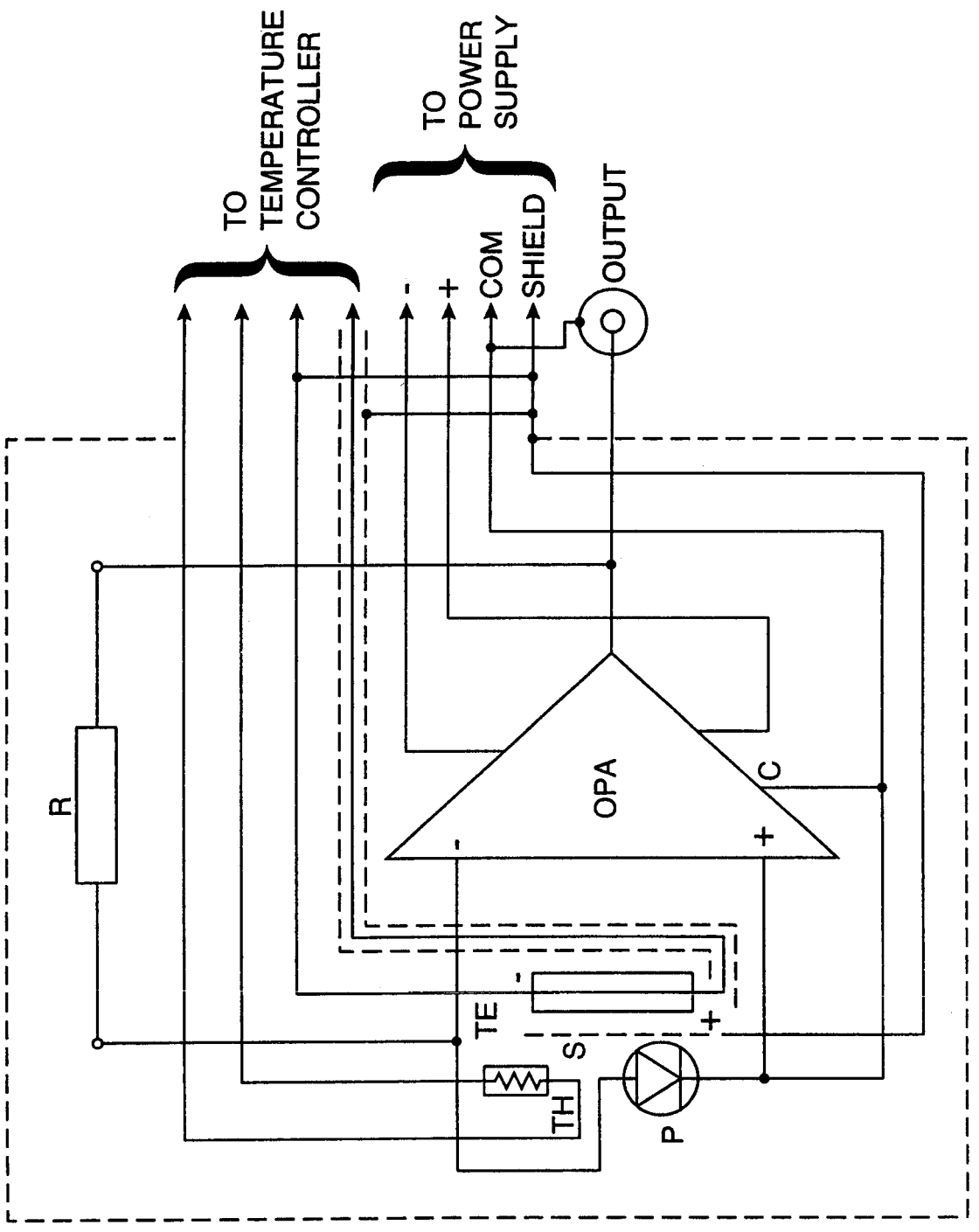

Figure 3. Circuit diagram of the temperature-controlled silicon radiometer head.

Volume 103, Number 2, March–April 1998
Journal of Research of the National Institute of Standards and Technology

[J. Res. Natl. Inst. Stand. Technol. **103**, 153 (1998)]

Chopped Radiation Measurements With Large Area Si Photodiodes

Volume 103 | Number 2 | March–April 1998

George Eppeldauer

National Institute of Standards and Technology,
Gaithersburg, MD 20899-0001

Frequency dependent response characteristics of photocurrent meters using large area, radiometric quality Si photodiodes have been analyzed. The current responsivity, the voltage noise and drift amplification, and the gain and bandwidth of the photocurrent-measuring analog control loop were calculated. The photodiodes were selected for high shunt resistance. The effect of the photodiode junction capacitance on the response characteristics was also analyzed. As a result of photocurrent gain dependent frequency compensations, the noise boosting effect was minimized at the output of the current meter. The loop gain and bandwidth were maximized. High-accuracy photocurrent measurements can be achieved using the described procedures for both dc and modulated optical radiation.

Key words: Bode plot; chopped light; detector; frequency dependence; gain; measurement; optical radiation; photocurrent; photodiode; radiometer; responsivity; silicon.

Accepted: December 17, 1997

1. Introduction

In many applications, the signal of optical radiation varies rapidly. Also, the optical radiation can be modulated or chopped. In these applications, the frequency dependent signal and noise gains of a photocurrent meter are to be optimized. In order to maximize the performance of the current meters for different photodiodes, their frequency dependent current-to-voltage (transimpedance) and voltage gains will be determined and the control loop gain and bandwidth will be optimized for the signal frequencies at all signal-gain ranges.

The dc and low-frequency characteristics of low-photocurrent measuring circuits of large area silicon photodiodes were analyzed earlier [1,2,3]. It was shown that for high sensitivity photocurrent measurements, high feedback resistors and high shunt resistance photodiodes are required. The high source resistance (parallel combination of the feedback and shunt resistances) requires current measuring operational amplifiers with low input bias currents. Such devices are the ultra low bias current Field Effect Transistor (FET) or the dielectrically isolated FET operational amplifiers. The high source resistance produces high thermal (Johnson) voltage noise, and the FET input stage of the operational amplifier has a large $1/f$ voltage noise. These dominant voltage noise sources were equalized when a measurement time of 400 s was used. Drifts and noise were equalized by regulating the device temperature [4] with an instability smaller than +/− 0.02 °C. The photodiodes were selected for a shunt resistance close to 10 GΩ in order to keep the voltage amplification close to unity. The equivalent photocurrent of the equalized noise and drift was 0.1 fA with an electrical bandwidth of 1.25 mHz. This implies a dynamic range of 14 orders of magnitude (10^{14}) for a silicon photodiode current meter. The time

constants (shunt resistance times junction capacitance) of the tested silicon photodiodes varied between 10 s and 200 s. When the bandwidth was increased to 300 mHz, the output noise of the photocurrent-measuring circuit increased significantly. The sensitivity decrease for the large-time-constant photodiodes was about a factor of 10. This was an indication of a frequency dependent noise boosting effect in the noise amplification of the current meter.

The optical radiation first is converted into an electrical signal by the photodiode itself; then, the electrical signal of the photodiode is measured. In radiometric applications, current measuring preamplifiers are connected to the photodiode. The internal speed of the photodiode depends on the time needed to convert the accumulated charge into current. The photodiode internal conversion time is determined by the diffusion time of carriers generated outside the depletion layer and the carrier transit time in the depletion layer [5]. The maximum frequency at which modern silicon photodiodes will produce current is somewhere in the 2 GHz range [6], depending on the area of the detector and the type of silicon material used. It is important to keep the internal capacitance of the photodiode low because this capacitance will produce an additional time constant in conjunction with the load resistance. This time constant τ works like a low-pass filter for the current of the photodiode. The junction capacitance is proportional to the active area and inversely proportional to the square or cube root of the width of the depletion layer. The depletion layer width is proportional to the product of the resistivity of the material and the reverse voltage [5] (if it is applied to the diode). The silicon bulk resistivity can be specified from 1 Ω cm to 10000 Ω cm [6]. The higher the resistivity, the lower the junction capacitance of the photodiode.

Most frequently, the photodiode rise time is reported instead of its 3 dB response roll-off frequency. The rise time is the time required for the output signal of the photodiode to change from 10 % to 90 %. For different types of large area silicon photodiodes the rise time is between 1 μs and 7 μs when a 1 kΩ load resistor and zero biasing voltage are applied [5]. An average junction capacitance for large area silicon photodiodes is about 1 nF. This gives a $\tau = 1$ μs time constant with the 1 kΩ load resistor at test. This is equivalent to a 3 dB signal response roll-off frequency of 160 kHz. Caution is necessary when the modulation frequency of the measured optical radiation is close to or higher than the 3 dB frequency. At those high frequencies the modulated optical signal can be damped because of the amplitude roll-off, resulting in a changing ac photocurrent response versus frequency. In these cases, ac to dc photocurrent conversions, realized by low pass filters, give higher accuracy than ac signal measurements. This idea was successfully utilized in mode-locked laser measurements using two different kinds of large area silicon photodiodes [7]. The laser pulse width was 5 ps, the repetition rate was 100 MHz, and the averaged (dc) photocurrent was measured. The responses of the photodiodes were equal for both pulsed and cw laser measurements.

The type of the load resistor or preamplifier connected to the terminals of the photodiode plays an important role in the response time of the overall optical radiation measurement. If the photodiode current is converted into a voltage through a single load resistor the dominating time constant will be the product of the photodiode capacitance and the load resistance. In order to measure the short circuit current, which is proportional to the detected optical power, the load resistor has to be much smaller than the photodiode resistance. Instead of a small load resistor, a current-to-voltage converting analog control loop can be used as a preamplifier [8]. A current meter like this has a low input impedance and a high current-to-voltage gain. However, the magnitude of the complex input impedance varies with frequency. This impedance is connected in parallel with the photodiode junction capacitance. The transformation of the feedback impedance to the input of the current meter and the frequency dependent diode current-to-voltage response will be determined below.

The advantage of ac signal measurements is that the measuring circuit can be made selective for the signal frequency. This way a narrow measurement bandwidth can be chosen close to the elbow of the preamplifier's $1/f$ noise range where the $1/f$ noise is small.

The shunt resistance and the junction capacitance of different large area Si photodiodes can change significantly. It is important to understand the effect of the photodiode impedance on the optical radiation measuring analog control loop when high sensitivity and fast operations are expected. The analog control loop will produce a high accuracy current-to-voltage conversion only if the loop gain and bandwidth are high enough at the signal frequencies. Also, the current measuring analog control loop, coupled to the output of the photodiode, is the first stage of the measuring circuit. The first stage dominates the signal-to-noise ratio for the output of the measuring circuit. It is important to keep the first stage amplification for the dominant voltage noise low within the electrical bandwidth of the measurement. The electronic circuits in the second stage, such as a lock-in amplifier or a digital voltmeter, cannot restore the established signal-to-noise ratio caused by the lack of optimization in the first stage.

In the present work, the previously described dc and low frequency analysis of large area and wide dynamic

range Si photodiode current meters is extended to higher signal frequencies. The purpose of this paper is to show how to maximize the performance of photocurrent meters for different photodiodes at different signal frequencies.

2. Photodiode Current Measuring Circuit

In order to achieve linear operation in a wide dynamic signal range, the short-circuit current of the photodiode has to be measured. The simplified scheme of widely used short-circuit current meters is shown in Fig. 1.

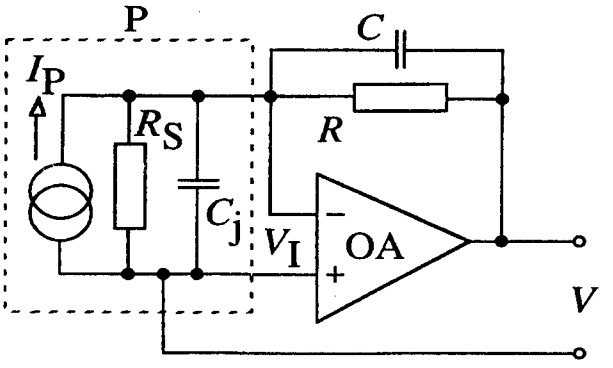

Fig. 1. Simplified circuit diagram of a photocurrent meter. The dashed line represents the photodiode P, and R and C are the feedback components of the operational amplifier OA.

The photocurrent I_P of the photodiode P is measured by a current-to-voltage converter. The current-to-voltage conversion is realized by an operational amplifier OA. P has a shunt resistance R_S and a junction capacitance C_j which together produce the photodiode impedance Z_d. I_P is converted into a voltage V through the feedback impedance of the OA. The feedback impedance Z is the parallel connection of the feedback resistor R and its parallel capacitance C. The OA input voltage V_I is small because of the large OA open loop gain, A. As the maximum of V is 10 V, and A is about 10^6, V_I is equal or smaller than 10 μV. This very small voltage drop on P produces a small load resistance R_I for the photodiode[3]:

$$R_I \approx \frac{R}{A}.$$

Determination of R_I is only sufficient for dc or low frequencies. It is the input impedance Z_I of the current meter that determines the time constant τ of the photodiode short-circuit current measurement at higher frequencies:

$$Z_I = \frac{Z}{A} = \frac{R}{A}\frac{1}{(1+j\omega CR)} = \frac{1}{\frac{A}{R}+j\omega AC}. \quad (1)$$

The rewritten (popular) form of Eq. (1) shows that the input impedance of the current meter can be calculated as the parallel connection of the down-transformed feedback resistor and the up-transformed feedback capacitor of the OA:

$$(Z_I)^{-1} = (\frac{R}{A})^{-1} + (\frac{1}{j\omega AC})^{-1}.$$

C_j will be increased significantly by the parallel connected, up-transformed feedback capacitor AC. If $R/A << R_S$, the measurement time constant is

$$\tau = \frac{(C_j + AC)R}{A}. \quad (2)$$

As an example, $AC = 2$ μF if $C = 2$ pF and $A = 10^6$. For $R = 10^9$ Ω, the input resistance will be $R_I = 10^3$ Ω. AC >> C_j for $C_j = 1$ nF; therefore, $\tau = RC = 2$ ms. Z and the impedance of the photodiode Z_d create a feedback network from the OA output to the OA input. The voltage attenuation of the feedback network is β.

For accurate dc and/or ac photocurrent measurements, the photodiodes have to be selected for shunt resistance and junction capacitance; and the other passive components of the feedback network are to be calculated. Thereafter, an OA has to be selected which satisfies the noise, drift, input current, and speed (bandwidth) requirements.

2.1 Drift and Noise Amplification

The OA input voltage-noise, which is the principal source of $1/f$ noise, and input offset-voltage with its drift [1,2,3], are amplified to the OA output by the closed loop voltage gain A_V of the photocurrent measuring analog control loop [9,10]:

$$A_V = \frac{A}{1+G} = \frac{1}{\beta}\frac{1}{1+G^{-1}}, \quad (3)$$

where the loop gain is $G = A\beta$. According to Eq. (3), if $G >> 1$, the feedback network determines A_V. The feedback attenuation is:

$$\beta \approx \frac{1}{A_V} = \frac{Z_d}{Z_d + Z}, \quad (4)$$

where $(Z_d)^{-1} = (R_S)^{-1} + j\omega C_j$ and $Z^{-1} = R^{-1} + j\omega C$. Therefore,

$$\beta = \frac{R_S(1 + j\omega RC)}{R_S(1 + j\omega RC) + R(1 + j\omega R_S C_j)}$$

$$= \frac{R_S(1 + j\omega RC)}{R_S + R + j\omega(R\,R_S\,C + R\,R_S\,C_j)}.$$

With

$$\beta_o = \frac{R_S}{R_S + R},$$

the feedback attenuation can be written as:

$$\beta = \beta_o \frac{1 + j\omega RC}{1 + j\omega \dfrac{R\,R_S\,C + R\,R_S\,C_j}{R + R_S}}. \quad (5)$$

The dc (or very low frequency) voltage amplification of the photocurrent measuring circuit is the reciprocal of β_o:

$$A_{Vo} = \frac{R_S + R}{R_S} = 1 + \frac{R}{R_S}. \quad (6)$$

The frequency dependent closed loop voltage gain can be written as the reciprocal of β in Eq. (5):

$$A_V = \frac{R_S + R}{R_S} \frac{1 + j\omega \dfrac{R\,R_S\,C + R\,R_S\,C_j}{R + R_S}}{1 + j\omega RC}, \quad (7)$$

where the integrating time constant is $\tau_1 = RC$. The differentiating time constant is

$$\tau_2 = \frac{R\,R_S\,C + R\,R_S\,C_j}{R + R_S} = \frac{R\,R_S}{R + R_S}(C + C_j). \quad (8)$$

τ_2 is calculated from the product of two factors. One factor is the resultant resistance of the parallel connected R and R_S. The other factor is the sum of C and C_j [10].

For fast operation, C has to be small. However, C has a minimum value of 1 pF to 2 pF, because of the stray capacitance parallel to R. For all large area photodiodes, $C_j >> C$ when the external C is not connected parallel to R. In this case, the frequency dependent voltage amplification of the measuring circuit can be written as:

$$A_V = A_{Vo} \frac{1 + j\omega \dfrac{R\,R_S\,C_j}{R + R_S}}{1 + j\omega RC}. \quad (9)$$

If $R >> R_S$ the voltage amplification is:

$$A_V^{(1)} = A_{Vo} \frac{1 + j\omega R_S C_j}{1 + j\omega RC}. \quad (10)$$

In this case, the differentiating time constant in the numerator is determined exclusively by the impedance of the photodiode. If $R_S >> R$, then

$$A_V^{(2)} = A_{Vo} \frac{1 + j\omega R C_j}{1 + j\omega RC}. \quad (11)$$

In Eq. (3),

$$A = A_o \frac{1}{1 + j\omega \tau_i}, \quad (12)$$

where τ_i is the integrating time constant of the OA. A_o is the dc open loop gain of the OA.

2.2 Frequency Dependent Signal Response

The frequency dependent current-to-voltage response of the photocurrent measuring circuit can be calculated as well. With the Norton to Thevenin source conversion formula [11] the photocurrent I_P can be converted into V_I:

$$V_I = I_P \frac{1}{1 + j\omega R_S C_j}. \quad (13)$$

As a next step, V_I is amplified by the OA. The voltage amplification here [9] is equal to the ratio of Z to Z_d:

$$\frac{V}{V_I} = \frac{R}{R_S} \frac{1 + j\omega R_S C_j}{1 + j\omega RC}. \quad (14)$$

When Eq. (13) is substituted into Eq. (14) the photocurrent-to-voltage conversion [13,14] A_I which is frequently called the transimpedance gain, can be written as:

$$A_I = \frac{V}{I_P} = R \frac{1}{1 + j\omega RC}. \quad (15)$$

Equation (15) shows that the dc signal gain (or response), which is the ratio of the output voltage V to the input photocurrent I_P is equal to R. The frequency dependent signal response is determined by the integrating time constant, $\tau_1 = RC$, of the feedback impedance. This time constant and the OA input-impedance-determined time constant τ, in Eq. (2), are the same: $\tau = \tau_1 = RC$. Equation (15) also describes the gain for the input current noise of the circuit. Because Eq. (15) does not show the frequency dependent contribution of the OA to the signal response, the equation works only if $\tau_i < \tau_1$.

Otherwise, the OA frequency dependent response can give an unwanted limitation for the signal response. Similarly to Eq. (3),

$$\frac{V}{I_P} = R\frac{1}{1+G^{-1}}. \qquad (16)$$

The current-to-voltage conversion, R, which is the signal gain, will be accurate only if $G >> 1$ at the signal frequency. This is a very important design requirement for the analog control loop.

3. Response Functions of Silicon Photodiode Current Meters

Gain versus frequency curves adequately describe the dynamic characteristics of analog control loops. Most frequently the responsivity (gain) products of the individual components of the open loop are shown on a log amplitude scale versus log frequency. These characteristics can be constructed quickly and fairly accurately by approximating the curves by piecewise linear regions. The construction rules are easy. E.g., a constant in the gain equation gives a horizontal line. $1 + j\omega\tau$ in the denominator gives a roll-off. Roll-off points are also called "poles". The slope of the roll-off is − 20 dB per decade. $1 + j\omega\tau$ in the numerator, gives a roll-on. A roll-on point is also called "zero". The slope of the roll-on is 20 dB per decade. The interconnected straight-line characteristics realized this way are called idealized Bode plots [12].

3.1 Voltage Gain Plot of a Si Photodiode Current Meter

The frequency dependent voltage amplification of a photodiode short circuit current meter is described by Eq. (7). The shape of this function will be illustrated first on the widely used silicon photodiode, Hamamatsu Model S1226-8BQ[1]. This photodiode has an active area of 1/3 cm^2. The photodiode was purchased with a selected $R_S = 6.5$ GΩ. The junction capacitance is typically $C_j = 1.3$ nF. This photodiode was tested earlier [3] and a noise floor of 0.1 fA was measured with an electrical bandwidth of 1.25 mHz. When the bandwidth was increased to 0.3 Hz, the noise floor increased to 0.6 fA. The feedback resistor was $R = 10^{11}$ Ω and the estimated stray capacitance was $C = 2$ pF. The 3 dB open-loop roll-off frequency of the OPA128LM operational amplifier used is $f_i = 3$ Hz. This OA was chosen for low input current (40 fA) and a peak-to-peak current noise of 2.3 fA. This selection was necessary to keep the effect of the OA input current small on the very high source resistance (parallel connected R and R_S). The dc open-loop gain of the operational amplifier is 110 dB.

A time constant of $\tau_1 = RC = 0.2$ s gives a signal roll-off frequency of $f_1 = 0.8$ Hz. From $\tau_2 = 8$ s, the roll-on frequency is $f_2 = 0.02$ Hz. The roll-off and roll-on slopes are − 20 dB per decade and 20 dB per decade, respectively. $A_{V_0} = 16.4$ from Eq. (6). In Fig. 2, log A_V versus log frequency is shown, together with the frequency dependent open loop gain of OA. The figure shows that the voltage amplification increases by 1.5 decade when the frequency increases from 0.02 Hz to 0.8 Hz. The photocurrent measuring electrical bandwidth can be limited by a low-pass filter or integrating DVM connected to the output of the photocurrent meter. If this out-of-loop limiting bandwidth is smaller than 0.02 Hz, the noise boosting effect of the photocurrent measuring circuit will be rejected. In this case, the measurement will be slow. However, when the measurement bandwidth is 0.3 Hz, as before [3], or larger, the OA input voltage noise components will be amplified in the 0.02 Hz to 0.8 Hz frequency range.

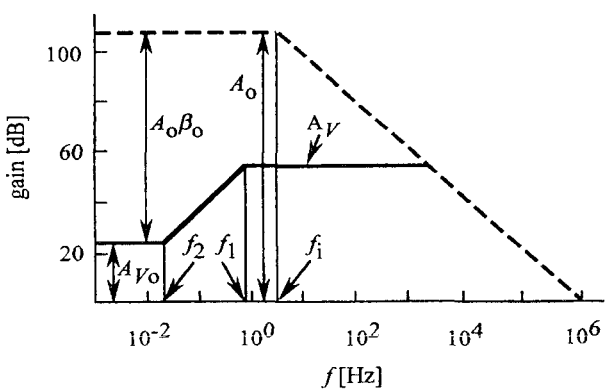

Fig. 2. Closed-loop voltage gain (solid lines) of a Hamamatsu S1226-8BQ silicon photodiode current meter. $R_S = 6.5$ GΩ, $C_j = 1.3$ nF, $R = 10^{11}$ Ω, and $C = 2$ pF. The dashed line shows the open loop gain of the OPA 128LM operational amplifier without any feedback.

The shape of the area between the OA open loop gain curve and the A_V voltage amplification curve gives information about the dynamic characteristics of the photocurrent measuring analog control loop. The information about the loop performance can be made more clear and more understandable if this area is illustrated by the Bode plot of the loop gain.

[1] Certain commercial equipment, instruments, or materials are identified in this paper to foster understanding. Such identification does not imply recommendation or endorsement by the National Institute of Standards and Technology, nor does it imply that the materials or equipment identified are necessarily the best available for the purpose.

3.2 Loop Gain Plot of a Si Photodiode Current Meter

The frequency dependent loop gain of the open analog control loop can be written from Eqs. (5) and (12):

$$G = A_o \beta_o \frac{1}{1 + j\omega \tau_i} \frac{1 + j\omega RC}{1 + j\omega \dfrac{R R_S C + R R_S C_j}{R + R_S}}, \quad (17)$$

where $RC = \tau_1$ is the integrating time constant in Eq. (7) (noise voltage gain). Here τ_1 is a differentiating time constant. Similarly, τ_2 of Eq. (8) was a differentiating time constant in the noise voltage gain equation. In Eq. (17), τ_2 is an integrating time constant. The OA time constant, τ_i, is always an integrating type time constant.

Figure 3 shows the Bode plot [12] of the open photocurrent measuring control loop, where $\beta_o = 0.06$, as calculated from Eqs. (4) and (5) with $R = 10^{11}$ Ω. $A_o \beta_o = 18000$. The solid curve shows the dynamic characteristics of the analog control loop. The curve intercepts the frequency axis with a slope of − 20 dB per decade showing that the phase shift (phase lag) in the open loop at this frequency is not more than − 90°. This phase shift corresponds to one integrating time constant. This − 90° phase shift, together with the − 180° phase shift of the negative feedback, results in a maximum phase shift of − 270°. Since this phase shift is less than − 360°, oscillations will not occur. Also, the loop gain, $G = A\beta$, is equal to or larger than 1000 (60 dB) from 0 Hz to about the 3 dB roll-off frequency of the signal response curve. The large G in the low frequency interval gives a high current-to-voltage conversion accuracy. The dashed photocurrent-to-voltage response curve, which is described by Eq. (15), was matched at its 3 dB point to the loop gain function.

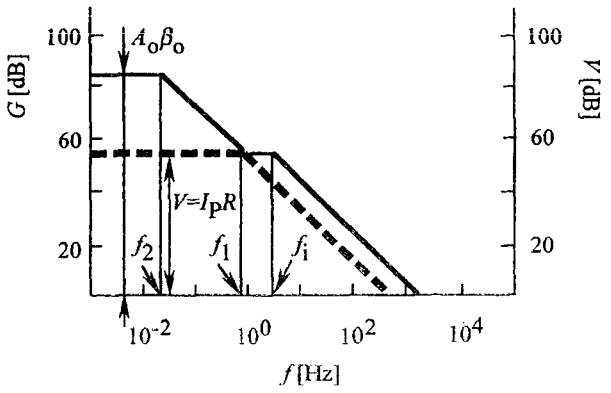

Fig. 3. Loop gain plot of the Hamamatsu S1226-8BQ Si photodiode current meter. $R_S = 6.5$ GΩ, $C_j = 1.3$ nF, $R = 10^{11}$ Ω, and $C = 2$ pF. The solid curve shows the gain of the open control loop. The dashed curve shows the current response function as matched at its 3 dB roll-off point to the loop gain function.

The overall electrical bandwidth of photocurrent measurements greatly depends on R. This is true for both the signal response in Eq. (15) and the loop bandwidth described by Eq. (17). The speed of the above analyzed high sensitivity photocurrent meter is slow because of the very large R. The speed can be increased by decreasing R. However, smaller R decreases the photocurrent responsivity. Figure 4 shows the voltage gain curves of the Hamamatsu S1226-8BQ silicon photodiode current meter. The noise boosting effect does not disappear with decreasing R. Decreasing R shifts the noise boosting interval to higher frequencies. Small feedback resistors are used when the photocurrent is large. In these cases, the noise boosting effect is less of a problem.

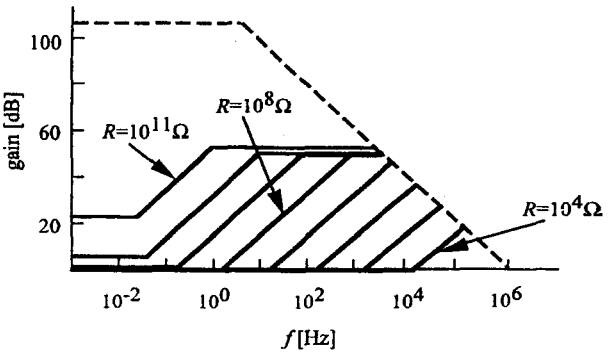

Fig. 4. Closed-loop voltage gain characteristics of the Hamamatsu S1226-8BQ Si photodiode current meter when the feedback resistors are changed from 10^{11} Ω to 10^4 Ω. $R_S = 6.5$ GΩ, $C_j = 1.3$ nF, and $C = 2$ pF. The dashed line shows the open loop gain of the OPA 128LM operational amplifier, without any feedback.

Decreasing R will increase both the loop bandwidth and the low frequency loop gain. Figure 5 shows the different loop gain plots of the Hamamatsu S1226-8BQ silicon photodiode circuit when R changes from 10^{11} Ω to 10^6 Ω. Similarly to Fig. 3, $f_2 < f_1$ for all feedback resistors when $C = 2$ pF = constant. When R decreases, both the roll-off frequency, f_2, and the roll-on frequency, f_1, increase. With decreasing R, f_1, which is equal to the signal 3 dB roll-off point, shifts towards the frequency axis. At $R = 10^8$ Ω, f_1 reaches the log f axis. At this frequency, the phase lag in the open loop is − 135°. τ_i and τ_2 integrating time constants shift − 180°, and τ_1 differentiating time constant gives a phase lead of + 45°. If R is further decreased, the phase shift at high frequencies (close to the unity gain cut-off frequency) can reach − 180°, resulting in oscillations in the closed loop. In order to increase stability and accuracy, f_1 has to be decreased by increasing τ_1. In our previous experimental circuits [1,2,3], when R was 10^6 Ω or smaller, τ_1 was increased using external capacitors, parallel connected

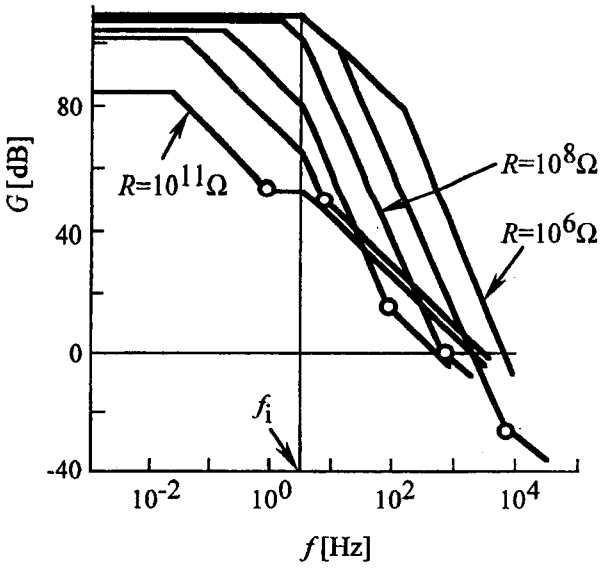

Fig. 5. Loop gain characteristics of the Hamamatsu S1226-8BQ photodiode current meter when the feedback resistors are changed from 10^{11} Ω to 10^6 Ω. R_S = 6.5 GΩ, C_j = 1.3 nF, and C = 2 pF (stray). No external capacitors are connected parallel to the feedback resistors. The open circles show the 3 dB roll-off points of the photocurrent response. They are matched to the loop gain curves for each R.

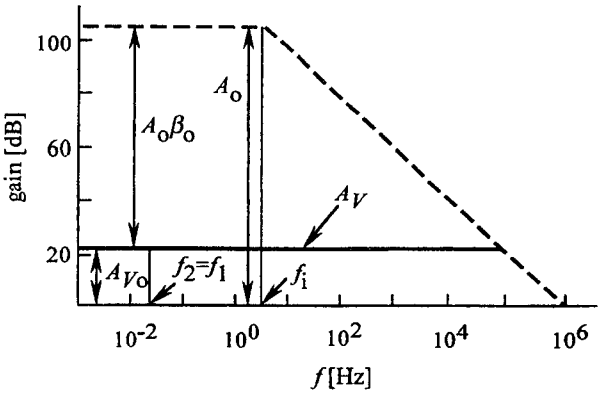

Fig. 6. Frequency compensated closed-loop voltage gain of the Hamamatsu S1226-8BQ Si photodiode current meter. R_S = 6.5 GΩ, C_j = 1.3 nF, R = 10^{11} Ω, and C = 80 pF. The dashed line shows the open loop gain of the OPA 128LM operational amplifier, without any feedback.

to the feedback resistors. Changing the feedback impedance by tuning the external parallel capacitor [15] can fundamentally modify the frequency dependent characteristics of the photocurrent meter.

3.3 Frequency Compensation of Current Meters

The noise boosting effect can be eliminated if $\tau_1 = \tau_2$. This compensation can be done easily by connecting an external capacitor of 78 pF parallel to $R = 10^{11}$ Ω. The sum of the 78 pF and the 2 pF stray capacitance will give the necessary C = 80 pF to achieve the frequency compensation. In this case, τ_1 will be 8 s. After the compensation, the shape of the solid curve, A_V, in Fig. 2 will change to a straight line, as shown in Fig. 6. The improved noise amplification will be $A_V = A_{Vo}$ for all frequencies within the loop.

If the compensation is made for all feedback resistors, the shape of the loop gain curves of Fig. 5 will be different. In each compensation, τ_1 canceled τ_2; therefore, τ_i became the only integrating time constant in the loop. Figure 7 shows the compensated loop gain curves for different feedback resistors. The loop bandwidth increased significantly because of the compensation. Without frequency compensation the loop gains were high enough only for dc and low signal frequencies. For feedback resistors between 10^{10} Ω and 10^4 Ω, the loop dynamic characteristics are very similar. There are no

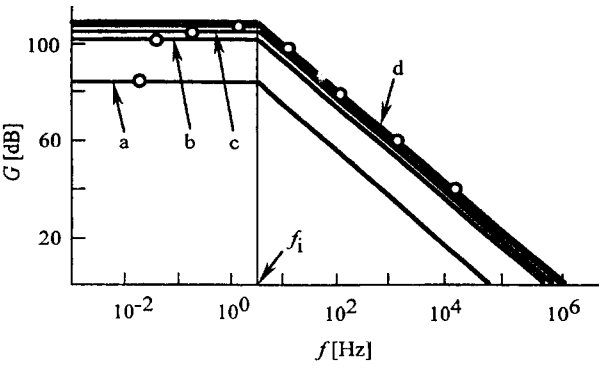

Fig. 7. Compensated loop gain characteristics of the Hamamatsu S1226-8BQ Si photocurrent meter. R_S = 6.5 GΩ and C_j = 1.3 nF. The feedback impedances are changed: a) $R = 10^{11}$ Ω, C = 80 pF; b) $R = 10^{10}$ Ω, C = 510 pF; c) $R = 10^9$ Ω, C = 1.1 nF; d) $R = 10^8$ Ω to 10^4 Ω and C = 1.3 nF. The open circles show the 3 dB roll-off points of the photocurrent response functions. They are matched to the loop gain curves for all feedback resistors, after compensation.

oscillation problems because the phase shift is less than − 90° even at high loop frequencies. The 3 dB roll-off points of the photocurrent response function of Eq. (15) are also shown for the different feedback impedances. For all feedback resistors, the compensated signal 3 dB points limit the speed of the photocurrent meter. The loop gains at the signal 3 dB points are always larger than 100. If a minimum loop gain of 1000 is required to achieve a 0.1 % relative standard uncertainty in photocurrent measurements, the signal frequency at the lowest signal gain of $R = 10^4$ Ω has to be limited to about 1 kHz. In the case of a wide dynamic signal range, this frequency limitation is not a problem, because the signal frequency limit is much lower at high signal gains. The

very low input current OPA128LM operational amplifier seemed to be the best selection for this very high sensitivity but very slow photocurrent meter.

The frequency compensation made the signal response of the current meter slower. This can be a problem when R is high. E.g., for $R = 10^{11}\ \Omega$, the $\tau_1 = 8$ s integrating time constant of the signal response requires about a 1 min wait for the digital voltmeter (DVM) to measure the signal accurately at the output of the current meter. The long waiting time before each DVM measurement is also necessary because of the roughly 2 min settling time of the OPA128LM operational amplifier when operated with this large feedback resistor. The measured settling time of the above discussed silicon photodiode current meter is shown in Fig. 8. The figure shows the output signal change of the meter after the shutter is closed. The duration of one measured point on the figure was determined by the integration time of the DVM, which was equal to the time of one power line cycle. This corresponds to an electrical bandwidth of 30 Hz [3]. A 16.2 s time constant was obtained from the curve fit to the measured data when an $R = 10^{11}\ \Omega$ feedback resistor was used. No external feedback capacitor was applied in this measurement. When $R = 10^{10}\ \Omega$ was selected, the settling time constant became shorter than the duration of one power line cycle.

As shown in Fig. 4, the dc voltage noise amplification decreased almost a decade when R was reduced from $10^{11}\ \Omega$ to $10^{10}\ \Omega$. At the same time, the photocurrent response also decreased by a factor of 10. Decreasing R results in a smaller source resistance noise for the input of the OA. As a result of the similar signal and noise changes, the signal-to-noise ratio for the output of the current meter is similar for these two signal gain selections.

Based on the above settling time and signal to noise ratio measurements, we conclude that $R = 10^{10}\ \Omega$ produces a faster measurement than $R = 10^{11}\ \Omega$ with similar photocurrent limit sensitivity.

3.4 Chopped Radiation Measurement

When dc or low frequency operation in a photocurrent measuring circuit is too slow to satisfy a certain measurement speed requirement, different photodiode and operational amplifier selections are needed.

The frequency dependent photocurrent-to-voltage conversion is described by Eq. (15). The RC time constant of the feedback impedance determines the bandwidth of the signal measurement. This time constant has to be small enough to keep the 3 dB signal roll-off frequency a decade higher than the frequency of the signal to be measured. E.g., with $C = 2$ pF, R can not be larger than $10^9\ \Omega$ to use a chopping frequency of 8 Hz. In this case $\tau_1 = 2$ ms and $f_1 = 80$ Hz. Because the voltage amplification can not be smaller than unity, for $R < 10^9\ \Omega$ the photodiode shunt resistance should not be larger than $10^9\ \Omega$. Also, if the junction capacitance is

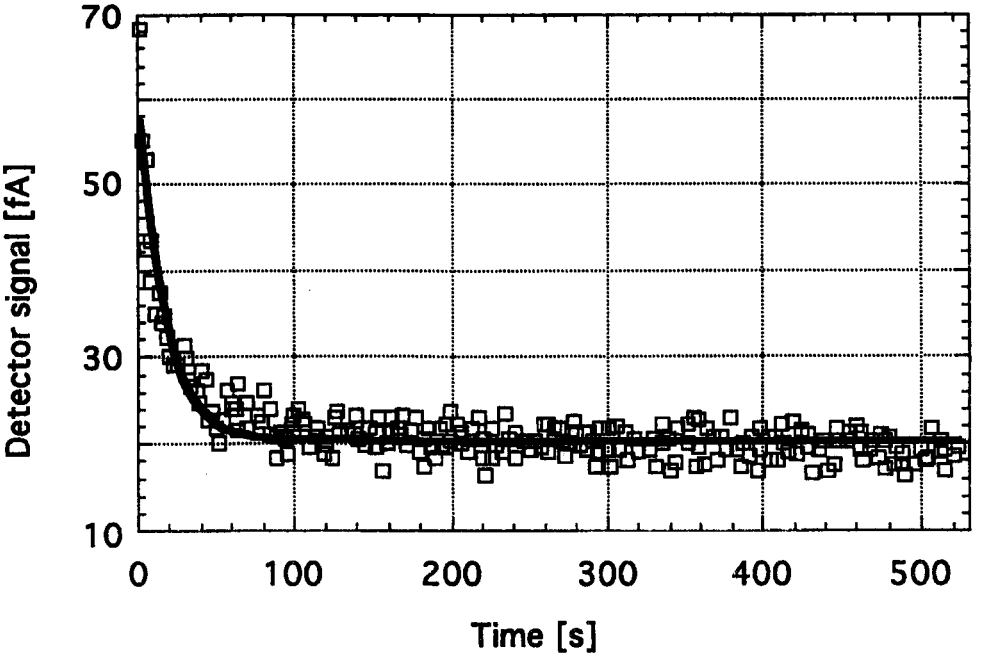

Fig. 8. The measured settling time of the Hamamatsu S1226-8BQ silicon photocurrent meter when $R = 10^{11}\ \Omega$. The time constant from the fit is 16.2 s.

low enough, the f_2 roll-on frequency of the voltage gain curve of Eq. (7) can be selected higher than the signal (chopping) frequency. A possible detector choice is the Hamamatsu S5226-8BQ silicon photodiode. This device has an active area of 1/3 cm^2. The shunt resistance is 1 GΩ and the junction capacitance is 430 pF. Figure 9 shows the voltage gain curves for the Hamamatsu S5226-8BQ silicon photodiode when used with the OPA627BM low noise and wide band operational amplifier. Partial frequency compensations were performed for all of those R where $f_2 < 80$ Hz. In these cases, the signal 3 dB points were tuned to 80 Hz. For those R where $f_2 > 80$ Hz, full frequency compensations were obtained. Frequencies f_1 were decreased to be equal to f_2. For each fully compensated gain ($R = 10^6$ Ω, 10^5 Ω, and 10^4 Ω), the sum of the stray and external capacitances was 432 pF. The signal 3 dB roll-off points are matched to the voltage gain functions for each R and are shown with open circles. The noise boosting effect disappeared after full compensations and decreased for partial compensations. If a chopping frequency of 8 Hz is selected and $R = 10^8$ Ω is used as a maximum feedback resistor, the noise amplification will be practically unity.

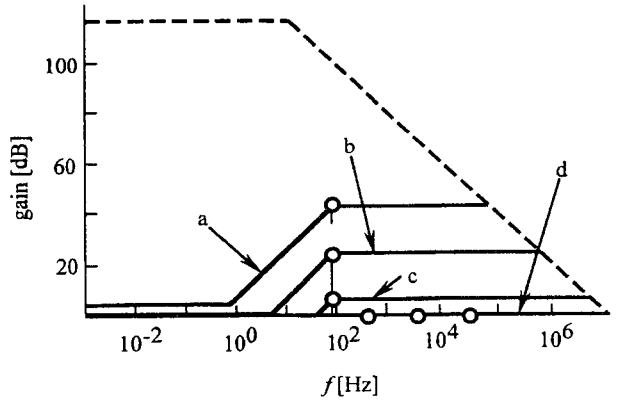

Fig. 9. Closed-loop voltage gains (solid curves) of a Hamamatsu S5226-8BQ Si photodiode ac current meter. $R_S = 1$ GΩ and $C_j = 430$ pF. The dashed curve shows the open loop gain of the OPA627BM operational amplifier, without any feedback. Partial frequency compensations were made at 80 Hz: a) $R = 10^9$ Ω and $C = 2$ pF; b) $R = 10^8$ Ω and $C = 20$ pF; and c) $R = 10^7$ Ω and $C = 200$ pF. Full compensations are shown by d) where $R = 10^6$ Ω to 10^4 Ω and $C = 432$ pF. The 3 dB roll-off points of the signal response curves are matched to the voltage gain curves and are shown with open circles.

The OA selection criteria for rapidly changing optical radiation is different than the earlier discussed very slow signal measurements. In the presently discussed ac measurement, the source resistance (parallel connection of R and R_S) was selected to be smaller than in the previously discussed dc and low frequency measurements. Consequently, the input bias current of the OA does not have to be extremely low. However, low noise, fast settling time, and fast operation are important OA requirements. The OPA627BM dielectrically isolated OA satisfies these expectations. This operational amplifier has low-noise, equal to bipolar-input amplifiers, larger bandwidth than that of FET input operational amplifiers, and the minimum slew rate is 40 V/μs.

The loop gain characteristics of the optimized ac silicon photodiode current meter for the different feedback impedances are shown in Fig. 10. The signal 3 dB roll-off points are matched to the loop gain curves and are shown again with open circles. The loop gain is higher than 300 at each signal 3 dB roll-off points for all R selections. Because of the large loop gains at signal frequencies smaller than the 3 dB point, the analog control loop errors are small and the implementation of Eq. (16) is accurate. E.g., $G > 10^3$ for signal frequencies smaller than 40 Hz.

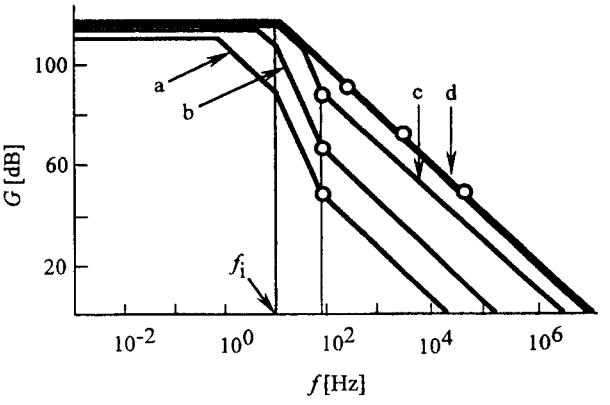

Fig. 10. Loop gain curves of an ac photocurrent meter using a Hamamatsu S5226-8BQ Si photodiode. $R_S = 1$ GΩ and $C_j = 430$ pF. OPA627BM operational amplifier is used. Partial frequency compensations are made at 80 Hz: a) $R = 10^9$ Ω and $C = 2$ pF; b) $R = 10^8$ Ω and $C = 20$ pF; and c) $R = 10^7$ Ω and $C = 200$ pF. Full compensations are shown by d) where $R = 10^6$ Ω to 10^4 Ω and $C = 432$ pF. The signal 3 dB roll-off points are matched to the loop gain curves and are shown with open circles.

If the radiation is chopped, a lock-in amplifier is usually connected to the output of the current meter. The lock-in, which is synchronized with the radiation chopper, performs a phase sensitive rectification of its input signal. The low-pass filter, coupled to the output of the lock-in, smooths the signal. The filter should be properly designed to take fast enough readings when the optical radiation changes. Usually, active filters (e.g., Bessel) are used to optimize filter characteristics [9]. If a very small bandwidth is realized by the low-pass filter (for an improved signal to noise ratio), the measurement will be very slow.

4. Conclusions

In addition to signal range and sensitivity, speed can be an important issue in photodiode short circuit current measurements. In order to calculate the frequency dependent signal and noise gains of different photodiode current meters, a detailed analysis of the photocurrent measuring analog control loops has been described. First, the most important gain equations were determined and then the current-to-voltage gain A_I, voltage gain A_V, and loop gain G were optimized for the signal frequencies. Both the active and passive components of photodiode current measuring circuits can be determined using the described method. Photodiodes can be selected for shunt resistance and junction capacitance according to the sensitivity and speed requirements of a measurement. The feedback impedances for the selected operational amplifier can be matched to the impedance of the selected photodiode. As a result of component selections and frequency compensations, the signal-to-noise ratios can be optimized for the outputs of the photocurrent meters, and improved loop gains can be achieved for reasonably wide frequency ranges. Because of improved loop gain and bandwidth, the accuracy of the photocurrent-to-voltage conversion is increased for higher signal frequencies. As a result of photodiode circuit optimization, the signal roll-off of large area silicon photodiode light meters can be increased to 80 Hz even at a signal gain of 10^9 V/A.

5. References

[1] G. Eppeldauer, Measurement of very low light intensities by photovoltaic cells, in Eleventh International Symposium on Photon Detectors, Weimar (GDR), 1984, Proc. 182, IMEKO, Budapest (1984).

[2] G. Eppeldauer and A. R. Schaefer, Application of PN and avalanche silicon photodiodes to low-level optical radiation measurements, in Second Workshop on Improvements to Photometry, Gaithersburg, 1987, NASA Conf. Publ. CP-10015, 111–151 (1988).

[3] G. Eppeldauer and J. Hardis, Fourteen-decade photocurrent measurements with large-area silicon photodiodes at room temperature, Appl. Opt. **30** (22), 3091–3099 (1991).

[4] G. Eppeldauer, Temperature monitored/controlled silicon photodiodes for standardization, in Surveillance Technologies, S. Gowrinathan, R. J. Mataloni, and S. J. Schwartz, eds., Proc. Soc. Photo-Opt. Instrum. Eng. **1479**, 71–77 (1991).

[5] Photodiodes, Hamamatsu Cat. No. KPD 0001E05, (Hamamatsu Corporation, Hamamatsu City, Japan, 1996), 8, 16-19.

[6] Y. Tamari, Custom silicon photodiodes offer design flexibility, Laser Focus World **33** (1), 123–126 (1997).

[7] T. R. Gentile and C. L. Cromer, Mode-locked lasers for high-accuracy radiometry, Metrologia **32** (6), 585–587 (1996).

[8] G. Eppeldauer, Some problems of photocurrent measurement of photovoltaic cells, Appl. Opt. **12** (2), 408–409 (1973).

[9] P. Horowitz and W. Hill, The Art of Electronics, Cambridge University Press, Cambridge (1987) pp. 127, 94, 153.

[10] Product Data Book of Burr-Brown, Burr-Brown Corporation, Tucson, AZ (1984) pp. 1–38.

[11] R. L. Boylestad, Introductory Circuit Analysis, 6th Edition, Merrill Publishing Company, Columbus, OH (1990) p. 719.

[12] J. W. Nilsson, Electric Circuits, Third Edition, Addison-Wesley Publishing Company, Reading, MA (1990) pp. 639–648.

[13] Transimpedance Applications, Fall 1994, Burr-Brown Applications Seminar.

[14] G. H. Rieke, Detection of Light: from the Ultraviolet to the Submillimeter, Cambridge University Press, Cambridge, GB (1994) p. 143.

[15] J. G. Graeme, Photodiode Amplifiers, McGraw-Hill, New York, NY (1996) p. 42.

About the author: *George Eppeldauer is a Ph.D. Electronics Engineer in the Optical Technology Division of the NIST Physics Laboratory. The National Institute of Standards and Technology is an agency of the Technology Administration, U.S. Department of Commerce.*

Volume 105, Number 2, March–April 2000
Journal of Research of the National Institute of Standards and Technology

[J. Res. Natl. Inst. Stand. Technol. **105**, 209 (2000)]

Noise-Optimized Silicon Radiometers

Volume 105 Number 2 March–April 2000

George P. Eppeldauer

National Institute of Standards and Technology,
Gaithersburg, MD 20899-8441

george.eppeldauer@nist.gov

This paper describes a new, experimentally verified, noise analysis and the design considerations of the dynamic characteristics of silicon radiometers. Transimpedance gain, loop gain, and voltage gain were optimized versus frequency for photodiode current meters measuring ac and dc optical radiation. Silicon radiometers with improved dynamic characteristics were built and tested. The frequency-dependent photocurrent gains were measured. The noise floor was optimized in an ac measurement mode using photodiodes of different shunt resistance and operational amplifiers with low $1/f$ voltage and current noise. In the dark (without any signal), the noise floor of the optimized silicon radiometers was dominated by the Johnson noise of the source resistance. The Johnson noise was decreased and equalized to the amplified $1/f$ input noise at a 9 Hz chopping frequency and 30 s integration time constant, resulting in an equivalent root-mean-square (rms) photocurrent noise of 8×10^{-17} A. The lowest noise floor of 5×10^{-17} A, equal to a noise equivalent power (NEP) of 1.4×10^{-16} W at the 730 nm peak responsivity, was obtained at a 100 s integration time constant. The radiometers, optimized for ac measurements, were tested in a dc measurement mode as well. Performances in ac and dc measurement modes were compared. In the ac mode, a ten times shorter (40 s) overall measurement time was needed than in the dc mode (400 s) to obtain the same 10^{-16} A noise floor.

Key words: chopped radiation; gain; noise; photocurrent; radiometer; sensitivity; silicon photodiodes.

Accepted: January 13, 2000

Available online: http://www.nist.gov/jres

1. Introduction

Low-noise photocurrent measurements are needed for the detection of weak optical radiation [1]. Silicon photodiodes are well known for their excellent optical and electronic characteristics, and for their high sensitivity and stability [2, 3].

The noise and drift characteristics of silicon photodiode current meters were analyzed earlier at low (dc) frequencies [4]. High shunt resistance silicon photodiodes and operational amplifiers with large feedback resistors were used to achieve high photocurrent sensitivity. Operational amplifiers with very low input-bias current were used to minimize $1/f$ noise from the amplifier. The dominant Johnson noise was equalized to the $1/f$ amplifier noise by decreasing the electrical bandwidth to 1.25 mHz. The drift was also equalized to the noise floor by regulating the temperature of the Si radiometer within $\pm$ 0.02 °C of the operating 25 °C value [5]. The root-mean-square (rms) equivalent photocurrent of the measured noise floor was 10^{-16} A. The time of the measurement was 400 s. When the bandwidth was increased to 300 mHz, the noise increased and ranged between 0.6 fA and 1 fA. The factor of 10 noise increase

was measured for the photodiode with the largest time constant (shunt resistance times junction capacitance). This output noise increase was due to a frequency-dependent noise-boosting effect in the voltage gain of the photocurrent meter.

The dynamic (ac) characteristics of photodiode current meters were analyzed in transimpedance amplifier applications [6,7,8]. The fundamental gain equations were summarized recently [9] to optimize signal (transimpedance) gain, voltage gain, and loop gain versus frequency. The gain equations can be used to optimize both low-frequency (dc) and modulated/chopped (ac) photocurrent meters. The feedback impedances of the selected operational amplifiers were matched to the impedance of the selected silicon photodiode in the analyzed ac photocurrent meters. The signal roll-off point of large-area silicon photodiode current meters could be increased to 80 Hz even at a signal gain of 10^9 V/A. The suggested silicon radiometer converts the optical radiation signal (chopped with 8 Hz) into an ac voltage signal which has negligible amplitude distortion and signal phase shift. The optimization of the frequency-dependent (three) gains was extended to Ge, InGaAs [10], and InSb [11] photodiodes as well.

Optimization of the dynamic (frequency-dependent) characteristics of silicon radiometers will not necessarily optimize the sensitivity of the meters. The fundamental gains and the noise floor have to be optimized together to get the best performance. This paper shows the proper method of analysis for performing this task in the ac measurement mode. The design considerations for both the dynamic characteristics and the noise performances are experimentally verified. Also, the performances of ac and dc silicon radiometers are compared.

2. Gain Equations of Photodiode Current Meters

The equivalent circuit of photocurrent-to-voltage converters is shown in Fig. 1. The photocurrent I_P from photodiode P is converted into a voltage V at the output of the operational amplifier OA. R_S is the shunt resistance and C_J is the junction capacitance of P. R is the feedback resistance and C is the feedback capacitance of the OA. The photocurrent-to-voltage conversion can be described by the transimpedance gain [9]:

$$A_I = \frac{V}{I_P} = R\,\frac{1}{1 + j\omega RC}\,. \tag{1}$$

Equation (1) shows that the dc signal gain (at $\omega = 0$), which is the ratio of the output voltage V to the input photocurrent I_P, is equal to R. The frequency-dependent

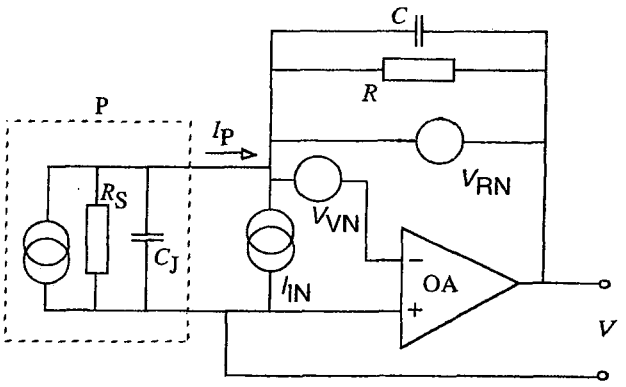

Fig. 1. Equivalent circuit of photodiode radiometers. The dashed line represents photodiode P. R and C are the feedback components of the operational amplifier OA.

signal response is determined by the integrating time constant $\tau_I = RC$ of the feedback impedance. Equation (1) also describes the gain for the input current noise I_{IN} of the circuit. Because Eq. (1) does not show the frequency dependent contribution of OA to the signal response, the equation works only if the roll-off time constant of the OA open-loop gain $\tau_i < \tau_I$. Otherwise, the OA frequency-dependent response gives an unwanted limitation for the signal response.

Similarly to Eq. (1),

$$\frac{V}{I_P} = R\,\frac{1}{1 + G^{-1}}\,, \tag{2}$$

where G is the loop gain. The photocurrent-to-voltage conversion R, which is the signal gain, will be accurate only if $G >> 1$ at the signal frequency. This is a very important design requirement for the analog control loop.

The loop gain, which is the product of the OA open loop gain A and the feedback attenuation β, can be written as

$$G = A_0\beta_0\,\frac{1}{1 + j\omega\,\tau_i}\,\frac{1 + j\omega\,\tau_I}{1 + j\omega\,\tau_2}\,, \tag{3}$$

where A_0 is the dc open loop gain and $\beta_0 = R_S/(R_S + R)$. The quantity $\tau_I = RC$ was the integrating time constant in Eq. (1). Here, in Eq. (3), τ_I is a differentiating time constant. The integrating time constant τ_2 here is the product of the parallel resistances and the parallel capacitances:

$$\tau_2 = \frac{R\,R_S\,C + R\,R_S\,C_J}{R + R_S} = \frac{R\,R_S}{R + R_S}\,(C + C_J). \tag{4}$$

τ_i is always an additional integrating type time constant.

The closed loop voltage gain, which is the reciprocal of β[12], determines the amplification for the input voltage noise V_{VN}:

$$A_V = A_{V_0} \frac{1 + j\omega\tau_2}{1 + j\omega\tau_1} \tag{5}$$

where

$$A_{V_0} = \frac{R_S + R}{R_S} \tag{6}$$

is the dc voltage gain.

In contrast to Eq. (3), τ_1 is an integrating and τ_2 is a differentiating time constant in Eq. (5). V_{RN} is the Johnson (resistor) noise. This "white" noise shows up directly at the OA output (without any amplification). The current noise I_{IN} is caused by the fluctuation of the OA input current. Both I_{IN} and V_{VN} have "white" and $1/f$ noise components superimposed on each other.

The photocurrent I_P produces a shot noise I_{PN} which is not shown in Fig. 1. The current I_{PN} is converted to the OA output similarly to I_P. This current noise component is $(2eI_P\Delta f)^{1/2}$, where e is the elementary electron charge, 1.60×10^{-19} C, I_P is the photocurrent, and Δf is the electrical bandwidth. A 10^{-14}A photocurrent produces an rms current noise of $I_{PN} = 7.1 \times 10^{-18}$ A at $\Delta f = 16$ mHz, which corresponds to an integration time constant of 10 s.

At the OA output, the signal-produced voltage V has to always be much larger than the superimposed total noise voltage originating from the above four noise components.

3. Design of Dynamic Characteristics

A test silicon radiometer was built that satisfies the three gain requirements discussed above with high photocurrent and loop gains and low voltage-gain at the signal frequencies.

According to the suggestion in our previous work [9], the Hamamatsu Model S5226-8BQ[1] 1/3 cm^2 area photodiode was selected and tested with $R_S = 2.2$ GΩ and $C_J = 410$ pF. The large shunt resistance kept A_V low. The small junction capacitance tuned the $f_2 = 1/(2\pi\tau_2)$ roll-up point in the voltage-gain curve to high frequencies, resulting in decreased noise-boosting effect. The Burr-Brown OPA111BM operational amplifier was selected because of its high dc open loop gain ($A_0 = 10^6$) and low $1/f$ noise. The dynamic characteristics below were designed with typical manufacturer's data regarding C_J, A_0, and the 3 dB roll-off frequency of the OA open-loop gain.

The largest feedback resistor used in these tests was $R = 10^{10}$ Ω. In order to obtain a high enough signal roll-off frequency $f_1 = 1/(2\pi\tau_1)$ at this signal gain, a small stray capacitance of $C_s = 1.25$ pF was realized. The overall feedback capacitance was $C = C_s + C_f$, where C_f was the externally connected feedback capacitor. C_f was selected for all gains (except $R = 10^{10}$ Ω) to obtain a signal roll-off frequency of at least 10 times the chopping frequency.

Figure 2 shows C_f, f_1, and f_2 versus R for the test radiometer. The f_1 and f_2 curves were calculated from τ_1 and τ_2 of Sec. 2. As is shown in Eq. (4), f_2 depends on C. A change in C_f will modify the starting value of f_2. C_f was selected for all signal gains to obtain a high enough f_1 for chopping frequencies between 7 Hz and 10 Hz. The frequency f_1 was decreased by increasing C_f in all signal gains (other than the highest) to tune f_1 close to f_2 as much as possible. This requirement is important for minimizing noise voltage amplification and maximizing loop gain for the signal frequencies. At the same time, f_1 had to be high enough to keep the signal bandwidth of the radiometer broad enough for all signal-gain selections. This is an important requirement to avoid distortion of the signal shape and to make the signal-phase-shift negligibly small. At full-frequency compensation, where $\tau_1 = \tau_2$, the differentiating time constant cancels (compensates) the integrating time constant. This way, the loop gain can be increased and the voltage gain can be decreased for the signal (chopping) frequencies. For gain selections of $R << R_S$ the $\tau_1 = \tau_2$ condition requires $C >> C_J$, resulting in large C_f values. The capacitance C_f will not be too large if C_J is small. Full frequency compensation was made at $R = 10^4$ Ω using $C_f = 4.7$ nF. No frequency compensation was made for $R = 10^{10}$ Ω to keep f_1 high. Full compensation for the high signal gains would make the radiometer very slow. Partial compensations satisfied the three gain requirements for all the other signal gains.

Figure 3 shows the frequency-dependent loop-gain characteristics of the above test radiometer. This is a Bode plot [13] where the characteristics can be constructed quickly and fairly accurately by approximating the curves with piecewise linear regions. The value of G at low frequencies is equal to $A_0\beta_0$. The first two roll-offs are at f_2 and f_i; f_1 determines the roll up. This is the frequency where the signal 3 dB roll-off points

[1] Certain commercial equipment, instruments, or materials are identified in this paper to foster understanding. Such identification does not imply recommendation or endorsement by the National Institute of Standards and Technology, nor does it imply that the materials or equipment identified are necessarily the best available for the purpose.

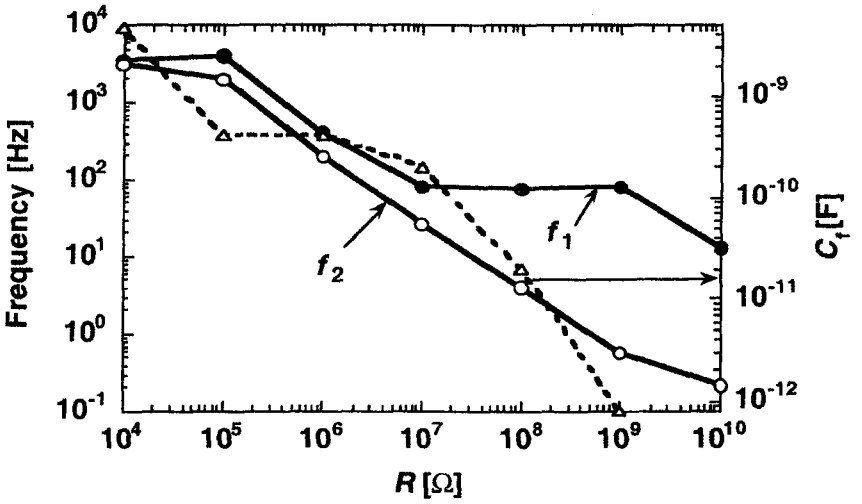

Fig. 2. Time constants-produced frequency roll-off and roll-up points of the test radiometer calculated for the decadic signal gains. The external feedback capacitor versus feedback resistor is shown by the dashed curve. The points are connected to help visual separation of the curves.

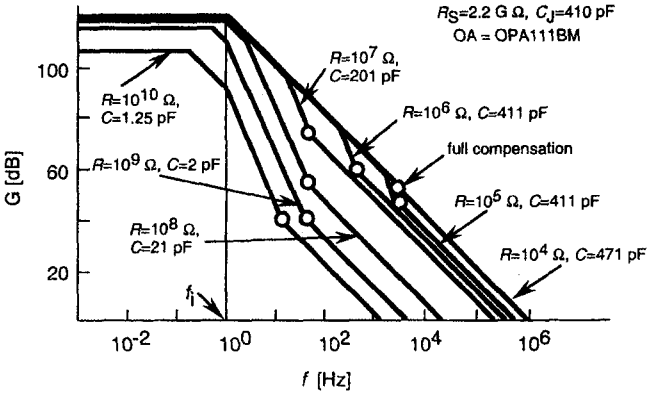

Fig. 3. Loop-gain characteristics of the test silicon (S5226-8BQ) radiometer. The open circles show the signal 3 dB roll-off points as they are matched to the loop-gain characteristics.

(shown with open circles) are attached to the loop-gain curves (solid lines). At $R = 10^{10}$ Ω, the signal 3 dB point is 13 Hz without any frequency compensation ($C_f = 0$). At $R = 10^9$ Ω, $C_f = 0.8$ pF will produce $C = 2$ pF with a roll-off frequency of $f_1 = 78$ Hz. As a result of the high open-loop gain of the OPA111BM operational amplifier, the loop gains at these two highest signal gains are 100 (40 dB). Partial frequency compensations were enough for the other signal gains to obtain high enough loop gains at the signal 3 dB roll-off points. For these cases, $f_1 = 75$ Hz, or higher, was selected. The full frequency compensation at the lowest signal gain was made as a design example.

Figure 4 shows the closed-loop voltage-gain characteristics (solid curves) of the test silicon radiometer. The open-loop gain curve of the OA is shown with thick dashed lines. The roll up here is determined by f_2. The roll-off is produced by f_1. At the highest gain, f_1 is relatively far from f_2, producing a gain increase of about two orders of magnitude. The real shape of this gain change is shown (for $R = 10^{10}$ Ω only) with the thin dashed curve. The noise boosting at a chopping frequency of 9 Hz is still significant.

4. Measurement of Photocurrent Gains

The frequency-dependent signal (transimpedance) gain of the test silicon radiometer was measured for all (except for the 10^4 V/A) signal-gain selections. The stable broad-band radiation of a 100 W tungsten halogen lamp was measured using a chopper. The frequency of

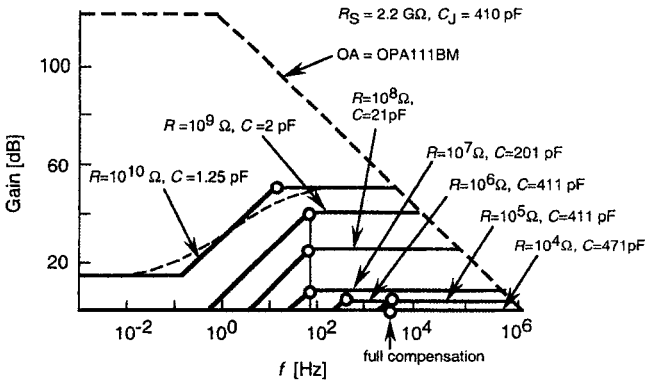

Fig. 4. Closed-loop voltage-gain characteristics (solid lines) of the test silicon (S5226-8BQ) radiometer. The thick dashed lines show the open-loop gain of the OA. The open circles are the signal 3 dB roll-off points as they are matched to the voltage-gain characteristics.

the chopper was tuned from about 10 Hz to 300 Hz by computer control. A chopper-synchronized, sine-wave measuring lock-in amplifier was connected to the output of the radiometer. The measured output voltage V curves are normalized and shown versus chopping frequency f in Fig. 5. At low (dc) frequencies, the output voltage V_0 is not attenuated. The 3 dB line on the graph shows where the signal-gain curves reach the 70.8 % (3 dB attenuation) value of V_0. The signal attenuation, according to Eq. (1), is caused by the $\tau_1 = RC$ time constant, which is different for all signal gain selections. There is no monotonic progression in the measured curves because the 3 dB signal frequencies agree with the design values (f_1) in Sec. 3. The 3 dB frequency for 10^9 V/A gain was larger (about 90 Hz) than the designed 78 Hz because the very small (calculated) external feedback capacitor ($C_f = 0.8$ pF) was not connected. For the most sensitive signal gain the 3 dB point was calculated from a curve fit to the measured data points. The fit is shown with the dashed curve. The fit equation is:

$$V(f) = \frac{V_0}{\sqrt{1 + (f/f_1)^2}}. \tag{7}$$

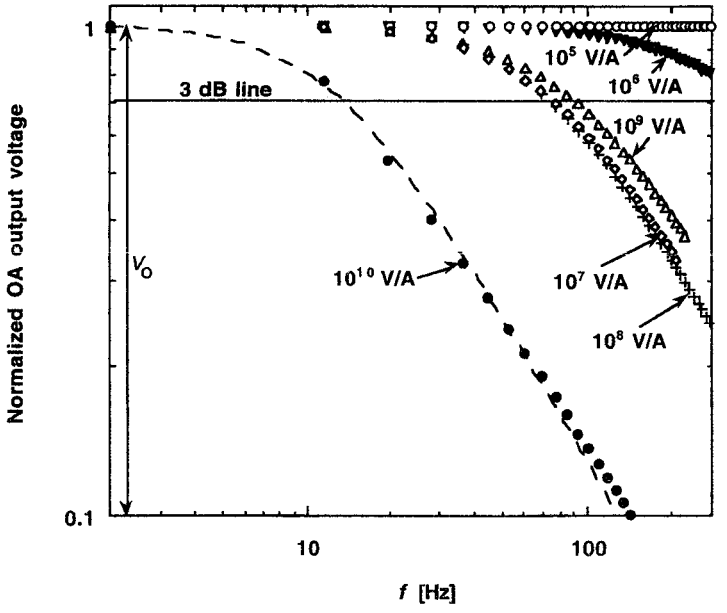

Fig. 5. Measured frequency-dependent signal-gain curves of the test silicon radiometer for different signal-gain settings; V_0 is the dc output voltage of the radiometer.

The 3 dB point from the fit was 12.9 Hz. The response at 2 Hz is a rough extrapolation to V_0 measured with the other signal gain selections. For a chopping frequency of 9 Hz the amplitude attenuation at the 10^{10} V/A signal-gain selection will be about 17 %. Because the operating point is on the slope of the roll-off curve, the chopping frequency should be stabilized for this gain selection. The quantity V_0 should be reported instead of V versus frequency if different chopping frequencies are used. The graph also shows that for the other gain selections the signal responses are flat around the 9 Hz chopping frequency.

5. AC Measurement of Dark Noise

In ac photocurrent measurements, amplifier drifts do not contribute to measurement uncertainties. It is the noise floor that determines the sensitivity limit. The dark noise gives basic information about the noise performance of a radiometer. In order to make high-sensitivity measurements, the dark noise has to be kept as low as possible. In our noise tests the output of the test radiometer was connected to the inputs of chopper-synchronized lock-in amplifiers. The photodiode was covered with a light-tight cap in order to measure the dark noise. The total output noise of the radiometer (dark) was measured at a chopping frequency of 9 Hz with an electrical bandwidth determined by the low-pass filter at the output of the lock-in amplifier. In these ac measurements the signal magnitudes M were calculated from the lock-in X and Y (filtered) output voltages using the mathematical vector sum process ($M = (X^2 + Y^2)^{1/2}$). When measuring noise (or a small signal in the noise), this process rectifies the noise, causing residual output offset. In order to estimate the noise measurement uncertainty caused by this problem, several dark noise tests were repeated and evaluated in a different way, i.e., by calculating the noise fluctuations in both X and Y. The lock-in X and Y output noise voltages and the magnitudes are shown in Table 1 for 30 s and 1 s integration time constants. The X and Y pairs were always simultaneous measurements. The M values, at a given time constant, were measured consecutively to the measurements of X and Y. Each reported noise value was calculated as the standard deviation of at least 20 readings. The measurement results show that the noise of M can be 38 % lower than the noise of X or Y, which are free of the residual output offset. The uncertainty of our noise magnitude measurements is dominated by this 38 % (coverage factor $k = 2$) relative expanded uncertainty.

Table 1. Lock-in X and Y output noise voltages and magnitudes M, for the dark S1226-8BQ photodiode and the OPA128LM operational amplifier at 9 Hz chopping frequency and 10^{10} V/A signal gain

Lock-in time constant (s)	M(μV)	X(μV)	Y(μV)
1	3.2	3.2	3.5
30	0.78	0.93	0.81

5.1 Noise Floor Optimization

The noise floor of the test silicon radiometer was optimized in the ac measurement mode using four photodiodes with different shunt resistances and three operational amplifiers with low $1/f$ voltage and current noise. The feedback capacitors were not changed for the different photodiode-amplifer combinations. Table 2 shows the model numbers and the impedances of the tested photodiodes. All tested photodiodes had an active area of 1/3 cm^2. The models in Table 2 were chosen in order to obtain a wide shunt resistance range for our tests. The range was extended by selecting the photodiodes for high shunt resistance. (The larger the resistivity of the photodiode material, the higher the shunt resistance.) The measured shunt resistances ranged from 0.5 GΩ to 7 GΩ. Only photodiodes with small junction capacitance were selected to obtain small voltage gain (low noise boosting) in ac signal measurements. C_J is proportional to the photodiode area and can be inversely proportional to either the square or the cube root of the width of the depletion layer [14]. The depletion layer

Table 2. The tested silicon photodiodes and the calculated voltage gain parameters

Model	R_S(GΩ)			C_J(nF)		A_{V_0}	f_2(Hz)
	Data Book Min.	Data Book Typical	Measured in the dark	Data Book Typical	Measured in the dark	For $R = 10^{10}$ Ω and measured R_S and C_J	
S1336-8BQ	0.1	0.4	0.5	0.38	0.18	21	1.9
S5226-8BQ	0.1	1	2.2	0.43	0.32	5.6	0.3
S1227-66BQ	0.2	1	5	0.95	0.62	3	0.08
S1226-8BQ	0.2	1	7	0.95	0.56	2.4	0.07

width is proportional to the resistivity of the material. This is why C_J was measured to be lower on the selected high shunt resistance photodiodes. During the capacitance measurements on the photodiodes the dc voltage drop was less than 13 mV and the ac voltage drop was less than 24 mV. The capacitances were measured in the dark and the diodes were reverse biased. The measured capacitances ranged from 0.18 nF to 0.62 nF. Table 2 also shows the dc voltage gain and f_2 for the 10^{10} V/A signal-gain. They were calculated from the measured R_S and C_J values.

The $1/f$ voltage and current noise of the three different types of operational amplifiers are shown in Table 3 for the frequency range between 0.1 Hz and 10 Hz. The manufacturer's data were helpful only to select candidate operational amplifiers. As noise figures for the small frequency interval (electrical bandwidth) at 9 Hz were not available, it was necessary to test the noise floor experimentally. Both the OPA128LM and the OPA627BM operational amplifiers were tested with all four photodiodes. The OPA111BM was tested only with two different shunt resistances using the S5226-8BQ and the S1227-66BQ photodiodes.

Figure 6 shows the measured noise floors of the different photodiode-operational amplifier combinations. These noise floor measurements were made at a current-to-voltage gain of 10^{10} V/A and 9 Hz. The time constant selected on the lock-in amplifier was 3.33 s. The low-pass filters of the lock-in amplifier had a roll-off slope of 20 dB per decade.

For the OPA128LM operational amplifier the output noise decreased to an equivalent rms photocurrent of 0.28 fA for photodiode shunt resistances of 5 GΩ and 7 GΩ. At these high shunt resistances the voltage gain was small enough to make the amplified OA input noise negligible relative to the dominant Johnson noise. The 0.5 GΩ shunt resistance increased the voltage gain by a factor of seven, resulting in a dominating output noise from the input voltage noise. Similar results were obtained with the OPA111BM operational amplifier.

With the OPA627BM operational amplifier a 0.36 fA noise floor was measured for shunt resistances of 2.2 GΩ or larger. This noise floor was 0.08 fA higher than the noise floor with the other two operational amplifiers. As compared to the others, this amplifier had a much larger $1/f$ input current noise and it dominated the OA input noise. With increasing shunt resistance the input voltage noise drop (caused by the input-current noise) increased and the voltage gain for it decreased. The result was a constant $1/f$ noise contribution to the dominating Johnson noise.

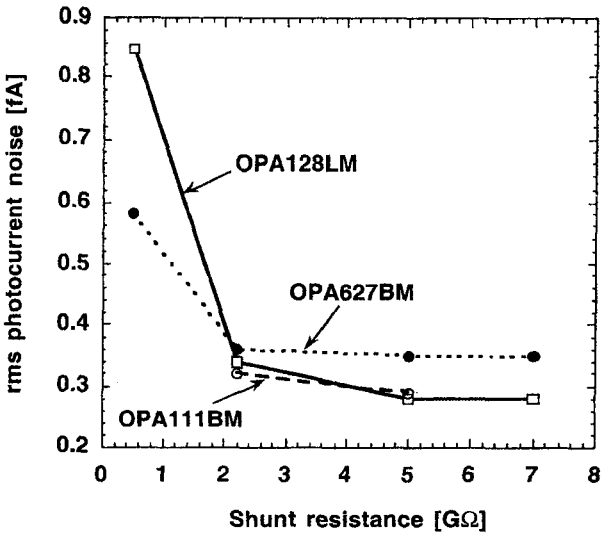

Fig. 6. Noise-equivalent photocurrent of photodiode-operational amplifier combinations at a signal-gain of 10^{10} V/A and a chopping frequency of 9 Hz.

The output (total) noise spectrum of the radiometer was measured at different chopping frequencies between 8 Hz and about 200 Hz. The signal gain of the radiometer was lowered to 10^9 V/A to increase the signal upper roll-off point from 13 Hz to 80 Hz. The time constant of the lock-in amplifier remained 3.33 s. The 2.2 GΩ shunt resistance of the S5226-8BQ photodiode was used in this test. The voltage gain, according to Fig. 4, increases almost two decades from 0.8 Hz to 80 Hz. The upper half of this frequency interval could be tested. As is shown in Fig. 7, the dominating noise (at the radiometer output) is the white Johnson noise, which makes the noise spectrum flat. The measured noise spectrum with the OPA128LM was smoother than with the OPA627BM because of the smaller OA input noise. The input noise of the OPA627BM was dominated by the above-discussed $1/f$ input current noise. In spite of

Table 3. Catalog data of OA $1/f$ noises from 0.1 Hz to 10 Hz (all voltages and currents are peak-to-peak)

OPA128LM		OPA627BM		OPA111BM	
Voltage	Current	Voltage	Current	Voltage	Current
4 μV	2.3 fA	1.6 μV (0.6 typical)	60 fA (30 typical)	2.5 μV	12 fA (7.5 typical)

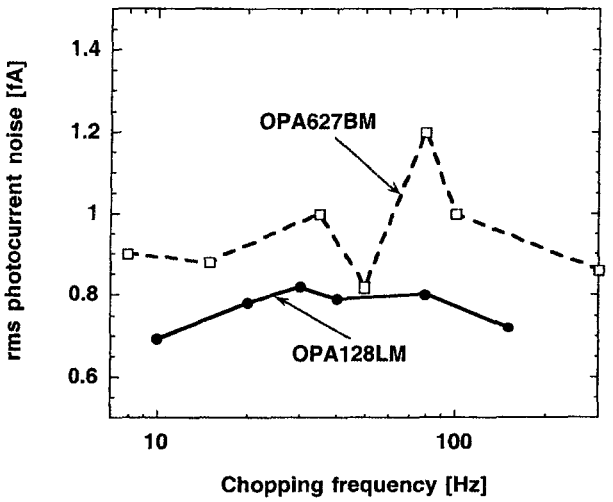

Fig. 7. Noise-equivalent photocurrent versus frequency of the silicon radiometer at a signal gain of 10^9 V/A and a time constant of 3.33 s. The detector was a S5226-8BQ photodiode ($R_S = 2.2$ GΩ; $C_J = 410$ pF).

this 1/*f* noise contribution, the noise spectrum remained flat. The smaller voltage gain compensated for the higher 1/*f* noise at the lower frequencies. Because of the flat noise floor at this signal gain, any signal (chopping) frequency can be selected within the tested frequency interval. However, the 3 dB point at 80 Hz will restrict the upper signal frequency limit. If the external feedback capacitor is not connected, this limit can be extended to about 130 Hz. In this case the loop gain at this signal frequency can be too low, resulting in poor current-to-voltage conversion accuracy. To avoid this problem, either a high open-loop gain operational amplifier (e.g., OPA111BM) has to be selected or the partial frequency compensation (e.g., for 80 Hz) has to be applied.

5.2 Dark Total Noise Versus Signal Gain

The optimized radiometer, with the S1227-66BQ ($R_S = 5$ GΩ) photodiode and the OPA111BM operational amplifier, was tested for output total noise versus signal-gain performance. Again, the signal (chopping) measurement frequency was 9 Hz and the time constant of the lock-in amplifier was 3.33 s (0.05 Hz bandwidth). The measurement results are shown in Fig. 8. The output total noise is shown by the dashed curve and the noise-equivalent photocurrent is represented by the solid curve. The shape of the total noise curve shows that with high feedback resistances the Johnson noise dominates the output noise. With small feedback resistances, where the Johnson noise is low, the input voltage noise of the amplifier (amplified by the unity voltage gain here) dominates the output noise of the radiometer. The

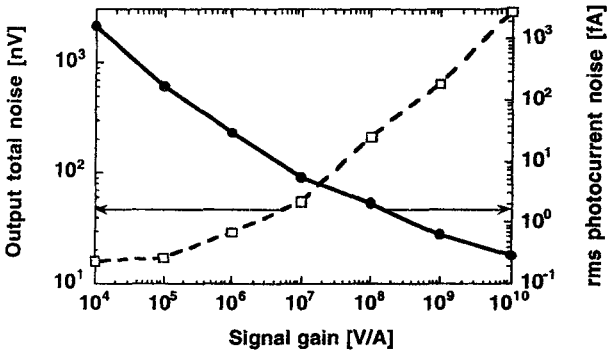

Fig. 8. Measured dark noise versus signal gain at 9 Hz and 3.3 s integration time constant. The S1227-66BQ photodiode and the OPA111BM operational amplifier were used in the noise-optimized radiometer.

measured 16 nV input voltage noise is a 1/*f* noise which cannot be reduced much by longer integration.

5.3 Dark Total Noise Versus Electrical Bandwidth

The Johnson noise in Fig. 8 can be further reduced by longer integration. The noise-optimized radiometer with the S1226-8BQ ($R_S = 7$ GΩ) photodiode and the OPA128LM operational amplifier was tested at a signal gain of 10^{10} V/A and a measurement frequency of 9 Hz. A digital lock-in amplifier (Stanford SR830) was used in this test. The time constant of the lock-in amplifier was changed between 100 s and 0.1 s. The waiting time was three times the time constant before each dark noise measurement. The measurement results are shown in Fig. 9.

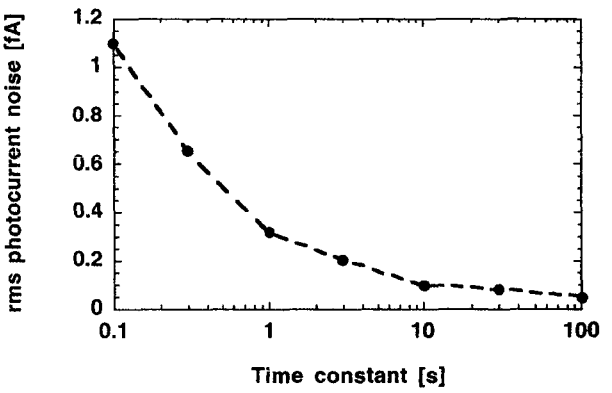

Fig. 9. Noise-equivalent photocurrent versus time constant of the digital lock-in amplifier for the S1226-8BQ photodiode and the OPA128LM operational amplifier at 9 Hz chopping frequency and 10^{10} V/A signal gain.

The dark noise floor was 0.1 fA with the 10 s time constant. This noise is equal to the earlier reported dc dark noise obtained with a measurement time of 400 s [4]. The present 9 Hz (ac) noise test needed a 40 s total measurement time to obtain the same noise-equivalent photocurrent. At the 100 s time constant the noise equivalent photocurrent decreased to 0.05 fA. The noise equivalent power (NEP), which is the ratio of the 0.05 fA to the 0.36 A/W peak responsivity of the diode, is equal to 0.14 fW. This test required a total measurement time of 400 s. The roll-off slopes of the low-pass filters, within the digital lock-in amplifier, were always selected to 80 dB per decade (24 dB per octave). This very steep roll-off slope produced a well-defined electrical bandwidth.

The Johnson noise could be calculated from $R_S = 7$ GΩ and $R = 10$ GΩ. The parallel connection of R and R_S gave a source resistance of $R_{SO} = 4.1 \times 10^9$ Ω. The rms noise voltage of the source resistance, at the output of the radiometer, was

$$V_N = (4kTR_{SO}\Delta f)^{1/2} = 1.81\ \mu V, \qquad (8)$$

where $k = 1.38 \times 10^{-23}$ J/K is the Boltzmann constant, $T = 300$ K was the temperature of the radiometer during the test, and $\Delta f = 0.048$ Hz was the measurement bandwidth as calculated from the 3.33 s time constant of the lock-in amplifier used in the noise measurements of Fig. 6.

The 0.28 fA noise-equivalent photocurrent in Fig. 6 was calculated from the measured 2.8 μV radiometer output noise voltage and the 10^{10} V/A photocurrent-to-voltage gain. Δf in that measurement was larger than in Eq. (8) because of the shallow (20 dB per decade) slope of the low-pass filter. That measurement was repeated with the digital lock-in amplifier, using a 3 s time constant with a roll-off slope of 80 dB per decade. With this time constant, the $\Delta f = 0.053$ Hz bandwidth resulted in a calculated Johnson noise voltage of 1.9 μV. In accordance with Fig. 9, the measured value was 2 μV. This noise voltage corresponds to a 0.2 fA photocurrent noise at a signal gain of 10^{10} V/A. The 80 dB per decade roll-off still does not give a perfect square shape for the measurement bandwidth. The 10 % (coverage factor $k = 2$) uncertainty of these Johnson noise determinations is well within the 38 % relative expanded uncertainty ($k = 2$) of the ac noise measurements.

6. DC Dark Noise Measurements

The silicon radiometer, noise-optimized with the S1226-8BQ photodiode ($R_S = 7$ GΩ) and the OPA128LM operational amplifier in the ac mode, was tested in the dc measurement mode as well. As in our earlier reported dc measurements [4], the bandwidth was again 0.3 Hz determined by the 100 power-line cycle integration time (1.7 s) of the dc digital voltmeter connected to the output of the radiometer. The temperature of the radiometer during the dc test was controlled to 25 °C ± 0.02 °C. The increase in the standard deviation of the measured noise data points due to drift was negligible. The dc dark noise measurement results are shown in Fig. 10.

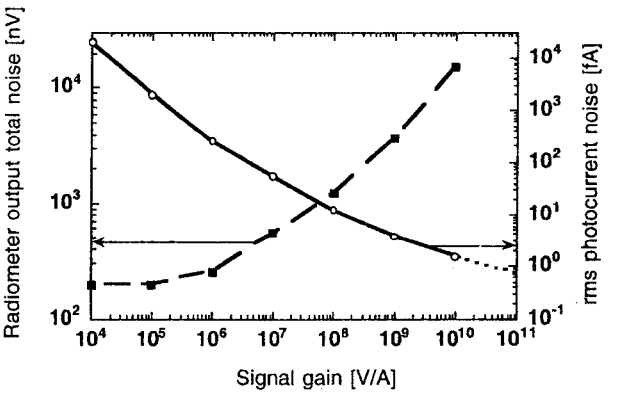

Fig. 10. The dc dark noise of the radiometer noise-optimized in the ac mode (with S1226-8BQ photodiode and OPA128LM operational amplifier) versus signal gain. The integration time is 1.7 s.

At the two lowest signal gains (10^4 V/A and 10^5 V/A) the output total noise of the radiometer was dominated by the 0.2 μV input voltage noise of the OA. This $1/f$ noise fits to the earlier reported 0.2 μV to 1 μV noise interval [4] measured on several OPA128LM operational amplifiers. It should be noted that the ac and the dc noise versus signal-gain tests were made with different photodiode-amplifier pairs. However, before the tests (both ac and dc), the two radiometer combinations were optimized to the same noise floor (0.28 fA) at 9 Hz, as discussed in Sec. 5.1.

At the highest (10^{10} V/A) signal gain of the radiometer, the noise-equivalent photocurrent was 1.5 fA. The noise-equivalent photocurrent increased to about 20 pA at the lowest (10^4 V/A) signal gain. When the equivalent photocurrent noise curve was extrapolated to the 10^{11} V/A gain, a noise floor of about 0.7 fA was obtained, equal to the noise floor of our previous dc measurements (using the same signal gain and the same 0.3 Hz bandwidth) [4]. The lower noise floor at 10^{11} V/A can be utilized only at very slow measurements because the settling time constant at this gain is 16.2 s [9]. At 10^{10} V/A signal gain the settling time constant is shorter than one power line cycle (16.7 ms). This three orders of magnitude settling-time difference rejects the application of the 10^{11} V/A signal gain from fast measurements.

The expanded relative uncertainty (coverage factor $k = 2$) of our dc noise measurements was 25 %.

7. AC and DC Dark Noise Comparison

In dc measurements, the noise-boosting effect (shown in Fig. 4) can be avoided if we restrict the measurement frequency and bandwidth to a limit which is lower than the frequency where the voltage-gain increase begins. We used this method in our previous work [4] where a 400 s measurement time (1.25 mHz bandwidth) eliminated the noise-boosting effect at the 10^{11} V/A signal gain and equalized the resistor noise to the $1/f$ noise.

Another method to eliminate (or decrease) noise boosting is to apply frequency compensation for the different signal gains of the radiometer. In a typical example, where the shunt resistance is 6.5 GΩ and the junction capacitance is 1.3 nF, full-frequency compensation will decrease the signal 3 dB roll-off points to 19 mHz at the two highest signal gains. (This requires a 85 pF capacitor parallel to $R = 10^{11}$ Ω and 850 pF parallel to $R = 10^{10}$ Ω.) Again, the result would be very slow signal measurements at high signal gains. However, full-frequency compensation is not needed at high signal gains because the large feedback resistance and shunt resistance make the Johnson noise dominate (as discussed in Sec. 5.1) relative to the amplified (boosted) input noise.

In both dc and ac measurements, partial frequency compensation give the best results. The voltage gains are decreased (with the partial compensation) by lowering f_1 (closer to f_2) until the signal response is not too low for the signal frequency. This was the design consideration for our test radiometer (as described in Sec. 3) where the signal roll-off frequency was at least 10 times the chopping frequency. As is shown in Figs. 3 and 4, the value of the compensating C_f capacitor depends on the chosen signal gain (R).

The input voltage noise at 9 Hz was 16 nV with the OPA111BM (as shown in Fig. 8) and 23 nV with the OPA128LM. The $1/f$ noise of each amplifier at this measurement frequency is much smaller than at very low (dc) frequencies. Earlier [4], a 50 nV to 200 nV $1/f$ input noise interval was reported on several OPA111BM operational amplifiers at very low frequencies. The $1/f$ noise interval was higher (about 0.3 μV to 1 μV) for the OPA128LM.

The decrease of the $1/f$ noise at higher frequencies made it possible to increase the signal measurement frequency from dc to 9 Hz. At 9 Hz the noise-boosting effect was still significant. However, the feedback resistor (R) could be lowered by a factor of 10, relative to the previously reported $R = 100$ GΩ in the most sensitive dc measurements [4]. The result of the smaller R was decreased voltage gain (A_V) and resistor noise.

Figure 8 shows that the dark noise floor measured at 9 Hz is about a decade lower than the dc dark noise floor shown in Fig. 10. The silicon radiometers in the ac and dc noise floor measurements were noise optimized (in ac mode) to the same 0.28 fA rms current level (as described in Sec. 5.1). The measurement times are reasonably short (a few seconds) in both cases. At 9 Hz, the integration time to obtain the same 10^{-16} A noise floor (as in the previous dc measurements) became shorter because of the lower resistor noise. Using the radiometer with the OPA128LM operational amplifier and a 30 s integration time constant (as shown in Fig. 9), an output rms $1/f$ noise of $(0.93^2 - 0.6^2)^{1/2}$ μV = 0.71 μV could be calculated. The 0.6 μV was the calculated rms Johnson noise and the 0.93 μV was the total rms output noise measured by the lock-in X channel (as shown in Table 1). The X-channel noise was used because it was free of the residual output offset in M. The calculated voltage gain (at 9 Hz) was 710 nV / 23 nV = 31. The relative uncertainty (coverage factor $k = 2$) of this voltage gain determination was 66 %. In this ac measurement, the Johnson noise was roughly equalized to the amplified $1/f$ noise. The noise equivalent photocurrent (from the lock-in magnitude M) was 8×10^{-17} A. According to Fig. 9, further increase of the lock-in integration time constant will not yield a significant decrease in the output total noise of the radiometer. The lowest noise-equivalent photocurrent of 5×10^{-17} A was measured with an integration time constant of 100 s. The total duration of this ac measurement was 400 s.

8. Conclusion

An experimentally verified noise analysis for silicon photodiode current meters of improved dynamic characteristics has been described. Transimpedance gain, loop gain, and voltage gain were optimized versus frequency using partial frequency compensation for the different signal gains. The effect of the Johnson noise, the OA input voltage noise, and the current noise of both the OA input current and the photocurrent were discussed. The transimpedance (current-to-voltage) gains of the test radiometer were measured versus frequency. The noise floor was optimized at a signal chopping frequency of 9 Hz by testing the combinations of four photodiodes of different shunt impedance and three selected operational amplifiers. The dominating Johnson noise at the tested 10^{10} V/A signal gain was further decreased by increasing the integration time constant of the ac signal measurements. At an integration time constant of 30 s (after 90 s wait), the Johnson noise was equalized to the ampli-

fied $1/f$ noise of the operational amplifier, resulting in an rms noise equivalent photocurrent of 0.08 fA. This photocurrent noise corresponds to an NEP of 2.2 fW at the 0.36 A/W peak responsivity of the photodiode. Earlier [4], a 400 s measurement (averaging) time was needed in the dc measurement mode to obtain an rms noise floor of 0.1 fA.

The silicon radiometer optimized in the ac measurement mode was tested in the dc measurement mode as well. The dc tests verified that a radiometer optimized for ac measurements may also have an optimum performance in the dc mode. Integrating-type digital voltmeters measured the radiometer output voltages for the duration of 100 power line cycles (1.7 s) to avoid long measurement (averaging) times. Also, the signal gain of the radiometer was maximized to 10^{10} V/A to avoid long settling times. The dc test resulted in a practical rms photocurrent sensitivity limit of 1.5 fA. In contrast, the practical sensitivity limit in the ac measurement mode (with a 10 s integration time constant) was 0.1 fA. The conclusion from comparing the ac and the dc photocurrent measurement modes is that well-designed ac radiometers can measure weaker optical signals with shorter measurement times.

The described frequency- and noise-optimized silicon photodiode current meters can be used as building blocks of high-sensitivity radiometers, photometers, pyrometers, and colorimeters. These radiometers have a signal (radiant power or photocurrent) dynamic range of greater than 14 decades. The discussed ac (including dc) noise-optimization method can be extended for ultraviolet and near-infrared photodiode current meters as well.

9. References

[1] G. Eppeldauer, Measurement of very low light intensities by photovoltaic cells, 11th Int. Symp. on Photon Detectors, Weimar (GDR), Proc. 182, IMEKO, Budapest (1984).

[2] G. Eppeldauer and A. R. Schaefer, Application of PN and avalanche silicon photodiodes to low-level optical radiation measurements, in Second Workshop on Improvements to Photometery, Gaithersburg, 1987, NASA Conf. Publ. CP-10015 (1988) pp. 111–151.

[3] R. Friedrich, J. Fischer, and M. Stock, Accurate calibration of filter radiometers against a cryogenic radiometer using a trap detector, Metrologia **32**, 509–13 (1995/96).

[4] G. Eppeldauer and J. Hardis, Fourteen-decade photocurrent measurements with large-area silicon photodiodes at room temperature, Appl. Opt. **30** (22), 3091–3099 (1991).

[5] G. Eppeldauer, Temperature monitored/controlled silicon photodiodes for standardization, SPIE, Proceedings, Vol. 1479 (1991) p. 71–77.

[6] G. H. Rieke, Detection of Light: from the Ultraviolet to the Submillimeter, Cambridge University Press, GB (1994) p. 142.

[7] Product Data Book of Burr-Brown, Burr-Brown Corporation, Tucson, AZ (1984) pp. 1–38.

[8] J. Graeme, Photodiode Amplifiers Op Amp solutions, McGraw-Hill, New York, NY (1996).

[9] G. Eppeldauer, Chopped Radiation Measurements With Large Area Si Photodiodes, J. Res. Natl. Inst. Stand. Technol. **103** (2), 153–162 (1998).

[10] G. Eppeldauer, Electronic characteristics of Ge and InGaAs radiometers, SPIE, Proceedings, Vol. 3061-97 (1997) pp. 833–838.

[11] G. P. Eppeldauer, A. L. Migdall, and L. M. Hanssen, InSb Working Standard Radiometers, NEWRAD'97, Tucson, AZ, October 27–29, 1997, Metrologia **35**, 485–90 (1998).

[12] P. Horowitz, W. Hill, The Art of Electronics, Cambridge University Press, Cambridge (1987) pp. 127.

[13] J. W. Nilsson, Electric Circuits, Third Edition, Addison-Wesley Publishing Company, Reading, MA (1990) pp. 639–648.

[14] Photodiodes, Hamamatsu Cat. No. KPD 0001E05, Hamamatsu Corporation, Hamamatsu City, Japan (1996) p. 8.

About the author: *George P. Eppeldauer is a Ph.D. Electronics Engineer in the Optical Technology Division of the NIST Physics Laboratory. The National Institute of Standards and Technology is an agency of the Technology Administration, U.S. Department of Commerce.*

Opto-mechanical and electronic design of a Tunnel-Trap Si-Radiometer

George P. Eppeldauer
Optical Technology Division
National Institute of Standards and Technology
Gaithersburg, MD 20899 USA

and

Donald C. Lynch
Reyer Corporation
New Market, MD 21774

Abstract

A transmission-type light-trap silicon radiometer has been developed to hold the NIST spectral power and irradiance responsivity scales between 406 nm and 920 nm. The device was built from different-area replaceable input apertures and tightly packed different-size silicon photodiodes. The photodiodes were positioned in a triangular shape tunnel such that beam clipping was entirely eliminated within an 8° field-of-view (FOV). A light trap was attached to the output of the radiometer to collect the transmitted radiation and to minimize the effect of ambient light. The photodiodes, selected for equal shunt resistance, were connected in parallel. The capacitance and the resultant shunt resistance of the device were measured and frequency compensations were applied in the feedback network of the photocurrent-to-voltage converter to optimize signal-, voltage-, and loop-gain characteristics. The trap-radiometer can measure either dc or ac optical radiation with high sensitivity. The noise-equivalent power of the optimized device was 47 fW in dc mode and 5.2 fW at 10 Hz chopping. The deviation from the cosine responsivity in irradiance mode was measured to be equal to or less than 0.02 % within 5° FOV and 0.05 % at 8° FOV. The trap-radiometer can transfer irradiance responsivities with uncertainties similar to those of primary standard radiometers. Illuminance and irradiance meters, holding the SI units (candela, color- and radiance-temperature), will be calibrated directly against the transfer standard trap-radiometer to obtain improved accuracy in the base-units.

Keywords: detector, irradiance, photo-current, photodiode, radiant power, reference detector, responsivity, spectral response, transfer standard.

1. Introduction

Light-trap detectors have been used as radiometric standards since 1983 [1]. At that time UDT UV100[1] n-on-p inversion layer silicon photodiodes were used in either four element (Model QED-100) or three element (Model QED-200) reflectance-type light-trap configurations [2, 3]. These primary standard devices measured the total power of the

[1] Identification of commercial equipment to specify adequately an experimental problem does not imply recommendation or endorsement by the National Institute of Standards and Technology nor does it imply that the equipment identified is necessarily the best available for the purpose.

incident, well collimated, radiation. Their power response uncertainty was 0.03 % (coverage factor k=1) between 440 nm and 460 nm where bias voltage was not applied to the photodiodes [4]. These non-linear devices had a limited dynamic range of operation [5].

Later, Hamamatsu S-1337 p-on-n silicon photodiodes were used in the Model QED-150 trap-detectors in an arrangement similar to the QED-200. These detectors were called "quantum-flat" because they have external quantum efficiencies (EQE) that are constant to within 0.1 % from 550 nm to 860 nm. The spectral responsivity of quantum detectors is proportional to their EQE and wavelength. The proportionality factor is e/hc, where e is the elementary electron charge, h is Planck's constant, and c is the velocity of light. Using the silicon photodiode self-calibration technique [6] for a single element S-1337 photodiode, the quantum flatness of these trap-detectors could be extended to 400 nm [7]. The S1337 trap-detectors with the constant relative spectral responsivity were calibrated against either a QED-200 between 440 nm and 460 nm or an electrical substitution cryogenic radiometer. The responsivity of S1337 trap-detectors could be extrapolated from the 440 nm to 460 nm range to longer wavelengths with very little loss of accuracy because the shape of the internal quantum efficiency (IQE) does not depend on typical diode-to-diode variations in the doping profile. IQE is the ratio of the number of collected electrons to the number of photons absorbed by the detector after the front surface reflection loss. EQE=(1-ρ)*IQE where ρ is the reflectance. Since the spectral shape of the IQE of S1337 type photodiodes can be modeled with very small uncertainty [8, 9], the spectral responsivity of S1337 reflectance-type trap-detectors could be interpolated between 406 nm and 920 nm with an uncertainty of 0.03 % (coverage factor k=1) if two or more absolute tie points were measured.

The reflectance-type (three-element) trap detectors have polarization dependent response variations of about 1 part in 10^4 [10]. The reflectance loss of the S-1337 reflectance-type trap detectors increases from 0.21 % at 920 nm to 1 % at 406 nm [9]. We measured the responsivity ratios of a QED-150 to a S1337 reflectance-trap versus wavelength. The ratio changed from 1.0005 at 920 nm to 1.0085 at 406 nm, indicating that the reflectances in the blue for the same S1337 photodiode model can be different by several tenths of a percent. The reflectance depends on the oxide thickness of the selected S1337 photodiode. A spatial response non-uniformity of 0.03 % was measured on the same S1337 reflectance-trap where the photodiodes were individually aligned to optimize the device FOV [11]. Later, 0.2 % spatial response non-uniformities were measured on three different QED-150 devices using the same characterization facility [12]. The measured active areas of the QED-150 trap detectors were neither symmetrical nor similar. The higher response non-uniformities and the different shapes of the measured areas indicated that either the FOV was smaller and non-symmetrical or the reproducibility of the photodiode device to device positioning was poor.

Typically, trap detectors have a small FOV. On a QED-150 we measured a 4° FOV when it was equipped with a 3.5 mm diameter aperture. The response deviation from the cosine function was 0.2 % in this angular range. The alignment of reflectance-type trap detectors can be difficult when measuring non-parallel beams. The beam convergence-angle should be always less than the FOV of the trap-detector to avoid beam clipping on the photodiodes. It is easy to obtain a false maximum in the output signal owing to reflections from shiny surfaces other than the active areas of the photodiodes.

At present, trap detectors are not commercially available. Also, the characteristics described above of reflectance-type trap detectors show that they should be significantly improved to transfer the 0.01% to 0.03 % uncertainties of primary standard radiometers with a minimum loss of accuracy. Our measurement-transfer policy is to shorten the scale derivation chain by making direct responsivity calibrations against transfer standard radiometers that have uncertainties similar to those of the primary standards.

Tunnel-trap detectors were reported several years ago that were constructed using four [13] and six photodiodes [14]. They were free of back reflectance, therefore separately calibrated filters or other optical components could be attached to their inputs without introducing additional uncertainties. The six-element version had a polarization independent responsivity [10, 13], lower reflectance loss, and improved spatial response uniformity. Because of these advantages, the six-element transmission-type trap-radiometer is the best choice to transfer responsivity with the lowest possible uncertainty. In order to make the transfer for an extended wavelength range, we wanted to utilize the physical model for IQE of S1337 photodiodes. In addition to traditional radiant power mode measurements, irradiance mode measurements are needed within a larger FOV for an extended range of applications. The sensitivity had to be increased because the collected flux in irradiance measurements is much smaller than in power mode where the total power in the beam is measured. The responsivity uncertainty in irradiance mode also had to be similar to the uncertainties of the primary standards.

We measured the angular response of the transmission-type trap-detector we developed earlier where six equal size photodiodes were used and the aperture diameter was 3.5 mm. In this experimental device, the positioning of the photodiodes was not designed and implemented carefully enough. The angular response of this device (#01 trap) will be shown below. The FOV was about 4° and the deviation from the cosine function was about 0.1 % in this angular range. The asymmetry was caused by beam clipping on the sixth photodiode.

The design goal for the new tunnel-trap radiometer was to achieve a deviation of less than 0.02 % from the cosine function in an angular range of 5° minimum. A signal dynamic range of eleven decades is needed to perform irradiance measurements over seven decades with a signal to noise ratio of 10^4. In order to achieve this requirement, a noise equivalent photocurrent of 0.1 pA had to be achieved.

A high accuracy current meter is necessary to measure the photocurrent. The lowest uncertainty of commercially available current meters is 0.03 %. The lowest signal level this uncertainty can be achieved is 0.1 μA. Higher sensitivity current preamplifiers have temperature coefficients of 0.022 %/°C at a gain selection of 10^9 V/A. These meters require ambient temperature control to within 0.5 °C to perform current-to-voltage conversion close to the 0.01 % uncertainty of trap-radiometer based measurement transfer. Also, these preamplifiers require source resistance (photodiode shunt resistance) greater than the used feedback resistance to achieve the specified current-to-voltage conversion accuracy. For instance, with a sensitivity selection of 1 nA/V a source resistance of larger than 1 GΩ is

needed. A 3.37 % conversion error was obtained at this preamplifier gain selection when the photocurrent of our 31 MΩ shunt resistance trap-detector was measured.

A procedure had to be introduced to select and group different size Hamamatsu S1337 photodiodes according to shunt resistance and junction capacitance. The photocurrent meter for a photodiode group had to be optimized to achieve an adequate noise floor and a 0.01 % uncertainty in the current-to-voltage conversion. Discussed in section 2 of this paper is a careful optical-mechanical design that made it possible to fabricate devices of equal performance. Section 3 describes a careful electronic design and circuit implementation that was necessary to achieve the electronic characteristics described above.

2. Opto-mechanical design

Medium and large size silicon photodiodes, equivalent to the S1337 model, were selected to utilize the physical model for spectral responsivity extrapolation and interpolation. Also, by choosing different size photodiodes, the aperture area and the FOV could be maximized.

Different arrangements of six photodiodes were investigated to determine the most suitable geometry for construction in terms of ease of fabrication, accuracy of mounting surfaces, and optimization of the aperture size and FOV. The FOV is dependent on two parameters: the total path length from the aperture to the last detector and the size of the aperture placed in front of the first detector. To obtain a large FOV, the total path length must be kept as short as possible.

The analysis began with the polarization-independent arrangement shown in Fig. 1, where six detectors are arranged such that the input and output beams are collinear [13]. The lower left portion of the figure depicts a parallel cylindrical beam being reflected from the six detector surfaces. As can be seen from the upper portion of the figure, the input and output beams have the same orientation. The total path length is at a minimum when the detectors begin to touch each other. In the early stages of the development, it became apparent that using detectors of two different sizes could shorten the path length. Smaller detectors can be used in the first two positions because a diverging beam (focused onto the aperture) covers only small portions of these two detector surfaces.

The arrangement shown in Fig. 1 was rejected for two reasons. First, it is difficult to produce a holder accurately for the detectors. Second, the first and sixth detectors mechanically interfere with each other when using the two different size detectors, unless the path length is increased which would reduce the FOV.

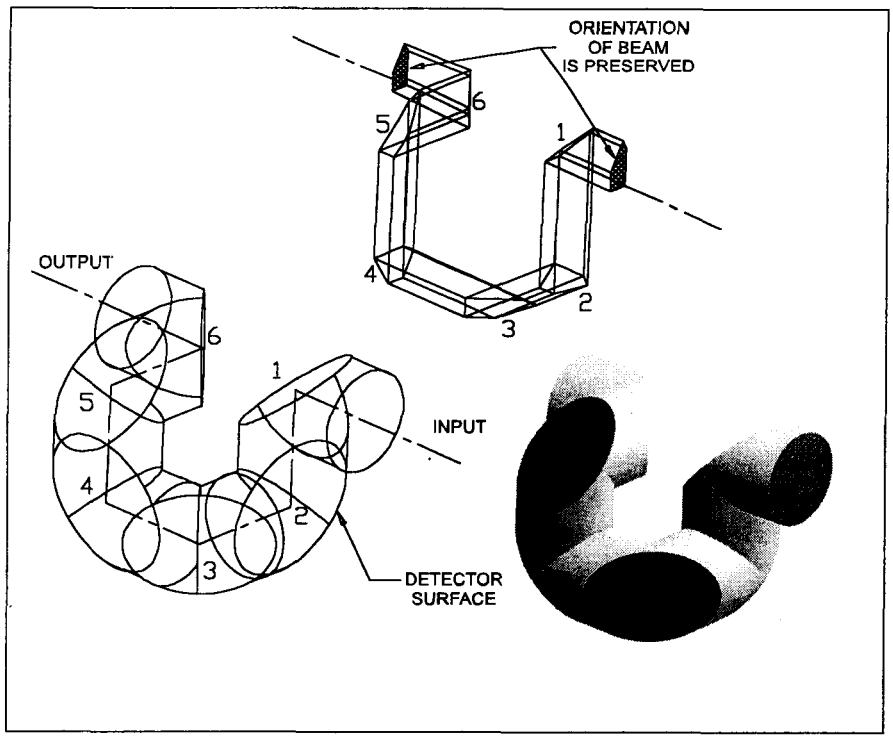

Fig. 1. Generic transmission-trap detector arrangement. The input and output beams are collinear.

Many detector arrangements can be produced by starting with the generic arrangement shown in Fig. 1 and simply rotating one, two or three adjacent detectors at a time about a portion of the optical axis that lies between two adjacent detectors. Of all the detector arrangements that were produced by rotating various groups of detectors, only two arrangements preserved the input and output beam orientation, the arrangement in Fig. 1 and that shown in Fig. 2. The arrangement in Fig. 2 was derived from that shown in Fig. 1 by rotating detectors numbered four through six about the axis between the third and fourth detector centers by 180 degrees. Here, for simplicity, all six detectors were of the same size.

As can be seen from the figure, the central view has a triangular-like shape, where views 1 through 3 show that each side of the triangle contain two detector surfaces. Each pair of detectors form the side of an equilateral triangle and two pairs form planes with a dihedral angle of 60 degrees. This tunnel-trap arrangement, which will be called the triangular tunnel-trap, was selected because it allowed a simple method of construction and minimized the total path length.

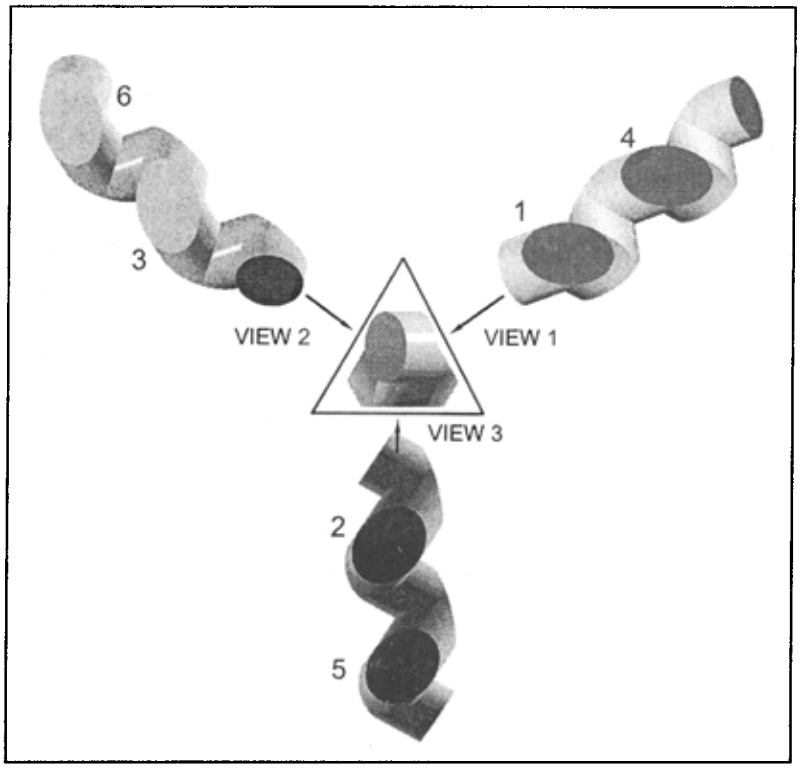

Fig. 2. The triangular tunnel-trap detector where the last three detectors of the generic arrangement were rotated by 180°.

The triangular tunnel-trap detector is shown in Fig 3 with a 6° diverging beam reflecting off the planes of the detector surfaces of two different sizes. The detectors are shown offset from the beam path to clearly show how the planes of the detector pairs of different sizes are parallel, but do not lie in the same plane, whereas the detectors of the same size (shown in Fig. 2) lie in the same plane.

The final photodiode arrangement is shown in Fig. 4. In this arrangement the detectors numbered three and six were left out so the placement of the detectors can be seen. The positions of both the photodiodes and the aperture were obtained from ray-tracing an f/4 incident beam focused on and normal to the reference plane. The reference plane, needed for irradiance measurements, is the front surface of the aperture. The diverging beam leaving the opening of the overfilled aperture was collected and measured by all of the photodiodes to maintain the cosine function of irradiance responsivity measurements. The input and output beams lie in the same plane which is parallel to the base plane of the radiometer housing. The triangular holder is mounted in this plane which is also parallel to the front surfaces of photodiodes two and five. The output beam is shifted relative to the input beam by 41.3 mm. This shift does not cause any measurable polarization dependence in the signal responsivity of the trap radiometer. The figure also shows that the first and second detector surfaces are more efficiently utilized and the position of detector four as well as detector three are not as critical.

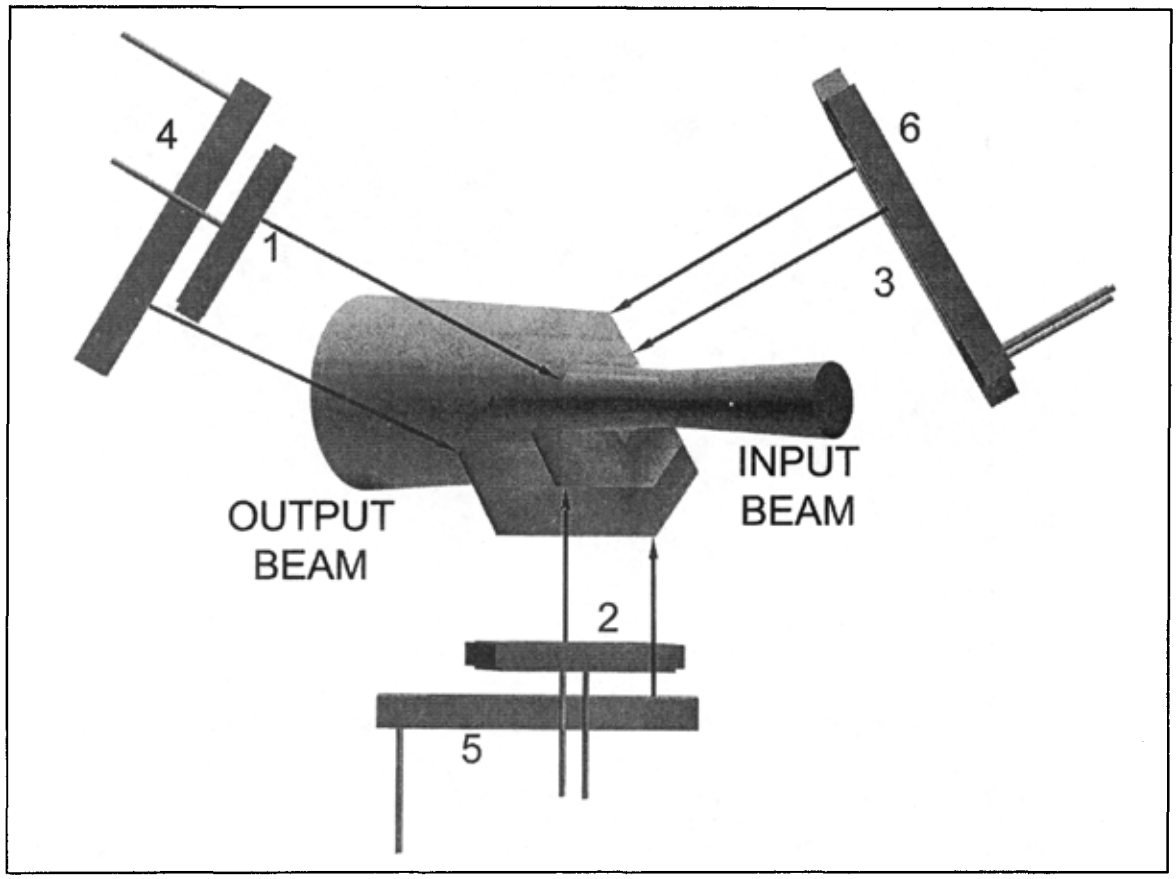

Fig. 3. Photodiode arrangement and beam geometry in the triangular tunnel-trap detector. The input beam hits photodiode 1 and then it propagates to photodiodes 2 to 6.

The last detector was rotated in the plane of the block to maximize the detector area with respect to the elliptical shape of the beam.

The construction, shown in Fig. 5, is made up of three blocks arranged in a triangular fashion. Six silicon photodiodes of two different sizes were used as detectors in the tunnel-trap radiometer. Two 10 mm by 10 mm photodiodes at the front were followed by four 18 mm by 18 mm devices. Windowless photodiodes were used to eliminate problems caused by additional reflections and laser interference. There are two blocks that hold detectors of two different sizes and therefore have a step to allow the smaller detector to be closer to the center of the triangle. The third block holds the larger detectors at the same distance from the center of the triangle. The three blocks are held in a triangular shaped block that has been ground both on the inside and outside to achieve flatness and thickness accuracy within a few hundredths of a mm. This holder simplified the alignment of the photodiodes before installation inside of the radiometer housing.

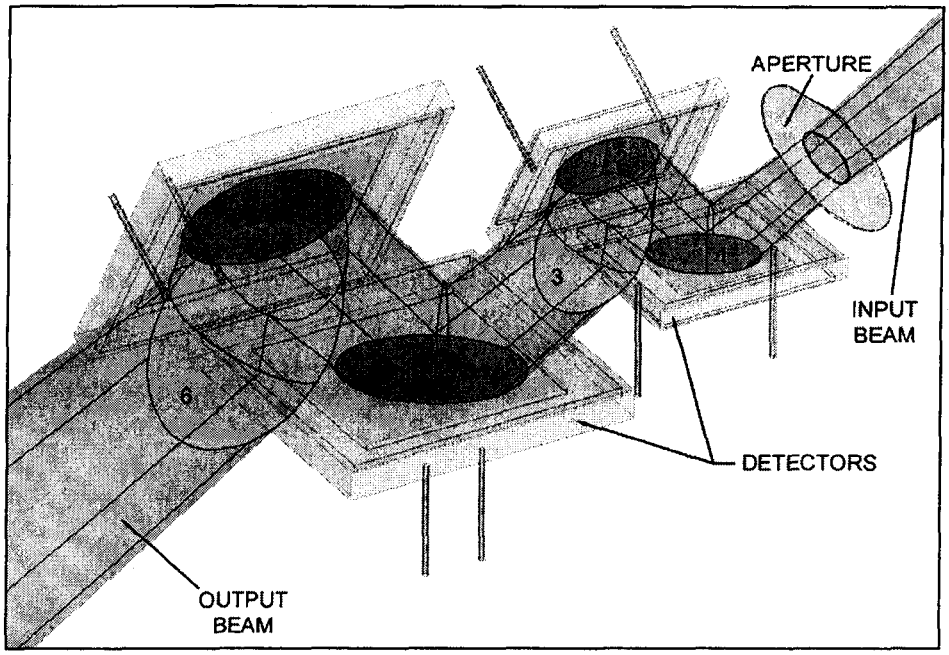

Fig. 4. Photodiode arrangement and beam propagation in the triangular tunnel-trap detector.

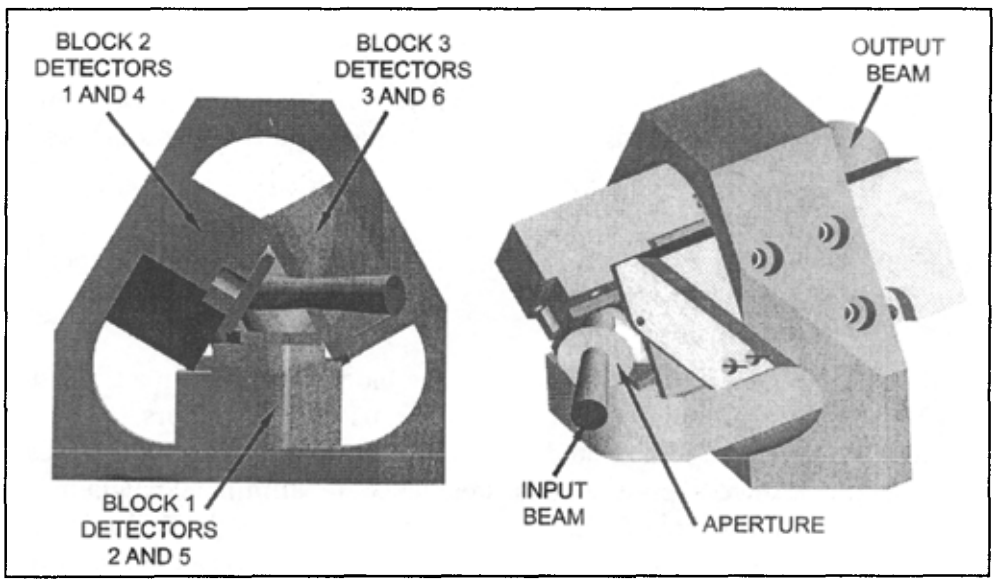

Fig. 5. Construction of the triangular tunnel-trap detector holder

The triangular shaped detector assembly block is housed in a square housing as shown in an exploded view of the triangular tunnel-trap radiometer (Fig. 6). Two precision apertures, with internal diameters of 5 mm and 3.5 mm and made of black-nickel coated copper disks of 0.1 mm thick can be applied at the input alternatively. They are mounted in a recess of 0.1 mm deep in the front cover to extend the aperture front plane to the overall front surface of the

trap-radiometer. This arrangement facilitates the distance measurements in irradiance mode. The aperture mounting positions are invariant. The FOV is 6° with the 5 mm and 8° with the 3.5 mm aperture. The installed aperture is fixed by a cylindrical holder threaded outside for either a protecting cap or an input baffle tube. The aperture retainer is beveled inside at the front with an angle of 45° relative to the aperture plane. This input geometry minimizes the stray radiation at the front of the radiometer. The incident radiation, overfilling the aperture, is reflected back from the front surfaces such that the reflected beams cannot enter the aperture opening. A light trap can be attached to the radiometer output to reject the ambient light from the trap detector. This can keep the blocked signal reading and the signal fluctuations low. The light trap and the protecting cap are attached to the housing most of the time to keep the dust outside. When the light trap is removed, the transmitted radiation can be measured. Also, the transmitted light can expedite the radiometer alignment. The cavity of the light trap is covered with specularly reflective black paint.

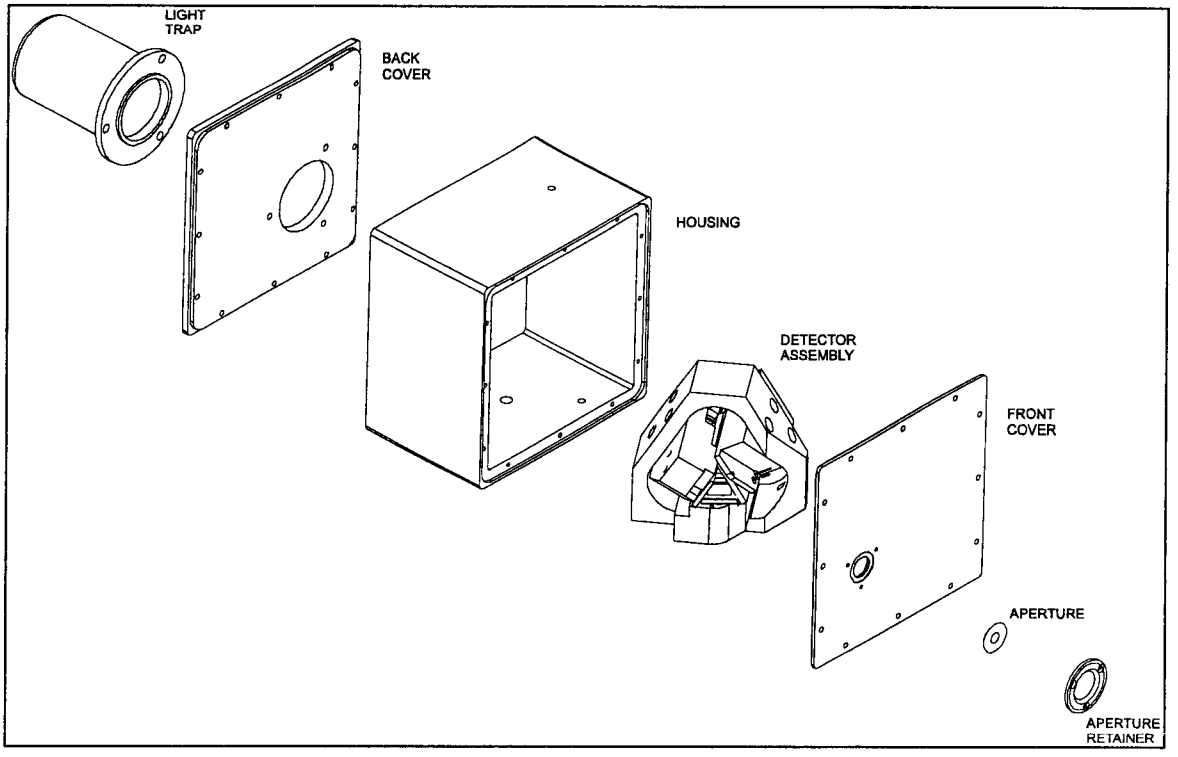

Fig. 6. Exploded view of the triangular tunnel-trap radiometer.

The tunnel trap radiometer built according to the above design considerations was tested for optical performance. Angular response scans were made by rotating the radiometer around the center of its 3.5 mm diameter aperture. The output signal was measured while the aperture was overfilled with the uniform irradiation from a point source. The source was a stable and low noise Wi-41G tungsten lamp located at a distance of 3 m from the aperture.

Since the projected area of the rotating aperture changes with cosine versus rotation angle, the irradiance response, which is proportional to the projected area, also should follow the cosine function. Deviations from the cosine response can be caused by internal reflections, beam clipping, stray radiation, and angular response dependence of the under-filled

photodiodes. When the source is different from a point source, the accuracy of irradiance measurements strongly depends on the deviation between the realized angular response and the cosine response within the angular range determined by the source size, the diameter of the detector aperture, and the separation between source and aperture. The radiometer FOV gives the final limitation for the angular range of an irradiance measurement. The FOV has a major impact for the maximum source size and/or the minimum source to aperture distance.

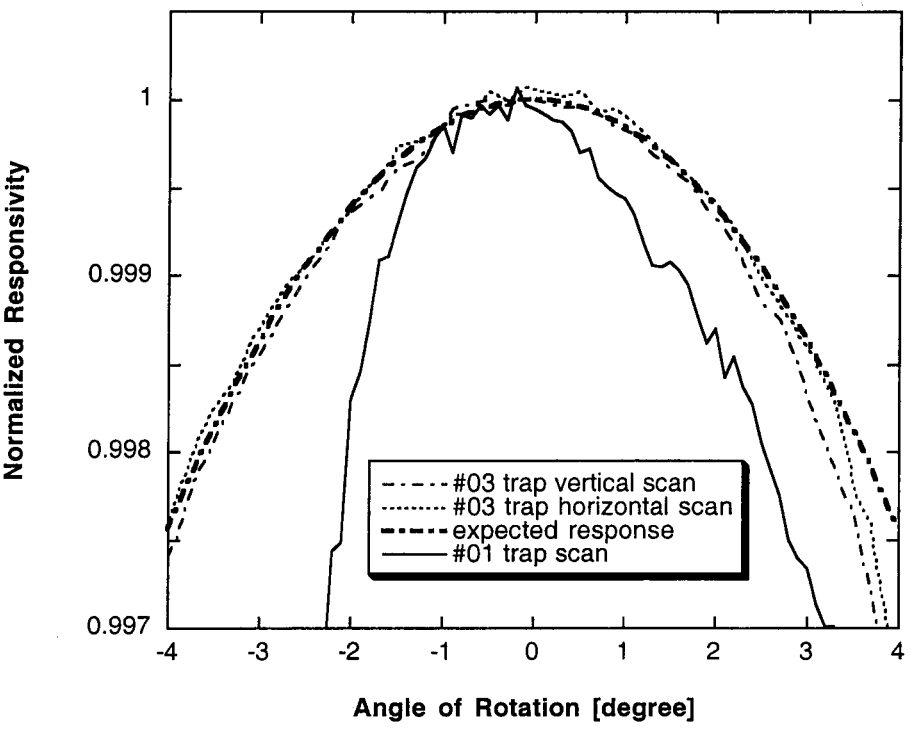

Fig. 7. Irradiance mode angular responses of tunnel-trap radiometers using 3.5 mm diameter apertures. The experimental #01 trap was built with six equal size photodiodes. The beam was clipped on the sixth (last) photodiode. The horizontal and vertical angular response scans of the optimized tunnel-trap radiometer #03 are very close to the expected cosine response within an angular range of 5°.

The normalized angular responses of the experimental #01 trap discussed earlier and the optimized #03 tunnel trap radiometers are shown in Fig. 7 and compared with a perfect cosine distribution. During the horizontal scan, radiometer #03 was rotated in the horizontal plane around its aperture center. Thereafter, it was rotated 90° around its optical axis and the "vertical" scan was done in the same way as the horizontal one. The graph shows that the deviation of the realized angular response from the expected cosine function is less than 0.02 % within a 5° FOV and about 0.05 % at 8° FOV. The cosine response of the optimized device is five times better than that of the experimental device where six equal size photodiodes were used. Also, the FOV increased significantly. These measurement results verified the optical and mechanical design expectations.

3. Electronic characteristics

To optimize the overall performance of the tunnel-trap radiometer, the photocurrent-to-voltage converter had to be optimized for the three fundamental gains: current-, voltage-, and loop-gains [15].

The impedance of the feedback components determines the photocurrent gain and the high frequency signal roll-off [15]. A high resistance feedback resistor gives high signal gain and can produce a low signal roll-off frequency even with a small feedback capacitance.

The loop gain of the photocurrent meter is the product of the open loop gain of the operational amplifier and the attenuation of the feedback network. The feedback network is a signal attenuator from the converter output to its input, implemented by the feedback impedance and the shunt impedance of the photodiode. The loop gain is frequency dependent. It is very important to keep the loop gain high enough at the signal frequency because the accuracy of the current-to-voltage conversion depends on its magnitude [15].

The closed loop voltage gain is equal to the reciprocal of the feedback attenuation of the converter if the loop gain is high enough [15]. The voltage gain depends on the signal frequency. The voltage gain determines the amplification for the input noise and the temperature-dependent offset-voltage of the operational amplifier. The voltage gain can be kept low if photodiodes with high shunt resistance are used. When ac signals are measured, the voltage gain has to be low at the selected signal frequency.

In order to optimize the fundamental gains, the S1337 photodiodes had to be selected for shunt resistance and the resultant junction capacitance of the parallel connected photodiodes had to be measured. Selection of the different size photodiodes for equal shunt resistance [16] was necessary to maximize the resultant shunt resistance of the six diodes connected in parallel.

The medium and large photodiodes were selected from several groups purchased at different times. The two photodiodes located directly behind the aperture were Model 1337-11 photodiodes with a 10 mm by 10 mm active area. The diode shunt resistances varied between 275 MΩ and 325 MΩ in the first group and between 130 MΩ and 267 MΩ in the second group. The last four diodes in the trap arrangement were Model 6337-01 photodiodes with an active area of 18 mm by 18 mm. The shunt resistances of these large area photodiodes varied between 355 MΩ and 500 MΩ in the first group and between 150 MΩ and 260 MΩ in the second group. Two 1337-11 and four 6337-01 photodiodes of similar shunt resistance were selected and connected in parallel in one radiometer. Eight such photodiode groups were assembled for the eight trap radiometers we built. Resultant shunt resistances between 30 MΩ and 55 MΩ were measured on the eight radiometers. A shunt resistance of 31 MΩ was measured on trap radiometer #03, which is characterized in detail in this paper.

In order to know the impedance of the parallel connected six photodiodes, the resultant capacitance of each photodiode group was measured. The capacitance of radiometer #03 was 7.5 nF in the dark.

3.1. Loop-gain characteristics

The loop gain at the signal frequency has to be high enough for all signal gain selections of the current-to-voltage converter to obtain a small enough uncertainty in the current-to-voltage conversion. For example, to achieve a 0.01 % uncertainty in a dc mode current-to-voltage conversion, a minimum loop gain of 10^4 is required for signal frequencies lower than 0.3 Hz (see below). Because the loop gain is the product of the amplifier open loop gain and the attenuation of the feedback network, it is also signal gain, and thus, feedback resistor dependent. Care should be made when high sensitivities are needed because increasing feedback resistance results in decreasing loop gain [15]. Frequency and feedback resistor dependent optimization of loop gains is one of the most important electronic design considerations in high accuracy photocurrent measurements and will be discussed in detail below.

The theory of loop-gain calculations in silicon radiometers has been described in a previous work [15]. The relatively small shunt resistance of the tunnel-trap-detector can cause a large attenuation in the feedback network especially at high feedback resistor selections. The large attenuation can result in low loop gains in the current-to-voltage converter. The feedback network in this case was implemented by the complex impedance of the six photodiodes connected in parallel and that of the feedback resistance and capacitance connected in parallel. Also, the large 7.5 nF capacitance of the parallel-connected photodiodes increased the integrating time constant in the analog control loop. Because of these two reasons, oscillations occurred in the output voltage of the current-to-voltage converter even at the highest signal-gain settings. In order to eliminate loop oscillations and to achieve 0.01 % current-to-voltage conversion accuracy and stability, the loop-gain characteristics of the trap-radiometer had to be analyzed and optimized versus frequency and feedback-resistor selections for both dc and ac mode optical radiation measurements.

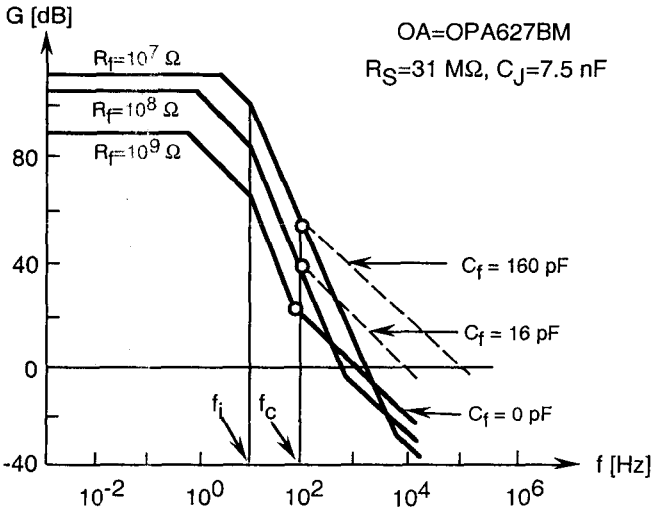

Fig. 8. Calculated loop gain characteristics of trap-radiometer #03 for the highest three signal-gains. The open-loop gain roll-off frequency of the operational amplifier is f_i. The dashed lines show the effect of the partial frequency compensations at frequency f_c. The open circles show the signal 3 dB roll-off points matched to the loop gain curves.

The calculated loop gain characteristics of the tunnel-trap radiometer for the highest three signal gain selections are shown in Fig. 8. The feedback resistor could not be higher than 1 GΩ to obtain a minimum dc loop gain of 10^4 (80 dB). The solid lines show the loop gain curves when no external capacitors are connected parallel to the feedback resistors. For 10^7 Ω and 10^8 Ω feedback resistor selections, two roll-off points can be seen on both curves above the 0 dB line causing a 180° phase shift lag at high frequencies. The roll-off points are caused by integrating type time constants. The larger time constant τ_1 is equal to the parallel connected photodiode shunt resistance and feedback resistance times the sum of the detector and feedback capacitance [15]. The shorter time constant $\tau_i=1/f_i$ is produced by the open-loop gain roll-off of the operational amplifier. The additional 180° phase shift, caused by the negative feedback itself, produces a total of 360° phase shift resulting in oscillations at high frequencies in the loop. At signal-gain 10^9 V/A, τ_2 differentiating time constant gives the roll-on (roll-back) in the loop gain. This time constant, produced by the feedback resistor and the parallel stray capacitance, is large enough to decrease the 180° phase lag caused by the two integrating time constants. At this signal gain selection, oscillations will not happen if an operational amplifier with high enough open loop gain and roll-off is selected. Our choice was the OPA627BM where the open loop gain is 10^6 and the roll-off of the open loop gain is at 10 Hz. The roll-off is only 1 Hz for the popular OPA111.

Frequency compensations can be applied in the feedback network of the operational amplifier to modify loop gain characteristics [15]. Partial frequency compensations have been applied for the next three signal gains of the trap-radiometer to eliminate oscillations. When an external capacitor of 160 pF was connected parallel to the 10^7 Ω feedback resistor and a 16 pF to the 10^8 Ω resistor, the signal roll-off points were tuned to f_c=100 Hz (shown with open circles) and the phase lag was decreased enough to eliminate oscillations. Similarly, a compensating capacitor of 1.6 nF was connected parallel to the feedback resistor 10^6 Ω. Full frequency compensations were applied for the signal gains of 10^5 Ω and 10^4 Ω. In a full compensation, the differentiating time constant of the loop was equalized to one of the loop integrating time constants. This integrating time constant was produced by the parallel connected photodiode shunt resistance and feedback resistance times the sum of the detector and feedback capacitances [15]. The values of the feedback components and the final signal roll-off frequencies of the trap radiometer are shown in Table 1. The circuit diagram of the trap radiometer is shown in Fig. 9. To minimize 60 Hz ripple and noise pick-up, the length of the wires, connected to the high-resistance inverting-input of the operational amplifier, was minimized and both the circuit board and the photodiodes were shielded. The temperature coefficient of the feedback resistors is equal to or less than 100 ppm/°C.

The optical radiation signal can be measured in either dc or ac (chopped) modes. In dc mode, if the integration is done for the duration of 100 power line cycles the electrical bandwidth is limited to 0.3 Hz. In this frequency range, the loop gain is 3 x 10^4 or higher for any signal gain selections. However, the upper frequency limit is determined by the integration time of the digital voltmeter (DVM) attached to the output of the current-to-voltage converter. Frequency compensations are still needed to avoid oscillations in the analog control loop of the current-to-voltage converter.

Table 1
Current-to-voltage converter feedback components and signal roll-off points for a silicon trap-detector of 31 MΩ shunt resistance, 2 pF stray capacitance, resultant junction capacitance of 7.5 nF, and operational amplifier OPA627BM.

Feedback resistor [Ω]	Feedback capacitor [pF]	Signal roll-off frequency [Hz]	Compensation type
10^9	0	80	No
10^8	16	100	Partial
10^7	160	100	Partial
10^6	1600	100	Partial
10^5	7480	213	Full
10^4	7500	2123	Full

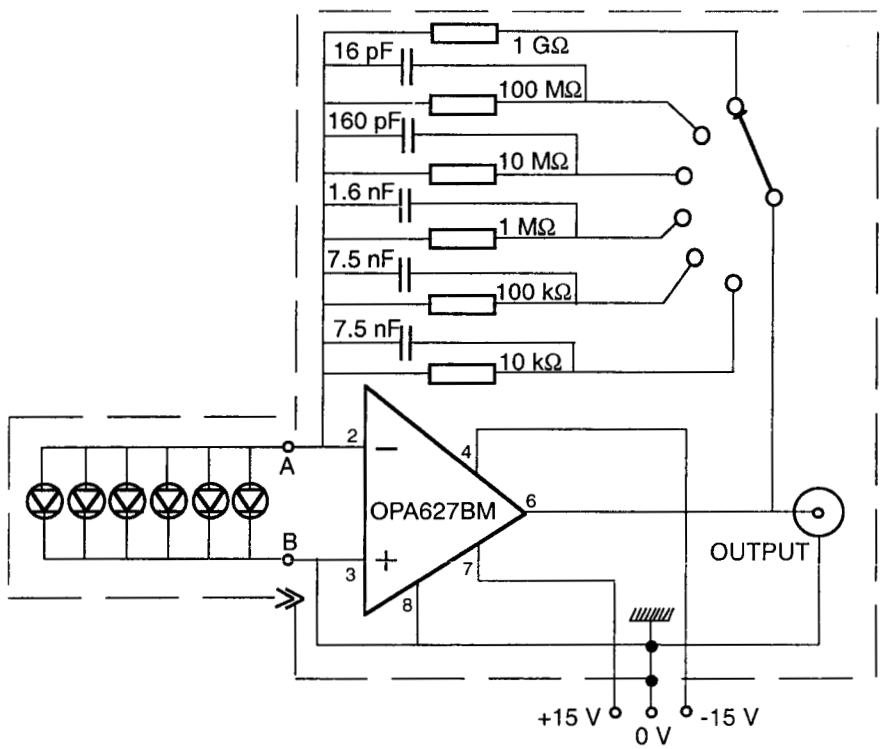

Fig. 9. Circuit diagram of the tunnel-trap radiometer.

In ac mode, the chopping frequency was selected to be 10 Hz, a decade lower than the 3 dB roll-off points, to obtain operating points on the plateau of the frequency-dependent signal gain curves. To achieve high current-to-voltage conversion accuracy in ac mode as well, the

loop gain had to be high enough at 10 Hz for all signal gain selections. The lowest 10 Hz-loop gain was equal to about 3 x 10^3 at the highest signal gain (10^9 Ω). This loop-gain resulted in the largest current-to-voltage conversion uncertainty of 0.03 %.

3.2. dc mode measurements

Figure 10 shows the dc noise measurements in the dark versus signal gain selections. The electrical bandwidth dominated by the integrating type DVM was 0.3 Hz. The noise equivalent rms photocurrent is shown with the solid line. The noise floor at 10^9 V/A signal gain was 32.2 fA. This corresponds to a noise equivalent power of 47.4 fW at 845 nm where the responsivity of the trap detector is 0.6794 A/W. The graph also shows the dc output offset voltage of the current-to-voltage converter. The dc output offset voltage can be subtracted together with the dark reading if a shutter is applied at the light source being measured by the trap radiometer.

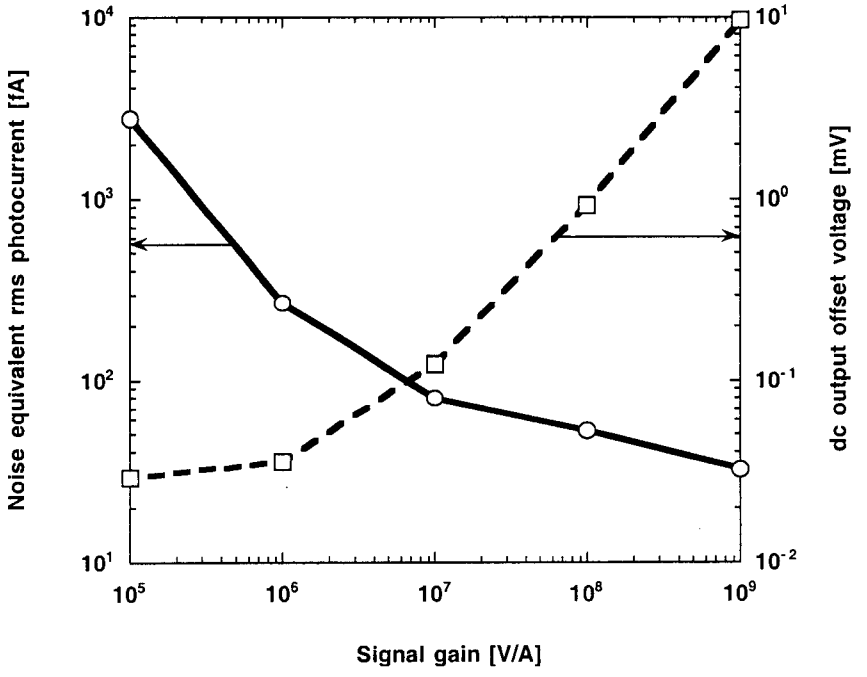

Fig. 10. dc noise and output offset voltage measurements in the dark versus signal gain.

The noise sources in dc mode photocurrent meters were discussed in an earlier work [16]. The Johnson (thermal) noise, which is caused by thermal motions of charge carriers in resistive circuit elements, could be calculated for the trap radiometer. At the highest signal gain, the source resistance, which is the parallel connection of R_S=31 MΩ and R=1 GΩ, is R_{SO}=3x10^7 Ω. The 31 MΩ shunt resistance dominates the source resistance at the highest two signal gains. The rms noise voltage of the source resistance, at the output of the trap radiometer is

$$V_N = (4kTR_{SO}\Delta f)^{1/2} = 0.39\ \mu V, \qquad (1)$$

where k=1.38 * 10^{-23} J/K is the Boltzmann constant, T=300 K was the temperature of the radiometer during the test, and Δf= 0.3 Hz was the measurement bandwidth determined by the DVM. The 0.39 μV is equivalent to an rms photocurrent of 0.39 fA. (The Johnson noise at R=0.1 GΩ is 0.34 μV.)

The total noise of 32.2 fA measured in dc mode indicates that the dominant noise originated from the 1/*f* noise of the operational amplifier. In 1/*f* noise, the noise power goes inversely as the frequency. The 1/*f* noise is very large in the measured frequency interval, below 0.3 Hz. The signal frequency had to be increased to get closer to the elbow of the 1/f noise spectrum. This way the 1/*f* noise contribution could be decreased.

In dc mode photocurrent measurements, the effect of the operational amplifier drifts has to be taken into consideration as well. The drift in the output voltage of the current-to-voltage converter originates from two sources. The first one is the amplified offset voltage drift of the operational amplifier. At a signal-gain selection of 10^9 V/A this will be 26 μV (0.8 μV/°C times the dc voltage gain of 33) for a temperature change of 1 °C. The other drift component is the roughly 0.02 pA/°C offset current drift that produces an output voltage of 20 μV through the same feedback resistor for the same temperature change. The signal produced voltage at the output of the current-to-voltage converter should be always 10^4 times larger than the resultant output drift voltage to achieve 0.01 % measurement uncertainty. In a worst case situation, the output signal should not be lower than 0.46 V for a temperature change of 1 °C. This signal requirement applies for the output noise component of the converter as well. The 0.46 V output signal is also more than 10^4 times larger than the measured 32.2 μV output noise (corresponds to the 32.2 fA noise discussed above). If the temperature of the operational amplifier is regulated to 0.1 °C the drift components in the output voltage of the converter will be lower than 5 μV and the noise will limit the output signal at about 0.3 V.

3.3. ac noise measurements

According to the calculated voltage-gain curves in Fig. 11, trap radiometer #03 has a voltage-gain increase with increasing signal frequency for the input 1/*f* voltage-noise between 1 Hz and 100 Hz. This is the frequency interval where ac measurements can be made. The voltage-gain curves are shown with solid lines for the highest three signal-gains. In each voltage-gain curve τ_1 is a differentiating time constant producing a roll-on and τ_2 is an integrating time constant producing a roll-off [15]. The long-dashed curve shows the frequency dependent open-loop gain of the OPA627BM operational amplifier which limits the voltage-gain at high frequencies. Frequency f_i shows the roll-off of the amplifier open-loop gain curve. The short-dashed lines show how the partial frequency compensations discussed above (at f_c=100 Hz) can modify the shape of the voltage-gain curves.

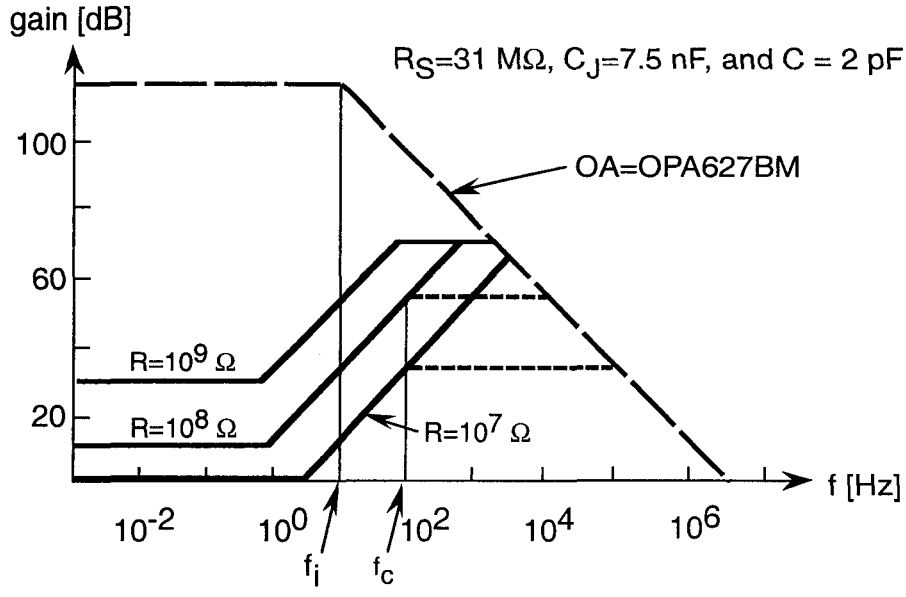

Fig. 11. Calculated voltage gain characteristics of the trap-radiometer. The open-loop gain roll-off frequency of the operational amplifier is f_i. The short dashed lines show the effect of the partial frequency compensations at frequency f_c.

The output total noise of the trap-radiometer was measured in the dark between 10 Hz and 40 Hz when the signal gain was 10^8 V/A and the signal roll-off was tuned to 400 Hz. The tuning was made by a 2 pF external capacitor connected parallel to the 10^8 Ω feedback resistor. Figure 12 shows that the 7.2 fA noise equivalent photocurrent at 10 Hz increased to 9.3 fA at 40 Hz. This result indicates that the effect of the increasing voltage-gain with increasing frequency supersedes the decrease of the $1/f$ noise.

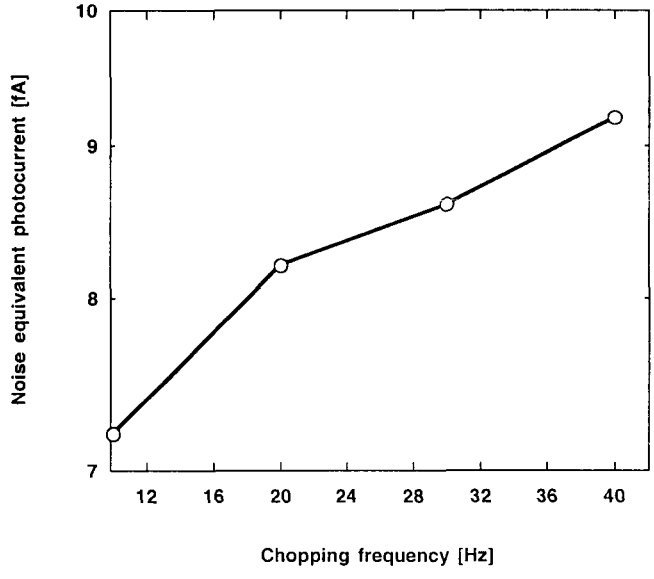

Fig. 12. Measured noise floor versus chopping frequency of the trap-radiometer at a signal gain of 10^8 V/A

The total noise of the trap-radiometer was measured at the optimum 10 Hz chopping frequency for all signal gain selections. An integrating time constant of 3.3 s was selected for the lock-in amplifier. The results, converted to noise equivalent power (NEP) using the 845 nm trap-detector responsivity, are shown with a solid curve in Fig. 13. The NEP is equal to the noise divided by responsivity.

3.4. Comparison of dc and ac noise

The dc noise measured in the dark, also converted to NEP, is shown with the dashed curve in Fig. 13. The lowest NEP, equal to 5.2 fW, was measured in ac mode at a signal gain of 10^9 V/A. The curves show that the ac NEP is about an order of magnitude smaller than the dc NEP. According to these NEP results, the dynamic range of trap-radiometer #03 is between 5 x 10^{-15} W and 10^{-2} W. This range is larger than twelve decades. However, the output voltage produced by the signal should not be lower than 35 mV if a signal-to-noise ratio of 10^4 is to be achieved. The 35 mV corresponds to 52 pW at 845 nm in ac mode.

Table 2 shows the dc to ac input voltage-noise, V_I, ratios for the two highest signal gains of the trap-radiometer. The ratios were calculated from the measured total noise V_T from Fig. 13 and the calculated voltage gains, A_V, (at dc and 10 Hz) from Fig. 11. The $1/f$ current noise and the Johnson noise were much smaller than the amplified $1/f$ input voltage-noise, though the calculated input $1/f$ voltage noise, V_I, at 10^8 Ω was 28 % higher (as compared to 10^9 Ω) owing to some Johnson-noise contribution in the measured total noise. The $1/f$ input voltage-noise decreased by about a factor of 50 when the signal frequency was changed from dc (less than 0.3 Hz) to 10 Hz. At the same time, as shown in Table 2, the voltage-gain increase from dc to 10 Hz was only a factor of 10. If we take the factor of 6 bandwidth difference between the dc and ac measurements into consideration, the one order of magnitude noise-floor difference in Fig. 13 can be understood. The results show that the highest sensitivity can be achieved at 10^9 V/A signal-gain selection in ac measurement mode with a chopping frequency of 10 Hz. The uncertainty of these noise measurements was 18 % (coverage factor k=1).

Table 2
dc input voltage-noise to ac input voltage-noise ratios
calculated from the measured total noise and calculated voltage-gains.

Signal Gain	Total noise, V_T [μV]		Voltage-gain, A_V		$V_I = V_T/A_V$		V_I(dc) / V_I(ac)
	dc	ac	dc	ac	dc	ac	
10^9	32.2	6.6	33.3	333	0.97	0.02	48.5
10^8	5.24	0.9	4.23	42.3	1.24	0.021	59

While the electrical bandwidth of the dc measurements was 0.3 Hz, that of the ac (10 Hz) measurements was six times smaller (0.05 Hz).

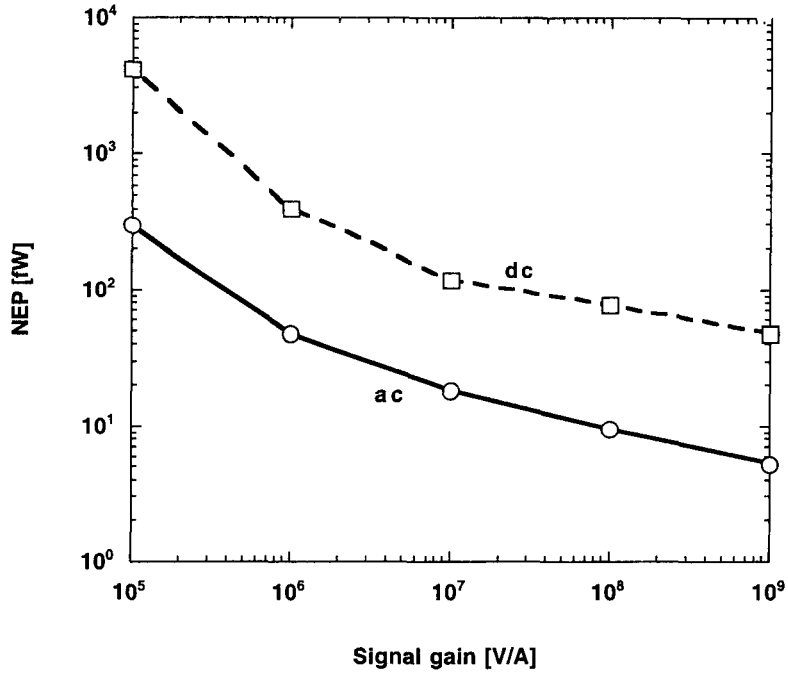

Fig. 13. Comparison of the measured dc and ac NEP values versus signal gain.

3.5. Calibration of the current-to-voltage converter

For state-of-the-art radiant power, radiance, and irradiance responsivity calibrations [19, 20], the calibration accuracy of the photocurrent meter has to be similar to that of the spectral power responsivity and aperture area measurements. As it was discussed earlier, the real values of the feedback resistances should determine the current-to-voltage conversion in a well designed converter. However, a feedback resistance is usually different from its nominal value. To achieve the expected high accuracy requirement, primary level current-to-voltage gain calibrations will be made against standard resistors. The standard resistors have temperature coefficients of less than 10 ppm/°C and are located in a temperature controlled and shielded box. They can be switched in decadic steps up to a maximum of 1 GΩ. The standard resistors can be serially connected to the input of the current-to-voltage converter. The source can be either a voltage or a current source. Both sources need high stability, but the voltage source does not need a large dynamic signal range. The feedback resistor of the converter can be calculated from voltage measurements at the input and output. The calibrated current-to-voltage converter can be used to calibrate other (test) current-to-voltage converters. A low drift and wide range current source, such as the Keithley Model 263 Calibrator/Current Source, can be switched to the inputs of either the standard or the test current-to-voltage converter while the converter output voltages are measured. This substitution type calibration-transfer can be used for all signal-gain selections of the current-to-voltage converters. Using the above described two-step method, an 0.01 % uncertainty level can be anticipated in current-to-voltage gain calibrations.

4. Conclusion

The optical and electronic design of the new power and irradiance measuring tunnel-trap radiometer is described here in detail. This improved performance transfer standard is used to realize and/or hold the high accuracy spectral power, irradiance, and radiance responsivity scales of NIST [19, 20].

At present, trap detectors are not commercially available. Also, previously developed trap devices cannot satisfy the increasing requirements of modern spectral power and irradiance responsivity measurements. In order to transfer responsivity scales to applications with uncertainties similar to those of the primary standards, the national standard laboratories, including NIST, had to develop their own improved performance transfer-standard trap-devices [17, 18,]. We improved the performance of the tunnel-trap radiometer we developed earlier from six equal size S1337 photodiodes. In the new optical and mechanical design, six photodiodes of two different sizes and an input aperture were packed tightly. A second light trap was attached to the radiometer output to absorb transmitted radiation, to minimize measurement of ambient light, and to simplify alignment and spectral responsivity calibrations. The stray radiation at the input was minimized as well. The separation between the aperture and the first photodiode was large enough to insert additional optical components, such as 10 mm long filter packages, without degrading the geometrical performance of the trap-device.

Because of the improved optical-mechanical design and fabrication of the new trap radiometer, the 0.1 % deviation from the cosine function within 4° FOV (as performed on the previously made experimental device) decreased by a factor of five within a FOV of 5°. The 0.02 % deviation increased to about 0.05 % at 8° FOV.

Commercially available current meters cannot achieve the 0.01 % uncertainty requirement of trap-detector photocurrent measurements. It was necessary to design a current-to-voltage converter that is matched to the impedance of the trap detector package to perform the expected accuracy of signal measurements.

The photodiodes in the trap-detector package were selected with similar shunt resistances to minimize voltage-gain for the $1/f$ input voltage noise and drift of the operational amplifier. The voltage-gain, the loop-gain, and the signal-gain were optimized for a signal (chopping) frequency of 10 Hz. A noise equivalent power of 47.4 fW was obtained in dc measurement mode and 5.2 fW at 10 Hz signal frequency for a wavelength of 845 nm. The bandwidth was 0.3 Hz in dc mode and 0.05 Hz in ac mode. The measured one order of magnitude noise-floor difference between dc and ac NEP was verified by a noise analysis. It was shown that the drift in the output voltage of the converter is roughly equal to the noise produced output voltage (in dc mode) if the temperature change of the operational amplifier is not larger than 1 °C.

As a result of the electronic device optimization, a simple and inexpensive trap-radiometer could be implemented with a signal dynamic range from 5×10^{-15} W to 10^{-2} W. This dynamic range is larger than twelve decades.

Linearity, polarization dependent responsivity, spatial response uniformity, spectral power and irradiance responsivity of the triangular trap-radiometer will be discussed in a following publication.

5. Acknowledgement

The authors would like to thank Yuqin Zong and Miklos Racz for participating in the angular response measurements, and Paul Thompson for measuring and selecting the photodiodes for shunt resistance. This work was supported by the U. S. Air Force Metrology under contract number 98-439.

6. References

[1] E. F. Zalewski and C. R. Duda, "Silicon photodiode device with 100 % external quantum efficiency," Appl. Opt. **22**, 2867-2873, 1983.

[2] United States Patent, No. 4,498,012, February 5, 1985.

[3] UDT Brochure on QED-200 Absolute Radiometric Standard, United Detector Technology, 12525 Chadron Avenue, CA 90250, February, 1986.

[4] J. Geist, R. Kohler, R. Goebel, A. M. Robinson, and C. R. James, "Numerical Modeling of Silicon Photodiodes for High-Accuracy Applications, Part II. Interpolating Oxide-Bias Experiments," J. Res. Natl. Inst. Stand. Technol. **96**, 471-479, 1991.

[5] J. L. Gardner and F. J. Wilkinson, "Response time and linearity of inversion layer silicon photodiodes," Appl. Opt. **24**, 1532-1534 (1985).

[6] E. F. Zalewski and J. Geist, "Silicon photodiode absolute spectral response self-calibration," Appl. Opt. **19**(8), 1214-1216, 1980.

[7] N. P. Fox, "Trap Detectors and their Properties," Metrologia, **28**, 197-202, 1991.

[8] J. Geist, A. M. Robinson, and C. R. James, "Numerical Modeling of Silicon Photodiodes for High-Accuracy Applications, Part III. Interpolating and Extrapolating Internal Quantum-Efficiency Calibrations," J. Res. Natl. Inst. Stand. Technol. **96**, 481-492, 1991.

[9] T. R. Gentile, J. M. Houston, and C. L. Cromer, "Realization of a scale of absolute spectral response using the NIST high accuracy cryogenic radiometer," Appl. Opt. **35**, 4392-4403 (1996).

[10] R. Goebel, S. Yilmaz, and R. Pello, "Polarization dependence of trap detectors," Metrologia, **33**, 207-213, 1996.

[11] J. M. Houston, C. L. Cromer, J. E. Hardis, and T. C. Larason, "Comparison of the NIST high accuracy cryogenic radiometer and the NIST scale of detector spectral response," Metrologia, **30**, 285-290, 1993.

[12] Private communication from Thomas C. Larason.

[13] J. L. Gardner, "Transmission trap detectors," Appl. Opt. **33**(25), 5914-5918, 1994.

[14] B. C. Johnson, C. L. Cromer, R. D. Saunders, G. Eppeldauer, J. Fowler, V. I. Sapritsky, and G. Dezsi, "A Method of Realizing Spectral Irradiance Based on an Absolute Cryogenic Radiometer," Metrologia, **30**, 309-315, 1993.

[15] G. Eppeldauer, "Chopped Radiation Measurements With Large Area Si Photodiodes," J. Res. Natl. Inst. Stand. Technol. **103**(2), 153-162, 1998.

[16] G. Eppeldauer and J. Hardis, "Fourteen-decade photocurrent measurements with large-area silicon photodiodes at room temperature," Appl. Opt. **30**(22), 3091-3099, 1991.

[17] R. Friedrich, J. Fischer,, and M. Stock, "Accurate calibration of fiter radiometers against a cryogenic radiometerusing a trap detector," Metrologia, **32**(6), 509-513 (1996)

[18] T. Kubarsepp, P Karha, and E. Ikonen, "Characterization of a polarization-independent transmission trap detector," Appl. Opt. **36**(13), 2807-2812, 1997.

[19] Steven W. Brown, George P. Eppeldauer and Keith R. Lykke, "NIST Facility for Spectral Irradiance and Radiance Response Calibrations with a Uniform Source," Newrad'99 Madrid, Spain, 1999. To be published in Metrologia.

[20] G. P. Eppeldauer, S. W. Brown, T. C. Larason, M. Racz, and K. R. Lykke, "Realization of a Spectral Radiance Responsivity Scale with a Laser-based Source and SiRadiance Meters," Newrad'99 Madrid, Spain, 1999. To be published in Metrologia.

Electronic characteristics of Ge and InGaAs radiometers

George Eppeldauer

Optical Technology Division
National Institute of Standards and Technology
Gaithersburg, Maryland 20899

ABSTRACT

Custom-made Ge and InGaAs photodiodes were tested for high sensitivity DC and AC radiometric applications. Equal size, large-area photodiodes were selected and used as optical sensors in NIST's near-infrared (NIR) standard radiometers. The DC electronic characteristics of the Ge and InGaAs radiometers were measured versus photodiode temperature. At -30 °C, a limit-sensitivity of 22 fA and a dark-current stability of 0.2 pA/16 hours was achieved with the InGaAs radiometer, which was three times better than the results obtained with the Ge radiometer. The Ge radiometer was used for DC signal measurements only, because at frequencies higher than 0.3 Hz the noise boosting effect decreased the photocurrent sensitivity. The frequency dependent gain characteristics were calculated and compared for the two types of radiometer. The InGaAs radiometer could measure optical radiation with a chopping frequency of 10 Hz without any response or limit-sensitivity degradation.

Keywords: dynamic range, frequency dependence, near infrared, noise, photocurrent, photodiode, radiometry, sensors, standard, temperature dependence

1. INTRODUCTION

Germanium (Ge) and Indium-Gallium-Arsenide (InGaAs) radiometers were designed and fabricated at NIST[1] to measure NIR radiometric quantities with high accuracy over a wide range of signal levels. Large-area, planar-structure InGaAs photodiodes with dielectric passivation were selected for most of the applications. For comparison purposes, large-area Ge photodiodes, with diffused, shallow n-type junction over the p-type base material, were built and tested as well.

Large photodiode surfaces of optical quality (polished) were necessary to make optical alignments simple and to eliminate radiation scatter. The diameter of the active area was 5 mm for both the InGaAs and the Ge photodiodes. The plane of the photodiode surface was 2° out of parallel with the wedged window to avoid interference during laser measurements. The photodiodes were selected for high shunt resistance to obtain low amplification of the voltage noise[2]. All photodiodes were hermetically sealed in standard housings of the same size and were cooled by two-stage thermoelectric coolers. The temperatures of the photodiodes were monitored by thermistors and controlled by temperature controllers[3].

2. LOW FREQUENCY (DC) CHARACTERISTICS OF THE NIR RADIOMETERS

The Ge and InGaAs photodiodes were temperature controlled between 25 °C and -30 °C in order to measure their temperature dependent characteristics. Short circuit current measuring circuits of low noise and low drift were attached to the photodiodes[2] to achieve linear operation over a wide radiant power range. The radiometer electronic characterizations included measurement of shunt resistance, voltage gain, output offset voltage, input noise, photocurrent sensitivity, and short term instabilities.

The shunt resistance of the selected Ge photodiode was 17 kΩ at 25 °C. This value increased to 20 MΩ at -30 °C. The three orders of magnitude shunt resistance change of the Ge photodiode had a large impact on the voltage gain[2] of the photocurrent-to-voltage (I-V) converter. The measured shunt resistance and the calculated DC voltage gain are shown versus temperature in Figure 1. The same measurements were repeated on the selected InGaAs photodiode

SPIE Vol. 3061 • 0277-786X/97/$10.00

radiometer. The shunt resistance and the DC voltage gain are shown versus the InGaAs photodiode temperature in Fig. 2. The changes with the InGaAs radiometer are about 40 times smaller as compared to the changes with the Ge radiometer.

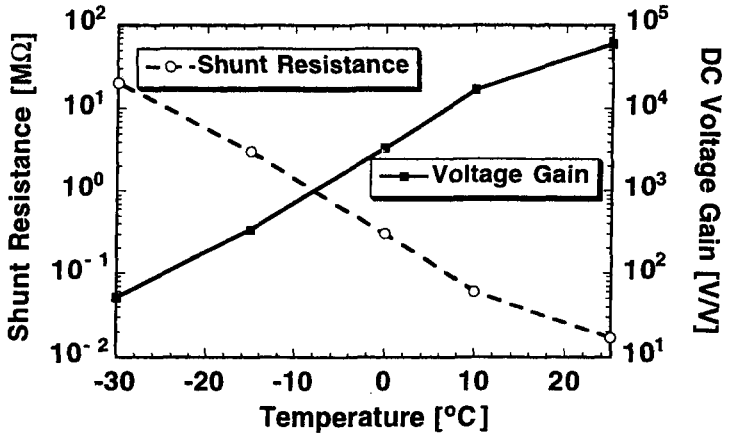

Figure 1. Temperature dependent shunt resistance and DC voltage gain of the Ge radiometer

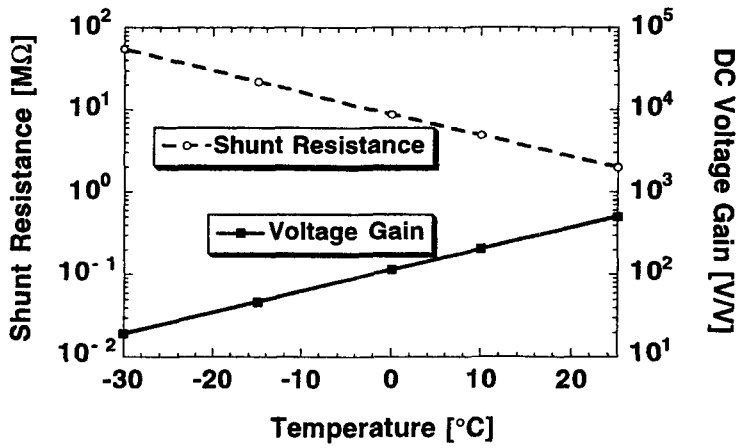

Figure 2. Temperature dependent shunt resistance and DC voltage gain of the InGaAs radiometer

The output offset voltages of the two radiometers were also measured versus temperature. The results are shown in Fig. 3. The output offset voltage of the Ge radiometer changed by more than 300 mV because of the large change in the voltage gain with temperature. The output offset voltage change with the InGaAs radiometer was only 6 mV. The maximum value was 290 mV with the Ge radiometer and 8.2 mV with the InGaAs radiometer. The estimated relative uncertainty (coverage factor k=1) of the offset voltage measurements was 5 % and that of the shunt resistance measurements was 10 %.

The input voltage noise characteristics were determined for both radiometers. The input voltage noise is the ratio of the measured output voltage noise to the voltage gain. The output voltage noise of the radiometer is equal to the standard deviation of the mean output offset voltage (when no optical radiation is measured by the photodiode). In Fig. 4, the measured input voltage noise characteristics are shown versus temperature for both radiometers. Both devices exhibit similar behavior. The same Model OPA111[4] operational amplifiers were used in both cases. The

noise at low photodiode temperatures is higher than at room temperature. At low temperatures the shunt resistance noise of the photodiode is comparable to the 1/*f* voltage noise of the operational amplifier. This is also illustrated in Fig. 5. The total input voltage noise is the superposition of these two major noise components. The total noise measurements of Fig. 5 were made on the InGaAs radiometer at a current-to-voltage gain of 10^9 V/A. At this gain the resistor noise was dominated by the 55 MΩ shunt resistance of the InGaAs photodiode (at -30 °C). The 1/*f* voltage noise of the operational amplifier was flat for shunt resistances less than about 10 MΩ. The resistor noise was calculated using the 0.3 Hz electrical bandwidth of our measurements.

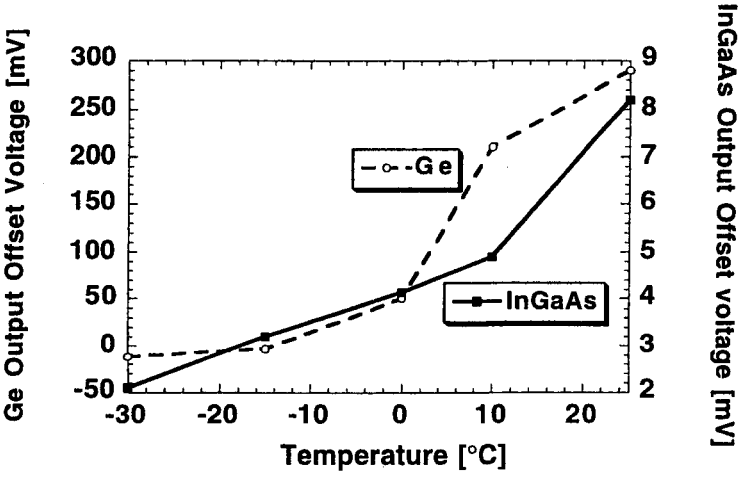

Figure 3. Temperature dependent output offset voltages of the Ge and InGaAs radiometers

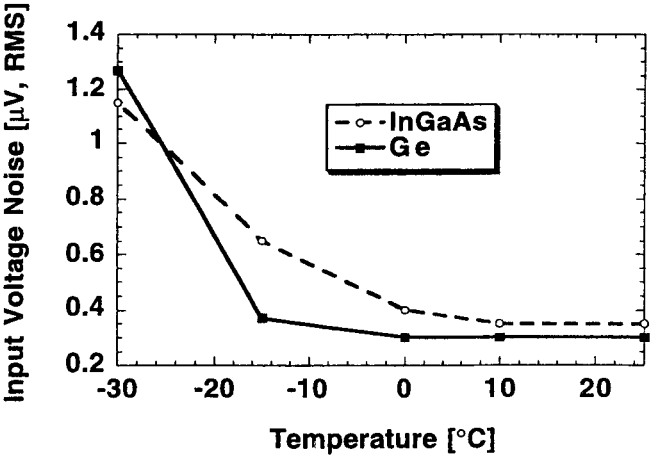

Figure 4. Temperature dependent input voltage noise of the Ge and InGaAs radiometers

The noise equivalent photocurrent is the ratio of the output voltage noise to the current-to-voltage gain (the feedback resistor of the I-V converter). The noise equivalent current gives the photocurrent sensitivity of the radiometer. Despite of the similar input noise characteristics of the Ge and InGaAs radiometers, the photocurrent sensitivities and their temperature dependences are different. This is shown in Fig. 6. The change of the photocurrent sensitivity with the InGaAs radiometer was less than a factor of 8, whereas that of the Ge radiometer was a factor of 290. To achieve high sensitivity and stability, temperature controlled cooling was required for the highly temperature dependent Ge photodiode. Temperature control was not necessary to get similar performance from the InGaAs photodiode. 22 fA noise equivalent photocurrent was measured at a bandwidth of 0.3 Hz with the InGaAs radiometer when the photodiode was cooled and controlled at -30 °C. The relative uncertainty (coverage factor k=1) of the noise measurements was 26 %.

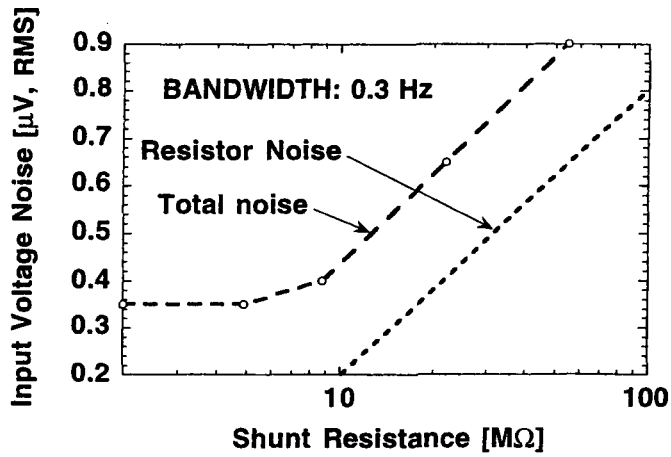

Figure 5. Shunt resistance dependent input total voltage noise (measured) and resistor noise (calculated) of the InGaAs radiometer.

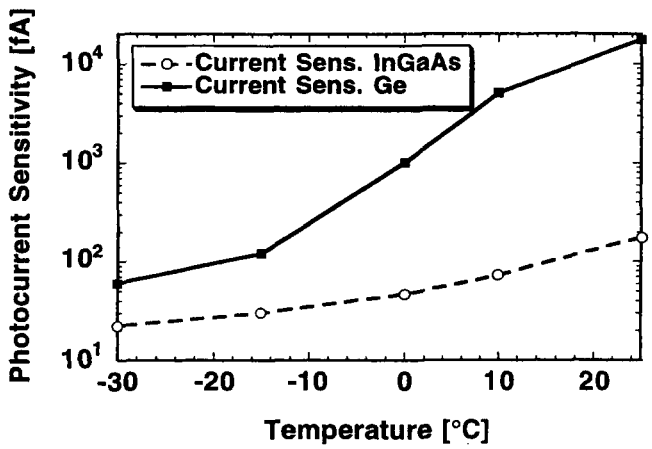

Figure 6. Temperature dependent photocurrent sensitivities of the Ge and InGaAs radiometers

During an 8 hour stability measurement, when the temperature was regulated at -30 °C and the signal gain was 10^9 V/A, the Ge radiometer showed a DC dark-current change of 0.5 pA. The DC dark-current change of the InGaAs radiometer under similar conditions was 0.2 pA during 16 hours.

3. DYNAMIC (AC) CHARACTERISTICS OF THE NIR RADIOMETERS

It is important to know the current-, voltage-, and loop-gain characteristics versus frequency for any photodiode I-V converter. The current gain is important, because the signal is the photocurrent. The high frequency roll-off of the current gain (response) curve is determined by the time constant given by the feedback resistor and capacitor of the I-V converter[5]. The voltage amplification of the I-V converter is equal to the closed loop voltage gain. The voltage gain versus frequency characteristics are important for all current (signal) gain ranges because these curves show whether the meter has any noise boosting effect (increased gain for a certain frequency interval) within the

measurement bandwidth.

Figure 7 shows the calculated voltage gain curves of the two NIR radiometers at a current-to-voltage gain of 10^9 V/A. The only capacitor connected in parallel to the R=1 GΩ feedback resistor is the C=2 pF (estimated) stray capacitance. The voltage gain roll-on for the Ge radiometer starts at 0.23 Hz. This roll-on frequency is determined by the time constant calculated from the product of two factors. One factor is the resultant resistance of the parallel connected feedback and photodiode shunt resistances. The other factor is the sum of the photodiode and feedback capacitances[6]. For this time constant, the dominating resistance is the shunt resistance, R_S, and the dominating capacitance is the junction capacitance, C_j. The junction capacitance is 36 nF for the Ge photodiode and 0.5 nF for the InGaAs photodiode. The shunt resistance of the Ge photodiode is 20 MΩ and that of the InGaAs photodiode is 55 MΩ at -30 °C. Accordingly, the roll-on frequency of the InGaAs radiometer is about 40 times higher than that of the Ge radiometer. The noise boosting effect starts at the roll-on frequency. The noise boosting can be eliminated if the roll-off time constant (given by the feedback impedance) is tuned to the roll-on time constant. This is called full frequency compensation. Frequently, full compensation cannot be achieved at high signal gains because the roll-off of the signal gain curves can be too low. In this situation partial compensation will decrease the noise boosting effect while keeping the signal gain roll-off at high enough frequencies.

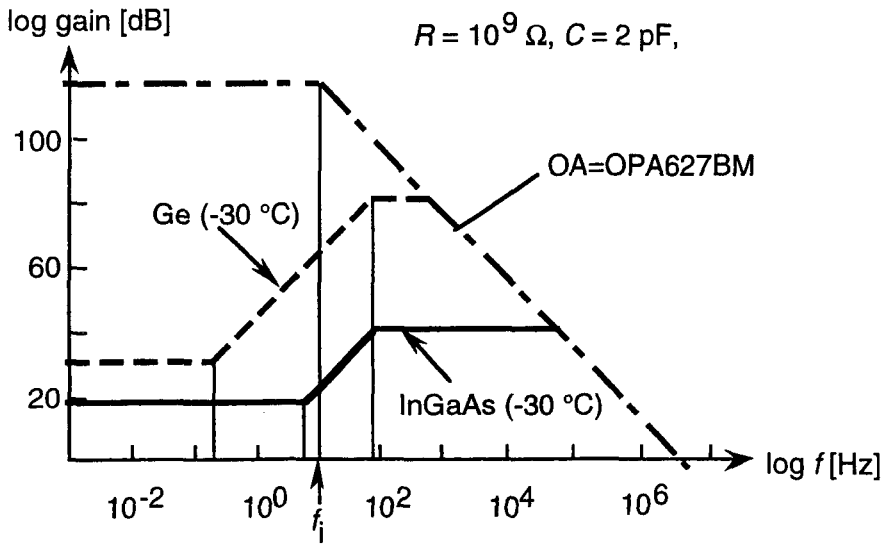

Figure 7
Frequency dependent voltage gain characteristics of the Ge and InGaAs radiometers

The DC characteristics were measured at a bandwidth of 0.3 Hz for both radiometers. Consequently, all measurements were made outside of those frequency intervals where the noise boosting is significant. The voltage gain curves also show that the low frequency (DC) amplification of the input voltage noise is about three times larger with Ge as compared to InGaAs. Similarly, the noise boosting effect at higher frequencies is roughly two decades higher with Ge as compared to InGaAs.

The shape of the loop gain curve (of the open analog control loop) shows whether the loop gain, G, is high enough at the signal frequency to achieve accurate and stable current-to-voltage conversion[7]. This requirement is important for both chopped (or modulated) and low frequency (DC) signal measurements. The OPA627BM operational amplifier selected for chopped radiation measurement has a larger DC open loop gain and a higher open loop gain roll-off point, f_i, than the OPA111 used at DC signal measurements. f_i is determined by the dominating integration time-constant of the operational amplifier. The shape of the loop gain curve indicates whether the phase shifts are small enough for frequencies within the loop bandwidth. Phase shifts for noise frequencies, equal to 180° or larger, can produce oscillations in the analog control loop of the I-V converter.

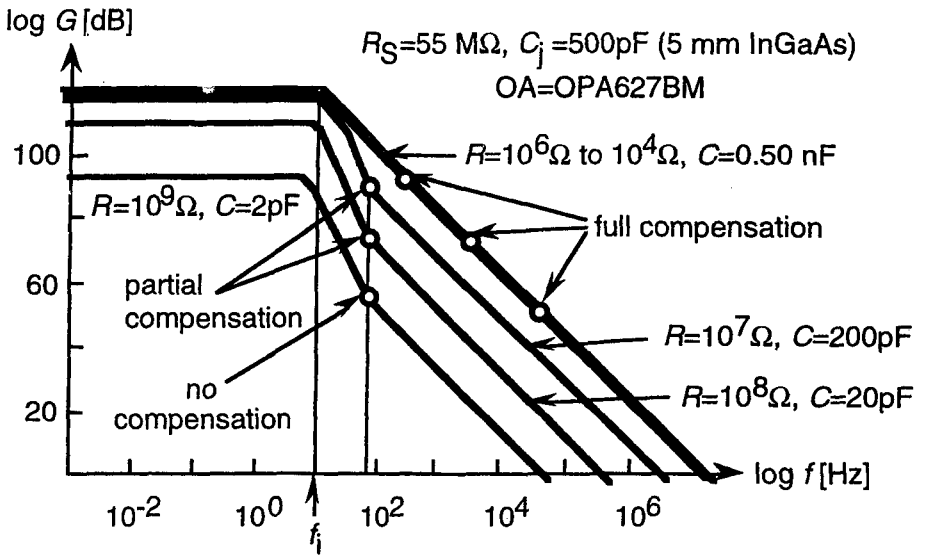

Figure 8. Frequency dependent loop gain characteristics of the InGaAs radiometer for different feedback resistors

Figure 8 shows the calculated loop gain versus frequency curves of the InGaAs radiometer for different feedback resistors. The roll-off points of the signal gain curves are shown with circles as they are matched to the loop gain curves. As a result of partial and full compensations, the roll-off points of the signal gain curves are at 80 Hz or higher. At a chopping frequency of about 10 Hz the loop gains are all larger than 10^4. If the chopping frequency is increased to 80 Hz, the loop gains are still equal or larger than 10^3. Because of the large loop gains at frequencies below 80 Hz, the relative uncertainty (coverage factor k=1) contribution from the loop gains will not be higher than 0.1 % in the photocurrent measurements.

REFERENCES

1. G. Eppeldauer, "Near Infrared Radiometer Standards," in *Optical Radiation Measurements III,* J.M. Palmer, Editor, Proc. SPIE 2815, 42-54 (1996).

2. G. Eppeldauer and J. Hardis, "Fourteen-decade Photocurrent Measurements with Large-area Silicon Photodiodes at Room Temperature," *Appl. Opt.*, Vol. 30, No. 22, 3091-3099 (1991).

3. G. Eppeldauer, "Temperature Monitored/Controlled Silicon Photodiodes for Standardization," in *Surveillance Technologies,* S. Gowrinathan, R.J. Mataloni, and S.J. Schwartz, Eds., Proc. SPIE 1479, 71-77 (1991).

4. Identification of commercial equipment to specify adequately an experimental problem does not imply recommendation or endorsement by the National Institute of Standards and Technology nor does it imply that the equipment identified is necessarily the best available for the purpose.

5. G.H. Rieke, *Detection of Light: from the Ultraviolet to the Submillimeter* (Cambridge University Press, Cambridge, GB, 1994), 143.

6. Product Data Book of Burr-Brown (Burr-Brown Corporation, Tucson, AZ, 1984), 1-38.

7. P. Horowitz and W. Hill, *The Art of Electronics* (Cambridge University Press, Cambridge, GB, 1987), 127-128.

InSb working standard radiometers

G. P. Eppeldauer, A. L. Migdall and L. M. Hanssen

Abstract. InSb radiometers have been developed and characterized for use as transfer standards at the National Institute of Standards and Technology (NIST). The InSb radiometers will hold a portion of the recently realized infrared spectral response scale of the NIST and will serve as working standards for the calibration of test detectors. These radiometers will measure radiant power or irradiance from 2 μm to 5.4 μm. They have a 17° field-of-view. The InSb detectors were selected for high shunt impedance to achieve high sensitivity. The transimpedance-gain, voltage-gain, and loop-gain of the current-to-voltage converters were optimized for optical radiation chopped at 40 Hz. At the peak response, the noise-equivalent-power is 0.6 pW in an electrical bandwidth of 0.3 Hz. The ratio of the dc ambient-background current to the ac noise-equivalent current is 10^7. Spatial and angular responsivities, linearity, stability, and flashing were also characterized.

1. Introduction

The spectral-power response scale of the NIST from 2 μm to 20 μm [1, 2] has been realized on a cryogenic Si composite bolometer. The bolometer was calibrated against a primary-standard cryogenic radiometer at the NIST [3]. The infrared spectral response scale of the bolometer will be transferred to working-standard radiometers. The working standards, InSb and HgCdTe radiometers, will hold the infrared spectral response scale for everyday use. Test detectors will be calibrated against the working-standard radiometers. The design considerations and characterizations of the InSb working-standard radiometers are discussed here. The InSb radiometers are suitable to measure both radiant power and irradiance. They will be used either at the output of an infrared monochromator where the signal level is low [4], or to measure the irradiance from a monochromatic uniform source [5]. The design goals for these radiometers are high sensitivity (low noise) and wide dynamic-signal range, large detector area with a high-precision aperture at the front, uniform spatial response, cosine angular response, linearity, high photocurrent-to-voltage conversion accuracy at the signal chop frequency, and high stability.

2. Optical and mechanical design considerations

The radiometers were designed to minimize background signal, to include a high-precision aperture for irradiance measurements, and to maintain cosine-law response for use with incident beams away from normal incidence [5]. The liquid-nitrogen-cooled InSb photovoltaic detectors (4 mm diameter) were set 1 mm behind a 3.5 mm diameter aperture. The geometry of a long-snout InSb detector Dewar is shown in Figure 1. A second aperture situated about 50 mm from the high-precision aperture limits the field-of-view (FOV) to 17°, yielding an overall view angle of about 26°. A recess at the front of the FOV aperture-holder allows optional cold filters to be mounted. The high-precision aperture can be either underfilled or overfilled. These radiometers have been designed to measure either the $f/4$ output beam of a monochromator or the radiation from a laser-based, small-sphere source, underfilling the high-precision aperture for radiant-power-response calibrations and overfilling for irradiance measurements [5]. A baffle between the two apertures helps maintain cosine response by minimizing internal reflections. A 3° horizontally wedged window allows the detectors to be used for the measurement of either coherent or incoherent radiation. In a short-snout version, the separation between the apertures is only 7 mm, but external optics can be easily added to the Dewar.

3. Electronic design considerations

The detector preamplifier, which is integral with the detector Dewar, was designed for maximum sensitivity and current-to-voltage conversion accuracy at the chop frequency. The high shunt resistance, R_s, of the InSb detector reduces voltage gain, which minimizes amplification of input noise voltage (which is dominated by the $1/f$ noise of the operational amplifier [6]). Figure 2 shows the voltage gain, G_V, versus frequency [7].

G. P. Eppeldauer, A. L. Migdall and L. M. Hanssen: Optical Technology Division, National Institute of Standards and Technology, Gaithersburg, MD 20899, USA.

Metrologia, 1998, **35**, 485-490

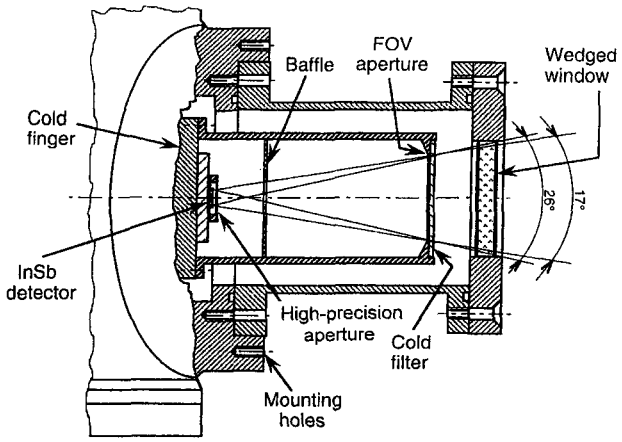

Figure 1. InSb Dewar mount with cold apertures and entrance window.

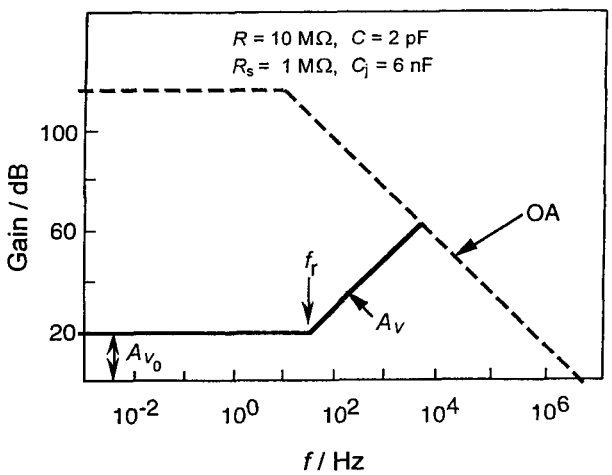

Figure 2. The voltage gain, A_V, of the InSb photodiode current-to-voltage converter is shown with the solid line. There is a noise-boosting effect from about 30 Hz to 8 kHz. The open-loop gain of the operational amplifier OA is shown with the dashed line.

An operational amplifier with low input-voltage noise and high dc-open-loop gain was selected for the photocurrent-to-voltage converter. The feedback resistor was limited to R = 10 MΩ to avoid saturation by the dc radiation background. The time-constant determining the roll-on frequency f_r is the product of two factors: the parallel resistance of R and R_s and the sum of C and C_j [8], the InSb junction capacitance. In our case, f_r was dominated by the detector impedance (R_s = 1 MΩ and C_j = 6 nF). For R = 10 MΩ, the low-frequency voltage gain, $A_{V_0} \approx 20$. The gain A_V starts to increase at the chop frequency of approximately 40 Hz. At 4 kHz the noise voltage gain would be 100 times larger, assuming only stray capacitance (estimated to be C = 2 pF).

Figure 3 shows the loop gain [9], G_{loop}, versus frequency with R = 10 MΩ. The loop gain must be high at the chopping frequency to achieve accurate photocurrent-to-voltage conversion. The solid curve

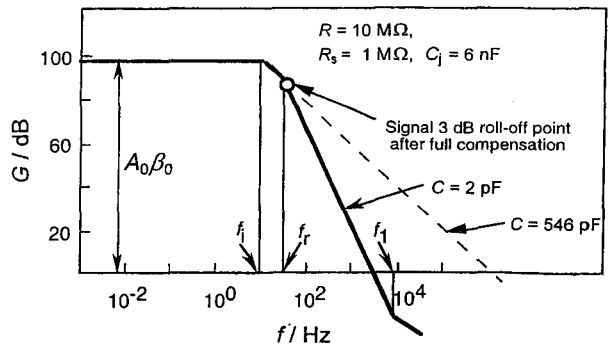

Figure 3. Loop gain, G, versus frequency. The solid curve is the uncompensated loop gain. The dashed curve shows the loop gain after full frequency compensation. The compensated 3 dB roll-off point of the signal response curve is shown with an open circle as it is matched to the dashed loop-gain curve. At low frequencies, $G = A_0\beta_0$, where A_0 is the dc open loop gain of the OA and β_0 is the dc feedback attenuation.

shows the uncompensated C = 2 pF gain with a long – 40 dB/decade slope because f_r and f_i are close to each other and far from f_1. The frequency f_i was determined from the dominant time-constant of the operational amplifier. In this figure, f_r shows a roll-off as opposed to the roll-on of Figure 2. The frequency f_1 is determined by the time-constant (RC) of the feedback impedance. The loop gain reaches unity at about 3 kHz, which is lower than the 8 kHz signal 3 dB roll-off point calculated from the parallel R = 10 MΩ and C = 2 pF impedances [10]. In this case, the loop bandwidth is smaller than the signal bandwidth, which is a condition to be avoided. Also, two integrating time-constants that are close in frequency can cause gain peaking, yielding a sharp increase in amplitude at high frequencies and ringing.

An external 544 pF capacitor was connected in parallel to R = 10 MΩ to achieve full frequency compensation. Tuning f_1 to f_r cancels the roll-off at f_r with the f_1 roll-on. The fully compensated (f_r = f_1 = 30 Hz) loop-gain curve, indicated by the dashed line in Figure 3, also eliminates the noise-boosting effect shown in Figure 2 ($A_V = A_{V_0}$ for all loop frequencies). However, the original f_1 = 8 kHz 3 dB roll-off point decreased to 30 Hz. To operate on the plateau of the signal gain curve, the chop frequency must be a decade lower than the 3 dB point. A 3 Hz chopping frequency satisfies this requirement but because 3 Hz is much lower than the planned 40 Hz frequency, full compensation could not be made for the highest signal gains.

The chopping frequency can be increased if partial frequency compensations are performed for the high signal gains as shown in Figure 4. Increasing the 3 dB roll-off points to a minimum of 400 Hz allows a 40 Hz chopping frequency. For R = 10 MΩ, the loop gain is still about 100 at the signal 3 dB roll-off point, yielding a 1 % error in the current-to-voltage

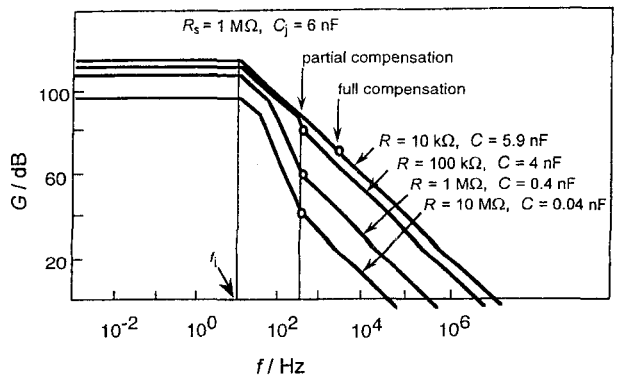

Figure 4. Partially and fully compensated loop-gain characteristics of the InSb photodiode current meter. The open circles show the 3 dB roll-off points of the photocurrent response functions matched to the loop-gain curves for each feedback resistor.

conversion. For the 1 MΩ and 100 kΩ feedback resistors, the loop gain increases further, resulting in higher signal-measurement accuracies. At R = 10 kΩ, full compensation can be realized with the 3 dB point still above 400 Hz. The loop gain at this 3 dB point is about 4000. At 40 Hz, the loop gain equals or exceeds 3×10^4 for all R.

Figure 5 shows the voltage-gain curves for the partially and fully compensated signal-gain ranges. At 40 Hz, the noise-boosting effect is practically eliminated, even for the partially compensated signal-gain ranges.

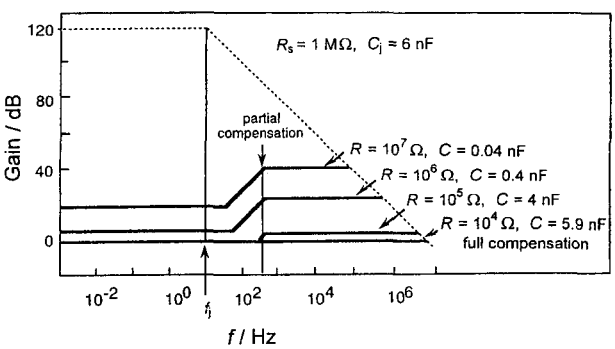

Figure 5. Voltage-gain curves (solid lines) for the partially and fully compensated signal gains of the InSb photocurrent meter. The signal chopping frequency is 40 Hz.

4. Radiometric characterizations

4.1 Responsivity versus time; flashing

A 0.25 % response change was observed during the 15.5 h hold time of the Dewar (see Figure 6). This hold time depends on the Dewar vacuum level. Immediately after repumping, Dewar hold times in excess of 24 hours are possible. The 0.1 % instability in the second half of Figure 6 was measured after 18:00 h, when the environment of the setup was at its quietest. The radiation source was a quartz-halogen lamp, operated at half of its nominal 100 W operating power. The low temperature of the source and the 2 μm cut-on (order-sorting) filter were required to maintain the stability to within 0.1 % because radiation wavelengths shorter than about 2 μm produce response fluctuations due to trapped charges accumulating within the detector. These variations, seen as sudden jumps in the output level, are referred to as "flashing". Flashing can reach the level of a few percent if the visible/near-infrared radiation reaches the detector. Figure 7 shows the typical flashing seen when the tungsten-halogen lamp is used at its full 100 W power, providing more short-wave radiation. The radiation from the lamp passed through a monochromator set to 3.6 μm and a 2 μm cut-on filter. The 10^{-3} filter blocking was not enough to cut out the short-wave radiation from the detector, which had a dynamic range of nine decades. The fluctuations measured this way indicate the extreme sensitivity of flashing to

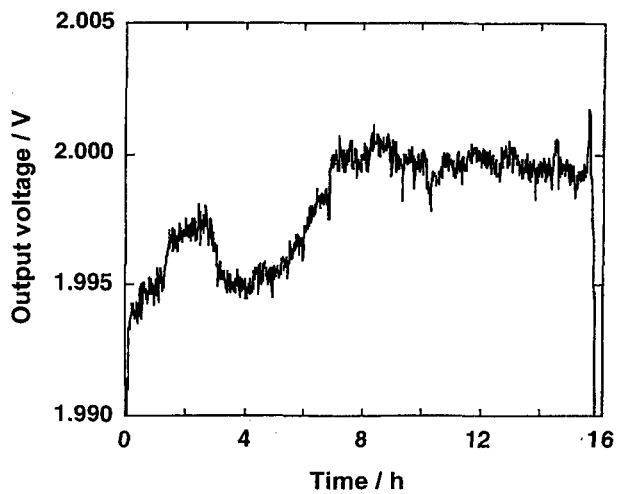

Figure 6. Test of InSb stability versus time at 3.8 μm.

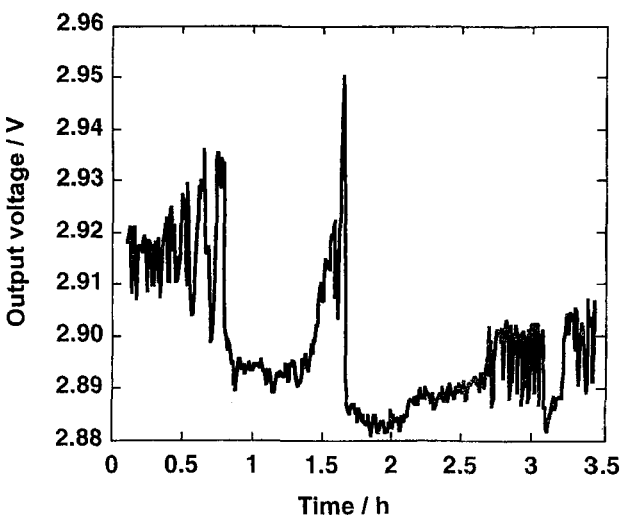

Figure 7. InSb flashing.

short-wave radiation. For accurate measurements, the flashing effect must be smaller than the expected uncertainties. This can be achieved by limiting the incident radiation below about 2 μm by employing cut-on filters and/or appropriate source-power distributions which have relatively low short-wavelength output. Flashing may also be reduced by better detector design, such as by applying an integrated aperture on the InSb chip outside the photosensitive area [11]. The InSb detector output should be monitored for a period of about 1 h to verify that flashing effects are below the desired level.

4.2 Responsivity versus frequency

The normalized, measured, frequency-dependent signal responsivities of the InSb radiometers at gains of 10^4, 10^5, and 10^6 V/A are shown in Figure 8. The results are in good agreement with the design values shown in Figure 4. The 3 dB point could not be measured at gain 10^7 V/A because no cold filter was installed in front of the detector. The detector measured the background radiation with its full broadband responsivity, resulting in a too-large dc background current for this signal-gain range.

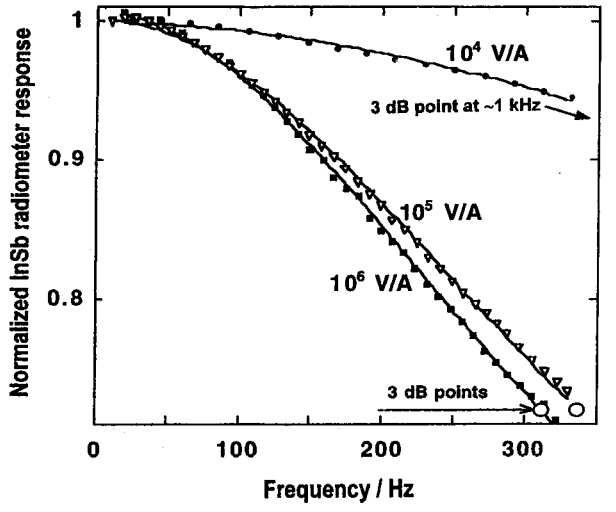

Figure 8. InSb radiometer response versus frequency, normalized to unity at dc, for three different gain settings. One-time-constant response curves are fitted (solid lines) to the measured data points.

4.3 Responsivity nonlinearity

The nonlinearity of the InSb radiometer was tested by comparison with a calibrated transfer-standard Ge detector over a range of input power levels. The measurements were made using a chopped diode-laser beam at 1.3 μm where the two detectors overlap spectrally. Neutral-density filters inserted into the beam were used to vary the radiant power level. The two detectors were substituted for each other.

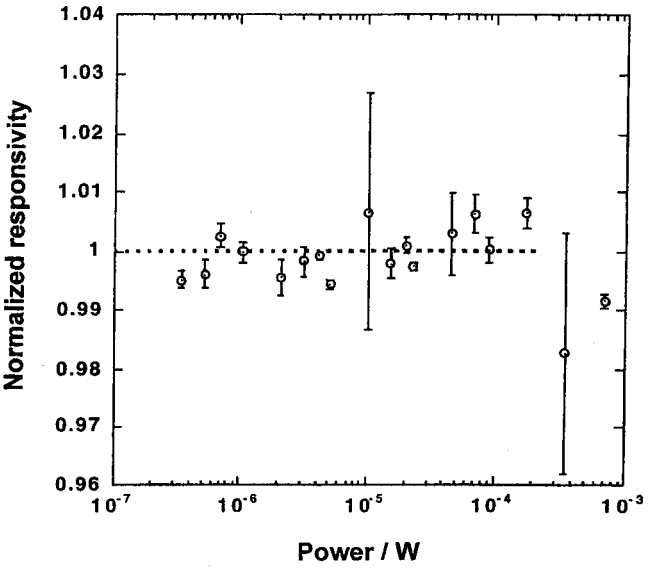

Figure 9. Ratios of InSb to Ge response (for identical radiant-power inputs) divided by a constant to yield a mean value near unity (see text).

Figure 9 shows the InSb to Ge response ratios measured versus radiant power (the ratios have been normalized by the average value over the range 2×10^{-7} W to 2×10^{-4} W). The uncertainty bars in the figure represent only the standard deviation of repeated measurements. If we exclude the two points in Figure 9 which show very large relative standard deviations owing to flashing (Section 4.1), the estimated overall relative standard uncertainty for the entire measurement range is 1 %. This includes major contributions from flashing, the lock-in-amplifier gain calibration, and the current-to-voltage amplifier calibration. The InSb detector is linear up to about 0.1 mW with evidence of about 1 % nonlinearity at 0.75 mW.

4.4 Dynamic range

The noise component from the input-voltage noise density of the operational amplifier was calculated at 43 Hz. At R = 1 MΩ, where the voltage gain was small (A_V = 2 as shown in Figure 5), the equivalent photocurrent noise was 0.06 pA/Hz$^{-1/2}$. The equivalent photocurrent of the Johnson noise was 0.1 pA/Hz$^{-1/2}$. The $1/f$ noise component was calculated from the amplifier catalogue for the 0.1 Hz to 10 Hz bandwidth. The equivalent effective photocurrent of this noise is about 0.6 pA/Hz$^{-1/2}$. At 43 Hz the $1/f$ noise is significantly lower.

The RMS total noise current was measured with an electrical bandwidth of 0.3 Hz at 43 Hz, at different wavelength settings of a monochromator. The total noise scale (left y-axis of Figure 10) indicates low background signal at 2 μm, and a large $1/f$ noise component. No heated IR source was used in this measurement. The background radiation was chopped

at 43 Hz, producing the detector ac mean current (right y-axis of Figure 10). The total current noise increased by more than a factor of two as the monochromator was tuned from 2 μm to 5 μm. The steep slope of the solid curve shows the background noise component increasing with wavelength. The total noise current was about 30 times smaller than the mean ac background-produced detector current at 5 μm. The dominant component of the total noise current in the long-wavelength range is the shot noise of the dc ambient background current. In an independent test, a 13.4 μA dc background current was measured without any spectral selection of the input radiation. The current noise, calculated from this dc background current, was 1.13 pA, just slightly lower than the total noise current observed at the longest wavelength measured. The total noise current of the detector determines the limiting noise-equivalent power (NEP) of the InSb radiometer. The measured NEP at the peak response (2 A/W) was 0.6 pW (RMS) in an electrical bandwidth of 0.3 Hz. The ratio of the dc ambient background current to the RMS total noise current was about 10^7.

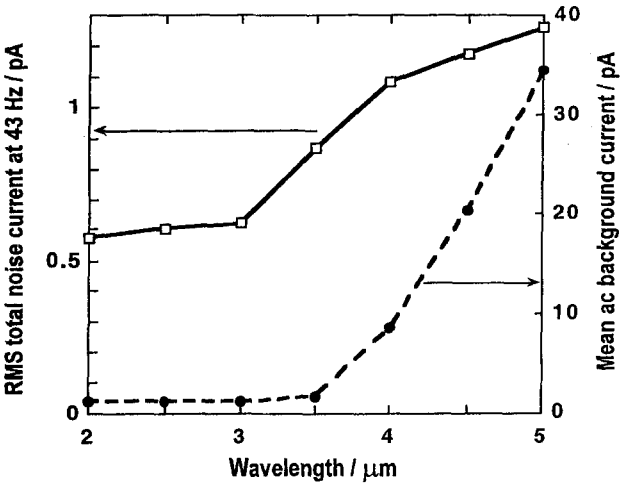

Figure 10. Total noise and ac background current versus monochromator wavelength.

The maximum detector current can be measured at a gain of 10^4 V/A. A 1 mA maximum current on the 10 V full-scale output corresponds to a maximum measurable radiant power of 0.5 mW at the InSb peak responsivity, and thus the dynamic range of the InSb radiometer is nine decades.

4.5 Spatial/angular responsivity

Spatial-response variations were measured along the horizontal and vertical diameters of the InSb detectors. Figure 11 shows a variation of less than 2% in the horizontal scan within the 3.5 mm diameter of the high-precision aperture. The angular response was tested by rotating the detector around its vertical axis. The axis of rotation was close to the centre of the high-precision

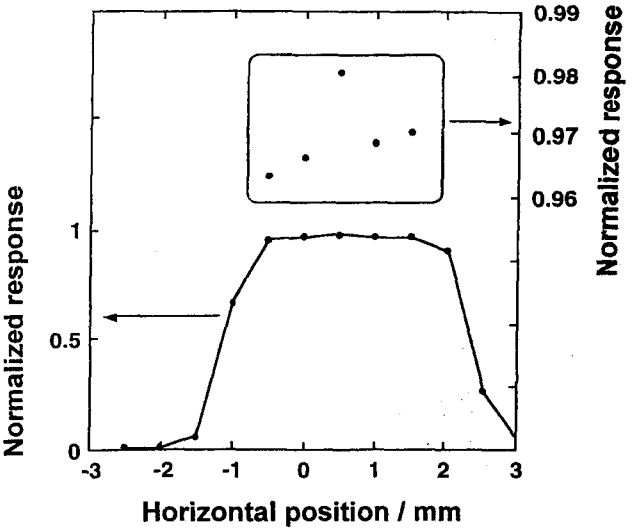

Figure 11. InSb radiometer: variation in horizontal spatial response. The inset shows the data on the expanded scale marked on the right.

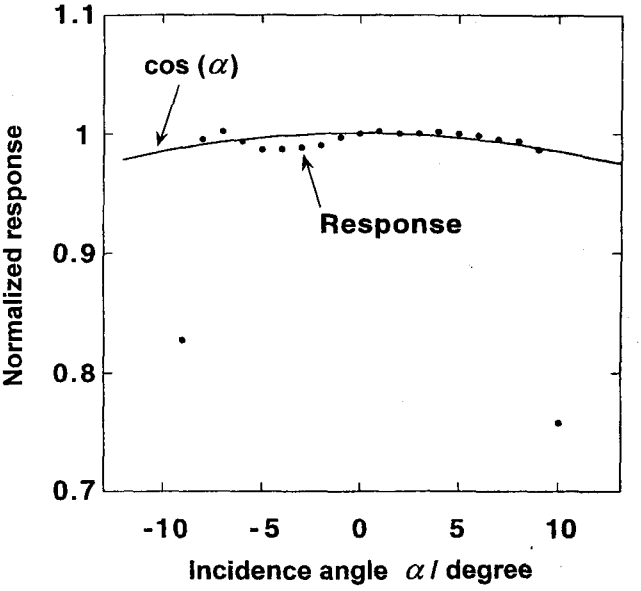

Figure 12. InSb radiometer: variation in angular response.

aperture. The measurement results shown in Figure 12 were obtained using a point source 1.2 m from the detector. The measured field-of-view is 17°. The maximum deviation of the measured angular response from a cosine law is ± 1 %. There was no baffle installed in the FOV-limiting tube during this measurement. The slight measured deviation may indicate a need for a baffle in the input beam, as shown in Figure 1.

5. Conclusion

Standard-quality InSb radiometers have been developed as working standards to hold the spectral response scale of the NIST between 2 μm and 5.4 μm. The

radiometers can measure radiant power or irradiance in a signal range of nine decades. The NEP is approximately 1 $pW/Hz^{1/2}$. Signal (photocurrent)-gain, voltage-gain, and loop-gain were optimized for operation at approximately 40 Hz. The area of the high-precision aperture is 0.1 cm^2, with an FOV of 17°. The spatial-response non-uniformity and the deviation of the angular response from a cosine function are about 1 %. The response non-linearity at the high-signal end (about 0.7 mW) is about 1 %. The 8 h stability of the radiometers is about 0.1 %.

References

1. Eppeldauer G., Migdall A. L., Gentile T. R., Cromer C. L., Absolute response calibration of a transfer standard cryogenic bolometer, In *Photodetectors and Power Meters II* (Edited by K. Muray and K. J. Kaufmann), *Proc. SPIE*, 1995, **2550**, 36-46.
2. Migdall A., Eppeldauer G., Realization of an infrared spectral radiant power response scale on a cryogenic bolometer, *Metrologia*, 1998, **35**, 307-315.
3. Gentile T. R., Houston J. M., Hardis J. E., Cromer C. L., Parr A. C., National Institute of Standards and Technology high accuracy cryogenic radiometer, *Appl. Opt.*, 1996, **35**, 1056-1068.
4. Migdall A., Eppeldauer G., Cromer C., IR detector spectral responsivity calibration facility at NIST, In *Cryogenic Optical Systems and Instruments VI* (Edited by J. B. Heaney and L. G. Burriesci), *Proc. SPIE*, 1994, **2227**, 46-53.
5. Eppeldauer G., Near Infrared Radiometer Standards, In *Optical Radiation Measurements III* (Edited by J. M. Palmer), *Proc. SPIE*, 1996, **2815**, 42-54.
6. Eppeldauer G., Hardis J., Fourteen-decade Photocurrent Measurements with Large-area Silicon Photodiodes at Room Temperature, *Appl. Opt.*, 1991, **30**, 3091-3099.
7. Eppeldauer G., Electronic Characteristics of Ge and InGaAs Radiometers, In *Infrared Technology and Applications XXIII, Proc. SPIE*, 1997, **3061**, 833-838.
8. *Product Data Book of Burr-Brown*, Tucson, Arizona, Burr-Brown Corporation, 1984, 1-38.
9. Horowitz P., Hill W., *The Art of Electronics*, Cambridge, Cambridge University Press, 1987, 127-128.
10. Rieke G. H., *Detection of Light: from the Ultraviolet to the Submillimeter*, Cambridge, Cambridge University Press, 1994, 143 p.
11. EG&G Judson Company, personal communication, 1997.

Domain-engineered pyroelectric radiometer

John Lehman, George Eppeldauer, J. Andrew Aust, and Miklos Racz

We built a large-area domain-engineered pyroelectric radiometer with high spatial and spectral response uniformity that is an excellent primary transfer standard for measurements in the near- and the mid-infrared wavelength regions. The domain engineering consisted of inverting the spontaneous polarization over a 10-mm-diameter area in the center of a uniformly poled, 15.5 mm × 15.5 mm square, 0.25-mm-thick $LiNbO_3$ plate. Gold black was used as the optical absorber on the detector surface, and an aperture was added to define the optically sensitive detector area. Our results indicate that we significantly reduced the acoustic sensitivity without loss of optical sensitivity. The detector noise equivalent power was not exceptionally low but was nearly constant for different acoustic backgrounds. In addition, the detector's spatial-response uniformity variation was less than 0.1% across the 7.5-mm-diameter aperture, and reflectance measurements indicated that the gold-black coating was spectrally uniform within .2%, from 800 to 1800 nm. Other detailed evaluations of the detector include detector responsivity as a function of temperature, electrical frequency response, angular response, and field of view.

OCIS codes: 040.0040, 120.5630, 230.0230.

1. Introduction

Recently it was shown that techniques employed for domain engineering of lithium niobate ($LiNbO_3$) optical parametric oscillators could be used to create large-area, pyroelectric detectors that have reduced acoustic sensitivity.[1] On the basis of our earlier success, we incorporated a unique, concentric-ring patterned, domain-engineered pyroelectric detector into a complete radiometer. First, we discuss the domain-engineering aspects of our design. Then we describe the most important optical and electronic design considerations along with our measurement results.

2. Acoustic Nulling

Ferroelectric pyroelectric detectors are also piezoelectric; therefore the acoustic sensitivity is related to the mechanical structure of the detector, its environment, and anything to which it is attached. A strategy to reduce the pyroelectric detector acoustic sensitivity is shown schematically in Fig. 1. Two detector regions, (a) and (b), with equal and opposite acoustic sensitivities, are exposed to ambient conditions, whereas radiant power reaches only one detector region. The two detectors are connected electrically in parallel so that the current signal from one is superimposed on the other. The result may be expressed as

$$i = i_{a,\mathrm{pyro}} + i_{a,\mathrm{piezo}} + i_{b,\mathrm{piezo}}, \quad (1)$$

where i_{pyro} is the current generated from radiant-power input and i_{piezo} is the current generated from ambient acoustic noise surrounding the detector. If the piezoelectric current generated by detector (a) is equal to detector (b) (that is, if both detectors are mechanically identical), then simply,

$$i = i_{a,\mathrm{pyro}}. \quad (2)$$

In the present device, the center of the detector is effectively region (a) and region (b) is the outer ring. One electrode is placed on each face of the $LiNbO_3$ plate, and, consequently, the two detector regions are electrically connected in parallel. The outer ring is optically and acoustically sensitive, but an aperture prevents incoming optical radiation from being received.

In the past we observed 40-dB reduction in common mode signals over a range of frequencies and nearly 120 dB at what appear to be resonant frequen-

J. Lehman (lehman@boulder.nist.gov) and J. A. Aust are with the Optoelectronics Division, National Institute of Standards and Technology, Boulder, Colorado 80303. G. Eppeldauer is with the Optical Technology Division, National Institute of Standards and Technology, Gaithersburg, Maryland 20899-3460. M. Racz is a guest researcher at the National Institute of Standards and Technology from the Hungarian Academy of Sciences Research Institute for Technical Physics and Materials Science, Budapest, Hungary.

Received 23 June 1999; revised manuscript received 3 September 1999.

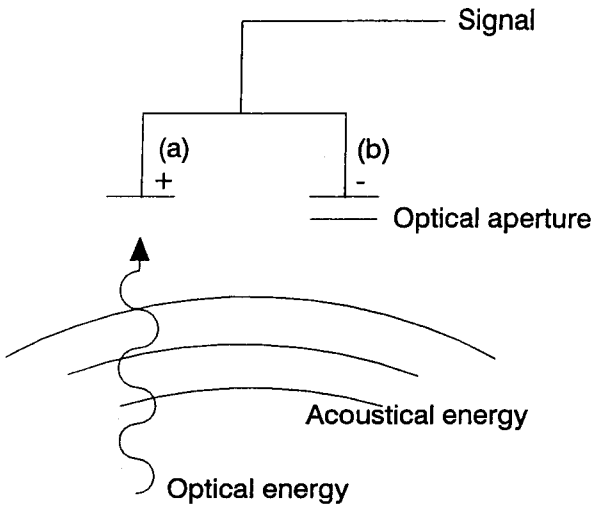

Fig. 1. Diagram of the acoustic nulling concept with equal and opposite pyroelectric domain areas.

cies in a bicell detector with bilateral symmetry. We chose a concentric-ring pattern to simplify the radiometer construction. In the future we expect to model different package geometries and domain patterns rather than rely on the process of trial and error to optimize the nulling capability of each detector.

In Section 4 (which deals with acoustic measurement) we compare two detectors. The steps for fabricating each detector are identical, with the exception of several intermediate steps taken in one of the detectors, to accomplish the selected-area electric field poling or the domain engineering. When we subsequently describe our measurements, the uniformly poled detector was designated J15 and the domain-engineered detector was designated J10. Detector J10 is then incorporated into the radiometer.

The pyroelectric detector elements were constructed from a commercially available, z-cut $LiNbO_3$ wafer. The wafer was 75 mm in diameter, 250 μm thick, and optically polished on both the positive and the negative z faces so that thickness variations were less than $\pm 0.25\%$ (manufacturer specification). The wafer was cut into 15.5 mm $\times$ 15.5 mm squares to form plates, which would eventually become the individual detector elements. To perform the domain reversal, the positive z face of the plate was coated with photoresist. A 10.8-mm-diameter opening was patterned in the center of the plate by use of standard photoresist processing. The sample was then clamped in an acrylic fixture with silicone O rings as shown in Fig. 2. Liquid electrodes were used to provide independent electrical contact to the positive and the negative z faces of the plate. The portion of the sample that underwent domain reversal was defined by the opening in the photoresist. Complete domain reversal of this area was achieved by application of a 24.5-kV/mm electric field across the electrodes.

The detector electrodes were fabricated by deposition of circular nickel films, 15.2 mm in diameter and 25 nm thick in the center of each z face of the plates. The final step in constructing the detector element was the deposition of the gold-black absorbing layer. The process by which the gold black is deposited is similar to that documented by others, most notably Blevin and Brown,[2] but is not substantially different from that documented by Harris *et al.* in 1948.[3] Our process depends on the product of the pressure of the nitrogen environment in which the gold is evaporated and on the distance from the filament source and the target (the nickel-coated $LiNbO_3$ plate). A rule of thumb is "10 Torr cm." In other words, the product of the distance between the evaporation source and the target should equal 12 Pa m (10 Torr cm). Depositing gold black on a thin, fragile, dielectric material, remains an art. The ability to conduct heat away from the crystal is crucial during the deposition, but a uniform and substantial heat sink (without contact resistance) is difficult to attach without scratching or breaking the $LiNbO_3$ plate. In this case we used gold foil sandwiched between the plate and a 3-mm-thick aluminum stage. The plate was held lightly with a spring retainer.

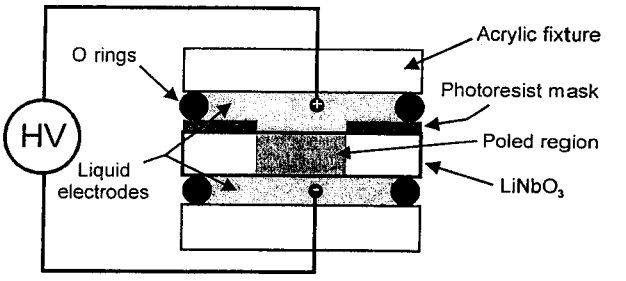

Fig. 2. Schematic diagram of the fixture for applying a high-voltage (HV) electric field across the $LiNbO_3$ plate.

A schematic view of the domain-engineered pyroelectric detector element is shown in Fig. 3. A cross-sectional view of the complete detector assembly is shown in Fig. 4. The detector element was attached electrically and mechanically to the container with electrically conducting epoxy on the perimeter of the aperture. As a result the signal electrode was not attached to a rigid heat sink and therefore provided a

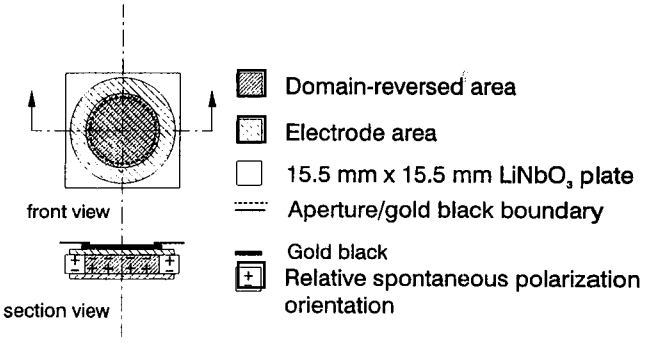

Fig. 3. Exploded view of spontaneous polarization, electrodes, aperture, and gold black.

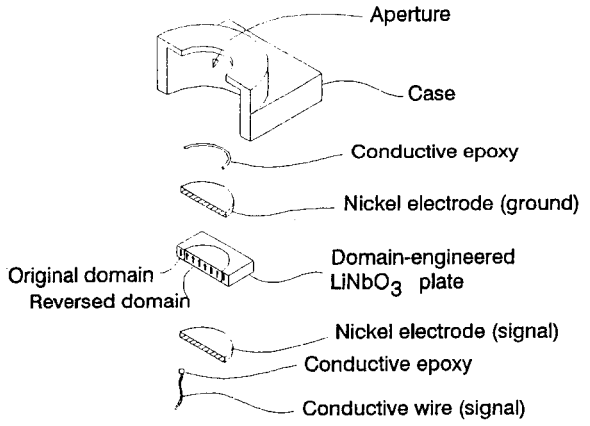

Fig. 4. Perspective-section view of $LiNbO_3$ packaging.

more spatially uniform response to optical input. The grounded case provided electromagnetic shielding for the signal electrode.

Because pyroelectric materials are also piezoelectric, the pyroelectric detector response may contain frequency components in the range of the optical chopping frequency. The typical detector figure of merit, noise-equivalent power (NEP), is normally specified (or should be) along with the wavelength, chopping frequency, bandwidth, detector area, and sometimes temperature and feedback resistance. NEP is a well-accepted, commonly used noise-sensitivity figure of merit for all types of optical detectors, but it is dubious for pyroelectric detectors, because it does not account for the acoustic background.

We compared the acoustic response of our domain-engineered detector, J10, which has equal and opposite areas of acoustic sensitivity, with an otherwise identical, uniformly poled detector, J15. We measured the relative acoustic frequency response by using a loudspeaker located 45 mm away from the detector aperture and facing it. The loudspeaker output was coupled to the pyroelectric detector through the surrounding air. The pyroelectric detector output was sampled and recorded over the frequency range of 5–100 Hz with a lock-in amplifier. The results are shown in Fig. 5. We were interested in low-frequency responsivity, because the minimum NEP typically is found at a frequency of less than 100 Hz.[4] Over the chopping frequency range of interest the responsivity of the domain-engineered detector was 7–15 dB less than that measured by the uniformly poled detector, for identical measurement conditions.

3. Radiometer Construction

The domain-engineered pyroelectric detector was placed in the radiometer assembly shown in Fig. 6. The detector and the connecting wires were mounted in an aluminum block. This block was attached to the aluminum, electrical-shield housing of the electronics. The output leads of the pyroelectric detector were connected to the current-to-voltage

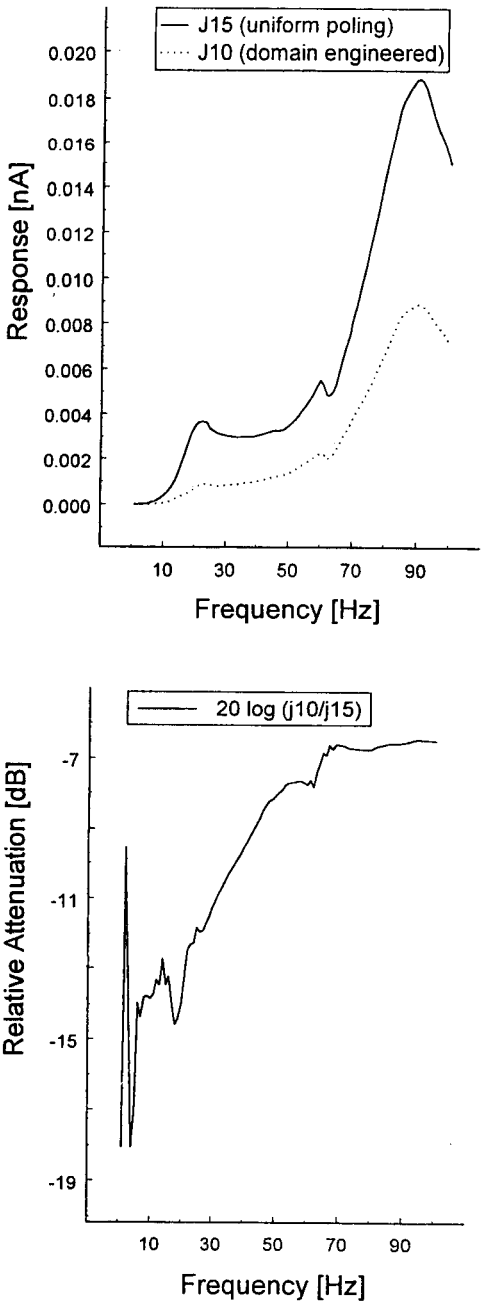

Fig. 5. Acoustic frequency response for two pyroelectric detectors that were identical except for the poling orientation (detector J15, uniform poling; detector J10, domain engineered).

converter input. To avoid 60-Hz pickup, the housing of the electronics and the detector block were continuously grounded. To avoid ground loops, the signal common and the shield were connected only at the 0-V output of the ±15-V power supply. A thermistor was mounted inside a copper plate with good thermal contact to the detector to monitor the detector temperature.[5]

We use a custom-made current-to-voltage converter (current preamplifier) along with a commercially available lock-in amplifier and chopper to obtain a usable signal from the pyroelectric detector.

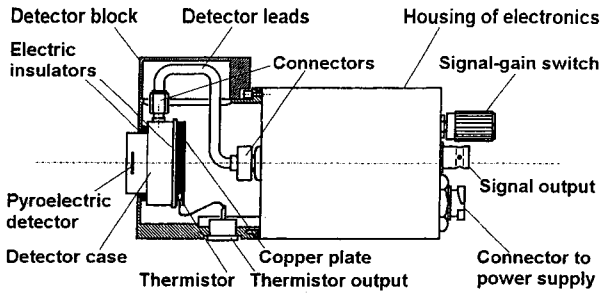

Fig. 6. Radiometer construction incorporating the domain-engineered pyroelectric, j10.

This is a common approach with pyroelectric detectors. However, there are many subtleties in designing and using the current-to-voltage converter to optimize the detector performance.

The equivalent circuit for any pyroelectric detector is modeled as a current generator along with a resistor and a capacitor, electrically connected in parallel. The current-to-voltage converter was used to measure the short-circuit current from the pyroelectric detector signal electrode. Connecting external capacitors, parallel to the feedback resistors of the converter, optimized the signal- and loop-gain requirements. The signal roll-off frequencies were tuned to a range between 100 and 1000 Hz. Optimization of the converter-voltage gain-versus-frequency curve was not necessary, because the dominant noise was the current noise of the pyroelectric detector. Consequently, selection of operational amplifiers for the converter was not a critical issue.

To avoid signal distortion, including amplitude decrease and signal phase shift, the signal shape of the output voltage must be similar to the shape of the chopped optical signal. To achieve this similarity, the fundamental gains of the photocurrent meter (including the detector and the converter) must be optimized at the signal frequencies.[6] The signal gains should be frequency independent (flat) around the signal (chopping) frequency to avoid signal-gain instabilities. To achieve this requirement, the 3-dB roll-off frequencies of the signal-gain characteristics were tuned 1 decade higher than the chopping frequency. Also, the chopping frequency was selected low. For the highest feedback resistor, the stray capacitance produced a relatively low signal roll-off frequency. It was necessary to carefully connect the feedback components of the converter to keep the stray capacitance low and the 3-dB roll-off signal frequency high. The 3-dB points should not be much more than 1 decade higher than the signal frequency, especially at low signal-gain ranges; otherwise the loop-gain at the chopping frequency can be too small, resulting in low-accuracy current-to-voltage conversion.

All of our electronic and radiometric tests were made with an ac data-acquisition system.[7] The voltage output of the pyroelectric radiometer was attached to the input of a dual-phase, sine-wave

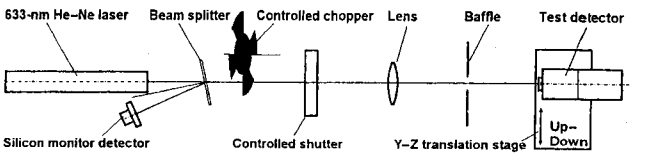

Fig. 7. Arrangement for frequency-response and spatial-response uniformity measurements.

measuring lock-in amplifier. The in-phase- and the quadrature-analog lock-in outputs were recorded by two simultaneously triggered digital voltmeters (DVM's) that served as analog-to-digital converters for the lock-in. These two DVM output channels (X and Y) are summed in quadrature digitally by the computer to extract the signal magnitude. Low-pass filtering of the analog signals is achieved by the integrating-time constants of the averaging times of both the lock-in outputs and the DVM's. In our measurements the lock-in output time constant was set to 333 ms. The DVM's were always operated with an averaging time of 100 power-line cycles.

4. Measurements

The frequency-dependent response of the radiometer was tested with the optical arrangement shown in Fig. 7. The primary beam from a He–Ne laser was chopped with a mechanical chopper and focused onto the pyroelectric detector with a plano–convex lens. The monitoring beam was reflected with a beam splitter and directed to underfill a silicon-monitor detector. The pyroelectric-detector signal was corrected with the monitor-detector signal to compensate for optical power fluctuations in the primary beam. A shutter and baffle minimized uncertainties due to stray radiation.

Figure 8 shows the gain-versus-frequency characteristics of the domain-engineered pyroelectric detector for the two highest signal-gain selections. Both curves were normalized to the zero-signal frequency. Two signal-gain ranges, 10^9 and 10^8 V/A, were the only ranges for which no external compensating capacitors were needed. The 3-dB roll-off point was 61

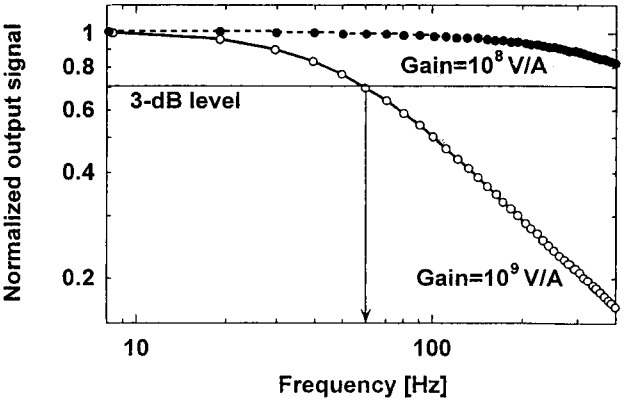

Fig. 8. Measured signal gain-versus-frequency curves of the domain-engineered pyroelectric radiometer.

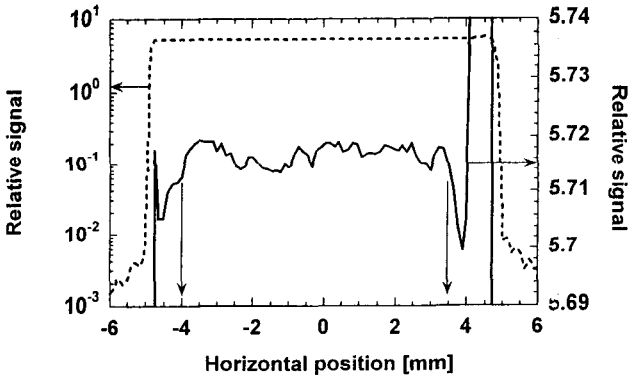

Fig. 9. Horizontal spatial-response scan of the pyroelectric radiometer.

Hz for the 10^9 V/A gain and 570 Hz for the 10^8 V/A gain. Figure 8 also shows that the signal-amplitude attenuation will be negligible even at the highest signal gain (10^9 V/A) if a sufficiently low chopping frequency is selected, in this case, 8–10 Hz.

The spatial-response uniformity of the pyroelectric detector was measured along two perpendicular axes across the center of the detector. The spot diameter of the probe beam on the detector was less than 0.5 mm. The horizontal- and the vertical-response scans are shown in Figs. 9 and 10. The graphs show that the spatial-response changes are 0.3% (maximum to minimum) across a properly positioned 7.5-mm-diameter aperture. With this aperture the standard deviation, calculated from the scanned points, was 0.03% for the horizontal and 0.09% for the vertical diameters. These uncertainties will be decreased if larger beam spots are used and positioned systematically at the center of the aperture. The response increase at the edges was caused by the reflected (converging) beam from the shiny housing around the detector.

The radiant-power response and the noise floor were measured with a mechanically chopped, 633-nm-wavelength laser beam for optical input. Neutral-density filters were used to attenuate the laser power at seven levels ranging from 624 μW to 1.7 nW. The chopper was positioned close to the

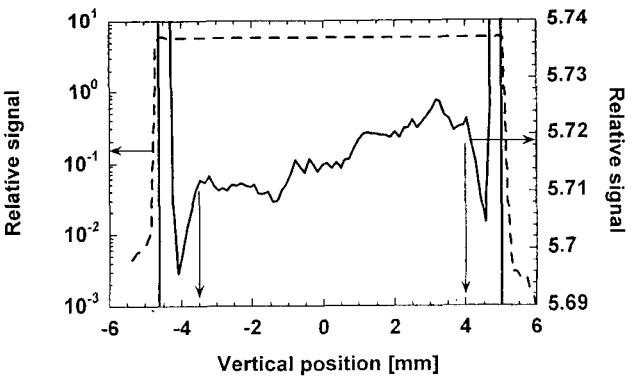

Fig. 10. Vertical spatial-response scan of the pyroelectric radiometer.

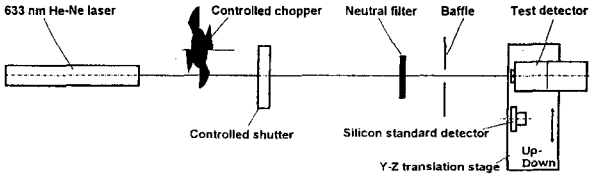

Fig. 11. Arrangement of the pyroelectric radiometer response and noise measurements.

laser to minimize detection of frequency-modulated stray radiation. Also, a baffle was located close to the detector to keep the field of view for the chopped radiation small. The reference for the power response and the response nonlinearity of the pyroelectric detector was a silicon photodiode with an area of 1 cm^2. During the test the pyroelectric detector position was alternated with the reference silicon photodiode position. The optical arrangement of the measurements is shown in Fig. 11.

The radiant-power response and the noise-floor measurements were used to calculate the detector's NEP at each radiant power. In nearly each case the power measurement was followed by a dark measurement. The difference between the power and the dark measurements was equal to the signal. The photocurrent-to-voltage gain for the pyroelectric detector preamplifier was 10^9 A/V, and the chopping frequency was 10 Hz. A pyroelectric detector response of 0.1045 μA/W was measured at 578-μW laser power.

For high signal-to-noise ratios the signal was calculated and averaged from approximately twenty samples. When the signal-to-noise ratio was low, the noise in the X and the Y channels was rectified, resulting in residual output offset. To avoid the output offset, the signal was calculated differently. Instead of subtracting a dark measurement result from the corresponding power measurement result, we made the averages separately for both the power and the dark values of the X and the Y channels. Thereafter, the difference of the average-dark measurement and the average-power measurement was calculated with the vectorial sum process.

We calculated the NEP values shown in Fig. 12

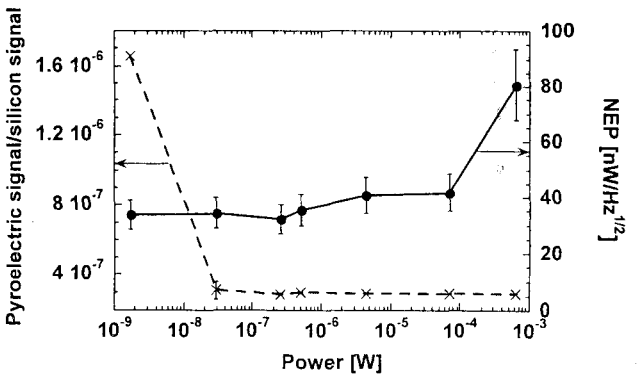

Fig. 12. Response linearity and NEP of the domain-engineered pyroelectric radiometer versus radiant power.

from the standard deviations of the power readings by evaluating the quadrature sum of the X and the Y output readings. The dark measurements were not used, to avoid the quadrature sum of the two noise readings.

Figure 12 shows that the NEP was flat from 1.7 nW to ~0.1 mW (solid curve) and is equal to ~38 nW/$Hz^{1/2}$. At high radiant power the measured NEP was twice the low-level NEP, probably because of additional noise sources, such as laser noise, in the measurement system. The relative uncertainty ($k = 1$) of the NEP determinations (calculated from 20 measurements) was 16%.[8] The results suggest that it is enough to measure NEP at one signal level, which can be in the dark. The typical dark NEP, measured separately (not shown in the figure), was 32 nW/$Hz^{1/2}$.

Figure 12 also shows the pyroelectric detector response linearity compared with a previously characterized silicon photodiode.[9] The ratio of the pyroelectric detector signal to the silicon detector signal (left-hand axis in Fig. 12) shows linear detector responsivity over 6 decades. The outlying point is caused by the poor signal-to-noise ratio of the pyroelectric detector at the low-power end. Here the uncertainty is 2.6 times larger than the measured ratio. This large error bar is not shown in the graph. The error bars (the uncertainties calculated from the relative standard uncertainties of the measured ratios) are shown for all the other ratios. At 29 nW the error bar can be seen well. At higher power the error bars are too small to be seen on the graph.

The ultimate check of our NEP measurements is practical and somewhat qualitative. Pyroelectric detectors are notoriously sensitive to ambient noise ranging from fan motors to slamming doors and other laboratory equipment. We measured the noise levels under various conditions. The radiometer was wrapped with insulation foam and situated in different locations on the detector stage when the servomotor (which moves the stage) was on and off. Identical tests were also performed without the insulation foam and in other locations in the lab. The NEP did not show any significant change during the tests. The NEP for other types of pyroelectric detectors varied by a factor of nearly 10, during similar tests.

In 1975 Byer described a complementary domain-engineered pyroelectric detector with reduced sensitivity to temperature changes. He also suggested that a domain-engineered detector with equally and oppositely poled areas within a single crystal should have a response completely independent of ambient temperature fluctuations. However, his results do not indicate that complete independence is achievable, nor do ours.[10] This is perhaps an area for future study, because $LiNbO_3$ (and $LiTaO_3$) pyroelectric detectors have a strong ambient temperature dependence, which is undesirable for highly accurate radiometers. For now, we are satisfied with slightly reduced temperature dependence in the domain-engineered pyroelectric detector and rely on correction factors, or active thermal stabilization, to ensure that the radiometer response is independent of ambient temperature fluctuations.

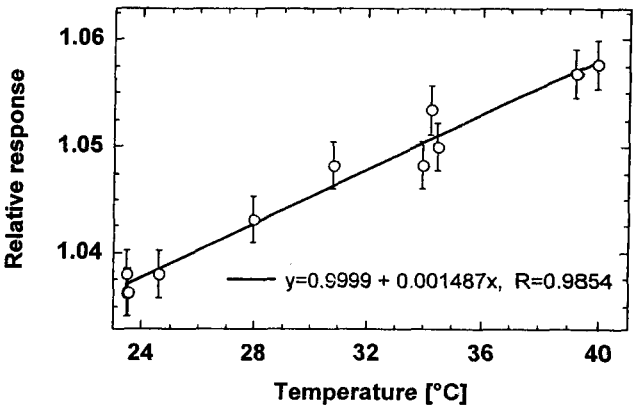

Fig. 13. Domain-engineered pyroelectric radiometer, relative response versus temperature.

The temperature-dependent response of the pyroelectric detector was tested to determine the response correction factors for a range of ambient temperatures. During the test the 633-nm laser beam, incident on the detector, was stabilized. An insulated-electric heater was attached to the outside surface of the detector package. The temperature was increased slowly from 23.5 to 40 °C. The signal and the temperature outputs were simultaneously recorded during both the heating and the cooling cycles at several different temperatures. The relative response-versus-temperature curve is shown in Fig. 13. A response temperature coefficient of 0.15%/°C was obtained from a linear fit to the measured data points. The error bars represent a 0.25% uncertainty (coverage factor, $k = 1$) for the measured values. From the data shown in Fig. 13, the relationship for the response of the pyroelectric detector at a calibration temperature T_c is R_c. The response at a different measurement temperature T_m will be

$$R_m = R_c f. \tag{3}$$

The response correction factor may be used where $f = 1 + (\Delta T \times C_T)$, $\Delta T = T_c - T_m$, and the response temperature coefficient is $C_T = 0.0015$.

Pyroelectric materials are inherently spectrally flat over a broad wavelength range.[11] Therefore the spectral responsivity of a pyroelectric detector is dependent on the reflectance of the face electrodes and other materials placed on the detector surface to efficiently convert optical energy into thermal energy. The advantages and disadvantages of commercially available optical coatings have been well documented.[12] Though easily damaged by the slightest touch, or excessive heat (greater than 200 mW/cm^2), gold black is our absorber of choice.

Published data show that gold-black coatings diffusely reflect less than 1% of incident radiation, over a spectral range from the ultraviolet to 15 μm.[13] We

have been unable reproduce these results on a material that has a small thermal mass and that is a poor heat conductor (such as a small $LiNbO_3$ plate). At shorter wavelengths, such as 633 nm, reflectance from the gold-black coating is diffuse and small.[14] From 2.5 to 10 μm, the reflectance gradually becomes more nearly specular and gradually increases to as much as 15%.

The absorptance of the gold-black coating determines the relative spectral responsivity, provided that the transmission through the detector is negligible and the reflectance is low. Then the relative spectral response of the detector can be determined from a spectral-reflectance measurement, if we assume that the gold-black transmittance is negligible and the relative detector response is proportional to 1 minus the measured reflectance.

The spectral reflectance was compared with a white polytetraflouroethylene (PTFE) reflectance standard. An oval beam, oriented at a 6° angle of incidence over the wavelength range 0.8 and 1.8 μm, made an 8 mm × 6 mm image at the detector. The 10-mm-diameter aperture of the detector was removed to avoid baffling. A 20-cm-diameter integrating sphere collected the diffuse radiation reflected back from the detector surface.

The measured signal from radiation reflected from the white-PTFE standard was used as the value for the 100% reflectance. Zero reflectance was recorded with a light trap, which replaced the detector at the sample port of the sphere. Ten wavelength scans were made in each measurement mode to improve the poor signal-to-noise ratio. The diffuse spectral reflectance of the detector was calculated from the averages of the ten measured reflectance values. The reflectance ρ at wavelength λ was calculated with

$$\rho(\lambda) = \frac{A_d(\lambda) - A_t(\lambda)}{A_s(\lambda) - A_t(\lambda)}. \tag{4}$$

In this expression, $A_s(\lambda)$ is the average signal of the white standard spectral-reflectance measurements, $A_d(\lambda)$ is the average signal of the detector spectral-reflectance measurements, and $A_t(\lambda)$ is the average signal of the light trap spectral-reflectance measurements.

Figure 14 shows the average reflectance, and standard uncertainty versus wavelength. We improved the signal-to-noise ratio of approximately 5:1 of the reflectance measurements by a factor of nearly 2 by averaging the measurement results of five neighboring wavelengths. A second-order polynomial fit to the calculated reflectance. The figure shows a spectral reflectance of 0.5–0.7% between 0.8 and 1.8 μm. This corresponds to a detector response change of 0.2% in this spectral range. Overall, the absolute reflectance from the gold black was low (less than 1%).

The angular response change of the detector was first measured in power measurement mode in which the detector aperture was underfilled by a 3-mm-diameter, He–Ne (633-nm) laser beam. Thereafter,

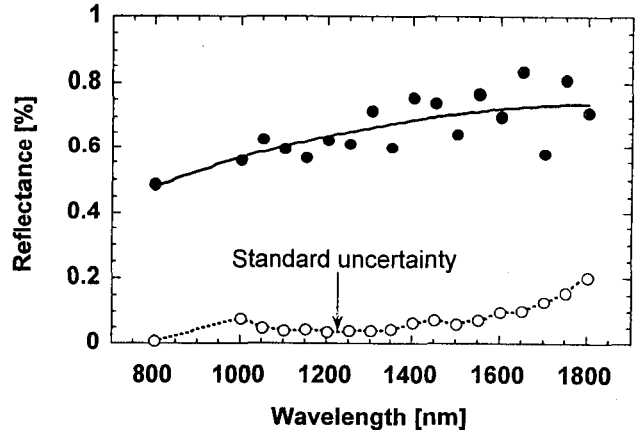

Fig. 14. Domain-engineered pyroelectric detector total reflectance and measurement standard uncertainty versus wavelength. Solid curve, polynomial fit to the averaged reflectance data.

the angular response was measured in irradiance mode in which the detector aperture was overfilled with a halogen lamp beam. For both measurement modes the aperture was circular and 8 mm in diameter. Figure 15 shows the optical arrangement for these tests. The detector was positioned a distance, D, 0.9 m from the laser and 0.55 m from the halogen lamp. The detector reflectance was then evaluated by rotation of the detector, incremental values of angle ϵ, relative to the optical axis, up and down (ϕ = 90°, $\epsilon = \pm 40°$), and side to side (ϕ = 0°, $\epsilon = \pm 40°$).

The directional error in underfilled mode was calculated as

$$f_2'(\epsilon, \phi) = \frac{E_r(\epsilon, \phi)}{E_r(\epsilon = 0°)} - 1, \tag{5}$$

where $E_r(\epsilon, \phi)$ and $E_r(\epsilon = 0°)$ were the detector readings for the incident radiation, E, arriving at incidence angles of ϵ and 0°. This definition is similar to the Commission Internationale de l'Eclairage (CIE) recommended directional error f_2 (ϵ, ϕ).[14]

Figure 16 shows the directional error, $f_2'(\epsilon)$, at a detector orientation of ϕ = 90°. The results of the horizontal (ϕ = 90°) and the vertical (ϕ = 0°) scans were very similar to each other. The response change was less than the measurement uncertainty in the range $\epsilon = \pm 11°$ and increased to ~0.1% at ϵ =

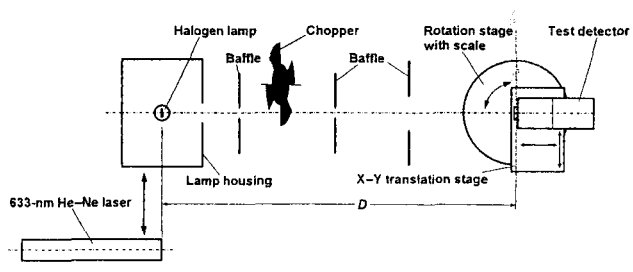

Fig. 15. Arrangement of the angular response measurements. The laser is used in underfilled mode, and the lamp is used in overfilled mode.

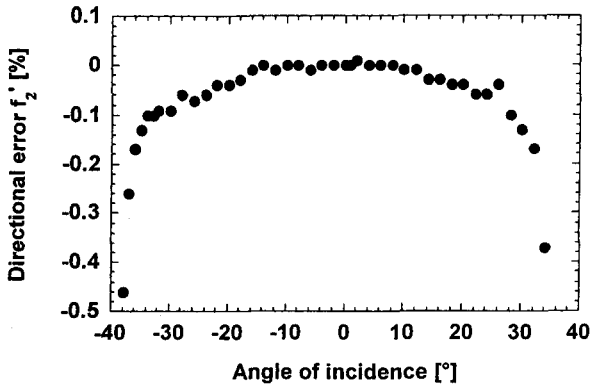

Fig. 16. Directional (relative angular) error of the pyroelectric detector in the vertical plane versus incidence angle. The incident laser radiation underfilled the detector aperture.

$\pm 30°$. The relative uncertainty ($k = 1$) of the directional error determinations was 0.04%.

The directional error in the overfilled-measurement mode was calculated according to the CIE recommendation, with the expression

$$f_2(\epsilon, \phi) = \frac{E_r(\epsilon, \phi)}{E_r(\epsilon = 0°)\cos \epsilon} - 1, \qquad (6)$$

where the denominator is the cosine response of an ideal detector-irradiance measurement.[15]

The measurement results of the horizontal-detector scan are shown in Fig. 17. According to the graph the angular response of the pyroelectric irradiance meter follows the cosine function, with a directional error of less than 0.1% within a $f/2$ field of view (31° full angle). The $\epsilon = 2°$ angular offset was caused by the asymmetric detector alignment on the rotation stage. The relative uncertainty of the directional error determinations in the irradiance measurement mode was 0.06% (coverage factor $k = 1$).

Comparison of the available detector candidates for infrared radiometric applications would constitute a paper in itself, but there are several key performance issues on which we can focus to abbreviate our discussion. In general, the uncertainty in radiometric measurements is reduced when detector variables such as response linearity, spatial and spectral uniformity, and temperature dependence are well characterized or known to be invariable.

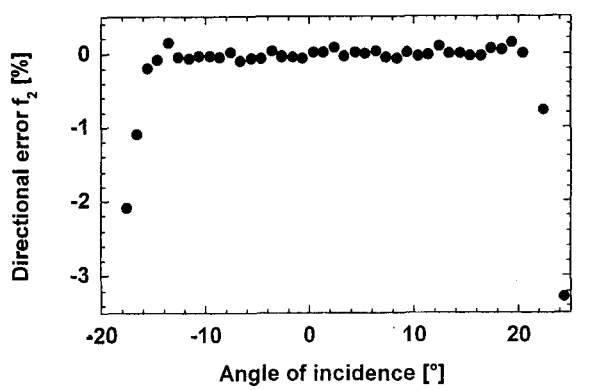

Fig. 17. Directional (relative angular) error of the pyroelectric detector in the horizontal plane versus incidence angle. The incident lamp radiation overfilled the detector aperture.

Table 1. Summary of Radiometer Properties

Property	Value
Power response at 633 nm	1.05×10^{-7} A/W
Temperature coefficient between 24 and 40 °C	0.15%/°C
Dark NEP	32 nW/Hz$^{1/2}$
NEP in the 1-nW–100-μW input radiant power range	38 nW/Hz$^{1/2}$
3-dB point with the OPA111 I-V converter in the 10^8-V/A range	570 Hz
3-dB point with the OPA111 I-V converter in the 10^9-V/A range	60.5 Hz
Spatial response nonuniformity within a 7.5-mm-diameter (633-nm, 0.5 mm-diameter) probe beam	±0.1%
Angular error in underfilled mode for $\epsilon \leq 30°$ incident angles	$f_2(\epsilon) < 0.1\%$
Angular error with 8-mm overfilled aperture for $\epsilon \leq 15°$	CIE $f_2(\epsilon) < 0.1\%$
Spectral reflectance variation (800–1800 nm)	<0.2%

The biggest drawbacks to using a pyroelectric detector are low optical sensitivity, high acoustic sensitivity, and the need to use an optical chopper. However, pyroelectric detectors can be operated at room temperature, and the chopper and the necessary electronics are not much more cumbersome than what is necessary for the competing alternatives. Photoconductors, such as mercury cadmium telluride (HgCdTe) and indium antimonide (InSb), have high sensitivity and are commonly used for transfer standards, but large-area (3–5-mm-diameter) devices are not highly uniform spatially and spectrally. The best photoconductors of this type have spatial nonuniformity variations as great as 3% and commonly to as great as 20% or more.[16] On this basis alone a pyroelectric detector with nearly four times the area (compared with the competing alternatives) and with 0.1% spatial-response variation is an excellent choice. In addition, we have demonstrated that domain-engineering techniques can reduce the acoustic sensitivity and give us confidence that the NEP is constant and linear at low power.

A summary of the properties of the domain-engineered pyroelectric radiometer is given in Table 1. Future improvements will be directed at reducing the temperature dependence and optimizing the domain-engineered areas and pattern, to further reduce the acoustic sensitivity. Further evaluation will include spectral responsivity and reflectance measurements at longer infrared wavelengths between 2 and 20 μm.

5. Conclusions

We have successfully used domain engineering to build a practical and convenient pyroelectric radi-

ometer with low acoustic sensitivity and high spatial and spectral response uniformity. We have demonstrated that a properly designed, applied, and characterized pyroelectric radiometer is well suited as a high-accuracy transfer standard for optical power and irradiance measurements. The domain-engineered pyroelectric radiometer is the only alternative compared with HgCdTe, InSb photoconductors, or commercially available pyroelectric detectors, capable of measurement uncertainty of the order of 0.1%. The primary role of the radiometer will be to extend and improve the National Institute of Standards and Technology spectral-responsivity scale from the visible to the near-infrared wavelength range.

References

1. J. H. Lehman and J. A. Aust, "Bicell pyroelectric optical detector made from a single $LiNbO_3$ domain-reversed electret," Appl. Opt. **37,** 4210–4212 (1998).
2. W. R. Blevin and W. J. Brown, "Black coatings for absolute radiometers," Metrologia **2,** 139–143 (1996).
3. L. Harris, R. McGinnies, and B. M. Siegel, "The preparation and optical properties of gold blacks, "J. Opt. Soc. Am. **38,** 582–589 (1948).
4. E. L. Dereniak and D. G. Crowe, *Optical Radiation Detectors* (Wiley, New York, 1984), p. 177.
5. G. Eppeldauer, "Temperature monitored/controlled silicon photodiodes for standardization," in *Advanced Fiber Communications Technologies*, L. G. Kazovsky, ed., Commission Internationale de l'Éclairage, Proc. SPIE **1479,** 71–77 (1991).
6. G. Eppeldauer, "Chopped radiation measurements with large area Si photodiodes," J. Res. Natl. Inst. Stand. Technol. **103,** 153–162 (1998).
7. A. L. Migdall and G. P. Eppeldauer, *Spectroradiometric Detector Measurements: III. Infrared Detectors*, Natl. Inst. Stand. Technol. Spec. Publ. 250–42 (National Institute of Standards and Technology Measurement Services, Gaithersburg, Md., 1998).
8. L. Lyons, *A Practical Guide to Data Analysis for Physical Science Students* (Cambridge U. Press, Cambridge, UK, 1991), p. 15.
9. T. C. Larason, S. S. Bruce, and A. C. Parr, *Spectroradiometric Detector Measurements: I. Ultraviolet Detectors and II. Visible to Near-Infrared Detectors*, Natl. Inst. Stand. Technol. Spec. Publ. 250–41 (National Institute of Standards and Technology Measurement Services, Gaithersburg, Md., 1998).
10. N. E. Byer, S. E. Stokowski, and J. D. Venables, "Complementary domain pyroelectric detectors with reduced sensitivity to mechanical vibrations and temperature changes," Appl. Phys. Lett. **27,** 639–641 (1975).
11. S. B. Lang, *Sourcebook of Pyroelectricity* (Gordon & Breach, New York, 1974), 40–48.
12. W. L. Wolfe and G. J. Zissis, *The Infrared Handbook* (Environmental Research Institute of Michigan, Ann Arbor, Mich., 1989), p. 7–79.
13. D. J. Advena, V. T. Bly, and J. T. Cox, "Deposition and characterization of far-infrared absorbing gold black films," Appl. Opt. **32,** 1136–1144 (1993).
14. G. W. Day, C. A. Hamilton, and K. W. Pyatt, "Spectral reference detector for the visible to 12-μm region; convenient, spectrally flat," Appl. Opt. **15,** 1865–1868 (1976).
15. Central Bureau of the Commission Internationale de L'Éclairage, *Methods of Characterizing the Performance of Radiometers and Photometers*, CIE Publications, 53 (TC-2.2) (Central Bureau of the Commission Internationale de L'Éclairage, Vienna, Austria, 1982).
16. E. Theocharous, N. P. Fox, and T. R. Prior, "A comparison of the performance of infrared detectors for radiometric applications, in *Optical Radiation Measurements III*, J. M. Palmer, ed., Proc. SPIE **2815,** 56–68 (1996).

The American Society of Mechanical Engineers

Reprinted From
HTD-Vol. 277, Thermal Phenomena at Molecular and in Cryogenic Infrared Detectors
Editors: M. Kaviany, D. A. Kaminski, A. Majumdar, P. E. Phelan, M. M. Yovanovich, and Z. M. Zhang
Book No. H00908 – 1994

A CRYOGENIC SILICON RESISTANCE BOLOMETER FOR USE AS AN INFRARED TRANSFER STANDARD DETECTOR

G. Eppeldauer, A. L. Migdall, and C. L. Cromer
Radiometric Physics Division
National Institute of Standards and Technology
Gaithersburg, Maryland

ABSTRACT

We are developing an infrared bolometer to meet the needs of two detector calibration facilities at the National Institute of Standards and Technology (NIST). These facilities require transfer standard detectors with high sensitivity, accuracy, stability and dynamic range as well as a large detector area, fast time response and flat spectral response. We describe the design and testing of a bolometer to meet these requirements. This device has a dynamic range of 5 decades, a noise floor of 36 pW/√Hz, a nonlinearity of less than 1%, a spatial response nonuniformity of about 0.3% and a flat frequency response out to about 100 Hz.

1 INTRODUCTION

Absolute calibrations of infrared (IR) detectors are of increasing importance. In general, detector calibrations are made absolute by comparison to a primary standard detector, which is internally calibrated, or to a transfer standard detector that has itself been tied to some primary standard. Two specific needs currently exist at the National Institute of Standards and Technology (NIST) for absolute calibrations that require the use of transfer standard detectors. An ambient temperature facility for the calibration of IR detectors is under development. Additionally, new spectral capability is being added to the Low Background Infrared Facility (LBIR) at NIST which is used for the calibration of cryogenic detectors and sources. Both of these facilities require transfer detectors with high sensitivity, accuracy, and dynamic range as well as a large detector area, fast time response and flat spectral response. The goal of this work is the development of a transfer standard detector in the 2 to 20 μm spectral region for use in these two applications.

2 BOLOMETER DESIGN

The detector requirements of our two applications, particularly the wide dynamic range and flat spectral response, match best the characteristics of cryogenic bolometers. Since we also require a sensitive area of about 4 mm diameter, we chose a bolometer of composite design. This allows for a larger detector area while maintaining the detector speed, by using a large, thin, low heat capacity absorber bonded to a small thermal sensor. The dynamic range requirement of the bolometer is determined by two factors. The bolometer must be able to accept a large enough power to allow it to be calibrated against the NIST's primary standard radiometer which requires ~1 mW to achieve maximum accuracy. The low end of the dynamic range is determined by the two applications for this device, both of which require measurements in the nW to μW range. Since stability is important for standards work and since the response stability of bolometers can be problematic, we have made efforts, which are discussed later, to measure and reduce response variations.

Our transfer standard detector development started with a commercial bolometer [1,2] which we characterized and modified to better meet our requirements. The composite bolometer consists of a sapphire disk (0.05 mm thick by 5 mm diameter) coated with gold black to absorb incident radiation. Gold black was chosen because it has a high absorptance, while its thermal mass is extremely low. The density of gold black has been reported as low as 1/500 that of solid bulk gold (Harris and Beasley, 1992). This allows a much faster detector response than is possible with more common absorbers such as black paint or solid resistive metal films. Also, the absorptance of gold black can be greater than 90%, as opposed to the resistive metal films which may absorb up to only 50% of the incident radiation.

The temperature rise due to absorbed radiation is sensed by a silicon resistance thermometer (SRT) bonded to the back of the sapphire disk. The SRT is a doped Si chip that is commonly used in both regular (Downey et al., 1984) and composite bolometers (Dereniak and Crowe, 1984). The resistance of the

SRT depends on both the temperature and the bias current. At 4.2 K the resistance of our SRT changed from 3.6 to 1 MΩ as the DC bias current was changed from 0 to 3.5 μA (Eppeldauer et al., 1993).

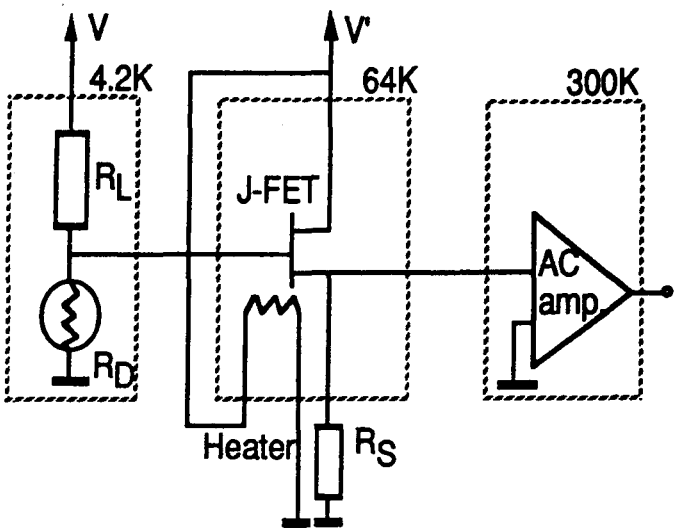

Fig. 1 SRT biasing circuit and amplifier. R_D is the SRT resistance, R_L is the current limiting resistor and R_S is the JFET source resistor. The temperatures of each section is indicated.

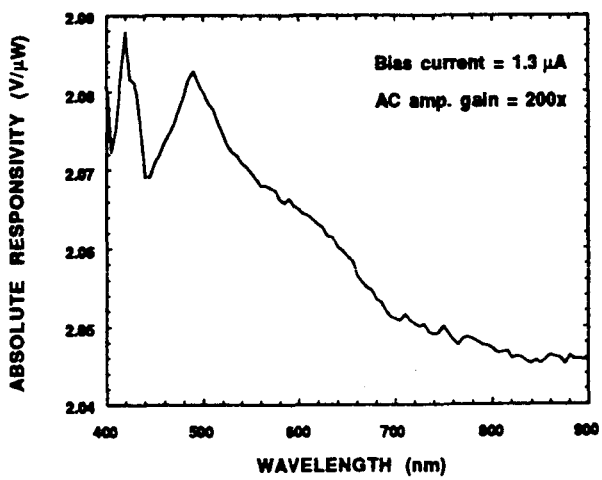

Fig. 2 Visible spectral response of the first bolometer as determined by comparison to the NIST absolute spectral response scale. The estimated 1σ uncertainty of the spectral response measurement is 0.2 %.

The SRT resistance change is measured using a unity gain Junction Field Effect Transistor (JFET) [3] followed by a selectable gain AC amplifier. The DC bias circuit of the SRT composite bolometer is shown on Fig. 1. The JFET stage is a unity gain impedance transformer between the high resistance (R_D=2.3 MΩ, R_L=10 MΩ) SRT circuit and the AC amplifier. The JFET is located in the cryogenic space near the bolometer and operates at about 64 K. The JFET's dominant noise comes from its inverse transconductance (resistor noise). Since the transconductance rises with increasing drain current, R_S should be small, but because at large drain currents the offset voltage drift, the common mode rejection, and the voltage gain stability are worse, a compromise was necessary, so R_S=10 kΩ was chosen.

3 BOLOMETER CHARACTERIZATION

The first version of our SRT composite bolometer had a flat frequency response (for chopped radiation) up to 111 Hz and a 3 dB rolloff point of 250 Hz. The responsivity was 10^4 V/W at a SRT bias current of 1.3 μA. At the nominal operating point the SRT resistance is about 2 MΩ and the electrical power dissipated in the bolometer is ~2 μW. The spectral response of the bolometer presented a problem. The spectral absorptance of the original gold black coating was found to vary a few percent in the visible and to fall to as low as 30% in the IR. Figure 2 shows the absolute peak-to-peak spectral response of the bolometer at an AC amplifier gain of 200, as calibrated against the NIST absolute spectral response scale between 400 and 900 nm (Cromer, 1991). The response variation across this range is 2%, which is significantly larger than the 1σ uncertainty of the scale realization which is 0.3% between 400 nm and 440 nm and 0.1% between 440 nm and 900 nm. Figure 3 shows Fourier Transform Infrared Spectrometer (FTIR) measurements of the total reflectance of two different gold black coatings. The reflectance of the first bolometer coating rises from less than 10% at 2 μm to greater than 70% at 14 μm. Since we intend to use this bolometer out to 20 μm we made additional specular reflectance measurements on another FTIR instrument capable of measuring up to 25 μm. Those results show that the reflectance peaks at 16.5 μm and falls toward a local minimum at 20 μm. These wide variations required us to work toward improved coatings.

The variation of response across the surface of the bolometer was checked at 900, 1200, and 1550 nm with a scan resolution of 1.1 mm. The measured variations were smaller than 0.3% over the entire 10 mm^2 aperture area.

We measured the signal and noise levels of the first bolometer with a KRS-5 window at a chop frequency of 57 Hz. The signal to noise ratio was $2x10^4$ at an incident radiant power of 7 μW. The incident power was equal to the noise floor at 20 pW with an electrical measurement bandwidth of 0.3 Hz (Eppeldauer and Hardis, 1991). We estimate the bolometer's

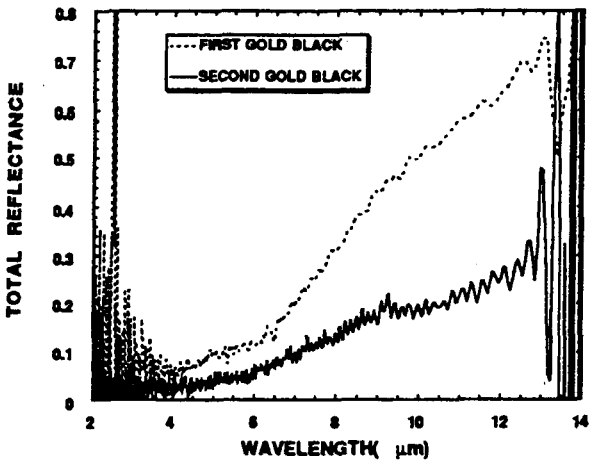

Fig. 3 Total (specular + diffuse) spectral reflectance of the first and second bolometers in the 2 to 14 μm spectral range.

minimum detectable temperature difference to be about 1 μK/√Hz from the 36 pW/√Hz noise density and the ~50 μW/K thermal conductance of the SRT leads. The bolometer dynamic range at the low power end was limited by fluctuations in the thermal background. This noise was reduced to 4 pW/√Hz when a large spherical gold mirror was placed in front of the bolometer window to image the cold bolometer absorber back on to itself (Makai and Andor, 1993). This noise is close to, but greater than, the calculated rms resistance noise of 2.2 pW/√Hz, due to the Johnson noise of R_D and R_L, scaled by the bolometer responsivity. The effective rms input noise of the AC amplifier was determined to be 1.4 pW/√Hz (using a responsivity of 10^4 V/W) which is also less than the calculated bolometer noise.

If we assume that the window passes all ambient background radiation below 100 μm, the calculated total radiant power within the f/4 field of view and incident on the bolometer is ~260 μW with fluctuations of 1.7 pW/√Hz due to shot noise (Boyd, 1983). It is not too surprising that the observed background effect is larger, as there was no attempt to control variations of the room temperature or atmospheric humidity. Note that noise observed with the bolometer looking into the room was measured only at 57 Hz with a 0.3 Hz bandwidth, so no information on the spectral variation of this noise was taken.

4 IMPROVEMENTS TO THE SILICON COMPOSITE BOLOMETER

Changes were made to improve the overall convenience of the bolometer, as well as its accuracy. There was a monotonic decrease in the bolometer responsivity after 11 hours, probably due to degradation of the dewar vacuum. Above 1.33×10^{-2} Pa (10^{-4} Torr), the poor vacuum affects the temperature of the cold plate on which the detector is mounted (Lange et al., 1983). To maintain good stability, the dewar had to be repumped every third day. During a 24 hour run, we found a period of 11 hours where the bolometer responsivity was constant to about ±0.25% (Eppeldauer et al., 1993). We suspect that the variations before and after this stable period is due to temperature variations of the cold plate and bolometer mount. The design of a new dewar with improved vacuum characteristics, temperature sensing and temperature stabilization has also been started. A carbon resistor has been added to the detector mount of the current bolometer to monitor its temperature variation.

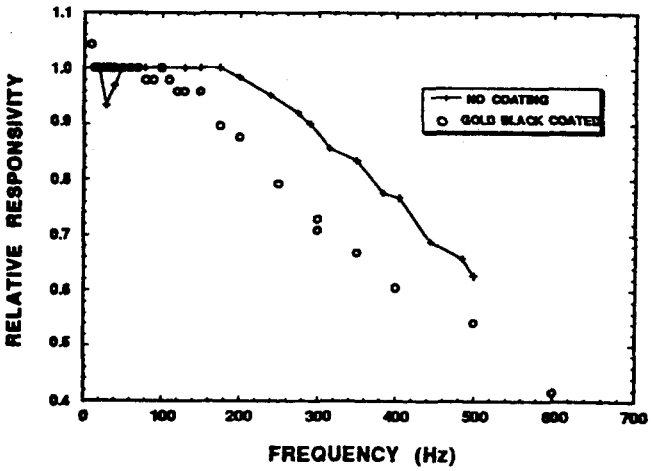

Fig. 4 Frequency response of bolometer before and after coating with gold black.

Because the first gold black coating showed high reflectivity in the IR, an improved second gold black coating was produced on a new sapphire absorber. A literature search indicated that a very low density gold black with a thickness of about 20 μm is required to achieve ~90% absorption in the 2 to 14 μm spectral region (Harris and Beasley, 1952; Harris et al., 1948). This was the goal of the second coating, although our expertise did not allow gold black coatings to be so precisely tailored. The difficulties in reproducing gold black are well noted in the literature (Advena et al., 1993; Harris, 1967). The AC frequency response of this second bolometer was measured before and after coating (see Fig. 4). The additional thermal mass of the coating shifted the 3 dB roll off point of this bolometer from 400 Hz (before coating) to 300 Hz (after coating). This is somewhat faster than the 250 Hz 3 dB point of the original bolometer. The spectral reflectivity of the second bolometer is compared to

the original in Fig. 3. This coating shows significantly lower reflectivity beyond ~6 μm, although it still does not approach the design goal of 90% absorption. More coating development is needed to improve this.

The responsivity of the modified bolometer was calibrated against the NIST absolute spectral response scale. The low frequency responsivity of the bolometer in the visible was 10^4 V/W at a bias current of 1.3 μA (and before the AC amplifer), similar to the responsivity of the first bolometer.

The AC amplifier of the bolometer was also modified to allow for one decade lower gain. This allowed us to extend the point at which high power nonlinearity occurred and to determine whether the nonlinearity is due to the electronics or the sensor itself. We measured the non-linearity by measuring the transmittance of a neutral density filter at different levels of incident laser power (Eppeldauer et al., 1993). We found that the level of incident power where the non-linearity reached ~1% was the same for both the original and the modified amplifiers, although the 4% nonlinearity point in the modified unit occurs at ~3 times higher power (20 μW) (Fig. 5). The nonlinearity rises steeply beyond 1% and 4% nonlinearity points of the original and modified bolometers respectively, indicating amplifer saturation at these points. This test indicates that for incident powers below 20 μW the modified bolometer linearity is limited not by the amplifier, but by the sensor.

Nonlinearity of the bolometer can result from three effects. We assume that any variation of the signal, ($\Delta V_D = \Delta(R_D * I_B)$ where I_B is the bias current and R_D is the bolometer resistance) is due solely to a linear dependence of R_D on temperature. So any variation of I_B or any nonlinear dependence of R_D with temperature will result in a nonlinear response. The measured nonlinearity due to the variation of I_B as a function of incident radiation accounts for only one tenth of the observed 4% nonlinearity. This was determined by measuring the SRT resistance change of 5.4% as the incident laser power varied from 22 μW to zero. The bulk of the nonlinearity was due to the variation of the SRT resistance with bias current and nonlinear temperature dependence of the SRT.

Background radiation variations can also affect the resistance of the SRT. When the background radiation for the bolometer was blocked by a reflective aluminum plate, positioned on its window, a 1 V increase was measured across the SRT. The voltage increase was only 66 mV when the chopped 22 μW laser beam was blocked by a shutter far from the bolometer. This means a 15 times larger R_D change for the aluminum plate caused background change. To keep the bias current constant at large background changes like this, R_L should be increased. Even if the bias current is constant, the

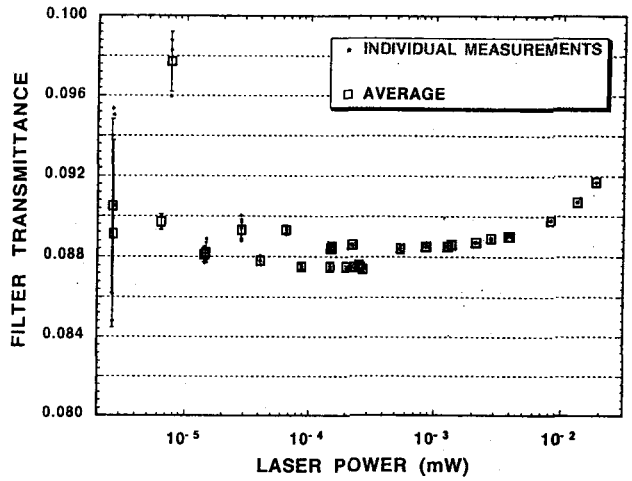

Fig. 5 Measured filter transmittance vs incident laser power with the filter removed using the second version of the bolometer. Deviation of the data from a constant value indicates nonlinearity of the bolometer. Individual measurements and the average of measurements are shown. The error bars are the standard deviations of each group of individual measurements. The apparent shift in transmittance between the two sets of points is due to repositioning the filter rather than measurement nonlinearity.

SRT resistance (and responsivity) still significantly changes for different background levels. Thus, it is important to measure the bolometer responsivity at a range of background levels. Smaller linearity and responsivity errors can be achieved if care is taken to minimize changes in the background radiation and to make R_L as large as necessary.

The dynamic range from the noise floor (with a 1 Hz bandwidth) to the 4% non-linearity point at an incident power level of 20 μW was over 5 decades. This extended high end measurement range is important for our applications as transfer standard detectors. Even with the nonlinearity, the extended range will help in tying the bolometer calibration to the primary standard High Accuracy Cryogenic Radiometer (HACR) of NIST. The signal to noise ratio of a radiometer similar to the HACR was measured to be 1.7×10^4 at an incident power of 200 μW, so we expect that at 20 μW the signal to noise ratio should be at least 1.7×10^3 (Martin et al., 1985). The HACR at NIST (Houston, 1994) has achieved similar signal to noise performance as the radiometer described by Martin et al. (1985). This signal to noise ratio for the HACR at this power level allows a scale transfer significantly better than measurement uncertainties due to the bolometer itself.

In addition to tying the bolometer calibration to the HACR, we will also use the newly acquired spectral capability of the LBIR facility mentioned earlier to independently determine the bolometer spectral response over a continuous range of IR wavelengths. The LBIR facility includes its own high sensitivity electrically calibrated absolute radiometer which has an overall absolute uncertainty of 0.12% (1σ) (Datla et al., 1992). By tying the spectral calibration of the bolometer to this absolute radiometer we will not have to depend on the accuracy of the bolometer coating spectral absorptance measurements.

5 CONCLUSION

We are developing a cryogenic transfer standard detector for use in the infrared wavelength range. This device will be used to tie IR detector calibrations to the nation's primary radiometric detector standard. Our characterization of the bolometer indicates that with the improvements already made and currently planned, we can expect to meet the requirements needed for that purpose.

ACKNOWLEDGEMENTS

We thank T. C. Larason for his help in measuring the absolute response of the bolometer in the visible. We also thank L. M. Hanssen and Z. M. Zhang for their help in measuring the reflectance of the gold black coatings.

REFERENCES

[1] References made in this paper to particular brand names or specific suppliers are for the ease of understanding by the reader and do not constitute an endorsement of products or services by the National Institute of Standards and Technology over other competitive suppliers of similar products or services, which may be equally or better suited for the purpose.

[2] Bolometer Unit #1646 in Dewar HD-3, Infrared Laboratories, Inc., 1808 E. 17th St., Tucson, AZ 85719.

[3] Siliconix family of ultra-low noise JFETs, 2N6484-E230-J230.

Advena, D.J., Bly, V.T., and Cox, J.T., 1993, "Deposition and Characterization of Far-Infrared Absorbing Gold Black Films," *Appl. Opt.*, Vol. 32, pp. 1136-1144.

Boyd, R.W., 1983, *Radiometry and the Detection of Optical Radiation*, John Wiley & Sons, New York, pp. 243.

Cromer, C.L., 1991, "A New Spectral Response Calibration Method Using a Silicon Photodiode Trap Detector," presented at the *1991 Proceedings of Measurement Science Conference*, Anaheim, CA, Jan. 31-Feb. 1.

Datla, R.U., Stock, K., Parr, A.C., Hoyt, C. C., Miller, P.J., and Foukal, P.V., 1992, "Characterization of an Absolute Cryogenic Radiometer as a Standard Detector for Radiant-Power Measurements," *Appl. Opt.*, Vol. 31, pp. 7219-7225.

Dereniak, E.L., and Crowe, D.G., 1984, *Optical Radiation Detectors*, John Wiley & Sons, New York, pp. 156-166.

Downey, P.M., Jeffries, A.D., Meyer, S.S., Weiss, R., Bachner, F.J., Donnelly, J.P., Lindley, W.T., Mountain, R.W, and Silversmith, D.J., 1984, "Monolithic Silicon Bolometers," *Appl. Opt.*, Vol. 23, pp. 910-914.

Eppeldauer, G., and Hardis, J.E., 1991, "Fourteen-Decade Photocurrent Measurements with Large-Area Silicon Photodiodes at Room Temperature," *Appl. Opt.*, Vol. 30, pp. 3091-3099.

Eppeldauer, G., Migdall, A.L., and Cromer, C.L., 1993, "Characterization of a High Sensitivity Composite Silicon Bolometer", *Metrologia*, Vol. 30, pp. 317-320.

Harris, L., 1967, "The Optical Properties of Metal Blacks and Carbon Blacks," The Eppley Foundation for Research, Newport, RI, Monograph Series No. 1, Dec. 1967.

Harris, L., and Beasley, J.K., 1952, "The Infrared Properties of Gold Smoke Deposits," *J. Opt. Soc. Am.*, Vol. 42, pp. 134-140.

Harris, L., McGinnies, R.T., and Siegel, B.M., 1948, "The Preparation and Optical Properties of Gold Blacks," *J. Opt. Soc. Am.*, Vol. 38, pp. 582-589.

Houston, J., 1994, private communication.

Lange, A.E., Kreysa, E., McBride, S.E., Richards, P.L., and Haller, E.E., 1983, "Improved Fabrication Techniques For Infrared Bolometers," *Int. J. IR and Mm Waves*, Vol. 4, pp. 689-706.

Makai, J.P., and Andor, G., 1993, private communication.

Martin, J.E., Fox, N.P., and Key, P.J., 1985, "A Cryogenic Radiometer for Absolute Radiometric Measurements," *Metrologia*, Vol. 21, pp. 147-155.

Linear HgCdTe radiometer

G. Eppeldauer and L. Novak[†]

Radiometric Physics Division, National Institute of Standards and Technology, Gaithersburg, Maryland 20899

ABSTRACT

The basic modes of electrical operation of photoconductive optical radiation detectors are analyzed. The nonlinearity inherent in "voltage mode" measurements can be eliminated by using "current mode" measurements. A HgCdTe photoconductive radiometer has been designed, based on this analysis, which measures the current through a biased detector. A built-in calibrating capability in the circuits of the radiometer makes it possible to eliminate the effects of a long-term drift in the bias voltage, thereby achieving a higher precision.

1. INTRODUCTION

Photoconductors exhibit a change in conductance (the inverse of resistance) when radiant power is applied to them. In order to sense the photogenerated conductance change, the photoconductor is operated with a bias current. A traditional biasing circuit[1] consists of a DC source and a load resistor, as shown later in Fig. 1. Manufacturers often recommend measurement of the voltage change across the detector while passing a constant current through it[2-4].

These practices give an output voltage that is a nonlinear function of the conductance change. The conductance change, to a good approximation, is proportional to the incident flux on the detector[5]. In multidecade radiant power measurements, the nonlinear response of the detector circuit introduces unwanted errors. In order to eliminate them, either the nonlinearity has to be electrically compensated using additional circuits[6] or an inherently linear circuit has to be used. The latter solution promises higher accuracy and simpler implementation. Therefore, we proceed to analyze the different ways a photoconductor can be used in a circuit, with a goal of designing a photoconductive radiometer which has an output signal proportional to the conductance change of the detector. This kind of design can be used more accurately for radiometric measurements over a wide dynamic range.

2. MODES OF ELECTRICAL OPERATION

2.1. Voltage mode measurements

A basic photoconductive detector biasing and measuring circuit is shown in Fig. 1. A steady voltage source V_B produces a biasing current I_B through the serially connected detector resistance R_D and load resistance R_L.

$$V_B = I_B (R_L + R_D) \tag{1}$$

The voltage across the load resistance is formed by the bias current,

$$V_L = I_B R_L \tag{2}$$

From Eqs. 1 and 2, V_L depends on the detector resistance R_D as:

$$V_L(R_D) = V_B \frac{R_L}{(R_L + R_D)} \tag{3}$$

As the detector resistance R_D is the reciprocal of its conductance, σ_D,

$$R_D = \frac{1}{\sigma_D} \tag{4}$$

V_L depends upon the conductivity σ_D as:

$$V_L(\sigma_D) = V_B \frac{R_L \sigma_D}{(1 + R_L \sigma_D)} \tag{5}$$

[†] Present Address: Czechoslovak Academy of Sciences, Prague, Czechoslovakia

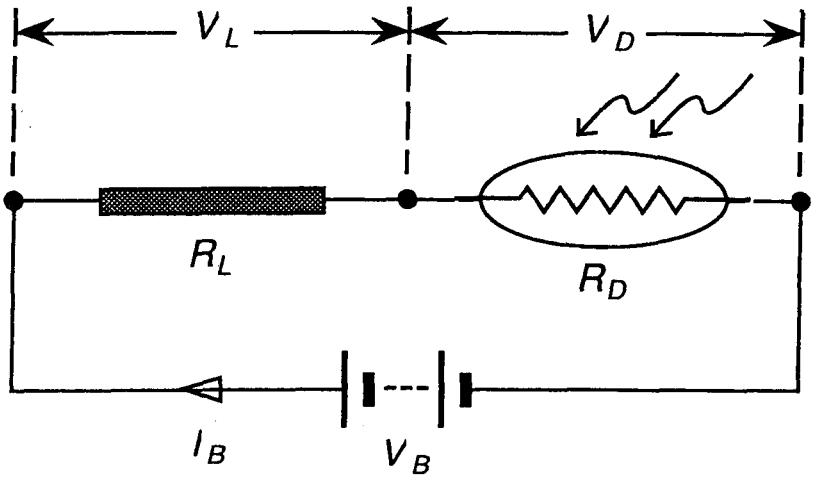

FIGURE 1: Voltage Mode

Eq. 5 shows that the output voltage on the load resistance is a nonlinear function of the detector conductance. Further, the relative magnitudes of R_L and R_D affect the measurement.

$$\text{When } R_L >> R_D, \quad V_L \cong V_B \tag{6}$$

$$\text{When } R_L << R_D, \quad V_L \cong V_B R_L \sigma_D \tag{7}$$

In the first case, the output signal is insensitive to changes in σ_D. In the second, there is a linear approximation at the expense of signal strength ($R_L \sigma_D << 1$). All told, measuring V_L to determine changes in σ_D (as when optical radiation is measured) leads to inaccuracies.

Alternatively, one can derive an output signal by measuring the voltage across the detector,

$$V_D = I_B R_D \tag{8}$$

From Eqs. 1 and 8, we can express the detector voltage as a function of the detector resistance,

$$V_D(R_D) = V_B \frac{R_D}{(R_L + R_D)} \tag{9}$$

and as function of detector conductance:

$$V_D(\sigma_D) = V_B \frac{1}{(1 + R_L \sigma_D)} \tag{10}$$

Eq. 10 shows that again the voltage measurement is a nonlinear function of the detector conductance. Proceeding as before,

$$\text{When } R_L << R_D, \quad V_D \cong V_B \tag{11}$$

$$\text{When } R_L >> R_D, \quad V_D \cong I_B / \sigma_D \tag{12}$$

Neither of these conditions are attractive. In the first, the output voltage is again insensitive to changes in detector conductance. In the other, where V_B and R_L act to form a constant current source I_B, the response is inversly proportional to the detector conductance. Both situations may lead to measurement errors when changes in V_D are presumed to be proportional to changes in σ_D.

2.2. Current mode measurements

Another basic photoconductive detector biasing and measuring circuit is shown in Fig. 2.

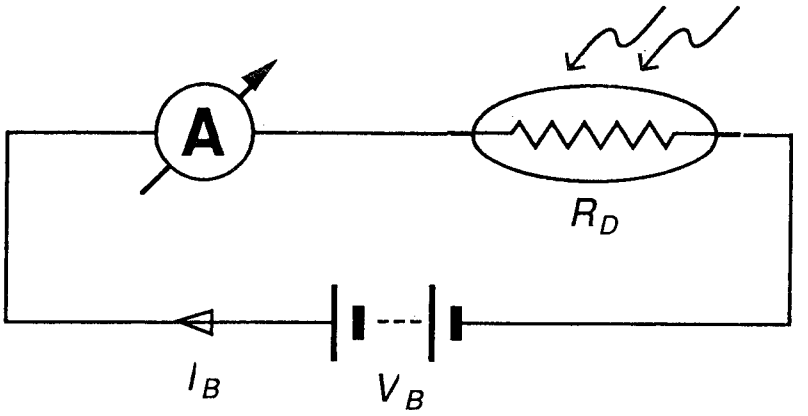

FIGURE 2: Current Mode

A current meter A measures the "short circuit current" of V_B and R_D treated together as a Thévenin voltage source, and is the limiting case of the previous circuit as R_L (and V_L) $\rightarrow 0$

$$I_B(\sigma_D) = V_B \sigma_D \tag{13}$$

This current, rather than a voltage, is linearly proportional to the detector conductance. For conductance changes (as when optical radiation is detected) it can be written

$$I_B = V_B (\sigma_D + \Delta\sigma_D) \tag{14}$$

or as:

$$I_B = I_B^{\circ} + V_B \Delta\sigma_D \tag{15}$$

We see that there is both a constant biasing current, I_B°, and a "useful" current component which is proportional to the conductance change and to the biasing voltage. This part is generally the small difference of two large numbers, I_B and I_B°. To achieve high accuracy, the biasing voltage has to be very stable. Its internal resistance, as well as the internal resistance of the current meter, has to be much smaller than the detector resistance in order to satisfy the assumptions of this derivation.

3. ELECTRONIC DESIGN

A large-area (2.54 mm × 2.54 mm) InfraRed Associates[2] HgCdTe (MCT) detector was selected for radiometric applications. The resistance range of large-area MCT detectors is roughly 15 to 30 ohm at 77 K. The selected one had a resistance of 24.7 ohm at this temperature. If we consider that the maximum resistance change of the detector for maximum optical radiation of 50 mW is about 10%, it follows that a 25 Ω detector will have a resistance change of about 25 μΩ if a radiant power level of 0.5 μW has to be measured.

An amplifier unit was matched to the detector by the manufacturer, working on the principles analyzed in Section 2.1. This circuit operated in the voltage mode, where the voltage on the detector resistance was measured. In order to get the maximum signal to noise ratio, the detector required a bias current of 70 mA. If the detector was to be used with a customer's bias circuitry and amplifier system, they suggested a serial load resistor ten times higher than the detector resistance. This corresponds to the nonlinear connection between the detector voltage and conductance described in Eq. 12.

In addition to the manufacturer's amplifier unit, we developed another amplifier that made a current mode measurement, following the analysis in Section 2.2. It was based on an operational amplifier in the standard configuration to measure short-circuit current at the input, and it included provisions for biasing the detector. However, the bias current would have produced an unwanted, amplified output voltage, which in most cases would have saturated the amplifier. To avoid this, a voltage compensation method was used, as shown in Fig. 3.

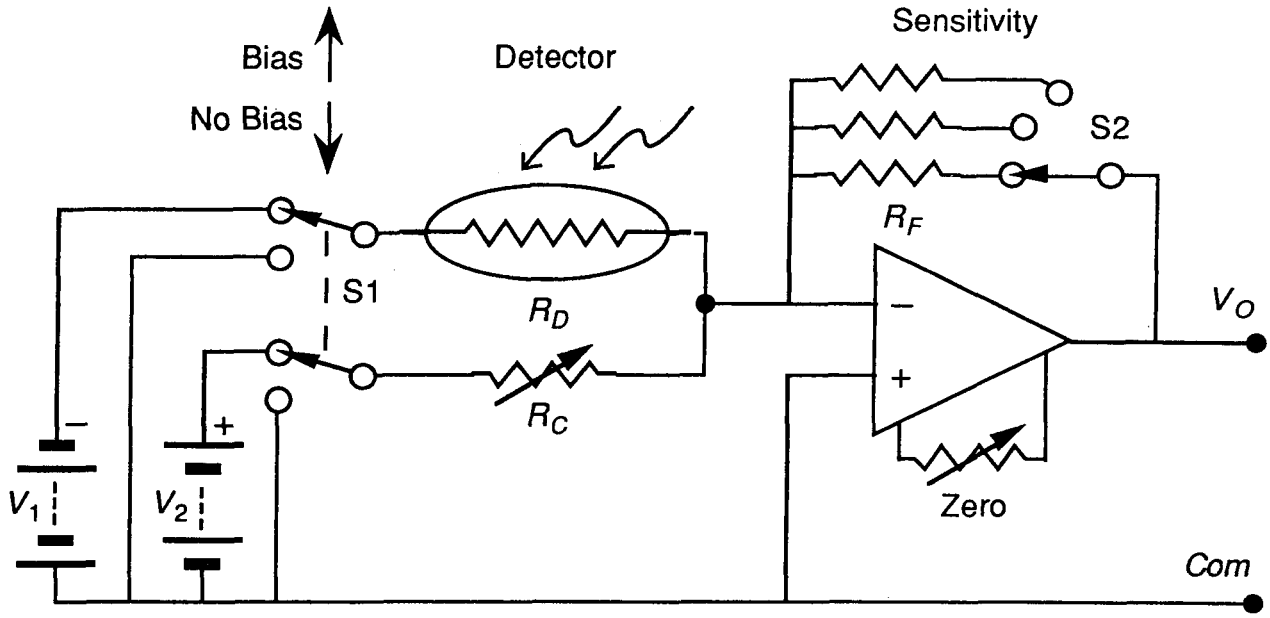

FIGURE 3: Current to Voltage Converter, Simplified Model

Voltage source V_1 is used to bias the detector and corresponds to V_B in the previous discussion. A compensating voltage V_2, of opposite polarity, couples to the summation point of the operational amplifier through a variable resistor, R_C. When switch S1 is in the "No Bias" position, the voltage sources are removed from the circuit and the amplifer can be zeroed. When S1 is in the "Bias" position, R_C is adjusted for a null output ($V_O = 0$) when the detector is in the dark. Both of these adjustments should be performed at the highest amplifier gain (largest value of R_F) used for subsequent measurements. Once they are made, the output of the amplifier circuit

$$V_O = V_1 R_F \Delta\sigma_D \tag{16}$$

To make a useful circuit, it is necessary to do the compensation carefully. The voltage sources should be very stable and have low output impedances. The zero adjustments should be checked repeatedly to counteract changes of the voltage sources and resistors. Because of the high amplification required to detect small changes in σ_D, the circuit should be well shielded and grounded to minimize interference at the output. Additionally, the operational amplifier must have low noise, low drift, a large gain-bandwidth product, and a large open-loop gain. The gain of the amplifier should be calibrated repeatedly to make sure that the optical radiation measurements stay consistent over time.

Our actual amplifer circuit had additional features to allow us to make these gain calibrations. A diagram of the complete circuit is shown in Fig. 4. When switch S2 is in the up position, this circuit is similar to the one shown in Fig. 3. However, when switch S2 is in the down position, two changes are made. First, the negative terminal of the bias source is connected to a real ground, rather than the virtual ground at the summation point of the operational amplifier. This maintains the detector as a load across the bias voltage. Secondly, the operational amplifier is connected to measure the bias voltage itself, through a 1000 Ω resistor. If the bias voltage changes, so does the proportionality factor shown in Eq. 16. To counteract this change, the effective feedback resistance R_F can be changed with potentiometer P2 such that the transfer gain of the amplifer remains constant. Potentiometer P2 is followed by a buffer amplifier to maintain a uniform output impedance.

To summarize, the adjustment procedure is to:

1) Switch S1 to "No Bias", S2 to "Measure", turn S3, the Sensitivity Range, to the highest scale (the 100 kΩ resistor), and set P1 for zero output voltage.
2) Leave S1 on "No Bias", switch S2 to "Calibrate", change the Sensitivity Range to the lowest scale (the 1000 Ω resistor), and adjust P2 for a -1.990±.002 V output voltage while the detector is in the dark.
3) Change S1 to "Bias" and S2 to "Measure", return the Sensitivity Range to the highest scale, and adjust P3 for a null (zero) output voltage while the detector is in the dark.

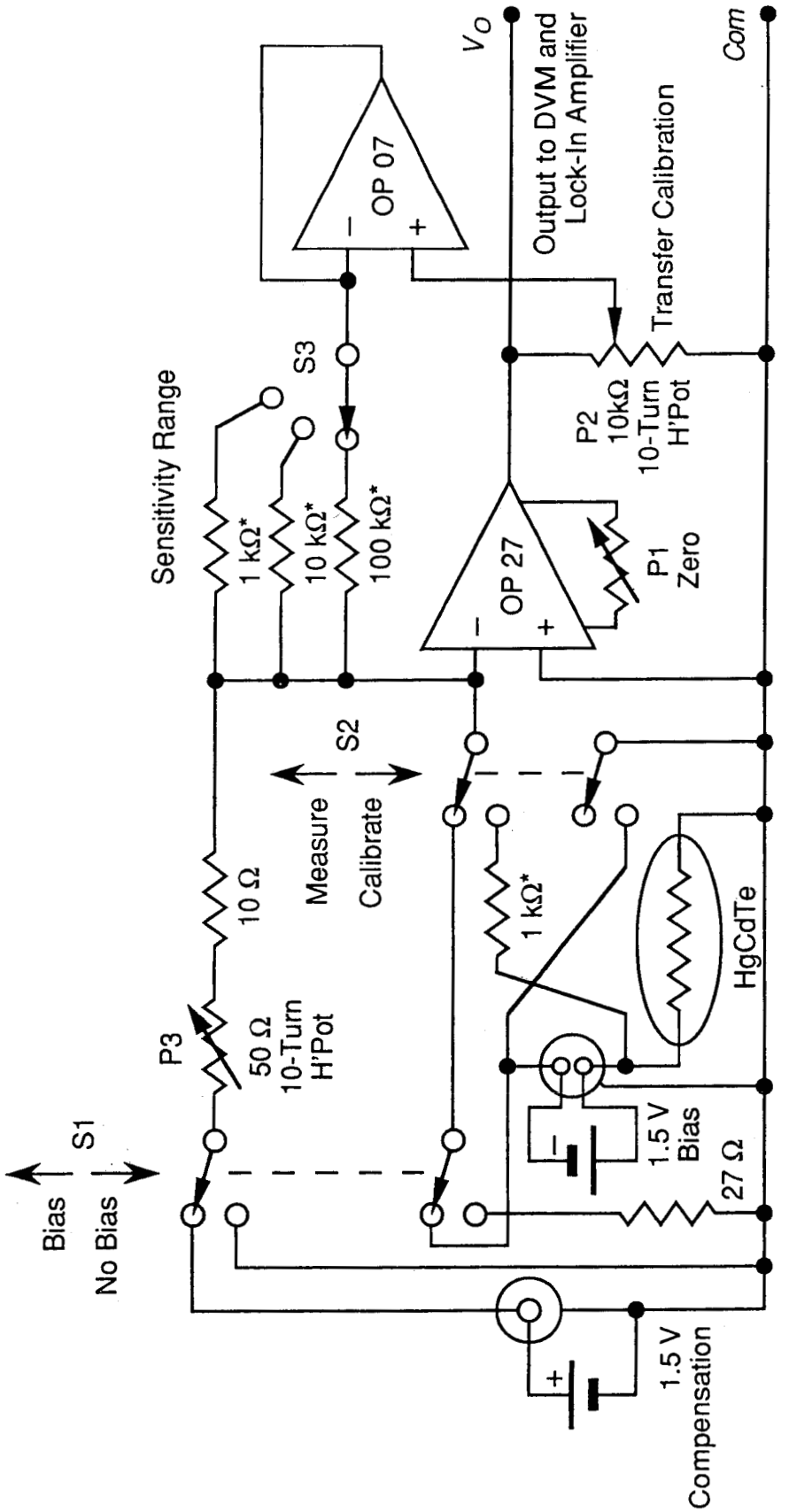

FIGURE 4: Current to Voltage Converter, Working Model

For biasing and compensation, we used with equal sucess both high charge-capacity alkaline batteries and electronically controlled, highly stable, ripple and noise free DC calibrators. If a battery is used as a biasing voltage source (it has minimum noise and ripple), the 70 mA load current may cause a long-term decrease in its output voltage. While the calibration of the amplifier transfer gain gives stability to the measuring circuit, it does not eliminate the bias-current dependent change in the detector responsivity. When a battery is used for biasing, the small changes in the bias voltage must be regarded as a potential source of error, which can be estimated using data provided by the detector manufacturer.

There is one more electronic detail concerning the measurement of optical radiation. In practice, the signal on the photodetector is chopped. The output of the amplifer circuit is detected by a "Lock-In Amplifier," which provides greater noise rejection than would a DC measurement, alone. Care must be taken that the amplifer has a sufficient bandwidth. In Fig. 5, we show a block diagram of the electronic instrumentation used for our measurements.

4. STABILITY

The use of this circuit for detector studies is beyond the scope of this paper. However, we would like to report that the radiometer operated stably over an extended period of time.

A tungsten strip lamp, fed from a highly stable DC current source and operating at about 100 °C, was imaged onto the MCT detector using a spherical mirror and an aperture 2 mm in diameter. The radiation was chopped at 13 Hz. The roll-off frequency of the low pass filter on the lock-in amplifier was set two decades lower. The sensitivity of the current to voltage converter was 10^5 Volts/Amp (the 100 kΩ feedback resistor).

Over the course of 122 minutes, 1269 voltage measurements were made at the output of the lock-in amplifier. These voltages held in the range between 9.078 and 9.173, with an average of 9.132. The standard deviation was 0.017 V, which corresponds to 0.19%.

Fig. 6 shows what happened after this data was taken. As the quantity of liquid nitrogen decreased in the dewer, the detector resistance changed, causing the compensation voltage and the bias voltage to be out of balance. However, when the dewer was refilled and the electronic adjustment procedure followed, the output readings matched the previous ones.

5. ACKNOWLEDGEMENTS

The authors thank Robert D. Saunders for participating in the stability measurements and Jonathan E. Hardis for help in preparing the manuscript.

6. REFERENCES

1. E. L. Dereniak and D. G. Crowe, *Optical Radiation Detectors*, p. 94, John Wiley & Sons (1984).
2. Commercial products – materials and instruments – are identified in this document for the sole purpose of adequately describing experimental or test procedures. In no event does such identification imply recommendation or endorsement by the National Institute of Standards and Technology of a particular product, nor does it imply that a named material or instrument is necessarily the best available for the purpose it serves.
3. *Infrared Components Brochure*, Edition 17, p. 58, Santa Barbara Research Center, Goleta, CA (1983).
4. *Technical Data Book, HgCdTe Instruction Manual*, p. 2, InfraRed Associates, Inc., Cranberry, NJ (1985).
5. E. L. Dereniak and D. G. Crowe, *ibid.*, p. 92.
6. *Linear and Conversion Applications Handbook*, pp. 240-241, Precision Monolithics, Inc., Santa Clara, CA (1986).

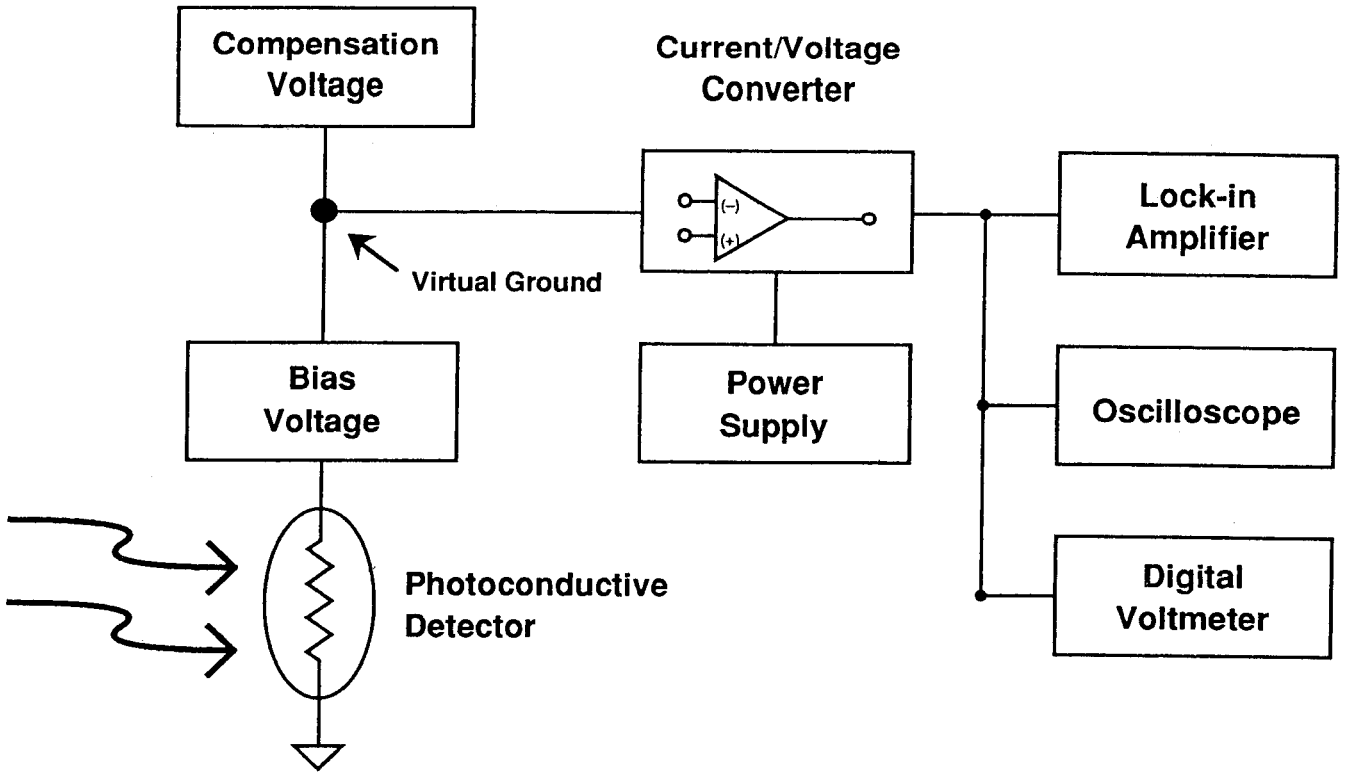

FIGURE 5: Block Diagram of Photoconductive Detector Radiometer

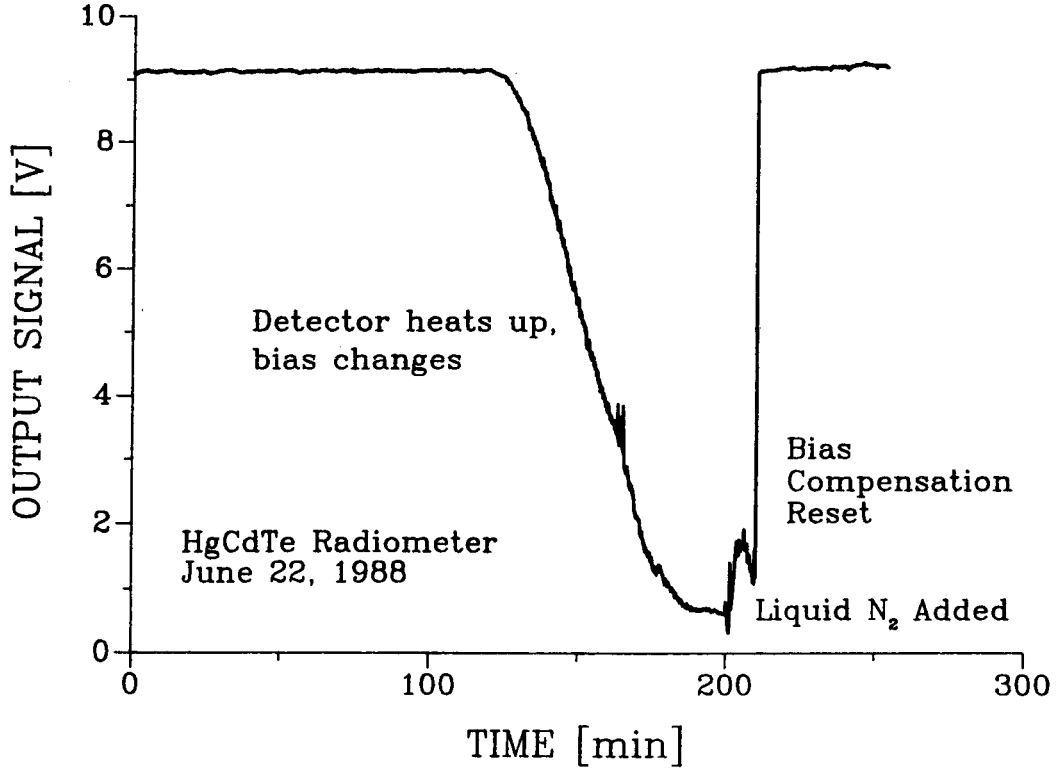

FIGURE 6: Detector Stability

Photocurrent measurement of PC and PV HgCdTe detectors.

George P. Eppeldauer[1] and Robert J. Martin[2]
[1]National Institute of Standards and Technology
Gaithersburg, Maryland 20899
[2]Analog/Digital Integrated Circuits, Inc.
Longwood, Florida 32750

Abstract

Novel preamplifiers for working standard photoconductive (PC) and photovoltaic (PV) HgCdTe detectors have been developed to maintain the spectral responsivity scale of the National Institute of Standards and Technology (NIST) in the wavelength range of 5 μm to 20 μm. The linear PC mode preamplifier does not need any compensating source to zero the effect of the detector bias current for the preamplifier output. The impedance multiplication concept with a positive feedback buffer amplifier was analyzed and utilized in a bootstrap transimpedance amplifer to measure photocurrent of a 200 Ω shunt resistance photodiode with a maximum signal gain of 10^8 V/A. In spite of the high performance lock-in used as a second-stage signal-amplifier, the signal-to-noise ratio had to be optimized for the output of the photocurrent preamplifiers. Noise and drift were equalized for the output of the PV mode preamplifier. The signal gain errors were calculated to determine the signal frequency range where photocurrent-to-voltage conversion can be performed with very low uncertainties. For the design of both PC and PV detector preamplifiers, the most important gain equations are described. Measurement results on signal ranges and noise performance are discussed.

1. Introduction

HgCdTe detectors are widely used for low-level optical radiation measurements in the infrared (IR) range. Working standard HgCdTe radiometers have been developed and calibrated against a transfer standard cryogenic bolometer [1]. The working standards hold the IR spectral responsivity scale and test detectors are calibrated against them. The expectation from the working standards is to propagate and maintain the 0.8 % (coverage factor k=1) standard relative uncertainty of the IR spectral responsivity scale with the smallest possible uncertainty increase. One of the most important requirements for working standards development was to produce linear operation in a wide radiant power range. Linear response can be obtained from both photovoltaic (PV) and photoconductive (PC) type devices if the detector short circuit current is measured [2]. HgCdTe detectors have low resistance-area (RA) product resulting in small detector-

resistance and high gain for the preamplifier input voltage-noise, even for small area detectors. It is an important design consideration to produce high sensitivity by keeping the voltage-noise gain low. Also, the spatial response non-uniformity of HgCdTe detectors is poor because of the difficulties associated with producing homogeneous material. For accurate measurements, it is necessary to overfill these detectors with a uniform field of radiation to average out high response non-uniformities. However, the signal loss can be significant in the overfilled (irradiance) measurement mode. Again, high sensitivity is necessary to measure the decreased radiant flux on the detector in this measurement mode. At low signal frequencies, the $1/f$ noise of HgCdTe detectors can be orders of magnitude larger than the noise from the background. It is important to keep the chopping frequency close to the $1/f$ noise elbow. As the elbow frequency depends on the bias voltage, biasing of PV detectors should be avoided in high sensitivity applications.

PV HgCdTe detectors can be used for optical radiation measurements from about 5 μm to 12 μm. At present, the optically sensitive diameter of these detectors is 2 mm or less. The shunt resistance of these devices is a few-hundred ohm and the capacitance is close to 1 nF for a 2 mm detector. The PV devices are linear only if the short-circuit current of the detector is measured. Photodiodes have smaller noise than PC detectors because the dominating photodiode shot-noise is much smaller than the generation-recombination noise of PC detectors. Bootstrapped preamplifiers have been reported [3, 4] that can keep the voltage drop on the photodiode very low resulting in an increased shunt resistance and better short circuit for the photodiode. The increased shunt resistance will result in smaller closed–loop voltage-gain and higher loop gain [5]. The smaller closed–loop voltage-gain produces lower voltage noise and voltage drift amplifications. The higher loop gain will decrease the uncertainty of the current-to-voltage conversion. Analysis and application of the bootstrap method for PV HgCdTe detectors is discussed below.

PC HgCdTe detectors can be used for longer wavelengths than PV detectors. We have used the PC HgCdTe detectors up to 20 μm, which is the long wavelength limit of the NIST IR spectral responsivity scale. PC detectors are operated with a dc bias current to sense the photogenerated conductance change, which is proportional to the radiant flux (power) on the detector. In a traditional biasing and measuring circuit, a dc source is connected to the detector through a load-resistor connected in series. The voltage change is measured across the detector while the high load-resistance keeps the bias current constant. It was shown in our earlier work [2] that the voltage measured on the detector is a nonlinear function of the conductance change. To eliminate this response non-linearity, a current measuring PC HgCdTe radiometer was developed [2]. This radiometer needed frequent zeroing to eliminate output voltage saturation caused by the

non-stable dc compensation of the biasing source. The main concern of the new linear preamplifier design, described here, was to eliminate the need for output dc voltage compensations.

2. PC HgCdTe detector and preamplifier

The tested PC HgCdTe detectors had active areas of 3 mm x 3 mm or 4 mm x 4 mm. No cut-lines were fabricated in the detector centers to avoid large and sudden changes in the spatial response uniformity. In most commercial PC HgCdTe detectors, the detector segments, isolated by cutlines, are connected in series to increase the resultant resistance of the detector. The tested cutline-free detectors had very low cold (77 K) resistances, ranging from 15 Ω to 22 Ω. A dc bias current of about 50 mA was needed for a detector to obtain a high enough detector responsivity. The test detector responsivities were very different. They ranged from a few V/W to 122 V/W when the broadband radiation of a ceramic glower was measured. The detector responsivity tests were made against pyroelectric detector standards of spectrally constant responsivity.

The preamplifier was constructed from ten current-to-voltage converters connected in parallel as shown in the schematic of Fig. 1. Only three of the ten amplifiers are shown in this drawing. The ten current-to-voltage converters produced 10 * 5 (50) mA dc current to bias the PC detector. The voltage drop on the detector was determined by the bias voltage V_b connected to the non-inverting inputs of the operational amplifiers. The dc bias current requirement and the cold dc resistance of an individual detector determined the feedback resistor value for the operational amplifiers. The same feedback resistor value, R_1=R_2=R_{10}=1875 Ω, was used in all of the ten parallel-connected amplifiers. The R_d=15 Ω corresponds to ten 150 Ω resistors connected in parallel, producing smaller feedback attenuation (from the operational amplifier output to its input) in each individual current-to-voltage converter. At low frequencies, the feedback network attenuation in each amplifier is 13.5 =(150+1875) Ω / 150 Ω. The loop gain, which is the product of the feedback attenuation and the amplifier open-loop-gain, is close to 10^6 for the applied AD797 [6] amplifiers. Large loop gains result in high accuracy current-to-voltage conversion [5]. Note that each amplifier needs an offset equalizing resistor (not shown in the figure) connected in series to the non-inverting input. This resistor is needed to allow the error current of each amplifier to prevent excess output voltage effect. A value of 10 Ω was used to compromise offset error versus gain error. The ac (10 Hz) signals from the ten channels of the preamplifier were combined with a sum-amplifier after the dc voltages at the outputs of the individual amplifiers were de-coupled. The low frequency roll-off point of the signal gain curve

was tuned to 0.3 Hz by using serially connected 10 kΩ resistor and 47 μF capacitor for each channel.

As the conductance of the detector varies, there is a proportional variation in the output voltage of each preamplifier and in the variation of the summation amplifier. The conductance of the detector G_d varies only a small amount about the dc operating point. This incremental conductance change follows the rate of the radiation-chopper. As the measured change in the detector-current is proportional to the change of the detector conductance [2], the equivalent transfer resistance gain is found by taking the derivative of the output voltage V_o with respect to the detector conductance G_d:

$$\partial V_o/\partial G_d = -V_b R_f R_T/R_i \qquad [V/S] \qquad (1)$$

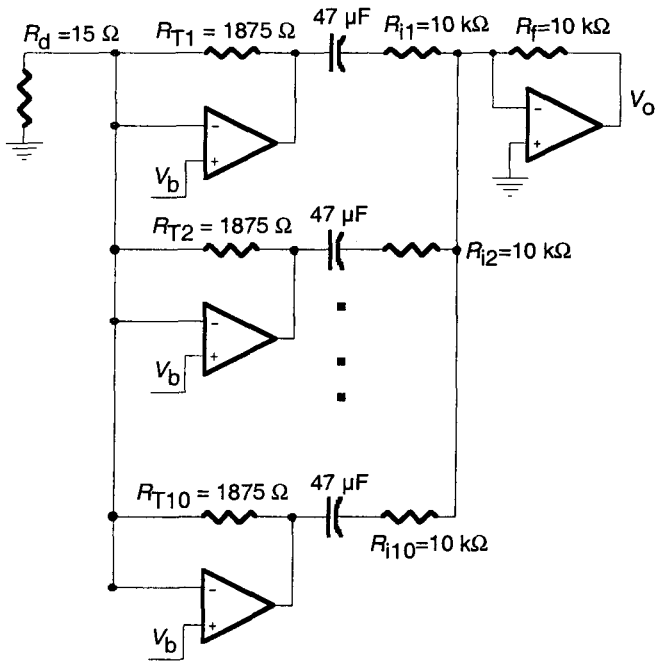

Fig. 1. Multiple amplifier current-to-voltage converter for the PC HgCdTe detector.

where V_o is the output voltage in V,
R_f is the feedback resistor in the summing amplifier in Ω,
R_i is the input summing resistor of the summing amplifier in Ω,
V_b is the bias voltage in V,
R_T is the transfer (feedback) resistance of one of the input stages in Ω, and
G_d=1/R_d is the conductance of the detector in S

Because of the summing operation, the transfer resistance (current-to-voltage gain) is independent of the number of amplifiers used.

The advantage of this preamplifier design is that the dc output voltages of the individual operational amplifiers do not go into saturation and no compensating source is needed at the input. A compensating voltage source could produce large (and dominating) noise and also repeated compensations for zeroing the output voltage might be necessary.

From preamplifier output noise measurements (without the detector at the input) and the nominal 125 V/V preamplifier voltage-gain (calculated from Eq. 1 for a 15 Ω detector resistance), an input noise of 0.6 nV/Hz$^{1/2}$ was obtained. This noise is comparable to the 0.5 nV/Hz$^{1/2}$ Johnson noise of the 15 Ω detector resistance.

The 0.6 nV/Hz$^{1/2}$ input voltage noise corresponds to a noise equivalent power (NEP) of 40 pW/Hz$^{1/2}$ for a detector responsivity (without the preamplifier voltage-gain) of 16 V/W. This responsivity was measured on a typical test detector at 50 mA bias current and 10 Hz chopping frequency. The measured NEP was one order of magnitude larger, 0.34 nW/Hz$^{1/2}$. The large noise was caused by the generation-recombination (G-R) noise of the biased PC HgCdTe detector. The calculated G-R current noise for 1 Hz bandwidth is:

$$I_{GR} = (2gqI_d\Delta f)^{1/2} = 0.57 \text{ nA}$$

where I_d is the detector current, in our case 0.05 A,
q is the electron charge, 1.6 * 10^{-19} C,
g is the photoconductive gain (typically about 20 electrons per electron), and
Δf is the electrical bandwidth in Hz.

Using the NEP=0.34 nW/Hz$^{1/2}$ and the detector area A=0.16 cm^2, a $D^*=A^{1/2}$/NEP = 10^9 cm Hz$^{1/2}$/W was calculated. The same detector was tested at a bias current of 10 mA where the detector responsivity decreased to 3.7 V/W.

At 50 mA bias, the resultant radiant power-to-voltage gain for the preamplifier output is 16 V/W * 125 V/V = 2000 V/W. The current-to-voltage gain is 1875 V/A. Accordingly, the power-to-current gain is about 1.1 A/W. From these gains and the measured 0.34 nW noise, a photoconductive gain of only 13 (from I_{GR} = 0.37 nA) is obtained.

For the NEP equal to 0.34 nW/Hz$^{1/2}$, the output noise voltage of the preamplifier is 0.68 μV at a bandwidth of 1 Hz. The signal dynamic range, for a minimum signal-to-noise

ratio of 100, will be from about 68 μV to 5 V (at the preamplifier output), which corresponds to a radiant power range of 34 nW to 2.5 mW. This is a dynamic range of close to five decades for radiant power measurements with 1% (coverage factor k=1) relative uncertainty.

3. PV HgCdTe detector and preamplifier

Instead of applying a bias voltage for the photodiode, we chose the bootstrap method to increase the shunt resistance of our PV HgCdTe detector. The shunt resistance increase was necessary to achieve high signal gains and to obtain low output noise for the preamplifier. The term bootstrapping refers to the use of an amplifier to increase the apparent impedance using near unity gain positive feedback [3, 4]. Large area photon detectors may have relatively large capacitance and low shunt resistance. One method of dealing with this relatively low impedance is to use a near unity gain buffer amplifier to increase the effective equivalent impedance of the detector.

3.1. Bootstrap impedance multiplication circuit

The impedance multiplication circuit, using the unity gain buffer amplifier, is shown in Fig. 2. The unity gain buffer is implemented with an operational amplifier OA. To demonstrate the impedance multiplication concept, a 1 V ac voltage source was connected to the input in a circuit simulation.

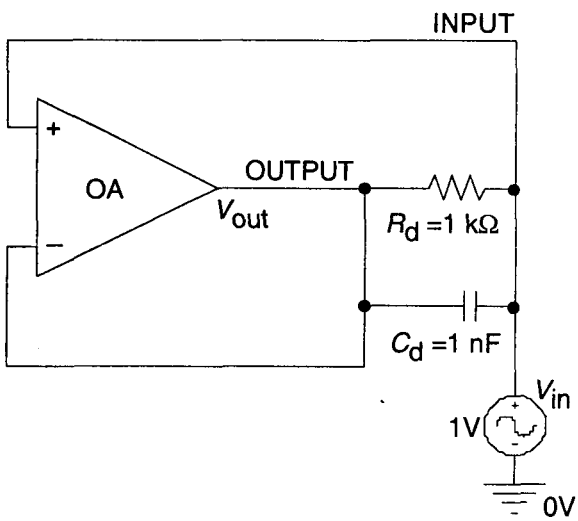

Fig. 2.
Computer simulation circuit to demonstrate the impedance multiplication concept.

The effective equivalent input impedance which will be connected to the input of a second stage transfer resistance amplifier (not shown in Fig. 2) will be determined first. The input current can be calculated from Kirchoff's and Ohm's laws:

$$I_{in}(s)=Y_d\,(V_{in}(s)-V_{out}(s)) \qquad [A] \qquad (2)$$

where $Y_d=G_d+C_d s$ is the detector admittance,

$G_d=1/R_d$ is the conductance of the detector in S,

C_d is the junction capacitance of the detector in F,

s is frequency in the steady state frequency domain in rad/s or $s=j2\pi f$, and

f is frequency in Hertz with $j=(-1)^{1/2}$,

$I_{in}(s)$ is the input current in A,

$V_{in}(s)$ is the input voltage in V, and

$V_{out}(s)$ is the amplifier output voltage in V.

The closed loop voltage gain of the operational amplifier can be defined in terms of the open loop voltage gain as:

$$\frac{V_{out}(s)}{V_{in}(s)}=\frac{A(s)}{A(s)+1} \qquad [V/V] \qquad (3)$$

where $A(s)$ is the open loop gain of the operational amplifier in V/V.

The equivalent input impedance is defined as the ratio of the input voltage to the input current. Further, in order to eliminate the output voltage, equation (2) is written in the following form:

$$I_{in}(s)=V_{in}(s)(1-V_{out}(s)/V_{in}(s))Y_d \qquad [A] \qquad (4)$$

Inserting equation (3) into equation (4) becomes

$$I_{in}(s)=V_{in}(s)(1-A(s)/(A(s)+1))Y_d \qquad [A] \qquad (5)$$

Simplifying equation (5) and taking the voltage to current ratio, the equivalent impedance may be expressed as:

$$Z_{in}(s)=(A(s)+1)Z_d \qquad [\Omega] \qquad (6)$$

where the detector impedance $Z_d = 1/Y_d$.

Assume that the general form of $A(s)$ may be expressed by a finite gain and a dominant pole [5], then:

$$A(s) = A_o/(\tau s + 1) \qquad [V/V] \qquad (7)$$

where A_o is the dc open loop voltage gain in V/V, and
τ is the time constant of the dominant pole of the amplifier in s.

Inserting equation (7) into equation (6), the general form of the equivalent input impedance is written as follows:

$$Z_{in}(s) = \frac{R_{in}(1+s/\omega_u)}{(\tau s+1)(R_d C_d s+1)} \qquad [\Omega] \qquad (8)$$

where $R_{in} = R_d(A_o+1)$ in Ω,
$\omega_u = (A_o+1)/\tau$ in rad/s and is commonly called the unity gain bandwidth product for the operational amplifier.

A typical operational amplifier would have an open loop gain of 400 V/mV and a dominant time constant of 16 ms. In the computer simulation, a 1kΩ shunt resistance and a 1 nF capacitor along with a standard operational amplifier was used to demonstrate the multiplication of impedance concept. The simulation results are shown in Fig. 3.

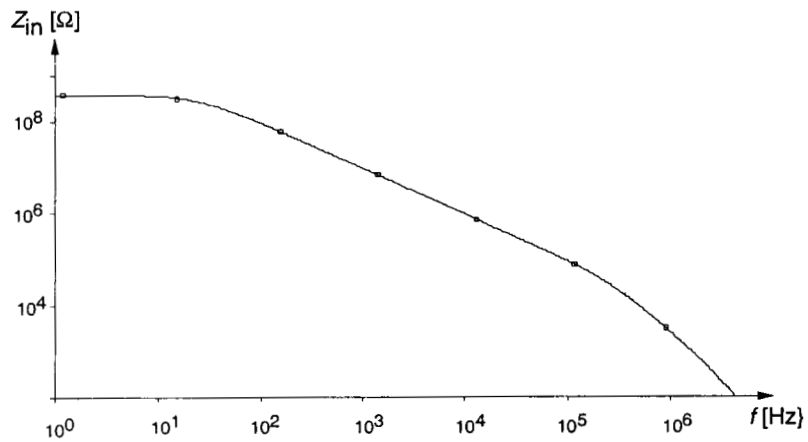

Fig. 3. The equivalent input impedance calculated for a

1 kΩ shunt resistance and a 1 nF junction capacitance.

For this example, at low frequencies the equivalent impedance is resistive and approaches 400 MΩ. There is a break point at 10 Hz and the impedance becomes capacitive over the band from 10 Hz to 1 MHz.

3.2. Bootstrap transimpedance amplifier, signal gain

If we combine the bootstrap impedance multiplier circuit with a transimpedance amplifier, an improved performance current-to-voltage converter can be realized (Fig. 4). The feedback network of the second operational amplifer OA2 consists of a feedback capacitor C_T connected in parallel with the feedback resistor R_T. The photocurrent I_{in} from the photodiode P is converted into an output voltage V_0. The equivalent transfer function of the combined circuit has to be determined to obtain the signal gain. An equivalent circuit is shown in Fig. 5 for nodes a, b, and c.

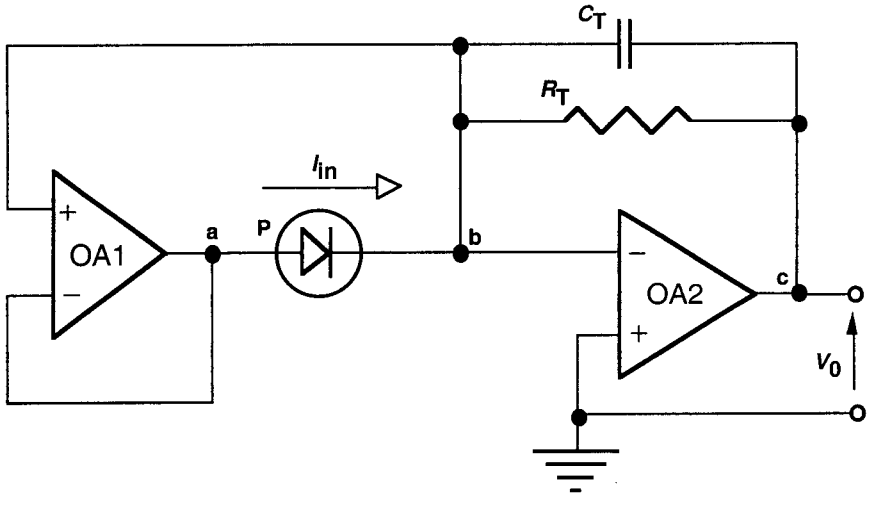

Fig. 4. Bootstrap transimpedance amplifier.

The node-voltages [7], shown with voltage sources (circles), are referenced to the common and expressed from the output voltage V_0. The voltage polarities are shown with both signs and arrows. The input voltage of the operational amplifier OA2 is on node b and it is equal to V_0/A_2. This voltage is multiplied by the gain of the buffer amplifier (shown by Eq. 3). The output voltage of the operational amplifier OA1 on node a will be $A_1 V_0 /(A_1+1)A_2$. The input current I_{in} is represented by a current source (double

circle). It can be calculated from the node-voltage equation using Kirchoff's current law [7] for node b:

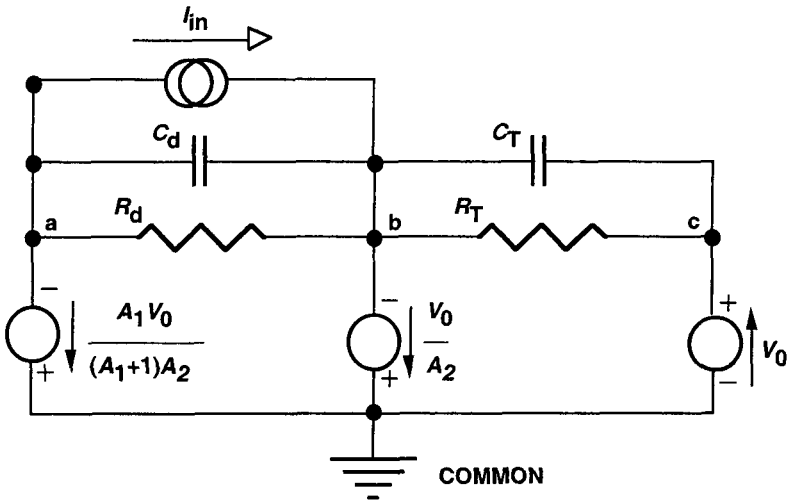

Fig. 5. Three-node equivalent circuit of the combined transimpedance amplifier.

$$I_{in}(s)=\left(\frac{V_0(s)A_1}{(A_1+1)A_2}-\frac{V_0(s)}{A_2}\right)\frac{1}{Z_d}-\left(\frac{V_0(s)}{A_2}+V_0(s)\right)\frac{1}{Z_T} \qquad [\text{A}] \qquad (9)$$

Both $V_0(s)$ and $I_{in}(s)$ are frequency dependent. After simplifying and collecting terms, the output voltage to input current ratio (signal gain) can be written as:

$$\frac{V_0(s)}{I_{in}(s)}=\frac{-R_T}{1+sR_TC_T+\frac{1}{A_2}(1+sR_TC_T+\frac{R_TG_d+sR_TC_d}{A_1+1})} \qquad [\Omega] \qquad (10)$$

where V_0(s) is the output voltage of OA2 in V,
I_{in}(s) is the input current from the PV detector (photodiode) in A,
A_2(s) is the open loop gain of OA2 in V/V,
A_1(s) is the open loop gain of the bootstrap operational amplifier OA1 in V/V,
R_d is the shunt resistance of the photodiode, and
C_d is the junction capacitance of the photodiode.

For high gain operational amplifiers, the transfer function in Eq. 10 becomes equal to $-R_T$ which is the low frequency (dc) current-to-voltage gain of the combined transimpedance amplifier. The denominator describes the frequency dependent error of the photocurrent-

to-voltage conversion. The error voltage curves of the signal conversion (gain) as calculated for the summing junction of the OA2 for an output signal of V_0=1V are shown in Fig. 6. The combined circuit used in this computer simulation is shown in Fig. 7. The error voltage curves were calculated for a detector resistance of 200 Ω and feedback resistors from 1 kΩ to 100MΩ. The transfer resistance curves, shown in Fig. 8, were calculated with feedback resistors up to 1MΩ only.

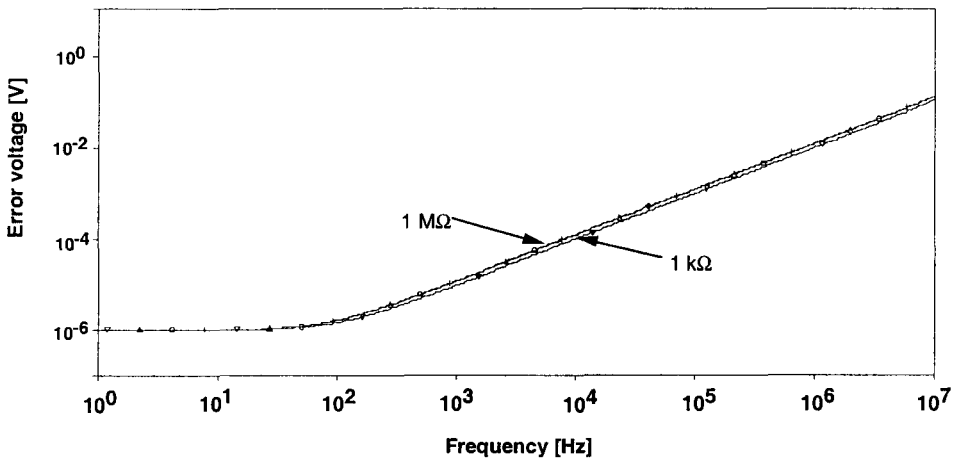

Fig. 6. Error voltages (referenced to V_0=1V) of the the bootstrap transimpedance amplifier for a shunt resistance of 200 Ω and feedback resistors of 1 kΩ to 1 MΩ.

The error voltage is reciprocal of the loop gain which is, at low frequencies, roughly equal to the open loop gain (4 x 10^5) of OA2. This is the result of the close to unity feedback attenuation at low frequencies, caused by the detector impedance multiplication.

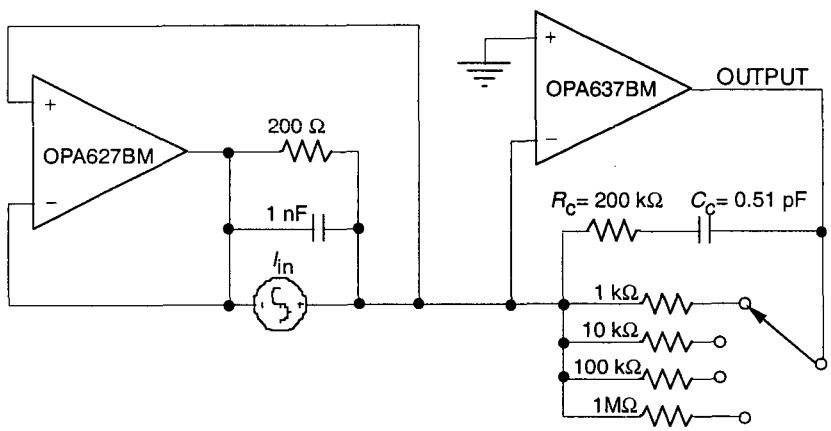

Fig. 7. Computer simulation circuit for a bootstrap transfer resistance amplifier.

The maximum signal current can be measured when the output signal is 1 V and the feedback resistance is 1 kΩ. This corresponds to a maximum photocurrent of 1 mA. The output signal maximum is determined by the largest full-scale signal of the lockin amplifier input where the output signal is connected. The relatively wide range of transfer resistance is one of the advantages of active impedance compensation. Note that R_c and C_c have been added to OA2 to provide voltage gain (gain peaking) compensation [5].

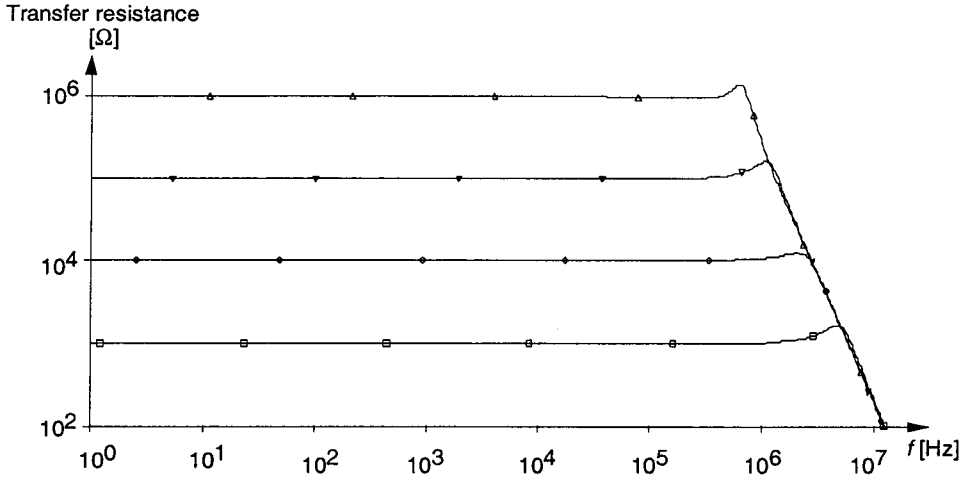

Fig. 8. Transfer resistance (signal gain) of the bootstrap transimpedance amplifier with feedback resistor selections from 1 kΩ to 1 MΩ.

3.3. Output noise

The output voltage as a power spectral density in volts squared per hertz can be written as:

$$e_{nout}^2 = \frac{(R_T G_d e_{n1} * A_1/(A_1+1))^2+(e_{n2}(1+R_T G_d/(A_1+1)))^2+4kTR_T+(R_T i_{n1})^2+(R_T i_{n1})^2+2qI_d R_T^2}{1+sR_T C_T+\frac{1}{A_2}(1+sR_T C_T+\frac{R_T G_d+sR_T C_d}{A_1+1})} \quad (11)$$

where e_{nout} is the equivalent output noise voltage density in V/Hz$^{1/2}$,

k is the Boltzmann's Constant (1.38*10^{-23} Joules/K),

T is the absolute temperature in K,

e_{n1} is the noise voltage density of the bootstrap amplifier in V/Hz$^{1/2}$,

e_{n2} is the noise voltage density of the transfer resistance amplifier in V/Hz$^{1/2}$,

i_{n1} is the equivalent input noise current density of the bootstrap amplifier in $A/Hz^{1/2}$,
i_{n2} is the equivalent input noise current density of the transfer resistance amplifier in $A/Hz^{1/2}$,
I_d is the average detector current and includes the dark leakage current in A, and
q is the electron charge equal to $1.602*10^{-19}$ Coulombs/electron.

The amplifier gains are taken at the frequency of interest and are in general complex.

For low enough frequencies and high enough amplifier open loop gains, and where the input current noise of the operational amplifiers may be neglected, Eq. 11 simplifies to:

$$e_{nout}^2 = (R_T G_d e_{n1})^2 + (e_{n2}(1+G_d R_T/A_1))^2 + 4kTR_T + 2qI_d R_T^2 \qquad [V^2/Hz] \qquad (12)$$

In Eq. 12 the denominator error drops out.

Equation 12 shows that the noise of the transfer resistance amplifier will in general be small compared to the voltage noise of the impedance feedback amplifier by virtue of the relatively large gain of this bootstrap operation. Clearly, for a large diode conductance, the noise of the bootstrap amplifier dominates. To avoid amplifier noise domination, the noise of the bootstrap amplifier's voltage noise density must be less than or equal to the detector noise. Care should be taken because the $1/f$ amplifier voltage noise, at very low (dc) frequencies, can be much larger than the detector noise.

The measured PV HgCdTe detector noise was 40 $pA/Hz^{1/2}$ at 25 Hz. This shot-noise-dominated PV detector noise is about an order-of-magnitude smaller than the G-R-noise-dominated PC HgCdTe detector noise in Section 2. In order to match the amplifier noise to this detector noise, operational amplifiers OPA627 and 637 (as shown in Fig. 7) were used in the computer model. Figure 9 illustrates the output noise versus frequency characteristics of the bootstrap transimpedance amplifier for R_d=200 Ω. The OA2 feedback resistors were selected in the simulator program between 1 kΩ and 1 MΩ in decadic steps.

When the feedback resistor is increased to R_T=100 MΩ the output voltage noise density will be close to 4 mV. This corresponds to a minimum signal current of 40 pA which is equal to about 25 pW at a wavelength of 9 μm as calculated from the 1.6 A/W

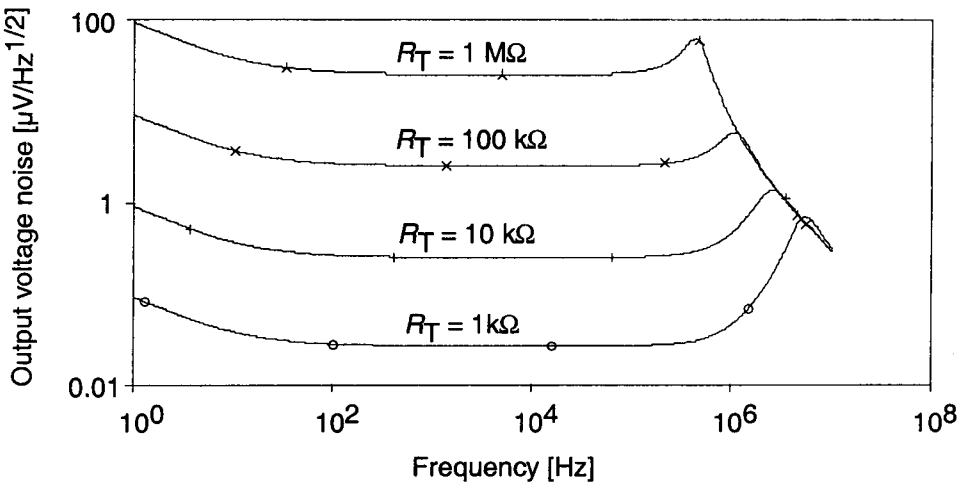

Fig. 9. Output voltage noise density of the bootstrap transimpedance amplifier (shown in Fig. 7) for a detector shunt resistance of 200 Ω and various transfer resistance values.

responsivity of the PV detector. With the described operational amplifier selection, the amplifier noise and the detector noise were equalized at the highest signal gain of 10^8 V/A. For a measurement relative uncertainty of 1 % (k=1) a signal range from about 4 nA to 1 mA could be achieved with the described component selections. As calculated from the 1.6 A/W responsivity, the 4 nA detector current corresponds to a radiant power of about 2.5 nW at the 9 μm peak responsivity of the 2 mm diameter PV HgCdTe detector.

3.4. Output offset and drift.

The output offset voltage and its thermal drift is another concern if very large transfer resistance values are used. The output offset voltage, in terms of the input offset voltage, is:

$$V_{outos}=\frac{-R_T G_d V_{os1} * A_1/(A_1+1) + V_{os2}(1+R_T G_d/(A_1+1)) + (I_{B1}+I_{B2}+I_{dark})R_T}{1+sR_T C_T + \frac{1}{A_2}(1+sR_T C_T + \frac{R_T G_d + sR_T C_d}{A_1+1})} \quad \text{[V]} \quad (13)$$

where V_{outos} is the output offset voltage in V,

V_{os1} is the input offset voltage of the bootstrap amplifier in V,

V_{os2} is the input offset voltage of the transfer resistance amplifier in V,

I_{B1} is the input bias current of the bootstrap amplifier in A,
I_{B2} is the input bias current of the transfer resistance amplifier in A, and
I_{dark} is the dark current of the detector in A. (Usually, the dark current of an unbiased photovoltaic detector is zero.)

To evaluate a high offset voltage sensitivity case, we consider a 200 Ω detector with a 100 MΩ transfer resistance. Only 1 μV input offset voltage can produce 0.5 V output voltage. This observation is against intuition as both amplifiers provide equivalent open loop gain. In addition, a drift of 1 μV/K will produce a 0.5 V/K output drift. If such a system is desired for dc signal measurements then the amplifiers must be under temperature control and precise offset voltage trim has to be implemented. For ac (chopped radiation) measurements, the temperature control for the amplifiers may not be necessary but the offset trimming is still important to avoid saturation of the output voltage of the transfer resistance amplifier. Practical amplifiers are limited to one or two μV/K drift.

Care should be taken when high signal gains (transfer resistances) are selected because the very high feedback resistor and a very small detector shunt resistance can produce a very high closed loop voltage gain. The closed loop voltage gain, calculated as the inverse attenuation produced by the feedback network , can not be larger than the open loop gain of the transfer resistance amplifier. From this restriction and the noise gain considerations in Section 3.3, the practical limit of the feedback resistor for a 200 Ω detector shunt resistance will be about 100 MΩ. This feedback network gives a closed-loop voltage gain of 5×10^5, roughly equal to the open-loop voltage gain.

4. Conclusion

Because room temperature thermopiles and pyroelectric detectors do not have high enough sensitivities to measure weak signals from monochromators, HgCdTe detectors were selected as working standards for the 5 μm to 20 μm wavelength range. The high sensitivity and low uncertainty requirements for spectral responsivity measurements made it necessary to design linear and low noise photocurrent meters for both photoconductive (PC) and photovoltaic (PV) HgCdTe detectors. Using the results of the circuit analysis described here, high signal responsivities and low output noise can be achieved for the output of the preamplifiers even if very low detector resistances are applied.

PC detectors were used for the longer wavelength range where the detectors were biased with a dc current of 50 mA. A novel preamplifier was developed where the 50 mA bias

was produced from ten current-to-voltage converters connected in parallel. The advantage of this preamplifier design was that the dc output voltages of the individual operational amplifiers did not go into saturation and no compensating voltage source was used at the input. Accordingly, repeated compensations were not needed and the dominating noise of the compensating source was eliminated. The input voltage noise of the parallel connected converters corresponded to an NEP of 40 $pW/Hz^{1/2}$. The cold resistance of the cut-line free 3 mm by 3 mm detector was 15 Ω and the signal responsivity was 16 V/W. The measured NEP was an order of magnitude larger, dominated by the G-R noise of the current-biased PC detector. A radiant power range of 34 nW to 2.5 mW can be measured by this PC HgCdTe detector current meter with a relative standard uncertainty of 1 % (coverage factor k=1).

Bootstrapping transimpedance amplifiers were designed and implemented to increase the equivalent impedance of PV HgCdTe detectors. The impedance multiplication concept has been analyzed and the equivalent input resistance has been computed versus frequency. For a detector shunt resistance of 1 kΩ and a junction capacitance of 1 nF, the equivalent impedance was resistive and approached 400 MΩ up to 10 Hz. When this impedance multiplier was applied for a 200 Ω and 1 nF impedance of a PV HgCdTe detector, and it was combined with a transfer resistance amplifier, a range of transfer resistances from 1 kΩ to 100 MΩ could be implemented. The relatively wide range of transfer resistance is one of the advantages of active impedance compensation. The frequency dependent transimpedance (signal) gain of the bootstrap current-to-voltage converter was determined. The maximum 100 MΩ transfer resistance was dominated by the voltage gain for the input drift of the bootstrap amplifier. Also, this highest transfer resistance multiplied by the high detector conductance produced a high voltage gain for the input voltage noise of the bootstrap amplifier resulting in a noise equivalent photocurrent roughly equal to the PV HgCdTe detector noise current of 40 $pA/Hz^{1/2}$. This noise current was measured on the PV HgCdTe detector used in our PV HgCdTe radiometer and it was about an order of magnitude smaller than the measured G-R noise of the current-biased PC HgCdTe detector. With a relative uncertainty of 1 % (k=1), signals from 4 nA to 1 mA could be measured with the PV HgCdTe radiometer. The 4 nA detector current corresponds to a radiant power of 2.5 nW at the 9 μm peak responsivity (1.6 A/W) of the 2 mm diameter detector. The frequency dependent error voltage of the photocurrent-to-voltage conversion was determined.

The described frequency dependent gain equations and photocurrent measurement considerations can be applied to other PV and PC detectors as well. Such other devices are Ge, extended-InGaAs, InSb, and InAs photodiodes, and PbS or PbSe PC detectors.

5. References

1. A.L. Migdall and G.P. Eppeldauer, *Spectroradiometric Detector Measurements: Part III - Infrared Detectors*, NIST Special Publication 250-42, 1998.

2. G. Eppeldauer and L. Novak, Linear HgCdTe radiometer, SPIE Proc. Vol. 1110, Edited by A.J. Huber, M.J. Triplett, and J.R. Wolverton, 267-273 (1989).

3. J. Graeme, Photodiode Amplifiers, McGraw-Hill, New York, p. 77 (1996).

4. J.P. Makai, J.J. Makai, and J. Balazs, Noise characteristics of bootstrapped photovoltaic and photoconductive detectors, SPIE Proc. Edited by S.M. Goodnick, W.F. Kailey, R.E. Longshore, and Y-H Zhang, Vol. 3794, 108-114 (1999).

5. G. Eppeldauer, Chopped Radiation Measurements With Large Area Si Photodiodes, J. Res. Natl. Inst. Stand. Technol. **103** (2),. p. 153-162 (1998).

6. Identification of commercial equipment to specify adequately an experimental problem does not imply recommendation or endorsement by the National Institute of Standards and Technology nor does it imply that the equipment identified is necessarily the best available for the purpose.

7. J.W. Nilsson, Electric Circuits, 3rd Edition, Addison Wesley Publishing Company, Inc., USA, 1990.

About the Authors:

George P. Eppeldauer is a Ph.D. Electronics Engineer in the Optical Technology Division of the NIST Physics Laboratory. The National Institute of Standards and Technology is an agency of the Technology Administration, U.S. Department of Commerce.

Robert James Martin is a Florida Registered Ph.D. Electronics Engineer at Analog Digital Integrated Circuits (ADIC) Inc. in Longwood, Florida. ADIC is a small company that specializes in analog discrete and integrated circuit design.

☆U.S. GOVERNMENT PRINTING OFFICE: 2001-472-068/46003

NIST Technical Publications

Periodical

Journal of Research of the National Institute of Standards and Technology—Reports NIST research and development in those disciplines of the physical and engineering sciences in which the Institute is active. These include physics, chemistry, engineering, mathematics, and computer sciences. Papers cover a broad range of subjects, with major emphasis on measurement methodology and the basic technology underlying standardization. Also included from time to time are survey articles on topics closely related to the Institute's technical and scientific programs. Issued six times a year.

Nonperiodicals

Monographs—Major contributions to the technical literature on various subjects related to the Institute's scientific and technical activities.

Handbooks—Recommended codes of engineering and industrial practice (including safety codes) developed in cooperation with interested industries, professional organizations, and regulatory bodies.

Special Publications—Include proceedings of conferences sponsored by NIST, NIST annual reports, and other special publications appropriate to this grouping such as wall charts, pocket cards, and bibliographies.

National Standard Reference Data Series—Provides quantitative data on the physical and chemical properties of materials, compiled from the world's literature and critically evaluated. Developed under a worldwide program coordinated by NIST under the authority of the National Standard Data Act (Public Law 90-396). NOTE: The Journal of Physical and Chemical Reference Data (JPCRD) is published bimonthly for NIST by the American Institute of Physics (AIP). Subscription orders and renewals are available from AIP, P.O. Box 503284, St. Louis, MO 63150-3284.

Building Science Series—Disseminates technical information developed at the Institute on building materials, components, systems, and whole structures. The series presents research results, test methods, and performance criteria related to the structural and environmental functions and the durability and safety characteristics of building elements and systems.

Technical Notes—Studies or reports which are complete in themselves but restrictive in their treatment of a subject. Analogous to monographs but not so comprehensive in scope or definitive in treatment of the subject area. Often serve as a vehicle for final reports of work performed at NIST under the sponsorship of other government agencies.

Voluntary Product Standards—Developed under procedures published by the Department of Commerce in Part 10, Title 15, of the Code of Federal Regulations. The standards establish nationally recognized requirements for products, and provide all concerned interests with a basis for common understanding of the characteristics of the products. NIST administers this program in support of the efforts of private-sector standardizing organizations.

Order the **following** *NIST publications—FIPS and NISTIRs—from the National Technical Information Service, Springfield, VA 22161.*

Federal Information Processing Standards Publications (FIPS PUB)—Publications in this series collectively constitute the Federal Information Processing Standards Register. The Register serves as the official source of information in the Federal Government regarding standards issued by NIST pursuant to the Federal Property and Administrative Services Act of 1949 as amended, Public Law 89-306 (79 Stat. 1127), and as implemented by Executive Order 11717 (38 FR 12315, dated May 11, 1973) and Part 6 of Title 15 CFR (Code of Federal Regulations).

NIST Interagency or Internal Reports (NISTIR)—The series includes interim or final reports on work performed by NIST for outside sponsors (both government and nongovernment). In general, initial distribution is handled by the sponsor; public distribution is handled by sales through the National Technical Information Service, Springfield, VA 22161, in hard copy, electronic media, or microfiche form. NISTIR's may also report results of NIST projects of transitory or limited interest, including those that will be published subsequently in more comprehensive form.